

**Towards an understanding of abiotic-biotic  
interactions for the development of novel  
biocomposite materials**

Daniel John Oliver MChem MRSC

A thesis submitted in partial fulfilment of the requirements of Nottingham Trent University  
for the degree of Doctor of Philosophy.

July 2020

This work is the intellectual property of the author. You may copy up to 5% of this work for private study, personal or non-commercial research. Any re-use of the information contained within this document should be fully referenced, quoting the author, title, university, degree level and pagination. Queries or requests for any other use, or if a more substantial copy is required should be directed in the first instance to the owner of the Intellectual Property Rights.

## Abstract

Developing a fundamental understanding of the interplay between primary peptide sequence and interaction with the target substrate with respect to the synthesised product is an active research area. In this study, a one-pot synthetic route to ZnO-Au heterostructures was devised using peptide mediation as the reaction control. To achieve this, binding interactions of known gold binders including A3 (AYSSGAPPMPFF), AuBP1 (WAGAKRLVLRRRE) and AuBP2 (WALRRSIRRQSY) to gold substrates were investigated to explore the interplay between the primary sequence and overall binding efficacy of a given peptide. Kinetic and thermodynamic data was collected with the kinetics being explored using a Langmuir-Kisliuk kinetic model developed during the programme of research which is capable of fitting kinetic data from 0.1-800 $\mu$ M with a high quality of fit ( $\text{adj-R}^2 > 0.9$ ). This study found that positively charged amino acid diads in the peptide sequence had a higher affinity for the gold substrate than the sulphur containing residues (Cys, Met). Further, multiple histidine residues or histidine diads in a sequence had a high affinity for the  $\text{Au}_{(111)}$  surface and a far lower affinity for the  $\text{Au}_{(110)}$  and  $\text{Au}_{(100)}$  surfaces.

A hybrid binding sequence to facilitate a one-pot synthesis of ZnO-Au heterostructures was engineered from a known gold binding peptide A3 (AYSSGAPPMPFF) and a known ZnO binding peptide G-12 (GLHVMHKVAPPR) which has been extensively studied within the Perry group. The engineered ZA2 peptide (GLHVMHKAYSSGAPPMPFF) was used to synthesise ZnO in both the presence and absence of gold resulting in pseudospherical ZnO-Au microstructures and micron sized ZnO nanoflowers respectively.

To expand understanding of the impact of peptide mediation and gold inclusions on ZnO behaviour both Mie theory modelling and a novel spectroscopic method termed 2D Fluorescence Mapping (2DFM) were used to study these systems. By careful deconvolution of the spectroscopic features to extract defect state contributions 2DFM was able to identify the complex emissive state topology of semiconductors including anthracene, CdS, CdSe, TiO<sub>2</sub>, ZnS, ZnSe & ZnO. Applying 2DFM to ZnO crystals prepared using different synthetic routes it was possible to show that the synthesis conditions strongly impact defect concentrations with all samples prepared in the presence of peptides having similar defect populations. The findings from these studies can be used to engineer novel binding sequences for peptide-mediated synthesis and begin to study the interplay between the primary sequence and the defect states formed in the synthesised matter.

## Dedication

To Anna and my family for your endless love, encouragement and support.

## Acknowledgements

Firstly, I would like to thank Distinguished Professor Carole C. Perry for offering me this opportunity and her continued support and guidance throughout my PhD programme. Special thanks also go to Dr Victor Volkov for his valuable discussions, support and guidance. Without his expertise and vast knowledge of spectroscopy, some of this would not have been possible. Thanks to Professor John Wallis and Dr Gareth Cave for their help and support during this project. I am very grateful to the US Air Force Office of Scientific Research (AFOSR) for funding FA9550-1-16-2013.

Additionally, I would like to extend my thanks to Kathryn Kroon for her guidance, advice and support facilitating the development of my microscopy skills and providing helpful discussions throughout my PhD, JEOL for their guidance on how to get the most out of our TEM, Dr Monika Michaelis for her circular dichroism (CD) spectroscopy expertise, useful discussions and fantastic organisation/sample preparation for our synchrotron visits. Last but not least thanks go to Dr Frank Wien for his help and guidance and I am very grateful to the Synchrotron SOLEIL for the ability to use their CD facility and for funding 201702777.

I am grateful that on this journey I have been able to work with a fantastic team and would like to extend thanks to all members of the Biomolecular and Materials Interface Research Group (BMIRG), both past and present, with whom I have shared this amazing experience. Special thanks to both Dr Graham Hickman and Dr David Belton who were always available to teach me a new technique or provide helpful discussions. I am grateful for all the new friendships I have made along this journey, including those with people who regrettably are no longer with us.

Finally, I would like to thank all the technical, catering and estates staff who keep the university running and without their diligent work, none of this would have been possible. I would particularly like to thank Sue for her conversations and great coffee during my past 7 years at NTU.

# Table of Contents

Abstract	ii
Dedication	iii
Acknowledgements	iii
Table of Contents	iv
Table of Abbreviations	viii
Chapter I: Introduction	1
1.1 Introduction to Biomimetic Chemistry	1
1.2 Biomineralisation	2
1.3 The Peptide-Mineral Interface	3
1.4 Phage Display - Identifying potential binders from a large library of sequences	4
1.5 Binding Peptides Mediated Synthesis	5
1.6 Zinc Oxide - Gold Nanocomposites	6
1.7 Gold	8
1.8 Zinc Oxide	11
1.9 Project Outline and Aims	14
Chapter II: Experimental Methods	16
2.1 Circular Dichroism Spectroscopy/ Synchrotron Radiation Circular Dichroism Spectroscopy	16
2.2 Confocal Laser Scanning Microscopy	16
2.3 Electron Microscopy	17
2.3.1 Scanning Electron Microscopy	18
2.3.2 Transmission Electron Microscopy / Scanning Transmission Electron Microscopy	19
2.4 Isothermal Titration Calorimetry	20
2.5 Multi-Parametric Surface Plasmon Resonance	22
2.6 Powder X-Ray Diffraction	22
2.7 Solid Phase Peptide Synthesis	24
2.8 Solid-State Fluorescence Spectroscopy	25
2.9 Ultraviolet-visible-Near Infrared Spectroscopy	26

Chapter III: Peptide Binding Kinetics	27
3.1 Introduction	27
3.2 Materials and Methods	29
3.2.1 Solid Phase Synthesis of Gold Binding Peptides	29
3.2.2 Multiparametric Surface Plasmon Resonance (MP-SPR) Binding Studies	29
3.3 Results and Discussion	29
3.3.1 Low Concentration (“Single Molecule”) Binding Studies	29
3.3.2 High Concentration (“Biomineralisation”) Binding Studies	32
3.4 Conclusions	39
Chapter IV: Towards an understanding of engineering binding sequences for Au systems through kinetic and thermodynamic studies	40
4.1 Introduction	40
4.2 Materials and Methods	42
4.2.1 Synthesis of Uncapped Gold Nanoparticles	42
4.2.2 Solid Phase Synthesis of Gold Binding Peptides	42
4.2.3 Multiparametric Surface Plasmon Resonance (MP-SPR) Binding Studies	43
4.2.4 Isothermal Titration Calorimetry (ITC) Binding Studies	43
4.2.5 Synchrotron Radiation Circular Dichroism (CD) Studies	43
4.2.6 Transmission electron microscopy (TEM) Studies	45
4.3 Results and Discussion	45
4.3.1 High Concentration ‘Biomineralisation’ MP-SPR studies	46
4.3.2 Isothermal Titration Calorimetry Binding Studies	56
4.3.3 Peptide Conformation & Assembly Studies	65
4.4 Conclusions	72
Chapter V: Two-Dimensional Fitting Approaches Towards An Understanding Of Semiconductor Fluorescent Behaviour	74
5.1 Introduction	74
5.2 Materials and Methods	75
5.2.1 Zinc Oxide Nanorods	76
5.3 Characterisation	76
5.3.1 Zinc Oxide Nanorods	76

5.3.2 Tecan i-Control M200 Pro	77
5.4 Results and Discussion	78
5.4.1 Two-Dimensional Fluorescence Mapping (2DFM) Technique	78
5.4.2 Two-Dimensional Fluorescence Fitting Methods (2DFMtd)	82
5.4.3 2DFMtd Fittings	86
5.5 Conclusion	90
Chapter VI: Quantification and Engineering of Trap State Emission using Two-Dimensional Fluorescence Mapping for Solid State Zinc Oxide micro/nano structures	92
6.1 Introduction	92
6.2 Materials and Methods	94
6.2.1 Zinc Oxide Microspheres	95
6.2.2 Zinc Oxide Nanorods	95
6.2.3 Solid Phase Synthesis of the ZA2 Binding Peptide	95
6.2.4 Peptide Mediated Zinc Oxide Synthesis	96
6.2.5 Zinc Oxide - Peptide - Au composite one-pot synthetic route	96
6.3 Characterisation	97
6.4 Results and Discussion	100
6.4.1 ZnO 2DFM Emissive State Topology & Fitting	100
6.4.2 First Approximation of the Quantum Yield of ZnO 2DFM Emissive Transitions	116
6.4.3 Discrete Au inclusion SPR absorbance within a ZnO Matrix	125
6.4.4 Nonlinear Fluorescence Behaviour in ZnO	132
6.5 Conclusion	135
Chapter VII: Conclusions & Future Work	138
7.1 Findings	138
7.2 Future work	143
7.3 Conclusion	145
References	146
Appendix	156
A3: Peptide Binding Kinetics	156
A3.1 Linear Regression	156

A3.2 Freundlich Fitting	156
A3.3 Langmuir Isotherm	157
A3.4 Von Bertalanffy/Monomolecular growth model	158
A3.5 Double First-Order Model (DFO Model)	158
A3.6 Kisliuk Isotherm	160
A3.7 Richards' Curve/Generalized Logistic Function	162
A4: Towards an understanding of engineering binding sequences for Au systems through kinetic and thermodynamic studies	163
A4.1 Calculation of gold nanoparticle concentration	163
A4.2 Calculation of gold Binding site concentration	164
A4.3 Appendix Tables and Figures	165
A5: Two-Dimensional Fitting Approaches Towards Of Semiconductor Fluorescent Behaviour	166
A6: Quantification and Engineering of Trap State Emission using Two-Dimensional Fluorescence Spectroscopy for Solid State Zinc Oxide micro/nano structures Communications	183
Publications ( <a href="https://orcid.org/0000-0001-7877-0900">https://orcid.org/0000-0001-7877-0900</a> )	197
Oral and Poster Presentations	197
Presentation Prizes	197

## Table of Abbreviations

Abbreviation	Chemical Name
A3	AYSSGAPPMPFF
A3s	AYSSGAPMPPF
A3s-C8	AYSSGAPCPPF
A3s-T2	ATSSGAPMPPF
AFOSR	Air Force Office of Scientific Research
ART	Absolute Rate Theory
AuBP1	WAGAKRLVLRRE
AuBP2	WALRRSIRRQSY
BMIRG	Biomolecular and Materials Interface Research Group
BSE	Back-scattered Electron
CB	Conduction Band
CD	Circular Dichroism
CLSM	Confocal laser scanning microscopy
DIC	N,N'-Diisopropylcarbodiimide
DLS	Dynamic Light Scattering
DMF	N,N'-Dimethylformamide
DODT	2,2'-(Ethylenedioxy)diethanethiol
EDX	Energy-dispersive X-ray Spectroscopy
G12	GLHVMHKVAPPR
GT16	GLHVMHKVAPPRGGGC
HMTA	Hexamethylenetetramine
HRE	AHHAHHAAD
ITC	Isothermal Titration Calorimetry
MP-SPR	Multiparametric Surface Plasmon Resonance
NBE	Near Band Gap Emission
NMP	N-Methyl-2-Pyrrolidone
O <sub>i</sub>	Oxygen Interstitial
O <sub>Zn</sub>	Oxygen antisite
Pd4	TSNAVHPTLRHL
SE	Secondary Electron

Abbreviation	Chemical Name
SEM	Scanning Electron Microscopy
SMPE	Single Molecule Pulling Experiments
SRCD	Synchrotron Radiation Circular Dichroism
SRH	Shockley-Read-Hall
SRT	Statistical Rate Theory
STEM	Scanning Transmission Electron Microscopy
TEM	Transmission Electron Microscopy
VB	Valence Band
$V_o$	Oxygen Vacancy
$V_oZn_i$	A complex of an Oxygen Vacancy and Zinc Interstitial
$V_{Zn}$	Zinc Vacancy
ZA2	GLHVMHKAYSSGAPPMPF
$Zn_i$	Zinc Interstitial
$ZnO$	Zinc Oxide

# Chapter I: Introduction

The digital age has brought an unprecedented rate of human advancement in the past half-century, bringing with it new questions about the world around us and also where humanity fits into this new paradigm. This relentless development and progression since the industrial revolution has led to environmental pollution and destruction to keep up with humanity's ever-growing requirements. Recently, chemists have begun to look to nature to harness the techniques employed during chemical synthesis in the natural world. This biomimetic approach enables novel synthetic strategies to be developed leading to higher yields, greater control and novel materials while having the potential for a lower environmental impact.<sup>1,2</sup>

## 1.1 Introduction to Biomimetic Chemistry

Over the past 3.7 billion years of natural selection, a multitude of highly optimised materials, systems and processes have been developed. These include the hollow bones birds have to assist with flight<sup>3</sup> and processes such as biominerallisation. The biomimetic approach takes inspiration from existing materials and systems developed by nature to design and engineer novel materials and systems to solve current real-world problems.<sup>4–6</sup> There is an abundance of both current and historic examples where complex engineering challenges have been overcome through using the biomimetic approach. These include the historic Wright brothers' plane, Velcro<sup>7</sup> and the current development of biomimetic torsos to facilitate back brace design.<sup>8</sup>

Recently, materials scientists have been attracted to the promises of the biomimetic approach.<sup>9–14</sup> Particular attention has been directed towards the hierarchical structures generated by natural systems to form functional devices.<sup>15</sup> Examples of this include the reflective diffraction grating present on a butterfly wing producing brilliant colouration,<sup>16</sup> and the self-cleaning superhydrophobic surfaces of lotus leaves.<sup>14</sup> Through studying these systems and understanding both the chemistry and physics nature has employed, a conceptual shift has occurred where the traditional "heat and beat" or "top-down" synthetic approaches are no longer being used to turn precursor materials into the desired products. Instead, a "bottom-up" approach is becoming more favourable, where the desired products are obtained through the combination of its constituent building blocks.<sup>17,18</sup>

Inorganic nanomaterials are an excellent example of the "bottom-up" synthetic approach where the reactivity as well as the magnetic, optical and electronic properties of the

material differ between the nanoscale and macroscale.<sup>19–22</sup> Even gold, the noblest of the elements, becomes reactive on the nanoscale with catalytic behaviour being reported.<sup>19</sup> While progress has been made in developing synthetic routes to create materials with controlled structural properties, the synthetic conditions used require harmful reagents and solvents in both high pressure and high temperature environments which are not environmentally friendly. In contrast, the synthetic strategies implemented by nature to generate hierarchical structures use gentler synthetic conditions and environments at physiological temperatures, pH and pressure all while remaining in aqueous media.<sup>23</sup> The development of a clear understanding of “how” nature performs synthesis is paramount to developing novel “green” synthetic routes with high yields and precise control of nano-morphology. Through harnessing nature’s precise control, development of novel materials to solve current real-world problems with minimal environmental impact may be achievable.<sup>12,24</sup>

## 1.2 Biomineralisation

Biomineralisation is the process organisms use to form inorganic structures such as bones, nails or shells. Tetrapods use this process to develop skeletal structures to which muscular tissue can be attached, forming the biomechanical components required for a given function. These biominerals are formed from a complex interplay between specialised biomacromolecules which include carbohydrates, lipids and proteins with inorganic minerals such as magnetite, calcium carbonate, silica and hydroxyapatite. The structural properties of these biominerals can differ between vertebrate species, an excellent example of this is the relatively low density of rodent bones compared to their avian counterparts, which are required to have strong, stiff & lightweight skeletal structures to facilitate flight.<sup>3,25,26</sup>

Human bones and teeth are both composed of soft organic components and hydroxyapatite, a hard calcium phosphate-based mineral.<sup>25</sup> However, the mechanical properties of both biominerals are very different, with the enamel layer of human teeth being the hardest component present in the human body,<sup>27</sup> while bones are comparatively more plastic.<sup>28</sup> These properties are achieved through the composition of the enamel being predominantly hydroxyapatite (ca~ 96%) with the remainder being composed of organics and water.<sup>29</sup> These biominerals are also useful for forensic applications such as the story of growth, repair, ageing & trauma which are recorded in the biomineral for experts in forensics and palaeontology to decipher.<sup>30</sup>

While the examples described above have focused on vertebrate life, biomineralisation is fundamentally important to all life, with higher plants such as bamboo using silica to

strengthen shoots<sup>31</sup> and magnetotactic bacteria using magnetite for navigation.<sup>32</sup> Research into biominerallisation was inspired by the beautifully symmetrical highly ordered structures of silica diatoms,<sup>33</sup> which contain a level of complexity unattainable by classical wet chemistry synthesis.<sup>2</sup>

Generally speaking, the biominerallisation process<sup>30</sup> begins with ion encapsulation in either a nucleate or vesicle within a cell. This proceeds to be either combined with an organic matrix or deposited on an extracellular organic scaffold to direct the growth of the developing biominerall. The composition of this organic matrix/scaffold is important as the biomolecule-mineral (biotic-abiotic) interactions are critical during each stage of the biominerallisation process.<sup>34</sup> Initially, the proteins undertake a templating role where they direct the formation of the initial crystalline structure through either binding to the crystal or being incorporated inside the structure which impacts the available sites for further deposition of ions.<sup>1,13,35,36</sup>

The key to maintaining a high degree of control during these processes is the isolation of the developing biominerall to a confined space, with the dimensions of this space impacting the biominerall's growth through confinement.<sup>30</sup> Modifications to the chemical environment in this space strongly influence the properties of the developing mineral; this can be seen in nature during the development of a sea urchin's spicule, where the shape can be modified by varying the concentration of a signalling molecule (rVEGF).<sup>37</sup> However, this study looks to focus on the role that the peptides and proteins play in controlling and directing growth.

### 1.3 The Peptide-Mineral Interface

The role of peptides and proteins, both long chain sequences of amino acids, in biominerallisation has attracted the attention of many research groups due to unique properties such as self-assembly to from pre-organised scaffolds<sup>38</sup>, nucleation of biomineralls<sup>35</sup> and reduction of HAuCl<sub>4</sub> to Au.<sup>39</sup> Pre-organised scaffolds can direct biominerall structure and morphology during biominerallisation; an excellent example is the proteins which form the dentin matrix which direct the growth of the epitaxial hydroxyapatite formation.<sup>35</sup> Metal coordination, observed in naturally occurring structures such as Cys<sub>2</sub>-His<sub>2</sub> zinc fingers is induced by chelating side-groups on amino acids,<sup>40</sup> for zinc fingers these are the imidazole group present on His.<sup>41</sup> Finally, these sequences are capable of recognising specific crystallographic facets and then binding with facet specificity to the growing inorganic material, for example the GT-16 ZnO binding sequence which controls the aspect ratio of nanorods formed using the HMTA synthetic route due to a binding preference to the (0001) crystal facet;<sup>42</sup> this binding to the surface

of the developing biomineral is termed “capping”. Through capping a peptide is effectively able to lower the surface energy of a given facet which in turn controls the direction of mineral growth along specific crystal planes.<sup>43</sup> A given peptide’s facet-recognition is highly dependent on its primary & secondary structure, with the recognition of the peptide ultimately determining the size, shape, crystallinity and catalytic properties of the formed nanomaterial.<sup>43,44</sup>

These properties are fundamental in the biofabrication process, allowing the biomolecule to have multiple roles as a linker, scaffold, binder and/or nucleator during the biominerallisation process, by facilitating a potentially “green” synthetic route. However, for this potential to be realised a fundamental understanding of the mechanism which operates at the biomolecule-material interface needs to be developed and as of time of writing this is an active research area. A complex interplay of interactions governs the biomolecule-material interface. These factors include: material structure, environmental pH, ion concentration, biomolecule concentration, temperature, aggregation and surface chemistry.<sup>45</sup>

For materials science to reach a state where the use of peptides and proteins are mastered and routinely used as efficient, specific, self-assembling synthetic tools for material synthesis, the chaotically intertwined variables must be carefully characterised and understood.<sup>46</sup> Furthermore, the development of this mastery of peptide-material interactions has the potential to bring a paradigm of biotechnological materials for advanced applications with minimal biological rejection.<sup>47–49</sup> To realise this goal, first the sequences which have an affinity to a surface must be determined and to achieve this we employ a technique called phage display. This is a biopanning technique used to determine binding sequences for a given surface from libraries which possess more than  $10^9$  different sequences.

#### 1.4 Phage Display - Identifying potential binders from a large library of sequences

Phosphoprotein which is present in the dentine matrix was the first identified inorganic binding protein which is involved in the mineralisation of hydroxyapatite. The link between a protein’s properties and its subsequent function was limited; however, it was understood the location, high molecular weight and high serine content of the protein were important properties for the epitactic nucleation of the dentine matrix.<sup>35</sup> Subsequently, researchers focused on identifying more inorganic binding proteins and studying their mechanisms which facilitated the replication of some mechanisms *in vitro*.<sup>50–52</sup> Despite these efforts there remained a shortage of identified mineralisation proteins, which was a major limitation to studying the nature of biotic-abiotic interfaces.<sup>53</sup>

The development of the phage display technique revolutionised the process of identifying binding sequences, as a series of randomised amino acid chains are screened against a given material such as plastics or inorganic matter in either a surface or nanoparticulate form.<sup>54</sup> To understand the impact of this technique on the field both George P. Smith and Sir Gregory P. Winter, the developers of this technique, were awarded the 2018 Nobel Prize in Chemistry.<sup>55</sup>

Phage display involves exposing a phage library which contains between  $10^6$ - $10^9$  unique peptide sequences, expressed on the phage's virion surface, to the substrate of interest.<sup>54</sup> The phages may bind to the substrate through the exposed sequences during an incubation period after which the substrate is washed to remove any unbound phage. The bound phage is then removed and amplified through infecting E. Coli. The resultant screened library is then exposed again to the substrate and the cycle repeated. Eventually, only the strongest binders will be left in the library and these can be sequenced to determine the binding sequences.<sup>54</sup>

Although phage display is an invaluable technique there are certain biases the experimentalist must be aware of, including an unequal distribution of amino acid expression. This is compounded by the fact that better binding sequences may fail to elute from the substrate or fail to infect the bacterial culture.<sup>56,57</sup> Methodologies have been developed to overcome these limitations, including the use of sonication for physical elution, and designing the sequence using statistical analysis of known physical/chemical property relationships for different sequences.<sup>57,58</sup>

Sequences isolated using phage display have been utilised in a range of detailed investigations into biomineralisation, peptide-mediated synthesis and binding behaviour with an array of materials including minerals (hydroxyapatite & calcite), metals (gold, silver, platinum & palladium) and metal oxides (silicon dioxide, germanium dioxide, titanium dioxide & zinc oxide).<sup>54,59-62</sup> These experimental investigations have provided an insight into how the sequence achieves material and facet specificity as well as the role of the peptide in the mechanisms of ion reduction and self-assembly.

## 1.5 Binding Peptides Mediated Synthesis

Nanoparticles, which are defined as materials possessing at least one dimension in the range of 1-100nm,<sup>63</sup> are desirable materials for a multitude of applications<sup>64-67</sup> due to their unique properties which are not expressed in either molecular compounds or the bulk material.<sup>68</sup> Synthetic conditions and control play a large role in the final properties of the

material including its surface chemistry, the surface to volume ratio and any electronic or quantum effects the matter may exhibit. Therefore, the ability for peptides to control and mediate the synthesis of the nanoparticles through stabilisation, directed growth, bridging/linking and capping can enable the properties of the product to be tuned for a given application during synthesis.<sup>43,44</sup>

Sequences identified through phage display and derived mutants have been found to bind to the surface of the developing nanomaterial and direct the formation; one such example is the use of known ZnO binding sequences G-12 and GT-16, which can control the aspect ratio of nanorods formed using the HMTA synthetic route due to a binding preference to either the (0001) or (1010) crystal facets.<sup>42</sup> The ability for facet and surface recognition can be disrupted through altering the buffer conditions of the reaction mixture, this can cause co-precipitation of both the buffer and peptide incorporating them in the developing mineral.<sup>69</sup> However, the synthetic application of peptides is not just limited to the formation of discrete nanoparticles, they can also be used to develop intricate superstructures formed of both organic and inorganic matter. The double-helical superstructures formed from gold and the PEPAu sequence are a perfect example as it showcases its unique optical and plasmonic properties.<sup>70,71</sup>

Inspired by these previous research efforts, this study seeks to develop a technique to understand how the defect states present in ZnO are affected by the synthetic strategy. The derived technique was used to study a range of ZnOs including a ZnO-Au nanocomposite material which has been synthesised using a novel one-pot peptide-mediated synthetic route. Discrete gold inclusions in ZnO-Au composites have been reported to enhance catalytic performance compared to ZnO matter.<sup>72-74</sup> Determining the effect of the synthetic route used and/or the presence of gold inclusions on the defect states present in ZnO matter would enable the engineering of new devices for optoelectronic or catalytic applications.

## 1.6 Zinc Oxide - Gold Nanocomposites

The aforementioned ZnO-Au nanocomposite matter belongs to the semiconductor-metal composite family of materials which have a wide range of applications including: charge rectification,<sup>75,76</sup> thermoelectric devices,<sup>77-79</sup> chemical sensing/biosensing,<sup>80-82</sup> nonlinear optics,<sup>83,84</sup> photocatalysis,<sup>85-87</sup> photovoltaics<sup>88,89</sup> and SERS.<sup>90,91</sup> From this multitude of potential applications ZnO-Au based nanocomposite materials are best suited for high performance biosensing and photocatalytic applications.<sup>72,80</sup>

The fabrication methods for ZnO-Au nanocomposite materials that have been reported in literature focus either on sputtering processes or use of rigid thiol linkers<sup>72,80,92</sup> to locate nanoscale gold particulates onto the ZnO structure. While these techniques attach the Au particles to the ZnO surface, the Au is not an intrinsic part of this structure. To overcome this Wang *et al.* proposed a synthetic method in 2007 which used ZnO nano-seeds to facilitate the precipitation of Au<sup>0</sup> from solution using a citrate reducing agent.<sup>93</sup> Although this synthetic strategy was successful, the technique did not allow for the properties of the formed nanocomposite to be tuned. Thiol linkers were a suggested modification to the synthesis proposed by Wang *et al.*; however, thiol groups are non-specific in a system where both Au and ZnO are present. This study proposes an alternative approach, where peptide-mediated synthesis would be used as a synthetic strategy to develop tunable ZnO-Au nanocomposites. The peptide-mediated strategy enables the experimentalist to control the formation of the nanomaterial while remaining a wet synthetic technique, offering benefits of hierarchical manufacturing using existing reaction setups, meaning this is a cheap manufacturing method.

The proposed one-pot peptide-mediated synthesis method requires a bespoke peptide sequence with discrete ZnO and Au binding regions. Leveraging previous ZnO binding studies performed within the Perry research group<sup>42,94,95</sup> the ZnO binding region was developed from the G12<sup>42</sup> (GLHVMHKVAPPR) sequence - a known ZnO binder with the ability to control the growth of ZnO during hydrothermal synthesis.<sup>42</sup> Previous studies have shown that the N-terminus of G12 is important for ZnO binding; however, the APPR motif at the C-terminus is not required. Consequently, GLHVMHKV was chosen as the ZnO binding region of the bespoke sequence developed, herein referred to as ZA2.

To develop the Au binding region this study proposes a series of binding studies similar to those conducted previously for ZnO. Known gold binding peptide sequences determined using phage display and reported in the literature including A3<sup>39</sup>, AuBP1<sup>96</sup>, AuBP2<sup>96</sup> and Pd4<sup>97</sup>, for see sequences see table 1.1, are screened to determine the optimum sequence to couple with G12 for ZA2. The mediation behaviour of these sequences is akin to G12 with the size of the Au particles formed being dependent on the sequence used.<sup>44</sup>

Table 1.1 - Peptides used in this study with their corresponding one-letter sequence.

Peptide Name	Sequence
AuBP1 <sup>96</sup>	WAGAKRLVLRRE
AuBP2 <sup>96</sup>	WALRRSIRRQSY
HRE <sup>9</sup>	AHHAHHAAD
Pd4 <sup>98</sup>	TSNAVHPTLRHL
A3 <sup>39,99</sup>	AYSSGAPPMPFF
A3s	AYSSGAPMPPF
A3sT2	ATSSGAPMPPF
A3sC8	AYSSGAPCPPF

### 1.7 Gold

Gold is a naturally occurring heavy metal which is inert to most acids and bases, making it the noblest of all the metals.<sup>100</sup> Interestingly, while very inert<sup>68</sup>, gold has a wide range of oxidation states ranging from -1 to +5. The most common of these oxidation states are +1 and +3, which form aurous and auric compounds respectively. Due to its relative rarity and resistance to corrosion, bulk gold has a long historic use in both jewellery and coinage applications.<sup>101</sup> Gold nanoparticles also have historic use with the earliest known application being the Lycurgus Cup from the 4th century AD; the cup appears green under reflected light and red under transmitted light.<sup>102</sup> It is likely that the creators of this cup did not know they had made gold nanoparticles when they added gold salts to the molten glass and the modern study of gold nanoparticles would not occur until Faraday's research in 1857.<sup>103</sup>

In the past century, the study of gold nanoparticles has become a broad new sub-discipline within the field of colloids and surfaces.<sup>104</sup> Due to the properties of the gold particles being both size and morphology dependent, a multitude of different synthetic routes have been devised using a range of different reducing and capping agents to control these parameters.<sup>105</sup> The most renowned of these methods is the Turkevich synthesis which uses citrate ions as both the reducing and capping agent.<sup>106</sup> However, as previously mentioned, materials science has begun to move away from these heat and beat methods, looking for a higher degree of control.

Using phage display a series of gold binding sequences have been identified including A3<sup>39</sup>, AuBP1<sup>96</sup>, AuBP2<sup>96</sup> and Pd4.<sup>97</sup> All these sequences are able to mediate the growth of spherical gold nanoparticles in biomimetic conditions with the size of the particle formed being dependent on the sequence used.<sup>44</sup> More elaborate sequences such as PepAu are capable of generating 3D motifs.<sup>70</sup>

To understand the complex control mechanisms and codependent behaviours involved in biomimetic synthesis both kinetic and thermodynamic experimental studies are required. Such experimental data allows for the development of novel models and furthermore broadens our understanding of required amino acid composition when developing bespoke peptide/protein sequences. Systematically testing different condition parameters such as the role of salinity in the reaction medium or primary structure of the peptide/protein used allows for the elucidation of key reaction components in biomimetic synthetic routes. An excellent example is the LDHSLHS silica binding peptide where the peptide-SiO<sub>2</sub> interaction shows a strong enthalpic drive in saline media (0.2M NaCl) driving the whole system to become more ordered.<sup>107</sup> While these investigations into the ideal composition of the reaction medium are important they are outside the scope of this study which will focus on key components of the primary sequence for effective gold binding. The primary sequence is of particular interest to this study as it governs the available chemistry and higher ordered structures (secondary, tertiary and quaternary structure) for a given peptide. An excellent example of this is A3 where the Tyr<sub>2</sub> residue allows for the reduction of the HAuCl<sub>4</sub> to Au<sup>0</sup>,<sup>39</sup> while the 7,8 and 10,11 Pro diads introduce a prolines twist either side of the Met<sub>9</sub> group which influences the ability of Met<sub>9</sub> to interact with a Au surface.<sup>98</sup>

Traditional experimental and computational binding studies focus on simplistic systems at low concentration which pushes the system to a Langmuir paradigm,<sup>96,98,108</sup> focusing solely on one peptide interacting with the surface and ignoring any peptide-peptide interactions which might cause constructive or destructive effects. The experiments performed as part of this study will use concentrations reflecting synthetic conditions where ‘high’ concentrations ( $1 \text{ mg}\cdot\text{mL}^{-1} \approx 800 \mu\text{M}$ ) are routinely used.<sup>39,42</sup> Ultimately, the strongest binder from these studies will be used for the Au binding region of the bespoke ZA2 sequence, which will be used in high-concentrations for one-pot ZnO-Au synthesis. Therefore, the binding studies undertaken will focus on higher concentration regimes (25, 50, 100, 200, 400 & 800  $\mu\text{M}$ ) to reflect the conditions which will be used for the ZA2 sequence.

Selecting the correct gold substrate to use in binding studies is of fundamental importance as the substrate used can directly impact the results collected. Gold is available in multiple forms; however, surfaces and nanoparticles are preferred for binding studies.<sup>96,109</sup> When comparing surfaces and nanoparticles multiple factors must be considered: firstly, the influence of surface curvature on the amino acid binding behaviour<sup>110</sup> and secondly the surface/facet present as this will also directly impact the binding behaviour, for

example the A3 binding peptide prefers to interact with Au<sub>(111)</sub> surfaces compared to Au<sub>(100)</sub> surfaces.<sup>98</sup> Comparing Au substrates, see table 1.2, the observable behaviour will be different for each system.

Table 1.2 - Comparison of the crystal facets/planes and surface curvature properties of gold surfaces and gold nanoparticles.

Au Substrate	Crystal Plane/Facets	Surface Curvature	Techniques used for
Surface	Au <sub>(111)</sub>	None	MP-SPR, QCM-D <sup>96</sup>
Nanoparticles <sup>111</sup>	Au <sub>(111)</sub> , Au <sub>(110)</sub>	Dependent on particle size & shape	ITC, Dye displacement studies <sup>109</sup>

The substrate selection also influences the technique used where surfaces facilitate the collection of kinetic data through techniques including MP-SPR and QCM-D. In contrast, using nanoparticles allows for the collection of thermodynamic data, for example using isothermal titration calorimetry. This study proposes using both MP-SPR and ITC to compare the thermodynamic constants obtained from the two gold substrates using a library of known gold binders, see table 1.1.

To obtain thermodynamic constants from kinetic data a kinetic model must be used to obtain a conceptual understanding of the underlying binding processes and kinetic constants. While empirical kinetic models exist this study shall focus on analytical solutions where terms have physical relevance. The most commonly used analytical model is the Langmuir kinetic model (monomolecular model), this is a 1:1 binding model with the following assumptions:<sup>112</sup>

1. The surface has a specific number of binding sites where the analyte can be adsorbed
2. The surface of the adsorbent is in contact with a solution containing the analyte which is strongly attracted to the surface.
3. The adsorption solely involves the formation of a monolayer where no further adsorption occurs.

The Langmuir model is limited to investigating systems where solely monolayer formation occurs as multilayer formation is not accounted for and no peptide-peptide interactions are considered. However, as higher concentration systems are being approached peptide-peptide interactions could become more prevalent meaning the Langmuirian assumptions would be invalid. To model these more complex kinetic processes accounting for mobile precursor kinetics which allows for a variety of adsorbate behaviour pre-adsorption, we can employ the Kisliuk adsorption model<sup>113</sup> which defines a precursor state that occurs when the adsorbate is proximal to the surface but not bound.

This study will review existing kinetic models to determine and compare their assumptions and relevance to peptide binding kinetics. Of particular interest to this study is the ability of Langmuirian and Kisliukian kinetics to fit kinetic data of the A3 sequence adsorbing onto a Au<sub>(111)</sub> surface under both a low and a high concentration regime as a representative system. Both kinetic models assume that all the surface sites are homogeneous which is a valid assumption as Au<sub>(111)</sub> sensors will be used in this study. It is hypothesised that under higher concentrations the simplistic 1:1 binding model such as the Langmuir kinetic model will no longer be suitable due to the assumptions no longer being valid. If the proposed hypothesis is true perhaps the more complex Kisliukian kinetics will offer a better description of the processes occurring in these systems. The aim for this study is to determine if one kinetic mode will be applicable across the complete concentration range.

Upon understanding the ideal kinetic model to explore the kinetic binding studies the derived thermodynamic constants will be compared to thermodynamic constants determined from isothermal titration calorimetry (ITC). Circular dichroism (CD) spectroscopy will be used to evaluate any structural changes that occur on binding and how this may impact the entropy of the system. Finally, transmission electron microscopy (TEM) was used to observe if any self-assembly/aggregation behaviour was observed. All this information will be used to determine which known gold binder would be best suited for the Au binding region of the ZA2 sequence.

### 1.8 Zinc Oxide

Zinc Oxide (ZnO) is a naturally occurring group II-VI binary semiconductor which has been widely studied for the past 6 decades.<sup>114–118</sup> While ZnO does occur naturally as the zincite mineral,<sup>119</sup> the majority of ZnO available is produced synthetically.<sup>120</sup> Through the use of different synthetic conditions, 3 different polymorphs can be produced: RockSalt, Zinc Blende & Wurtzite. The former 2 polymorphs are cubic systems whereas the latter is hexagonal.<sup>121</sup> The wurtzite polymorph is of particular interest to this study as it is known for its structural diversity with respect to native defect states, and has the highest stability out of all the polymorphs under ambient conditions. Depending upon the preparation technique selected single crystals,<sup>122</sup> thin films,<sup>123</sup> wires,<sup>124</sup> nanocrystals<sup>125</sup> and nanobelts<sup>126</sup> can be formed, each with different electronic and optical properties. The tunable optical and luminescence characteristics<sup>127–129</sup> of ZnO make the II-VI semiconductor suitable for a range of applications which include: medicine,<sup>130,131</sup> engineering novel electronics,<sup>132–134</sup> flat-panel displays<sup>129,135,136</sup> and sensing devices.<sup>137,138</sup>

ZnO is ionic in nature which causes lattice stability issues, particularly when ZnO matter with high surface to volume ratios is placed in an aqueous environment. The instability of the lattice can lead to a series of point defects in the lattice which include species such as Zn interstitials ( $Zn_i$ ) & oxygen vacancies ( $V_O$ ). The presence of point defects will affect both the optical response of photoexcited ZnO and the lattice constants for this matter.<sup>139–144</sup> The lattice constants for ideal wurtzite ZnO are  $3.2488 \pm 0.013 \text{ \AA}$ ,  $5.2059 \pm 0.0016 \text{ \AA}$  and  $1.5983 \pm 0.0053$  for the  $a$ -parameter,  $c$ -parameter &  $c/a$  ratio respectively;<sup>139–144</sup> however the reported uncertainty is comparable to the  $0.01 \text{ \AA}$  uncertainty found in the gold lattice constant.<sup>145,146</sup>

Variation in the lattice constants caused by point defects can impact the band structure of ZnO, which is of fundamental importance as it determines the material's potential utility. Theoretical approaches to determine the band structure have been used to varying degrees of complexity and success.<sup>147–150</sup> In parallel, experimental studies have also been used to probe the band structure,<sup>116,151,152</sup> using techniques such as XPS to measure the core electronic levels present in the material and determine the location of the Zn 3d level electrons.<sup>153</sup> The first published theoretical work on the band structure of ZnO<sup>147</sup> proved to be inaccurate when the predicted values were compared to those determined experimentally. Future calculations would simplify the system by considering the Zn 3d states as core levels, these calculations had a good qualitative agreement with the experimental findings.<sup>148,149,154,155</sup> However, it was not until the influence of the s- and p-derived valence bands were considered that a more quantitative agreement was reached.<sup>150,156–158</sup> The band-gap value was determined to be ca~  $3.3 \text{ eV}$ <sup>117</sup>, with ZnO being classified as a wide band-gap semiconductor with native n-type doping. The n-type doping arises from oxygen vacancies or zinc interstitials in the lattice.<sup>159</sup>

Although the lattice parameters are of fundamental importance this study will focus on the optical response of ZnO under photoexcitation and use this to determine the population of defect states within the sample. Optical spectroscopy is well suited for characterising the electronic, structural and dynamic properties of solids<sup>160</sup> making it a natural choice to explore the properties of semiconductors such as ZnO. This study will focus on fluorescence spectroscopy in particular as it directly measures the photons produced by radiative relaxation processes within the sample. These processes include radiative recombination, stimulated emission & relaxation to trap/defect states.

When photons interact with semiconductors, electron-hole pairs are induced, promoting the electrons from their ground state to an excited state. The electron is unlikely to remain in the excited state permanently and instead can undergo radiative recombination where

the electron hole pair recombines through relaxation of an electron from the conductance band (CB) to the valence band (VB). Alternatively, radiative decay occurs where an electron relaxes to a lower energy in-band gap trap state within the material. Both of these types of relaxation are forms of spontaneous emission where the energy absorbed by the material is released as photons.<sup>161,162</sup> The electrons which relax to an in-gap trap state primarily undergo non-radiative recombination with their respective holes, this trap-assisted recombination is referred to as Shockley-Read-Hall (SRH) recombination.<sup>163</sup>

Generally, ZnO spontaneous spectral emission can be divided into two subsets: ultraviolet (UV) emission and visible emission, for wavelengths see table 1.3. The ultraviolet emission is a subset of discrete narrow emissions generated by band gap transitions,<sup>164,165</sup> while the visible emission can emit over a broad spectral range with discrete emission often categorised as ‘green’,<sup>129,136</sup> ‘blue’,<sup>166</sup> ‘yellow’<sup>166,167</sup> and ‘red’.<sup>159</sup> Visible emissions can be attributed to native trap states within ZnO (i.e. V<sub>Zn</sub>), where CB->trap state transitions produce spontaneous fluorescence emission. The ability to tune the spectral emission of ZnO with no additional dopants solely through controlling defect/trap state’s populations within the matter is attractive for a range of photoelectric applications. While most of the tunable emission resides within the visible range, low energy transitions have been reported to produce emission in the near infrared region.<sup>168</sup> Consequently, the spontaneous emission from ZnO directly reports on the defect states present within the matter.

Table 1.3 - Wavelengths and corresponding energies for ZnO emission

	Colour	Wavelength (nm)	Energy (eV)
Visible	UV <sup>164,165</sup>	387	3.20
	Blue <sup>166</sup>	440	2.82
	Green <sup>129,136</sup>	510	2.43
	Yellow <sup>166,167</sup>	640	1.94
	Red <sup>159</sup>	708	1.75

A two-dimensional approach to spontaneous emission spectroscopy (SES) was reported by Marose *et al.* for molecular systems<sup>169</sup> with application for monitoring bioprocesses which has been further developed by Kovrigin.<sup>170</sup> Due to the nature of spontaneous emission in solid state materials with allowed and disallowed transitions due to symmetry effects, utilising 2D-SES has the potential to view the emission topology. This allows for observation of the emissive states which are present within a material with dependence on excitation energy.

The application of 2D-SES to semiconductors is a novel approach. In this study the viability and potential of this technique is explored with the aim to determine if two-dimensional fluorescence spectroscopy can be used to analyse the states present, including in-band defect states, within semiconductors for potential academic and QC industrial applications. Defect state population and emissive behaviour for ZnO samples formed using different synthetic conditions will be investigated to provide information about how to control defect state populations through modulating the wet chemical synthetic conditions.

### 1.9 Project Outline and Aims

This study seeks to determine the applicability of 2D spontaneous emission spectroscopy as a tool capable of analysing the states present, including in-band defect states, within semiconductors for potential academic and QC industrial applications. ZnO matter is of particular interest as this material is known for its structural plasticity; understanding the relationship between defect state populations and the synthetic route used would facilitate a greater degree of control during wet chemical synthesis.

Multiple different ZnO samples synthesised using different synthetic routes will be tested as well as a ZnO-Au nanocomposite material which has been synthesised using a one-pot peptide-mediated synthetic route. The discrete gold inclusions in ZnO-Au composites have been reported to enhance catalytic performance compared to ZnO matter.<sup>72-74</sup> Understanding the effect of the synthetic route used and/or the presence of gold inclusions on the defect states present in ZnO matter would enable the engineering of new devices for optoelectronic or catalytic applications.

The proposed one-pot peptide-mediated synthesis method requires a bespoke peptide sequence with discrete ZnO and Au binding regions, herein referred to as ZA2. Leveraging the previous ZnO binding studies performed within the research group<sup>42,94,95</sup> the ZnO binding region was developed from the G12 (GLHVMHKVAPPR) sequence.<sup>42</sup> For the gold binding region of the ZA2 sequences kinetic and thermodynamic peptide-Au binding studies will be undertaken, investigating known binding sequences such as A3<sup>39</sup>, AuBP1<sup>96</sup>, AuBP2<sup>96</sup> and Pd4.<sup>97</sup> The kinetic studies will focus on developing an understanding of the peptide interactions at the Au<sub>(111)</sub> surface exploring both Langmuir and Kisliuk kinetic models. Thermodynamic studies will explore binding interactions with gold nanoparticles which have the Au<sub>(111)</sub>, Au<sub>(110)</sub> and Au<sub>(100)</sub> facets. This information will be used to determine which known gold binder would be best suited for the Au binding region of the ZA2 sequence.

To conclude, this study proposes to investigate the binding kinetics of peptide-Au at high concentrations and review the kinetic models applied to these systems. The intention is to use this understanding to develop a bespoke hybrid binding sequence, ZA2, and use this sequence to synthesise ZnO-Au in a one-pot synthetic route. Finally, the applicability of 2D spontaneous emission spectroscopy will be assessed as a tool capable of analysing the states present, including in-band defect states, within semiconductors for potential academic and QC industrial applications.

## Chapter II: Experimental Methods

The experimental techniques used in this study are compiled below in alphabetical order.

### 2.1 Circular Dichroism Spectroscopy/ Synchrotron Radiation Circular Dichroism Spectroscopy

Circular Dichroism (CD) spectroscopy is used to characterise chiral molecules due to their different interaction and absorption of left and right circular polarised light.<sup>171</sup> The differences in absorption behaviour are due to the different refractive indices of the two radiation sources, this leads to different velocities through the chiral medium and different levels of absorption. This is a commonly used technique to identify and quantify the secondary structures present in biomolecules in a solvent. Due to the wide ensemble of possible secondary structures which can be formed, empirical methods are applied utilising knowledge derived from biomolecules with known crystal structures and CD spectra.<sup>172</sup>

Chromophores which are responsible for the colours of an organic compound are present in biomolecules such as C=C with a  $\lambda_{\text{max}}$  value of 175 nm or C=O with  $\lambda_{\text{max}}$  values of 190 & 280 nm. In a peptide bond, optically active groups are arranged in a planar orientation generating a chromophore<sup>171</sup>. If a chromophore is excited upon interaction with circularly polarised radiation the electronic and magnetic dipole moments will be altered, which in turn will affect the CD signal.<sup>173</sup> The excitation of different structural components in the biomolecule leads to a characteristic CD spectrum for the sample.<sup>174</sup>

In this study, CD spectra were collected in triplicate at 25°C using an Applied Photophysics (Massachusetts, USA) Chirascan spectrometer running the Pro-Data Chirascan software (v4.2.22) to collect in the range of 250-190 nm with an interval of 1 nm. The region below 190 nm was collected using synchrotron CD radiation and these datasets were combined to obtain the full spectrum. The sample in aqueous media was placed in a 0.01 cm Suprasil quartz cell (Hellma UK Ltd.). Analysis of the ensemble of secondary structural components was performed using the BeStSel web server.<sup>175,176</sup>

### 2.2 Confocal Laser Scanning Microscopy

Confocal laser scanning microscopy (CLSM), hereafter referred to as confocal microscopy, is an optical imaging technique. The improved imaging capabilities of this microscope are achieved by utilising a spatial pinhole to block out-of-focus light in image formation.<sup>177</sup> CLSM scans the sample utilising a series of moving mirrors to raster the beam linearly across the sample. However, due to mechanical limitations, some devices

utilise multiple pinholes on a spinning disk to achieve a faster scan rate to image the sample.

Unlike widefield microscopy where the interactions of photons with the specimen can be safely assumed to be independent of the illumination intensity, upon excitation with laser powers above 1mW non-linear response behaviour can be observed using a confocal microscope. These departures from a linear regime are due to the high flux levels achieved by CLSMs.

The ability to remove out of focus light from the image reaching the detector greatly improves the resolution and overall quality of the image obtained. This setup also enables higher resolution in the z-plane allowing for optical slices of a sample to be taken, assisting in determining 3D-localisation of fluorescent centres in a specimen. Through the use of mirrors, the fluorescent emission of the specimen can be separated into different spectral components and collected enabling localised spectra to be obtained for different fluorescent centres.

In this study, all confocal images have been collected on a Leica (Wetzlar, Germany) SP5 confocal microscope; the samples were dry crystalline matter placed on a borosilicate glass coverslip. The sample was held by gravity and intermolecular forces, no additional fixatives were used.

### 2.3 Electron Microscopy

Electron microscopy uses an electron beam as the illumination source in an evacuated chamber, to enable high-resolution images to be taken at the micro, nano or atomic scale depending upon the configuration of the microscope. The high magnification power which is achievable on electron microscopes compared to their optical counterparts is due to the maximal resolving power of the illumination source used. The relationship between resolving power and wavelength can be expressed as:<sup>178</sup>

$$R = 0.61 \frac{\lambda}{NA} \quad 2.1$$

Where  $R$  is the resolving power (nm),  $NA$  is the numerical aperture,  $\lambda$  is the wavelength (nm).

For visible light ( $\lambda_{avg} = 550$  nm) the resolving power is 200 nm; however on electron microscopes an accelerating voltage is used to obtain a higher resolution. For example using an accelerating voltage of 200keV increases the resolving power to 2.51pm. This

relationship between the accelerating voltage applied and the wavelength of the beam can be determined using the De Broglie equation, see equation 2.2.<sup>179</sup>

$$\lambda = \frac{h}{p} = \frac{h}{mv} = \sqrt{\frac{h}{2meV}} \quad 2.2$$

Where  $h$  is Planck's constant,  $p$  is the momentum of a particle,  $m$ ,  $v$  &  $e$  are the mass, velocity and charge of an electron respectively and  $V$  is the accelerating voltage.

When higher acceleration voltages such as 200-300 keV are used the electrons are travelling at 70% of the speed of light and relativistic effects occur. These relativistic effects include an increase in electron mass, length contraction and time-dilation. The relationship can be updated to include relativistic effects, see equation 2.3.

$$\lambda = \sqrt{\frac{h}{2meV}} \frac{1}{\sqrt{1 + \frac{eV}{2mc^2}}} \quad 2.3$$

Where  $c$  is the speed of light ( $299\ 972\ 458\ m\cdot s^{-1}$ ), this means the wavelength of an electron when an accelerating voltage of 200 keV is applied is 2.51 pm the resolving power of this beam depending on the lens setup is 1Å.

Common electron microscopes are transmission electron microscopes (TEM), scanning transmission electron microscope (STEM) and scanning electron microscope (SEM). These microscopes can be used to study micro and nano specimens to provide information on the morphology, aggregation, orientation and size populations. SEM is primarily used to study surface structures or near-surface structures in samples. STEM and TEM are more suited to imaging smaller samples (<100 nm) due to the higher resolving power of the beam where STEM provides information about the surface structures and TEM provides information about the composition through the specimen.

### 2.3.1 Scanning Electron Microscopy

Scanning Electron Microscopy (SEM) is used to analyse the morphology of substrates with micro/nano resolution. The sample is illuminated with a beam of electrons where an accelerating voltage (0-30 kV) is applied; the beam then travels through lenses and scanning coils before reaching the sample. These scanning coils deflect and position the beam rastering it across the sample. Once the beam reaches the sample it penetrates the surface, with the depth of the penetration being dependent on both the accelerating voltage and the density of the sample. Upon the beam penetrating the sample's surface, a

teardrop is formed generating different types of emission. These emissions include secondary electrons, backscattered electrons and x-rays.

The secondary electron (SE) emission is lower energy than that of the incident beam (5 eV), this means that only electrons <10 nm from the surface of the sample will be detected and imaged. However, high-energy reflected electrons from the incident beam produce back-scattered electrons (BSE). This emission can be correlated to the density of the centres present in the specimen providing qualitative elemental information. Characteristic x-rays are also emitted from a depth of <2 µm from the surface, these can be used to provide quantitative elemental information for the specimen (EDX).

In this study, the morphologies of samples were studied using a JEOL (Tokyo, Japan) JSM-7100F at an accelerating voltage of 5 eV. The SEM was fitted with SE and BSE detectors, image capture & storage was handled by a JEOL software packaged. An Oxford Instruments (Abingdon, United Kingdom) X-Max EDX unit was used for elemental analysis and the Aztec software package was used to collect, store and analyse collected data.

### 2.3.2 Transmission Electron Microscopy / Scanning Transmission Electron Microscopy

Transmission Electron Microscopy (TEM) is used to analyse thin specimens to obtain images with both high magnification and resolution. For materials science, it is routine to use accelerating voltages of 200 keV allowing for a high-resolution image to be taken and fresnel fringes to be observed. For higher resolution, 300 keV TEMs can be used which have aberration correction allowing for atomic resolution imaging.

Different types of electron source are available for these microscopes such as filaments (Tungsten or LaB<sub>6</sub>) or Field Emission Guns (FEG). The shape of the beam generated depends on the electron source used, which ultimately impacts upon its resolving power. The electron source forms the cathode in the microscope with the anode having a positive potential applied across it. This, in turn, accelerates the electrons down the column. During the electrons' transit down the column, they pass through apertures, astigmators and lenses. These align the beam down the column through the lenses and tidy the edge of the beam before reaching the sample. By this point, the sample is magnified around 50-100 times. The objective lenses further magnify the sample before reaching the projector lens and finally the phosphor screen or CCD camera for imaging.

Scanning transmission electron microscopy (STEM) mode rasters the electron beam across the specimen and behaves like an SEM with the BSE image being collected above the sample and the annular bright and dark field images being collected below the

sample. The greater resolving power of STEM provides an advantage over conventional SEM for nanoscale specimens.

In both TEM and STEM modes, characteristic x-rays are emitted from the sample and can be used to quantitatively characterise the elemental composition of the sample using an EDX detector.

The microscope used was a JEOL (Tokyo, Japan) 2100 Plus TEM/STEM with LaB<sub>6</sub> filament & energy dispersive X-ray fitted. TEM imaging was performed using a Gatan Rio camera and STEM imaging was performed using JEOL EM-24512SIOD. Samples were suspended in Type I water either in native solution or with BSA dispersal agent<sup>180</sup> and drop cast onto quantifoil 300 Mesh Cu grids (Quantifoil). EDX data was collected using JEOL EX-24200M1G2T and analysed using the analysis station software package provided by JEOL.

## 2.4 Isothermal Titration Calorimetry

Isothermal Titration Calorimetry (ITC) is a highly sensitive technique which is used to study the thermodynamics of chemical/biochemical interactions in a stepwise protocol. The instrument measures both endo and exothermic events as a reaction/interaction takes place. Experiments are performed by titrating a reagent such as a biomolecule into a sample solution which contains the other reagent such as silica. Upon each addition the thermal changes are recorded in a time-dependent manner with sampling usually occurring every 2 seconds and the corresponding region from each injection is integrated, allowing for quantitative characterisation of the given process ie. a binding interaction.<sup>181,182</sup> The dataset is reduced after integration to a concentration-dependent dataset allowing for a binding isotherm to be plotted and information about the concentration kinetics and thermodynamics to be obtained. This information includes; dissociative constant ( $K_D$ ), enthalpy ( $\Delta H$ ), entropy ( $\Delta S$ ), Gibbs free energy ( $\Delta G$ ) for the given interactions can be determined by:

$$\Delta G = RT \ln(K_D) = \Delta H - T\Delta S \quad 2.4$$

Where  $R$  is the ideal gas constant ( $8.314 \text{ J}\cdot\text{mol}^{-1}\cdot\text{K}^{-1}$ ),  $T$  is the temperature (K).

The instrumental setup consists of two main components: a stirring syringe assembly and a calorimeter which is composed of two thermally conductive chemically inert cells. The syringe assembly consists of a high precision syringe pump controlling a glass stirring syringe, this setup is employed to enable accurate injections of titrant while ensuring the distribution of the titrant is homogenous in the solution.

In the calorimeter, both cells are filled with the sample analyte in the same solvent. However, the sample cell will have the titrant added to it and the thermal differences between the cells will be compared and measured in power units ( $\mu\text{cal}\cdot\text{s}^{-1}$ ); this is known as differential power (DP) signal. As both these cells are being compared at every sampling window (2 seconds) it is critical that they are properly equilibrated before the experiment starts so a real measurement may be obtained. The DP is constantly monitored throughout the experiment and the time window corresponding to each injection is integrated to give a single DP value for that injection once the experiment is complete. This value reflects the energy absorbed or released in the system upon the interaction occurring, these values are then converted into normalised heat change ( $\text{Kcal}\cdot\text{mol}^{-1}$ ) which are plotted with dependency on the molar ratio.

Traditionally a blank dataset (ie peptide solvation) would be subtracted from the collected dataset (ie peptide-silica interaction) and either an identical or two independent sites binding model would be applied to the dataset,<sup>46,183</sup> however this is not always appropriate due to the complex nature of these interactions. Titrants such as polypeptides may form aggregates during solvation and behave differently when the macromolecule (silica) is present in solution. Therefore, the linear slope of the binding curve is fitted to obtain  $K_A$ . The accuracy of this value can be measured using the critical parameter (C) which is the product of the stoichiometry of the interaction ( $n$ ) and the associative constant ( $K_A$ ). The value of C should be between 10-100<sup>184</sup>, this value also determines the shape of the isotherm. To determine the overall  $\Delta H$  value<sup>185</sup> the amplitude of the interaction is taken. This empirical approach is advantageous for a complex system as it does not introduce any error by incorrectly modelling the system.

Due to sensitivity of the instrument, optimisation of the experimental parameters is required to satisfy the following criteria: i) the saturation endpoint of the reaction is reached, ii) appropriately space data points along the binding curve to determine its shape with enough points on the linear region & iii) ensure DP returns to basal value before next injection minimising injection-injection interference. Optimisation of the system can be achieved by altering the concentration of titrant and sample which alters the molar ratio and signal strength with the reference power being altered accordingly. The injection volume, duration and spacing are also altered to minimise interference. For the studies performed temperature was kept at a constant value of 25°C.

In this study, all ITC experiments were performed on a MicroCal VP-ITC (Malvern, UK). The raw data is extracted using Origin v7.0 using algorithms provided by MicroCal to

obtain the extracted datasets. The extracted data were analysed on Originlab Origin 2015 (Northampton, USA). For fitting a linear least-mean-square algorithm was used.

## 2.5 Multi-Parametric Surface Plasmon Resonance

Multi-Parametric Surface Plasmon Resonance (MP-SPR) is a powerful technique used to measure the kinetics of interactions in real-time. This technique is the development of Surface plasmon resonance (SPR) spectroscopy, which is an established technique used to measure biomolecule interactions in a label-free protocol.<sup>186</sup> The difference between conventional SPR and MP-SPR is the optical setup used, MP-SPR uses a goniometric SPR configuration which allows for the spectrometer to scan over multiple angles of incidence. In contrast a traditional SPR spectrometer solely operates at a fixed angle. This means both angular dependent SPR curves and time-dependent sensorgrams can be obtained from this technique. The sensorgrams allow for the study of the kinetics of interactions in real-time, making it ideal for studying surface interactions, whereas the angular SPR curves allow for the study of nanolayer formation and layer dynamics.<sup>187,188</sup>

In this study, we focus on studying surface interactions between peptides and (111) gold surfaces (Bionavis) we use a BioNavis (Tampere, Finland) SPR Navi 200 spectrometer operated by SPR-Navi software package provided by BioNavis. The temperature and flow rate for the system was fixed at 20°C and 23 µL·min<sup>-1</sup> respectively. The time-dependent sensorgrams were analysed using Origin 2015 and a range of different fitting methods have been applied.

## 2.6 Powder X-Ray Diffraction

Powder X-ray Diffraction (XRD) is a versatile and powerful technique used for the identification of the crystalline nature of solid-state samples. Each crystalline material has its own unique diffraction profile and therefore a unique XRD pattern. A crystalline phase is a highly ordered structure which is composed of elements such as atoms, molecules or ions. When the X-ray beam hits the sample the planes of atoms act as a diffraction grating scattering the radiation uniformly in all directions. These diffractions can be related to the constructive interference which is occurring using the following equation:<sup>189</sup>

$$n\lambda = 2d\sin(\theta) \quad 2.5$$

Where  $n$  is the order of the diffraction,  $\lambda$  is the wavelength of the radiation,  $\theta$  is the angle of incidence between the beam and sample (Bragg diffraction angle),  $d$  is the interplanar distance.

The intensity of the diffracted beam is plotted with dependence on  $2\theta$  to produce a diffraction profile, with each peak relating to a specific set of crystal planes present in the sample.<sup>190,191</sup>

There is a reciprocal relationship between the broadening of peaks in the diffraction profile ( $\beta$ ) and the size of the crystallite ( $D$ ). This is caused by a cumulative averaging in larger crystals, the bigger the crystals the more reflections and thus the greater the signal and sharper the peak. Using the Scherrer equation, the crystallites domain size can be determined, see equation 2.6.<sup>192</sup>

$$D = \frac{K\lambda}{\beta \cos(\theta)} \quad 2.6$$

Where  $K$  is the shape factor (0.9 for spherical crystals),  $D$  is the crystallite domain size,  $\lambda$  is the wavelength of the radiation,  $\theta$  is the Bragg diffraction angle and  $\beta$  is the full width at half maxima (FWHM) for the peak.

The values determined for the crystallite domain size are solely a lower bound as there are multiple additional factors which can cause peak broadening. So-called over-broadening is commonly caused by lattice defects such as interstitials, vacancies, dislocations and layer faults.<sup>193–195</sup> These defects cause lower overall order in the system and inhomogeneous strain which leads to varied shifts of  $2\theta$ .

In this study, XRD data has been collected using a PANalytical X'Pert PRO X-ray diffractometer using CuKa radiation ( $\lambda = 0.154060$  nm) to identify and characterise the crystal phases present in the samples. Polydimethylsiloxane (PDMS) filled aluminium sample holders were used to reduce the quantity of sample required and hold nanoparticulate samples. Diffraction profiles were collected for  $2\theta$  between 5–90°, using an accelerating voltage of 45kV, 40mA filament current, and a scan speed of 0.08 °·s<sup>-1</sup>. All diffraction profiles were collected at room temperature. Analysis of the diffraction profiles was performed using X'Pert-HighScore Plus (Version 4.5), where background subtraction, Fourier-filtering and peak identification methods were performed.

## 2.7 Solid Phase Peptide Synthesis

Solid Phase Peptide Synthesis is a technique which grows a peptide sequence on an insoluble polymer support (resin). These resins are available pre-loaded (with an amino acid already attached) or unloaded (with no amino acid attached). The sequence is constructed amino acid by amino acid moving from the c-terminus to the n-terminus, through a series of coupling and deprotection steps.<sup>196</sup> Upon completion of the peptide sequence the remaining protective groups (on the side chains) and the resin is removed in a cleavage process, this method was revolutionary as it allowed for fast synthesis with higher yields as the peptide is bound to the linker stopping polymerisation. While this method is vastly improved over the classical method, there are still considerations which must be made such as double coupling for R residues as there is a lot of steric hindrance due to the protective group chemistry used (Pbf protecting group). Another consideration is that the protective groups on the side chains are inert to the cleavage conditions for either the Boc or Fmoc chemistry selected to stop any side reactions occurring.

When Fmoc chemistry is used for the protection of the n-terminus of the residues, the cleavage solution used can be a strong acid (HF), a moderate acid (TFA) or a weak acid (low % TFA solution) with nucleophilic scavenging agents (ie. thioanisole) which react with the cationic species formed during cleavage. The cleaved peptide passed through a filter to remove the resin and precipitated in ice-cold diethyl ether and washed three times to remove any reagents leftover from the cleavage. The solvent is then evaporated off, techniques such as placing in a vacuum oven can be used to speed up the drying process.<sup>197</sup>

For this study, peptides were prepared using a CEM (Matthews, US) Liberty Blue microwave-assisted solid-phase peptide synthesiser. Preloaded Wang resins (Novabiochem) were used with Fmoc protective chemistry.<sup>198</sup> Amino acids were purchased pre-protected (Novabiochem) the following amino acids had protected side groups: R (Pbf), C (Trt), E (OtBu), K (Boc). The activator and activator base selected were N,N'-diisopropyl carbodiimide (DIC) and oxyma, both were prepared in DMF. The deprotect solution was piperazine in NMP/10% EtOH solution and all couplings were single couplings except for R which had a double coupling step. A one-step cleavage cocktail was used containing; TFA, thioanisole, DODT, Type I water and the peptide was precipitated in diethyl ether and washed 3 times. Upon evaporating to dryness the pellet was redissolved in water and lyophilised at -70°C using a Virtis-110 freeze-drying unit. Characterisation of the peptide was performed using an Applied Biosystems (Foster City, US) quadrupole time-of-flight MALDI and a Dionex (Sunnyvale, US) HPLC fitted with a UV

detector and Phenomenex C12 reverse phase column, to confirm the mass of the sequence and determine purity respectively.

## 2.8 Solid-State Fluorescence Spectroscopy

Fluorescence spectroscopy measures the electronic transitions of samples in both molecular and solid-state regimes. The electron transitions observed are stimulated utilising optical excitation by monochromated light typically from a flash xenon lamp source.

In solid-state metallic oxide systems upon excitation, electrons are first promoted from the valence band to an above band-gap excited state. These electrons dissipate some of the original excitation energy and relax to a lower vibronic energy state in the conduction band, this process is called internal conversion. Fluorescence emission occurs when the electrons, which are in the conductance band, return to the valence band. While the electron is returning to the valence band a photon is emitted with equivalent energy to the transition. The relationship between the energy of a photon and its wavelength can be expressed as:

$$E = h\nu = \frac{hc}{\lambda} \quad 2.7$$

Where  $h$  is Planck's constant ( $6.626 \times 10^{-34}$  J·s),  $\nu$  is the frequency of light (Hz),  $c$  is the speed of light ( $299\ 792\ 458\ \text{m}\cdot\text{s}^{-1}$ ) and  $\lambda$  is the wavelength (nm).

1D-Fluorescence spectroscopy using above band-gap excitation is routinely used to characterise electronic states semiconductor samples such as Zinc Oxide.<sup>199-201</sup> However, states which are inaccessible through above band-gap excitation will not be observed utilising this technique. A 2D representation of the fluorescence response would allow for the topography of different electronic states to be observed as different excitation wavelengths can be used to probe different electronic states in the system. While 2D-fluorescence approaches for molecular systems<sup>202</sup> have been suggested before this technique has not been previously applied to solid-state systems.

In this study, all fluorescence spectroscopy has been performed with solid-state samples placed into black 96-well plates (Costar) ensuring there is an even coverage. 1D-fluorescence emission spectra were collected using a TECAN i-control M200 spectrometer (Tecan Group Ltd., Switzerland). The emission wavelengths used were 230-600nm with a 10nm step, emission collection started 30nm after the emission wavelength. These 1D-spectra were assembled into a 2D-matrix using an in-house python script<sup>203,204</sup>

with the columns relating to each wavelength and the emission relating to the rows, for wavelengths where no emission data could be collected these values were set to zero.

## 2.9 Ultraviolet-visible-Near Infrared Spectroscopy

Ultraviolet-visible-Near Infrared (UV-Vis-NIR) spectroscopy is a versatile technique used to investigate the interaction of a sample with electromagnetic radiation at different wavelengths. The technique measures these interactions by monitoring the intensity of radiation transmitted through a sample.

The intensity of the radiation being transmitted through the sample can be affected by multiple phenomena such as scattering or electronic interactions. If the energy of an incoming photon matches the energy required to promote an electron to a higher electronic state this occurs in conjugated organic systems. Scattering of the radiation is both shape and size-dependent.<sup>205</sup> The ability of a chemical compound to attenuate light is called the molar extinction coefficient ( $\epsilon$ ) which is measured in  $\text{L}\cdot\text{mol}^{-1}\cdot\text{cm}^{-1}$ . The relationship between the molar extinction coefficient and the absorbance of the compound (A) can be expressed by the Beer-Lambert law:

$$A = \epsilon cl \quad 2.8$$

Where  $c$  is the concentration ( $\text{mol}\cdot\text{L}^{-1}$ ) and  $l$  is the pathlength (cm).

This is an important relation to account for when relating simulated spectra with experimental data as the absorbance measured will be modulated by both the concentration and pathlength selected. When working with gold nanoparticles a plasmonic response is observed around 500 nm, this can be used to determine the nanoparticulate size for spheroidal particulates.<sup>206</sup>

In this study, UV-Vis-NIR spectroscopy has been used to characterise gold nanoparticles and measure their responses inside nanocomposite structures. All data was collected on an Agilent (Santa Clara, US) Cary 50 Bio Uv-vis spectrometer using a scan range of 300-700nm with a step of 1nm.

# Chapter III: Peptide Binding Kinetics

Research presented in section 3.4.1 in this chapter will be included in “Gamma Estimator of Jarzynski Equality: Recovering Binding Energies From Noisy Dynamic Data Sets” which is currently under-going editorial revision prior to final acceptance.

## 3.1 Introduction

In order to understand what is occurring in the time and/or concentration dependent data obtained from different binding studies, mathematical models must be used. The choice of mathematical model depends upon what interactions are considered and can have a large impact on the findings. While empirical fitting techniques exist for such datasets, ie. taking the amplitude of the kinetic data and plotting these values in a concentration plot and fitting with a Freundlich fitting,<sup>207</sup> this will not be explored during this chapter. However, these are discussed in the section 3 of the appendices. Here we shall focus on analytical solutions where terms have physical relevance.

Two different families of analytical kinetic models exist: Absolute Rate Theory (ART) and Statistical Rate Theory (SRT) models<sup>208</sup>, in this chapter the SRT family of models will not be explored as the assumptions in the ART models allow the binding processes to become more tangible.

The family of ART models have been used extensively to describe the adsorption and desorption processes for a variety of experimental datasets including systems where solely physisorption occurs. The Langmuir isotherm was originally developed to model the adsorption of gas molecules on tungsten filaments in incandescent lighting, and describes the adsorption and desorption processes using the simple steps shown below.<sup>112</sup>



Where g and s represent the gas in the gaseous and adsorbed states.

These interactions are treated as chemical reactions which can be an invalid assumption depending upon the interaction type. Therefore, it is important to understand the assumptions the different models operate under to ensure the appropriate model is selected.

The most common kinetic model used for fitting is the Langmuir kinetic model (monomolecular model), this is a 1:1 binding model and therefore has the following assumptions:

1. The surface has a specific number of binding sites where the analyte can be adsorbed
2. The surface of the adsorbent is in contact with a solution containing the analyte which is strongly attracted to the surface.
3. The adsorption solely involves the formation of a monolayer no further adsorption occurs.

Therefore, this model is limited to investigating systems where solely monolayer formation occurs as multilayer formation is not accounted for and no peptide-peptide interactions are considered. If we wish to model more complex kinetic processes accounting for mobile precursor kinetics, allowing for a variety of adsorbate behaviour pre-adsorption, we can employ the Kisliuk adsorption model.<sup>113</sup>

The Kisliuk adsorption model<sup>113</sup> employs a precursor state which occurs when the adsorbate is proximal to the surface. If the adsorbate enters the proximal region over an empty site, it is referred to as an intrinsic precursor (IP) and has the probability to absorb or desorb from the proximal region of  $p_a$  and  $p_d$  respectively. However, if the adsorbate enters the proximal region over a filled site, it is referred to as an extrinsic precursor (EP) and has the probability to absorb or desorb from the proximal region of  $p_a'$  and  $p_d'$  respectively. This model also accounts for the probability of migration from one site to another while in the precursor state, these probabilities are represented by  $p_c$  and  $p_c'$  for the IP and EP types respectively. Upon moving to a new site, if the IP is over a filled site it becomes an EP and vice-versa. Using a combination of these probabilities the sticking coefficient  $K$ , herein referred to as the Kisliuk Constant  $K_c$ , can be determined. For further information see section 3 of the appendices.

In this chapter the ability of Langmuirian and Kisliukian kinetics to fit kinetic data of the A3 sequence adsorbing onto a  $\text{Au}_{(111)}$  surface will be explored under both a low and high concentration regime. Both kinetic models assume that all the surface sites are homogeneous which is a valid assumption as solely  $\text{Au}_{(111)}$  sensors will be used in this study. It is hypothesised that under higher concentrations the simplistic 1:1 binding model such as the Langmuir kinetic model will no longer be suitable due to the assumptions no longer being valid. If the proposed hypothesis is true perhaps the more complex Kisliukian kinetics will offer a better description of the processes occurring in these systems. The aim for this study is to determine if one kinetic model will be applicable across the complete concentration range.

## 3.2 Materials and Methods

### 3.2.1 Solid Phase Synthesis of Gold Binding Peptides

The A3 (AYSSGAPPMPFF) peptide was synthesized using Fmoc-protective group chemistry leveraging the microwave-assisted solid-phase peptide synthesis technique (Liberty Blue Peptide Synthesizer CEM Corp). Peptide purity and the molecular weight of the sequence were determined using high-performance liquid chromatography (Dionex RP-HPLC equipped with phenomenex peptide C18 column) and matrix-assisted laser desorption/ionisation time-of-flight mass spectrometry (Bruker Ultraflex III MALDI-TOF), see Table A4.1.

### 3.2.2 Multiparametric Surface Plasmon Resonance (MP-SPR) Binding Studies

Multiparametric Surface Plasmon Resonance (MP-SPR) studies were conducted using a BioNavis SPR Navi 200 Spectrometer (BioNavis, Finland). In particular, the A3 (AYSSGAPPMPFF) peptide<sup>39</sup> was dispersed in type 1 water at a pH of 7. For low and high concentration regimes, A3 peptide solutions were prepared at: 0.1, 0.5, 1, 25  $\mu\text{M}$  & 25, 50, 100, 200, 300, 400  $\mu\text{M}$  respectively. For both concentration ranges the cell temperature and flow rate were 20°C and 23  $\mu\text{L}\cdot\text{min}^{-1}$  respectively. The duration of each experiment was ca. 30 minutes. The datasets were processed by initially fitting all the kinetic (time-dependent) data to obtain the relevant constants, which were then plotted with dependence on concentration. This concentration dependent plot was fitted to yield a value for the dissociation constant ( $K_D$ ). Due to the non-linear nature of the models used to fit the data, optimisation of the fits has been performed using the Levenberg-Marquardt algorithm<sup>209,210</sup> in OriginPro 2016.

## 3.3 Results and Discussion

### 3.3.1 Low Concentration (“Single Molecule”) Binding Studies

Single-molecule pulling experiments (SMPE) are a popular experimental technique used to determine the interaction energy of a single peptide-surface interaction.<sup>211–213</sup> Recently, an R package developed by Dr. Zhifeng Kuang, allows for datasets which are usually too small for the accurate mean estimation of interaction to be accurately determined through the use of the underlying gamma function. The publication containing Dr. Kuang’s R package to process the SMPE data is currently in revision as of the time of writing. In collaborative work with Dr. Kuang, validation of this processing methodology was proposed via complementary experimental techniques. The peptide selected for these studies was the widely studied A3 (AYSSGAPPMPFF) sequence<sup>39,99,214,215</sup> and a pristine Au<sub>(111)</sub> surface should be used allowing for a robust computational comparison.

Initially multiple techniques were proposed to perform the validation experiments on, such techniques included isothermal titration calorimetry (ITC), fluorescence titration and multi-parametric surface plasmon resonance spectroscopy (MP-SPR). However, ITC experiments were dismissed due to the substrate used being nanoparticles which possess multiple different crystal facets, which is known to affect the peptide binding behaviour<sup>43,214,216</sup> as opposed to SMPE which measures interactions on a single crystal face,  $\text{Au}_{(111)}$ . Concentration dependent experiments such as fluorescence titration techniques<sup>109</sup> have been dismissed due to the kinetic nature of the SMPE measurements, therefore the end-point style measurements of fluorescence titrations may miss features which are observable in the continuous SMPE measurement. Both quartz crystal microbalance dissipation (QCM-D) and MP-SPR are kinetic techniques measuring interactions in real-time and were shortlisted for this study. Ultimately, MP-SPR was selected due to both its lower flow rates than QCM-D and widely available  $\text{Au}_{(111)}$  sensors. This makes MP-SPR a suitable comparison as the surfaces used can express the same crystal face and the low flow rate should enable the kinetics to be comparable.

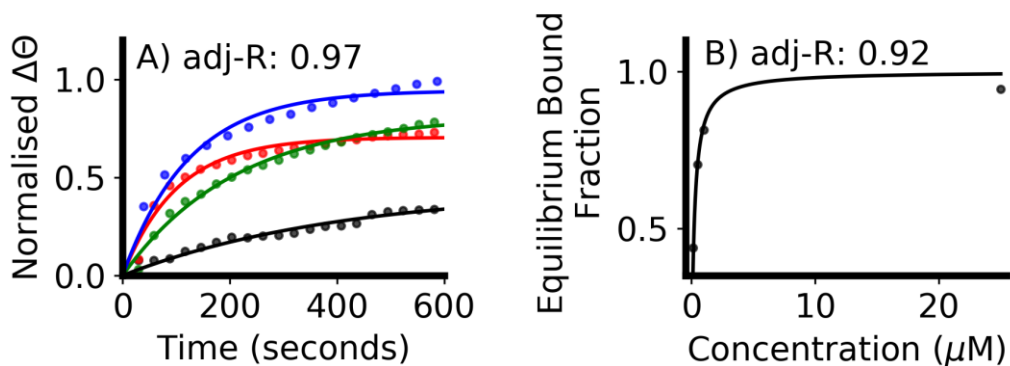


Figure 3.1 - MP-SPR kinetic data for the interaction of the A3 peptide with  $\text{Au}_{111}$  surfaces A) Fitting of the kinetic MP-SPR data using the monomolecular model. The experimental data is denoted by the line markers and the solid lines are their respective fittings. The peptide concentration used is denoted by the point/line colour which is black, red, green & blue for 0.1, 0.5, 1 & 2.5  $\mu\text{M}$ , respectively. B) Plotting the equilibrium bound fraction ( $\alpha$ ) obtained against concentration to obtain the value for the equilibrium dissociation constant  $K_D$ .

To obtain the interaction free energy ( $\Delta G$ ) using MP-SPR kinetic data was collected from the following range of peptide concentrations: 0.1, 0.5, 1 & 25  $\mu\text{M}$ . The resultant kinetic data was processed to obtain the change in angle with dependence on time ( $\Delta\theta(t)$ ). The time-dependent angular change for each concentration is plotted and fitted by the Langmuir kinetic model<sup>217,218</sup> shown below:

$$\theta_t = \alpha(1 - e^{-kt})$$

3.3

Where  $\alpha$  is the equilibrium bound fraction,  $k$  is the rate of reaction and  $t$  is time.

The plotted data and their respective fittings are shown in figure 3.1A. The monomolecular growth model was selected due to its 1:1 binding mechanism solely accounting for peptide-surface interactions. This means our calculated values should have a good parellity to the SMPE results. Upon fitting of the monomolecular model  $k$  &  $\alpha$  parameters are obtained for each concentration; the  $\alpha$  parameter can be expressed as:

$$\alpha = \frac{c}{c + K_D} \quad 3.4$$

Therefore, plotting  $\alpha$  with dependence on concentration allows for the determination of the equilibrium dissociation constant  $K_D$ , as shown in figure 3.1B. The value for  $K_D$  determined from the fitting is  $0.206 \pm 0.02 \mu\text{M}$ , which in turn can be used for the calculation of Gibbs free energy ( $\Delta G$ ) using the following equation:

$$\Delta G = RT \ln \left( \frac{K_D}{c^\ominus} \right) \quad 3.5$$

Where  $R$  is the ideal gas constant,  $T$  is the temperature in Kelvin and  $c^\ominus$  is the standard reference concentration (1 M).<sup>219</sup>

Using the above equation the adsorption free energy ( $\Delta G$ ) determined for this system was  $-8.97 \pm 0.08 \text{ kcal}\cdot\text{mol}^{-1}$ . This is in agreement with the single-molecule pulling experiments which determine the absorption free energy to be  $9.458 \pm 0.105 \text{ kcal}\cdot\text{mol}^{-1}$  (note the sign is inverted due to the SMPE technique measuring the energy required to remove a bound peptide from a surface). This achieves the initial aim of validating Dr Kuang's approach; however, interestingly the highest concentration of A3 appears to be poorly described using a 1:1 binding model (see figure 3.1A) which is routinely used in such studies. To understand what is occurring under a higher concentration regime a series of experiments were performed using a wider concentration range from  $25\text{-}800 \mu\text{M}$ , this range was selected as it relates both single peptide investigation concentrations (as shown above) and biominerallisation concentrations.

### 3.3.2 High Concentration (“Biomineralisation”) Binding Studies

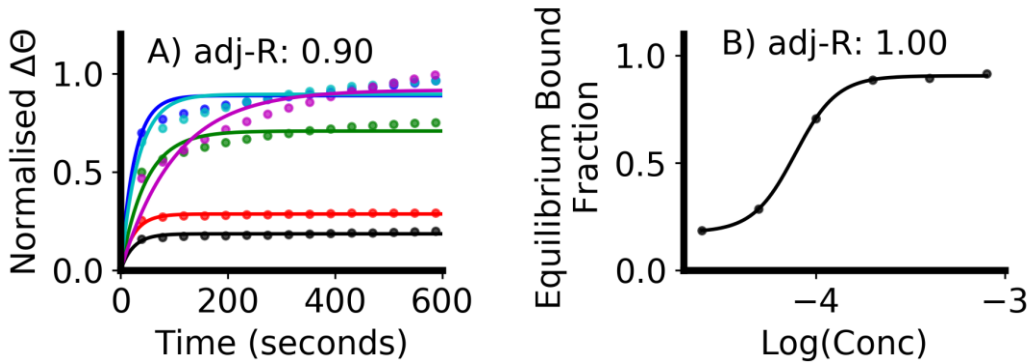


Figure 3.2 - MP-SPR kinetic data for the interaction of the A3 peptide with  $\text{Au}_{(111)}$  surfaces under a high concentration regime A) Fitting of the kinetic MP-SPR data using the monomolecular model. The experimental data is denoted by the line markers and the solid lines are their respective fittings. The peptide concentration used is denoted by the point/line colour which is black, red, green blue, cyan and magenta for 25, 50, 100, 200, 400 & 800  $\mu\text{M}$ , respectively. B) Plotting the equilibrium bound fraction ( $\alpha$ ) obtained against concentration to obtain the value for the equilibrium dissociation constant  $K_D$ .

To obtain the interaction free energy ( $\Delta G$ ) using MP-SPR, kinetic data was collected from the following range of peptide (A3) concentrations: 25, 50, 100, 200, 400 & 800  $\mu\text{M}$  using  $\text{Au}_{(111)}$  surfaces. Upon fitting this data with the monomolecular model, see figure 3.2A, there appears to be an inverse correlation between the concentration and the ability of the monomolecular model<sup>217,218</sup> to completely describe the system. The cause of this inverse relationship is likely due to the assumptions made by this model which include no multilayer formation occurring and only peptide-surface interactions being considered. This results in the  $R^2$  value for the fits dropping to ca~0.8 for the highest concentrations.

Plotting the  $\alpha$  parameter against concentration and fitting using equation 3.5, see figure 3.2B, the value of  $K_D$  calculated is  $108.397 \pm 11.70 \mu\text{M}$ . Comparing the fits between figure 3.1B and figure 3.2B, we observe that there is a lower quality fit obtained in figure 3.2B. The cause of the worse fitting is due to the poor initial fitting of the kinetic data in figure 3.2A. If this value of  $K_D$  is used to determine  $\Delta G$  using equation 3.5 the value obtained is  $-5.32 \pm 0.06 \text{ kcal}\cdot\text{mol}^{-1}$ , which is ca~3.7  $\text{kcal}\cdot\text{mol}^{-1}$  lower than previously calculated in the low concentration regime. Therefore, this indicates the assumptions made in the Langmuir kinetic model are no longer suitable under a higher concentration regime.

When in the high concentration regime it is likely a peptide in solution which is proximal to the surface will interact with a bound peptide, this notion is supported by reported peptide aggregation behavior in the literature.<sup>220,221</sup> The bound peptide-peptide interaction is less favorable than the peptide-surface interaction and can be described as a precursor state. The presence of peptide in solution being “trapped” in this precursor state increases the probability of peptide adsorption due to its proximity to a free surface site. Precursor based kinetic were proposed by Paul Kisliuk in 1957, the Kisliuk kinetic model (equation 3.6) accounts for both the peptide-surface interactions that are accounted in the Langmuirian kinetics and peptide assisted adsorption through the precursor state.

$$\theta_t = \alpha \frac{1 - e^{-R'(1+k_E)t}}{1 + k_E \cdot e^{-R'(1+k_E)t}} \quad 3.6$$

Kisliuk kinetic model shown above (equation 3.6), where  $R'$  is the Kisliuk rate term,  $k_E$  is the sticking parameter and  $\alpha$  is the equilibrium bound fraction (equation 3.4). Using the Kisliuk kinetic model (equation 3.6), the time-dependent sensograms were fitted and the resulting  $\alpha$  constants plotted against concentration to determine  $K_D$ , the respective plots are shown in figure 3.3. Interestingly when comparing figure 3.1B and figure 3.3B the nature of the curve appears to have changed with figure 3.3B showing more sigmoidal character and a poorer fit of the constants. The resultant thermodynamic constant calculated using the Kisliuk kinetic model is  $-5.57 \pm 0.11 \text{ kcal}\cdot\text{mol}^{-1}$ , this is ca~3  $\text{kcal}\cdot\text{mol}^{-1}$  less than we measure in a molecular based system.

While the Kisliuk kinetics are more descriptive of the initial binding kinetics, the model for the end point state under higher concentrations has not improved. A combination of Langmuirian and Kisliuk adsorption kinetics may overcome this issue as over the concentration range of interest the dominant kinetics could change depending on the concentration of peptide used. Also, the ability to directly compare this model with Langmuirian kinetic systems would be of use to compare with historic data.<sup>96</sup>

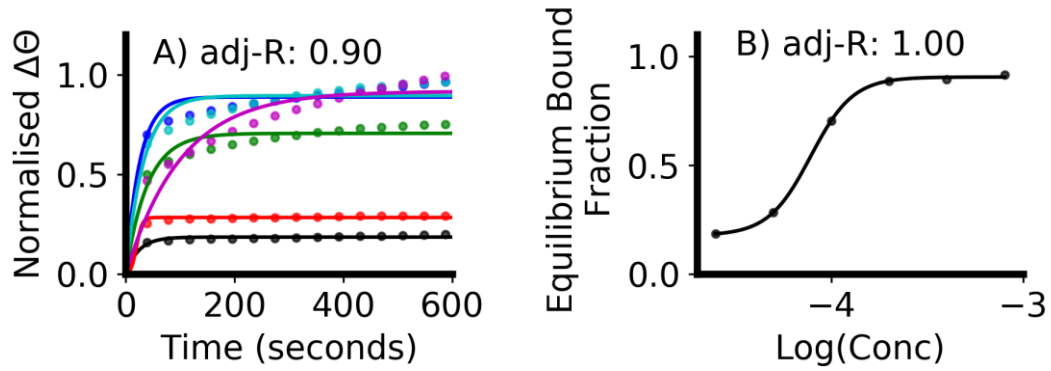


Figure 3.3 - MP-SPR kinetic data for the interaction of the A3 peptide with  $\text{Au}_{(111)}$  surfaces under a high concentration regime A) Fitting of the kinetic MP-SPR data using the kisliuk kinetic model. The experimental data is denoted by the line markers and the solid lines are their respective fittings. The peptide concentration used is denoted by the point/line colour which is black, red, green blue, cyan and magenta for 25, 50, 100, 200, 400 & 800  $\mu\text{M}$ , respectively. B) Plotting the equilibrium bound fraction ( $\alpha$ ) obtained against concentration to obtain the value for the equilibrium dissociation constant  $K_D$ .

To derive such a kinetic model, we return to the kinetic theory of gases<sup>222</sup> upon which modern adsorption kinetics is founded on. Interactions occur when an adsorbate molecule strikes a free site on the surface, this flux of gas molecules is expressed by equation 3.7 where  $p$  is the partial pressure of adsorbate,  $m$  is the mass of the adsorbate,  $k_B$  is the Boltzmann constant and  $T$  is temperature.

$$I = \frac{p}{\sqrt{2\pi m k_B T}} \quad 3.7$$

However, not all collisions between the adsorbate and the surface will yield an interaction which leads to adsorption. The ratio between the rate of adsorption and the collisions between the adsorbate and adsorbent is referred to as the sticking coefficient ( $s$ ). Therefore, the rate of absorption can be expressed as equation 3.8.

$$r_a = sI \quad 3.8$$

The sticking coefficient for a system can be expressed in terms of initial stick probability ( $s_0$ ) and a function of relative surface coverage ( $\theta_r$ ) which is the ratio of fill sites against initial number of available sites, as shown in equation 3.9.

$$s = s_0 f(\theta_r) \quad 3.9$$

The function of relative surface coverage for a first order Langmuirian system<sup>112</sup> and the equivalent function for the Kisliukian system<sup>113</sup> are shown in equation 3.10 and equation 3.11. Where  $K_c$  is the Kisliuk constant, upon this term becoming 1 the bottom of the fraction reduces to 1 returning to the Langmuirian function.

$$f(\theta_r) = 1 - \theta_r \quad 3.10$$

$$f(\theta_r) = \frac{1 - \theta_r}{1 + \theta_r(K_c - 1)} \quad 3.11$$

By substituting equation 3.9 into equation 3.8, equation 3.12 is obtained where the rate of adsorption ( $r_a$ ) can be expressed as the change in relative surface coverage over change time.

$$r_a = \frac{d\theta_r}{dt} = Is_0 f(\theta_r) \quad 3.12$$

Substituting the functions of surface coverage (equation 3.10 and equation 3.11) into equation 3.12 differential equations are obtained for both the Langmuirian and Kisliukian kinetics (eq and eq respectively), where the latter is capable to reduce to the Langmuirian regime when  $K_c=1$ .

$$\frac{d\theta_r}{dt} = IS_0(1 - \theta_r) \quad 3.13$$

$$\frac{d\theta_r}{dt} = Is_0 \left( \frac{1 - \theta_r}{1 + \theta_r(K_c - 1)} \right) \quad 3.14$$

These differential equations can be solved for  $\theta_r$ :

Collect  $\theta$   
terms

$$\int (1 - \theta_r)^{-1} d\theta_r = \int IS_0 dt$$

$$\int \left( \frac{1 - \theta_r}{1 + \theta_r(K_c - 1)} \right)^{-1} d\theta_r = \int IS_0 dt$$

Integrate

$$-\ln(1 - \theta_r) = IS_0 t$$

$$-\ln\left(\frac{1 - \theta_r}{1 + \theta_r(K_c - 1)}\right) = IS_0 t$$

Solve for  $\theta_r$

$$\theta_r = 1 - e^{-IS_0 t}$$

$$\theta_r = \frac{1 - e^{-IS_0 t}}{1 + (K_c - 1)e^{-IS_0 t}}$$

Let  $k = IS_0$

$$\theta_r = 1 - e^{-kt} \quad 3.15$$

3.16

$$\theta_r = \frac{1 - e^{-kt}}{1 + (K_c - 1)e^{-kt}}$$

Upon solving for  $\theta_r$  we obtain equation 3.15 which is equivalent to the monomolecular model (equation 3.3) if the scaling term ( $\alpha$ ) is introduced. Equation 3.16 is the derived kinetic model fitting our initial criteria, herein this model will be referred to as the Langmuir-Kisliuk kinetic model. To enable this model to account for concentrations which do not fill all the sites the  $\alpha$  parameter is introduced representing the equilibrium bound fraction, as shown in equation 3.17.

$$\theta_r = \alpha \left( \frac{1 - e^{-kt}}{1 + (K_c - 1)e^{-kt}} \right) \quad 3.17$$

The high concentration A3 kinetic dataset was refitted using equation 3.17 as shown in figure 3.4A. The R-squared values for all the kinetic fits are over 0.94, which is over 0.1 better than that of the original Langmuir fitting. All the fittings show that the  $K_c$  value is less than one; however, the value does increase with increasing concentration. This means that chemisorption is dominating the binding kinetics observed and it is improbable that upon a peptide becoming proximal to a surface it will desorb.

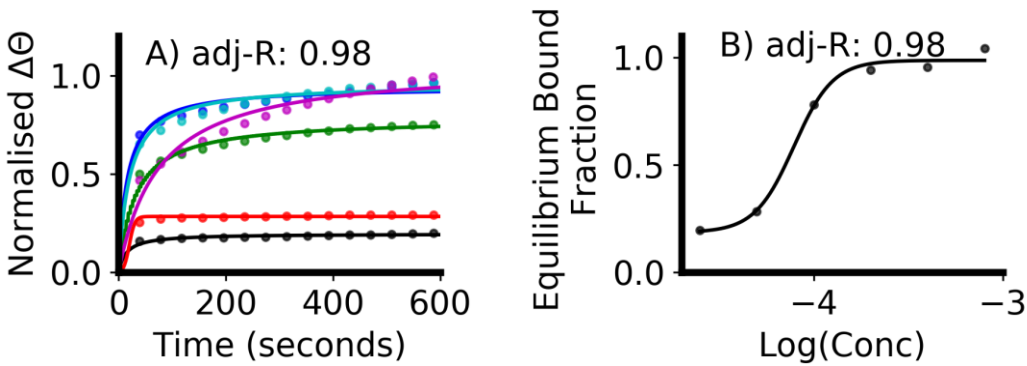


Figure 3.4: MP-SPR kinetic data for the interaction of the A3 peptide with  $\text{Au}_{(111)}$  surfaces under a high concentration regime A) Fitting of the kinetic MP-SPR data using the Langmuir-Kisliuk kinetic model. The experimental data is denoted by the line markers and the solid lines are their respective fittings. The peptide concentration used is denoted by the point/line colour which is black, red, green blue, cyan and magenta for 25, 50, 100, 200, 400 & 800  $\mu\text{M}$ , respectively. B) Plotting the equilibrium bound fraction ( $\alpha$ ) obtained against  $\log(\text{concentration})$  and fitted with a dose-response curve to obtain the value for the equilibrium dissociation constant  $K_D$  and Hill slope  $n$ .

To determine the  $K_D$  and  $\Delta G$  values for this system the  $\alpha$  parameter for each concentration was plotted against  $\log(\text{concentration})$  which is shown in figure 3.4B. Unlike in figure 3.1B and figure 3.3B the curve has been fitted using the dose-response function (equation 3.18) due to the sigmoidal nature of the datapoints.

$$y = A_2 + \frac{A_1 - A_2}{1 + 10^{-(x - \log(x_0))n}} \Rightarrow \frac{B}{B_0} = \frac{1}{1 + 10^{-(x - \log(x_0))n}} \quad 3.18$$

Where  $A_1$  and  $A_2$  describe the asymptotes,  $x_0$  is the midpoint of the sigmoid and  $n$  corresponds to the gradient of the slope, under the conditions where  $n=1$  then the hill regime is adopted. This also required the change of the x-terms from concentration to  $\log(\text{concentration})$ . To determine  $K_D$  using the sigmoidal fitting the midpoint ( $x_0$ ) is taken and then  $K_D$  calculated using equation 3.19 and was determined as  $78.9 \pm 7.43 \mu\text{M}$ .

$$K_D = 10^{x_0} \quad 3.19$$

Determining the value for  $\Delta G$  using equation 3.5 returns a value of  $-5.50 \pm 0.05 \text{ kcal}\cdot\text{mol}^{-1}$ , this is ca~3  $\text{kcal}\cdot\text{mol}^{-1}$  less than we measure in a molecular based system. However, if we account for the partial molar volume of the solvent ( $18\text{M}\Omega$  Water,  $0.018\text{M}^{-1}$ ) using the equation, the determined value of  $\Delta G$  is  $-7.84 \pm 0.06 \text{ kcal}\cdot\text{mol}^{-1}$ , this is ca. 1  $\text{kcal}\cdot\text{mol}^{-1}$  different to our calculations in the molecular regime. While the partial molar volume of the

solvent can be introduced for the previous high concentration kinetic fits (Langmuir and Kisliuk) the description of the kinetic processes would still not be appropriate and the model could fail in cases where the low concentration dataset has not been collected.

The remaining differences may be due to unaccounted for peptide-peptide interactions in solution. However the hill slope ( $n$ ) which is also obtained from the dose-response fitting is  $>1$  for this system indicating that even if this is present in solution we will not observe this behavior as the surface-bound state is preferred and peptide assistive adsorption will occur. Finally if the original low concentration data explored in section 3.4.1 is fitted using the Langmuir-Kisliuk kinetic model, figure 3.5, a good approximation of the kinetic events occurring can still be made. The kinetic model provides a fit with an R-squared value of 0.96 or higher for all data fitted in figure 3.5A and the  $\Delta G$  value obtained was  $-8.97 \text{ kcal}\cdot\text{mol}^{-1}$ , there were too few data points for the uncertainty of the sigmoidal fit to be calculated. However, if the determined value of  $\Delta G$  is compared to the  $-8.97 \pm 0.08 \text{ kcal}\cdot\text{mol}^{-1}$  originally calculated we can see the fits are in excellent agreement confirming the ability of the proposed model to fit both high and low concentration datasets.

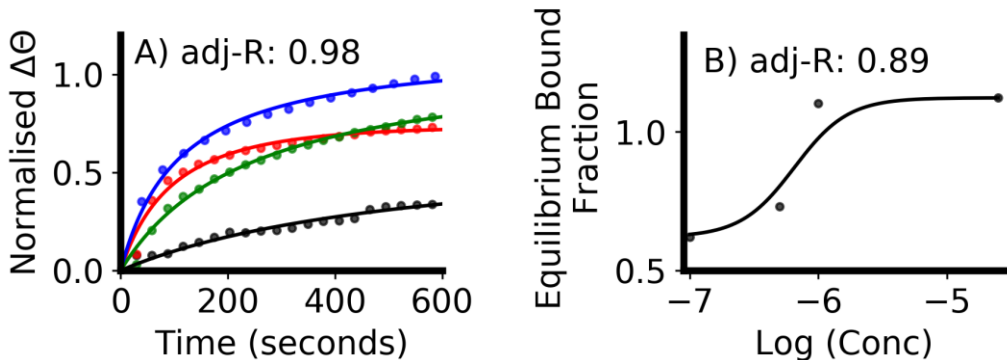


Figure 3.5 - MP-SPR kinetic data for the interaction of the A3 peptide with  $\text{Au}_{(111)}$  surfaces under a low concentration regime A) Fitting of the kinetic MP-SPR data using the Langmuir-Kisliuk kinetic model. The experimental data is denoted by the line markers and the solid lines are their respective fittings. The peptide concentration used is denoted by the point/line colour which is black, red, green & blue for 0.1, 0.5, 1 & 2.5  $\mu\text{M}$ , respectively. B) Plotting the equilibrium bound fraction ( $\alpha$ ) obtained against  $\log(\text{concentration})$  and fitted with a dose-response curve to obtain the value for the equilibrium dissociation constant  $K_D$  and Hill slope  $n$ .

### 3.4 Conclusions

In this chapter the Langmuir-Kisliuk kinetic model is proposed as a way to model the kinetics of peptide adsorption onto surfaces and in this study's case specifically gold surfaces. This model is able to relate back to the traditional Langmuirian kinetic models for comparison with more historic data, as well as being suited to processing data collected at both the high and low concentration regimes. Fitting of the data using a dose-response curve allows for the determination of both  $K_D$  and the Hill slope ( $n$ ), the latter being useful to predict what state the peptide prefers to be in and whether or not peptide assistive adsorption will occur. Finally introducing the partial molar volume of the solvent in the calculation of  $\Delta G$  allows us to closely approximate the thermodynamic constants for a system even under higher concentrations. The Langmuir-Kisliuk model was trialled on the original low concentration data, section 3.3.1, with the fitting having excellent agreement with the original results. In the following chapter, the Langmuir-Kisliuk model will be applied to the kinetics of other gold binding sequences adsorbing to a  $\text{Au}_{(111)}$  surface. These findings will be compared to ITC measurements where the thermodynamic constants are directly determined.

## Chapter IV: Towards an understanding of engineering binding sequences for Au systems through kinetic and thermodynamic studies

### 4.1 Introduction

Nature's precise control during chemical synthesis is envied by 21st century chemists,<sup>2</sup> leading to biomimetic research projects focused on understanding the processes involved in biomineralisation.<sup>30,33,34</sup> Biomineralisation yields highly ordered structures with defined composition, predictable morphologies and structural properties through peptide or protein mediation. The peptides and proteins can self-assemble to form pre-organised scaffolds<sup>38</sup> and coordinate to metal centres through the side-groups on the residues in the primary sequence,<sup>40</sup> for example the imidazole group present in histidine which forms Cys<sub>2</sub>-His<sub>2</sub> Zn fingers.<sup>41</sup>

High-precision synthetic control in wet synthetic conditions has numerous real world applications from prostheses<sup>47–49</sup> to photocatalytic devices.<sup>12</sup> Synthesis of nanomaterials is an excellent example of where a high degree of synthetic control is fundamental as the control during the synthesis directly impacts the final properties of the nanomaterial including the possible chemistry at its surface. An excellent example of this is Au nanoparticles with diameters <5 nm which tend to absorb CO while those with diameters >10nm do not significantly absorb CO.<sup>223</sup> Therefore, the ability of biomolecules including peptides to control and mediate the synthesis of nanoparticles through reduction,<sup>39</sup> nucleation,<sup>10</sup> stabilisation, directed growth, bridging/linking and capping can enable the properties of the product to be tuned for a given application during synthesis.<sup>43,44</sup>

Research into biomineralisation was inspired by the beautifully symmetrical highly ordered structures of silica diatoms,<sup>33</sup> which contain a level of complexity unattainable by classical wet chemistry synthesis.<sup>2</sup> The role of peptides and proteins, both long chain sequences of amino acids, in biomineralisation has attracted the attention of many research groups due to unique properties such as self-assembly to from pre-organised scaffolds<sup>38</sup>, nucleation of biominerals<sup>35</sup> and reduction of HAuCl<sub>4</sub> to Au.<sup>39</sup> To understand the complex control mechanisms and codependent behaviours involved in biomimetic peptide mediated synthesis, both kinetic and thermodynamic experimental binding studies are required. Such experimental data allowed for the development of novel models i.e. the Langmuir-Kisliuk model as described in Chapter III, and further broadens our understanding of amino acid composition required when developing bespoke peptide/protein sequences for peptide-mediated synthesis. Systematically testing different condition parameters, such as

the role of salinity in the reaction medium or primary structure of the peptide/protein used, also allows for the elucidation of key reaction components in biomimetic synthetic routes.<sup>9,10,96,107,109,216</sup> An excellent example is the LDHSLHS silica binding peptide where the peptide-SiO<sub>2</sub> interaction gains a strong enthalpic drive upon the addition of 0.2M NaCl and the whole system becomes more ordered.<sup>107</sup> While investigations into the ideal composition of the reaction medium are important they are outside the scope of this study which will focus on key components of the primary sequence for effective binding to a developing material, in this case gold.

The application of the Langmuir-Kisliuk isotherm to multi-parametric surface plasmon resonance (MP-SPR) datasets is a novel approach and in this chapter the Langmuir-Kisliuk kinetics and derived thermodynamic constants will be compared to thermodynamic constants determined using isothermal titration calorimetry (ITC). The MP-SPR studies report on thermodynamic constants for the peptide-Au<sub>(111)</sub> binding due to the Au<sub>(111)</sub> surfaces used. However, the ITC studies will report an average of the peptide binding constants for Au<sub>(111)</sub>, Au<sub>(110)</sub> and Au<sub>(100)</sub> facets which are expressed by the spheroidal gold nanoparticles used. Circular dichroism (CD) spectroscopy will also be used to evaluate any structural changes that occur on binding and how this may impact the entropy of the system. Finally transmission electron microscopy (TEM) was used to observe if any self-assembly/aggregation behaviour was observed for AuNPs exposed to different peptide solutions, for sequences see table 4.1.

Table 4.1 - Peptides used in this study with their corresponding one-letter sequence.

Peptide Name	Sequence
AuBP1 <sup>96</sup>	WAGAKRLVLRRE
AuBP2 <sup>96</sup>	WALRRSIRRQSY
HRE <sup>9</sup>	AHHAHHAAD
Pd4 <sup>98</sup>	TSNAVHPTLRHL
A3 <sup>39,99</sup>	AYSSGAPPMPFF
A3s	AYSSGAPMPFF
A3sT2	ATSSGAPMPFF
A3sC8	AYSSGAPCPPF

The peptide library selected for this study includes both widely studied peptide sequences as well as sequences developed in-house from the A3<sup>39,99</sup> parent peptide, see table 4.1. The AuBP1,<sup>96</sup> AuBP2<sup>96</sup> and HRE<sup>9</sup> sequences were selected as they are strong gold binding sequences reported in the literature which did not contain sulphur residues. A3 is a known sulphur containing gold binder from literature and A3s, A3sT2 and A3sC8 are sequences derived from A3. The A3s sequence was developed by removing the Pro<sub>8</sub>

residue from the primary sequence, to determine if removing the 7,8 proline twist would increase binding strength through the Met<sub>9</sub> residue. The A3sT2 and A3sC8 sequences are derived from the A3s parent focusing on two key residues in A3-Au binding interactions that have been reported in the literature. The Tyr<sub>2</sub> residue was reported to be important in anchoring the A3 sequence,<sup>98</sup> and to determine if the aromatic nature of this hydroxyl residue assists in binding interactions it was substituted for Thr<sub>2</sub> in the A3sT2 sequence. Cysteine groups are under-represented in phage-display techniques and from a reactivity perspective a primary thiol should be more reactive and a better binder than a secondary thiol. To test this theory Met<sub>8</sub> was substituted for Cys<sub>8</sub> in the A3sC8 sequence.

The primary aim of this study is to elucidate the interplay between the gold substrate used and the primary sequence on the overall binding efficacy of a given peptide sequence. This can be simplified to two secondary aims which are: the investigation into the role of the primary sequence/ amino acid composition on binding efficacy and the investigation of the effect of the gold substrate used (surfaces or nanoparticles) on the obtained thermodynamic constants. Understanding the interplay between these key factors will assist future studies in engineering and synthesising novel bespoke sequences for peptide-mediated synthetic routes to materials.

## 4.2 Materials and Methods

### 4.2.1 Synthesis of Uncapped Gold Nanoparticles

Freshly prepared NaBH<sub>4</sub> (0.1 M, 0.25 ml, Alfa Aesar) was added to an aqueous solution of HAuCl<sub>4</sub> ( $2.5 \times 10^{-4}$  M, 50 ml, Sigma). The solution was stirred while under reflux for 1.5 hours. The formed Au nanoparticles had a ruby red hue in aqueous solution with a diameter of  $17 \pm 3$  nm and a pseudo spheroidal geometry which was determined from a sample of 76 particles, see figure A4.1. The nanoparticle concentration within the synthesised solution was determined to be 2 nM, for calculation see section A3.1 in the appendices.

### 4.2.2 Solid Phase Synthesis of Gold Binding Peptides

The peptides tabulated in table 4.1 were synthesized using Fmoc-protective group chemistry leveraging the microwave-assisted solid-phase peptide synthesis technique (Liberty Blue Peptide Synthesizer CEM Corp). Peptide purity and the molecular weight of the sequence were determined using high-performance liquid chromatography (Dionex RP-HPLC equipped with phenomenex peptide C18 column) and matrix-assisted laser desorption/ionisation time-of-flight mass spectrometry (Bruker Ultraflex III MALDI-TOF), see Table A4.1.

#### 4.2.3 Multiparametric Surface Plasmon Resonance (MP-SPR) Binding Studies

Multiparametric Surface Plasmon Resonance (MP-SPR) studies were conducted using a BioNavis SPR Navi 200 Spectrometer (BioNavis, Finland). In particular, the peptides (table 4.1) were dispersed in type 1 water. Peptide solutions were prepared at: 25, 50, 100, 200, 400, 800  $\mu\text{M}$ . The cell temperature and flow rate were 20°C and 23  $\mu\text{L}\cdot\text{min}^{-1}$  respectively. The duration of each experiment was ca. 30 minutes. The datasets were processed by initially fitting all the kinetic (time-dependent) data to obtain the relevant constants, see table 4.2. The  $\alpha$  values were then plotted with dependence on concentration for each kinetic model. This concentration dependent plot was fitted to yield a value for the dissociation constant ( $K_D$ ). Due to the non-linear nature of the models used to fit the data, optimisation of the fits has been performed using the Levenberg-Marquardt algorithm<sup>209,210</sup> in OriginPro 2016.

Table 4.2 - Kinetic models used in this study with their corresponding kinetic constants.

Kinetic Model	Kinetic constants
Langmuir	$k, \alpha$
Kisliuk	$k_E, R', \alpha$
Langmuir-Kisliuk	$k_C, k, \alpha$

#### 4.2.4 Isothermal Titration Calorimetry (ITC) Binding Studies

Isothermal titration calorimetry (ITC) studies were conducted using a Malvern MicroCal VP instrument, Malvern, UK. In particular, peptide and gold nanoparticles were dispersed in type 1 water to prepare 100  $\mu\text{M}$  and 2 nM stock solutions respectively. The concentration of gold binding sites present in the AuNPs stock solution was determined to be 1  $\mu\text{M}$ , for the calculation see section A3.2 in the appendices. The cell temperature and the reference power were 25°C and 10  $\mu\text{cal}\cdot\text{s}^{-1}$  respectively. The stirring speed of 307 rpm was used to keep the nanoparticles in suspension and ensure the reaction mixture was homogenous. The time delay between injections was 17 minutes to allow equilibrium to be reached after each injection. Each experiment had a total duration of around 6 hours and was repeated at least in duplicate to ensure reliability of the results. For obtaining the values for the association constant a linear fitting was used, while enthalpy was taken from the amplitudes of the data.

#### 4.2.5 Synchrotron Radiation Circular Dichroism (CD) Studies

All circular dichroism (CD) measurements were performed in either aqueous peptide or peptide-coated nanoparticle solutions using a stock concentration of 10 mg·ml<sup>-1</sup> on the DISCO beamline at the Synchrotron SOLEIL (Saint-Aubin, France). The measurement of

the CD spectra for the peptides adsorbed on the surface of gold nanoparticles was achieved using the following protocol: incubation of peptide stock solution ( $10 \text{ mg}\cdot\text{ml}^{-1}$ ) with the nanoparticle solution (2 nM) in a 1:1 ratio by volume for 2 hours in an overhead shaker (Loopster digital, IKA, Germany) at 30 rpm. Post-incubation the mixture was centrifuged at 14000 g for 10 min (Microcentrifuge 1814, VWR, Germany) and the supernatant collected for absorbance measurements at 205 and 214 nm. The pellet was resuspended in a solvent volume corresponding to the volume of the removed supernatant and the CD spectra for this sample were collected as fast as possible to avoid desorption of the bound peptide.

Spectral scans for each sample were collected at least in triplicate at  $25^\circ\text{C}$  using a wavelength range between 170 and 260 nm inclusive with a 1 nm step. CaF or Quartz cells were used to hold the sample with pathlengths ranging from 0.033 to 0.01 cm. The acquired scans were averaged and the appropriate baseline subtracted before smoothing with a Savitzky-Golay filter using a smoothing window of between 5 to 10 data points. The discussed processing was performed with the CDTool package.<sup>224</sup> To remove the influence the nanoparticles have on the CD spectra a baseline of nanoparticles (1 nM) was collected using the same conditions and subtracted from the associated CD spectra for the measurements with the bound peptides.

The determined raw CD ellipticity ( $\Theta$ ) was converted to mean residue ellipticity ( $\Theta_{\text{MRE}}$ ) using equation 4.1.<sup>174</sup>

$$\Theta_{\text{MRE}} = \frac{\Theta}{c \cdot l \cdot n} \quad 4.1$$

Where  $c$  is the concentration of the peptide ( $\text{mol}\cdot\text{L}^{-1}$ ),  $l$  is the pathlength (mm) and  $n$  is the number of amino acids in the solvated peptide. The  $\Theta_{\text{MRE}}$  values determined for the bound peptide samples used a concentration value that was determined in respect to their residual peptide concentration in the supernatant, allowing for direct comparison between the aqueous and bound CD spectra. It is understood that this procedure is not entirely free from possible uncertainties caused by the possible partial desorption of the bound peptides in the resuspended samples and any variations in the spectral contributions of gold, despite the care being taken to ensure that the baselines (reference samples) contained the same amount of nanoparticles as the bound peptide samples.

#### 4.2.6 Transmission electron microscopy (TEM) Studies

Transmission electron microscopy (TEM) was used to characterise the size and morphology of the synthesised uncoated AuNPs as well as to determine if self-assembly/aggregation behaviour was observed when AuNPs were exposed to aqueous peptide solutions. The peptide-coated samples were prepared by the incubation of a peptide stock solution (800 µM) with the nanoparticle solution (2 nM) in a 1:1 ratio by volume mixed using a vortex mixer and left for 2 hrs. The incubated solution was agitated using a vortex mixer to ensure the suspends was homogeneous before 5µL of sample was taken and drop-cast onto Quantifoil grids (1.2 µm diameter, 200 Mesh Cu) and left to dry for 30 minutes; any remaining liquid was wicked away from the surface of the grid using a piece of filter paper. Two samples of the AuNPs were prepared without the addition of binding peptide, the first sample used a BSA dispersant following a published protocol<sup>180</sup> and was used to image the size and shape of the gold nanoparticles. The second sample had no additional dispersant and was used to look at the native aggregation and group behaviours of gold nanoparticles. Both of these samples were prepared using the same drop-cast technique as described above.

To determine agglomeration/assembly behaviour in the collected micrographs each micrograph was binarised and then a distance map determined from the binarised image. The local maxima were determined from the distance map to determine the particle centers, this method was chosen due to particle overlap in the TEM micrographs which may not be correctly accounted for by the observer. A delaunay triangulation<sup>225</sup> was performed on the particle centers to determine the average distance between a center and its neighbours, see figure 4.10. All steps of this image processing were performed using FIJI (version 1.52p).

The microscope used was a JEOL 2100 Plus TEM/STEM microscope fitted with a LaB<sub>6</sub> source. An accelerating voltage of 200kV was used for TEM. Under prolonged exposure to the 200kV electron beam uncoated AuNPs that are proximal to each other had a tendency to fuse into a single particle.

### 4.3 Results and Discussion

The type of gold substrate used in binding studies is of fundamental importance as the substrate used can directly impact the results collected. This study investigates gold in either the surface or nanoparticle form. When comparing surfaces and nanoparticles multiple factors must be considered, firstly the influence of surface curvature on the amino acid binding behaviour<sup>110</sup> and secondly the surface/facet present as this will also directly

impact the binding behaviour. For example the A3 binding peptide prefers to interact with Au<sub>(111)</sub> surfaces compared to Au<sub>(100)</sub> surfaces.<sup>98</sup>

Surface curvature effects are not considered in this study as if we assume the diameter of an amino acid is 3.5 ± 0.1 Å<sup>226–229</sup> (therefore if we simplify a peptide to a cylinder the diameter will be 3.5 ± 0.1 Å) the surface curvature of spherical particles relative to the peptides studied can be approximated by the Arc's Measure, see equation 4.2.

$$\frac{\text{Arc Length} \cdot 360}{\pi \cdot \text{particle diameter}} = \text{Arc's Measure}$$

Sub. 0.35nm  
as Arc Length    4.2

$$\frac{126}{\pi \cdot \text{particle diameter}} = \text{Arc's Measure}$$

This study uses nanoparticles which have a diameter of 17±3 nm meaning the surface curvature is 2.4 ± 0.4 degrees, this surface is relatively flat compared to 1, 2 or 4nm gold particles which have 40, 20 & 10 degrees of surface curvature respectively. Instead this study focused on the differences in crystal surface/facets expressed by the two gold substrates studied. Kinetic MP-SPR studies were conducted to determine both the kinetics and binding efficacy of a library of known gold binding sequences, see table 4.1, to a Au<sub>(111)</sub> surface. The ITC studies reported on the thermodynamics of the library of known gold binder, see table 4.1, binding to gold nanoparticles with Au<sub>(111)</sub>, Au<sub>(110)</sub> & Au<sub>(100)</sub> crystal facets.

#### 4.3.1 High Concentration 'Biomineralisation' MP-SPR studies

To develop an understanding of the kinetic processes occurring in peptide-Au binding interactions, MP-SPR spectra were collected for the studied peptide library, see table 4.1. Kinetic MP-SPR spectra were fitted using the Langmuir, Kisliuk and Langmuir-Kisliuk kinetic models to determine the optimal model for this study, see figure 4.1 and figure 4.2 for the fittings of the A3 derived sequences and non-sulphur containing sequences respectively. The average adjusted R<sup>2</sup> (adj-R<sup>2</sup>) values for each kinetic model are presented in table 4.3. When comparing the quality of fits generally the adj-R<sup>2</sup> values don't differ significantly between the Langmuir and Kisliuk models with different regions in the kinetic curve being over/underestimated by the models, this is most obvious in figure 4.1-4.

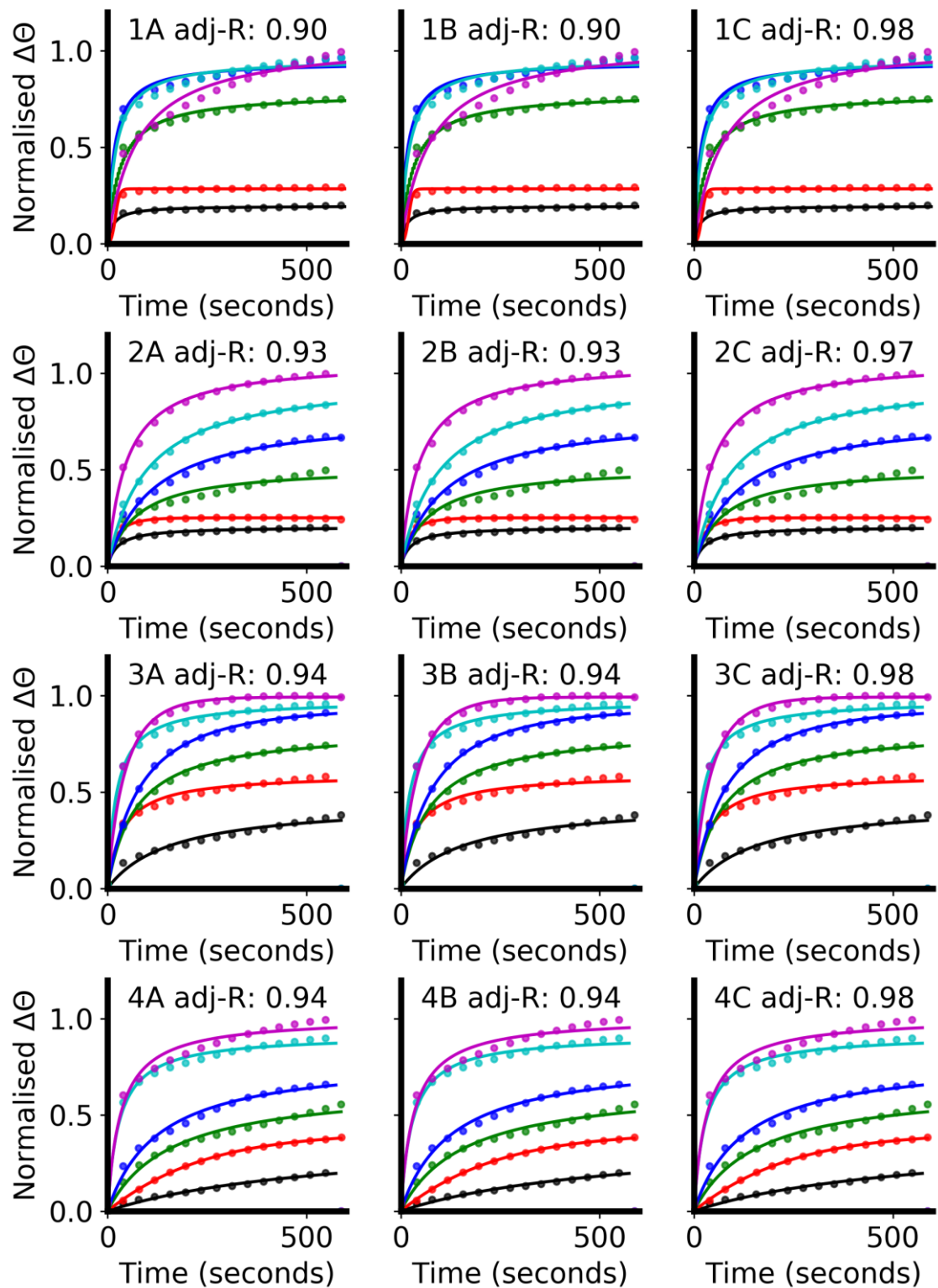


Figure 4.1 - Kinetic fits for the A3 sequences from the peptide library studied with the associated averaged adjusted- $R^2$  values. The points represent the experimental data and the fittings are denoted by the solid line where A, B & C represent the Langmuir, Kisliuk & Langmuir-Kisliuk fits respectively. The peptide concentration used is denoted by the point/line colour which is black, red, green blue, cyan and magenta for 25, 50, 100, 200, 400 & 800  $\mu\text{M}$ , respectively. The numbers represent the following peptides: 1) A3, 2) A3s, 3) A3sC8 & 4) A3sT2.

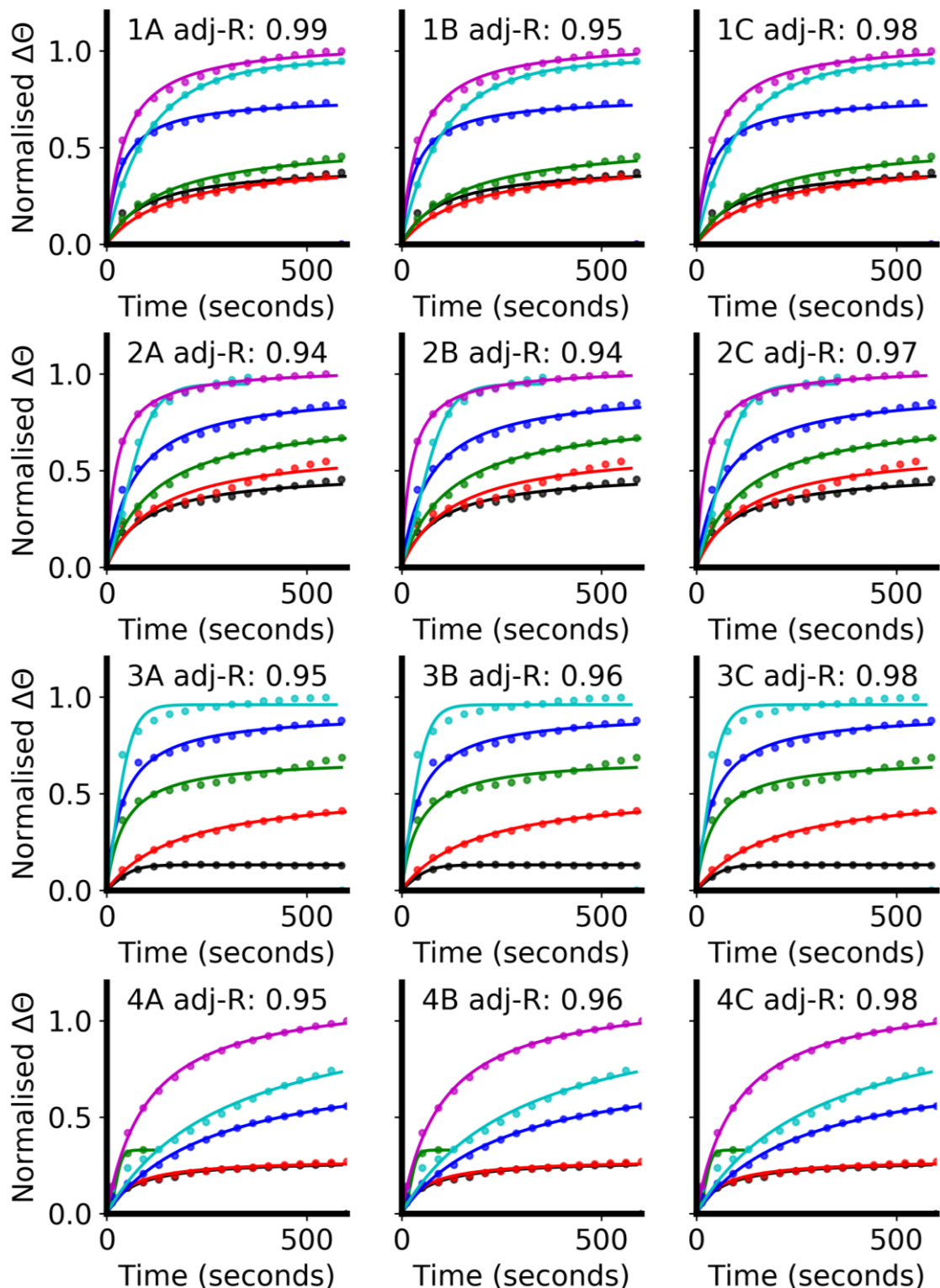


Figure 4.2 - Kinetic fits for the non-sulphur containing sequences from the peptide library studied with the associated averaged adjusted-R<sup>2</sup> values. The points represent the experimental data and the fittings are denoted by the solid line where A, B & C represent the Langmuir, Kisliuk & Langmuir-Kisliuk fits respectively. The peptide concentration used is denoted by the point/line colour which is black, red, green blue, cyan and magenta for 25, 50, 100, 200, 400 & 800  $\mu\text{M}$ , respectively. The numbers represent the following peptides: 1) AuBP1, 2) AuBP2, 3) HRE & 4) Pd4.

The Langmuir-Kisliuk kinetic model suggested in Chapter III has an improved quality of fit compared to either the Langmuir or Kisliuk model. The Langmuir-Kisliuk model offers a superior fit with adj-R<sup>2</sup> values being ≥0.969 for the Langmuir-Kisliuk fits compared to the adj-R<sup>2</sup> values of ≥0.895 or ≥0.899 for the Langmuir and Kisliuk models respectively. This kinetic model offers a superior fit for all datasets, out-performing either the Langmuir or Kisliuk models in all cases except for AuBP1 where the Langmuir fit has an approximately equivalent adj-R<sup>2</sup> to the Langmuir-Kisliuk model. However, for the sequences studied there appears to be a concentration where the experimental system is neither Langmuirian or Kisliukian. this concentration is 50µM for A3sC8, AuBP1 and 100µM for A3s, A3s-T2, Pd4, HRE, AuBP1. The author proposes at this ‘cross-over’ point both Langmuirian and Kisliukian binding events are occurring and these two simultaneous events are not accounted for by this model. Further exploration of this crossover region is outside the scope of this study but should be addressed in future. When approaching this problem, the two simultaneous kinetic events should be accounted for using two models; one where both kinetic events are dependent on each other and the latter where both events are independent. By comparing the quality of fit for both models the most probable kinetic event can be determined.

Table 4.3 - Average adjusted R<sup>2</sup> values for each kinetic model when used to fit the MP-SPR data recorded for each peptide under different concentrations. The values in bold are used to highlight the best fitting method(s) for each sequence.

Peptide	Sequence	Adjusted R <sup>2</sup> value		
		Langmuir	Kisliuk	Langmuir-Kisliuk
A3	AYSSGAPPMPFF	0.895	0.899	<b>0.985</b>
A3s	AYSSGAPMPFF	0.930	0.928	<b>0.972</b>
A3s-C8	AYSSGAPCPPF	0.941	0.940	<b>0.979</b>
A3s-T2	ATSSGAPMPFF	0.944	0.942	<b>0.980</b>
AuBP1	WAGAKRLVLRRE	<b>0.986</b>	0.948	<b>0.982</b>
AuBP2	WALRRSIRRQSY	0.936	0.937	<b>0.969</b>
HRE	AHHAHHAAD	0.955	0.956	<b>0.976</b>
Pd4	TSNAVHPTLRHL	0.951	0.959	<b>0.983</b>

The adj-R<sup>2</sup> values as shown in table 4.3 not only comment on which kinetic model is optimal for fitting, but also provide information about the probabilities of certain events occurring during the binding process. The K<sub>c</sub> term can be expressed as the ratio of direct desorption from the surface ( $p'_d$ ) against the adsorption ( $p_a$ ) and desorption ( $p_d$ ) from the intrinsic layer, see equation 4.3. The approximately equal adj-R<sup>2</sup> values for both the Langmuir and Kisliuk model suggests that the binding mechanism is concentration

dependent with both Langmuirian and Kisliukian characteristics. This model does not simplify  $K_c$  further which removes the need for any simplifying assumptions and therefore is able to more accurately model the binding interactions. The Langmuir-Kisliuk model offers the highest quality of fit for all the systems studied except AuBP1, this suggests that peptide-assisted binding occurs, as the Langmuir model where only peptide surface interactions are considered offers a poorer quality of fit. Peptide-assisted binding described by the Langmuir-Kisliuk model is where peptides bound to the surface assist in the adsorption of peptides in the intrinsic layer onto the surface.

$$K_c = \frac{p'_d}{p_a \cdot p_d} \quad 4.3$$

$$K_c = \frac{p'_d}{p_a \cdot p_d} \approx \frac{p_d}{p_a \cdot p_d} \quad 4.4$$

AuBP1 is a unique case and can be fitted with an equal quality of fit with either the Langmuir or the Langmuir-Kisliuk model, see figure 4.2-1 A & C for the Langmuir and Langmuir-Kisliuk fits respectively. This indicates that the Langmuir assumptions are true and 1:1 binding occurs. For the  $K_c$  term this means it can be approximated by the ratio of probabilities relating solely to the intrinsic layer, see equation 4.4.<sup>113</sup>

Generally the  $K_c$  values, see table 4.4, are low with the majority of fits being below 1 indicating that desorption from the surface is improbable. However, some fits have a  $K_c$  value greater than 1 suggesting a higher probability for peptides bound to the surface to desorb. The large spike in  $K_c$  for 50μM A3 at first was considered to be an outlier; however, the trend of an increase in  $K_c$  is observed at 50μM for both A3s & A3s-T2 but not with A3s-C8 indicating that there may be a sequence related peptide-peptide interaction or rearrangement at this concentration, which is not observed upon the Cys-Au interaction.<sup>230–232</sup>

Table 4.4 - Langmuir-Kisliuk parameters (Amplitude ( $\alpha$ ), langmuir rate constant (k) & Kisliuk constant (K<sub>c</sub>) for all the MP-SPR kinetic data collected.

Conc (μM)		A3	A3s	A3sC8	A3sT2	AuBP1	AuBP2	HRE	Pd4
25	$\alpha$	2.0E-1	2.0E-1	4.4E-1	3.7E-1	4.0E-1	4.9E-1	1.3E-1	2.7E-01
	k	3.0E-12	3.1E-4	3.8E-4	2.1E-4	2.6E-4	1.8E-4	3.4E-2	5.3E-04
	K <sub>c</sub>	<b>4.4E-11</b>	<b>7.9E-3</b>	<b>6.0E-2</b>	<b>1.2E-1</b>	<b>2.6E-2</b>	<b>1.7E-2</b>	<b>2.5</b>	<b>3.4E-02</b>
50	$\alpha$	2.8E-1	2.5E-1	5.9E-1	4.1E-1	4.3E-1	6.1E-1	5.2E-1	2.8E-01
	k	1.9E-1	2.2E-2	4.2E-4	4.8E-3	4.1E-4	3.5E-4	3.1E-4	3.6E-04
	K <sub>c</sub>	<b>4.9E+1</b>	<b>4.0E-1</b>	<b>1.6E-2</b>	<b>1.2</b>	<b>6.5E-2</b>	<b>4.5E-2</b>	<b>5.6E-2</b>	<b>2.1E-2</b>
100	$\alpha$	7.8E-1	5.1E-1	8.3E-1	6.4E-1	5.2E-1	7.8E-1	6.8E-1	3.3E-1
	k	2.8E-17	3.8E-4	3.8E-5	3.5E-4	3.7E-4	4.6E-4	3.8E-5	1.2E-1
	K <sub>c</sub>	<b>9.0E-16</b>	<b>2.7E-2</b>	<b>2.7E-3</b>	<b>5.5E-2</b>	<b>5.3E-2</b>	<b>5.4E-2</b>	<b>1.7E-3</b>	<b>1.7E+1</b>
200	$\alpha$	9.4E-1	7.7E-1	9.4E-1	7.8E-1	7.6E-1	9.1E-1	9.2E-1	7.9E-1
	k	2.4E-5	4.6E-4	4.1E-3	4.4E-4	2.0E-4	2.8E-4	2.8E-6	1.7E-4
	K <sub>c</sub>	<b>3.9E-4</b>	<b>5.0E-2</b>	<b>3.1E-1</b>	<b>5.5E-2</b>	<b>6.9E-3</b>	<b>1.9E-2</b>	<b>1.1E-4</b>	<b>4.6E-2</b>
400	$\alpha$	9.6E-1	9.6E-1	9.7E-1	9.1E-1	9.5E-1	9.5E-1	9.6E-1	1.1
	k	3.0E-4	5.1E-4	5.0E-5	2.8E-4	6.6E-3	2.7E-2	4.0E-2	2.9E-4
	K <sub>c</sub>	<b>6.2E-3</b>	<b>4.8E-2</b>	<b>1.1E-3</b>	<b>8.1E-3</b>	<b>6.4E-1</b>	<b>4.0</b>	<b>2.6</b>	<b>8.6E-2</b>
800	$\alpha$	1.0	1.1	9.9E-1	1.0	1.0	1.0		1.1
	k	3.9E-4	5.1E-4	1.4E-2	1.4E-4	5.2E-4	2.7E-4	Not Collected	3.3E-4
	K <sub>c</sub>	<b>2.9E-2</b>	<b>2.3E-2</b>	<b>5.4E-1</b>	<b>4.6E-3</b>	<b>2.2E-2</b>	<b>6.7E-3</b>		<b>3.4E-2</b>

To determine the K<sub>D</sub> and ΔG values for this system the  $\alpha$  parameter, discussed in section 3.3.2, for each concentration was plotted against log(concentration) and fitted using a dose-response function as discussed in Chapter III, see figure 4.3 and figure 4.4 overleaf for the fittings of the A3 derived sequences and non-sulphur containing sequences respectively. K<sub>D</sub> was determined by calculating 10 to the power of the midpoint ( $x_0$ ) and subsequently the K<sub>D</sub> value was used to determine ΔG, as detailed in Chapter III. Ultimately, the Langmuir-Kisliuk kinetic model was selected as the model used to study the kinetics occurring at the Au<sub>(111)</sub>-Peptide interface in our MP-SPR studies due to a consistently high quality of fit across all samples investigated, see table 4.3.

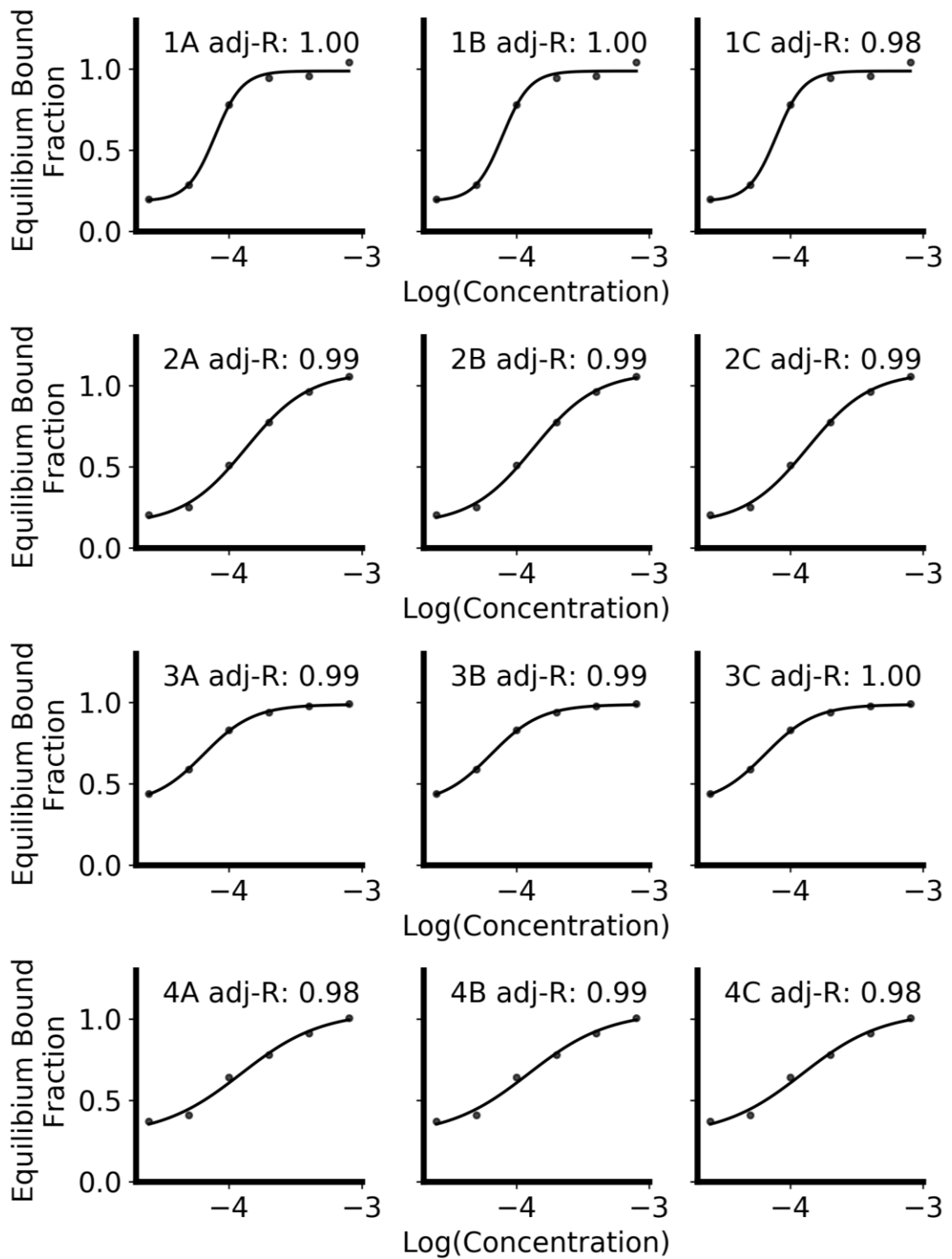


Figure 4.3 - Sigmoidal fits for the A3 sequences from the peptide library studied with the associated averaged adjusted- $R^2$  values. The points represent the experimental data and the fittings are denoted by the solid line where A, B & C represent the equilibrium bound fraction determined by Langmuir, Kisliuk & Langmuir-Kisliuk fits respectively. The numbers represent the following peptides: 1) A3, 2) A3s, 3) A3sC8 & 4) A3sT2.

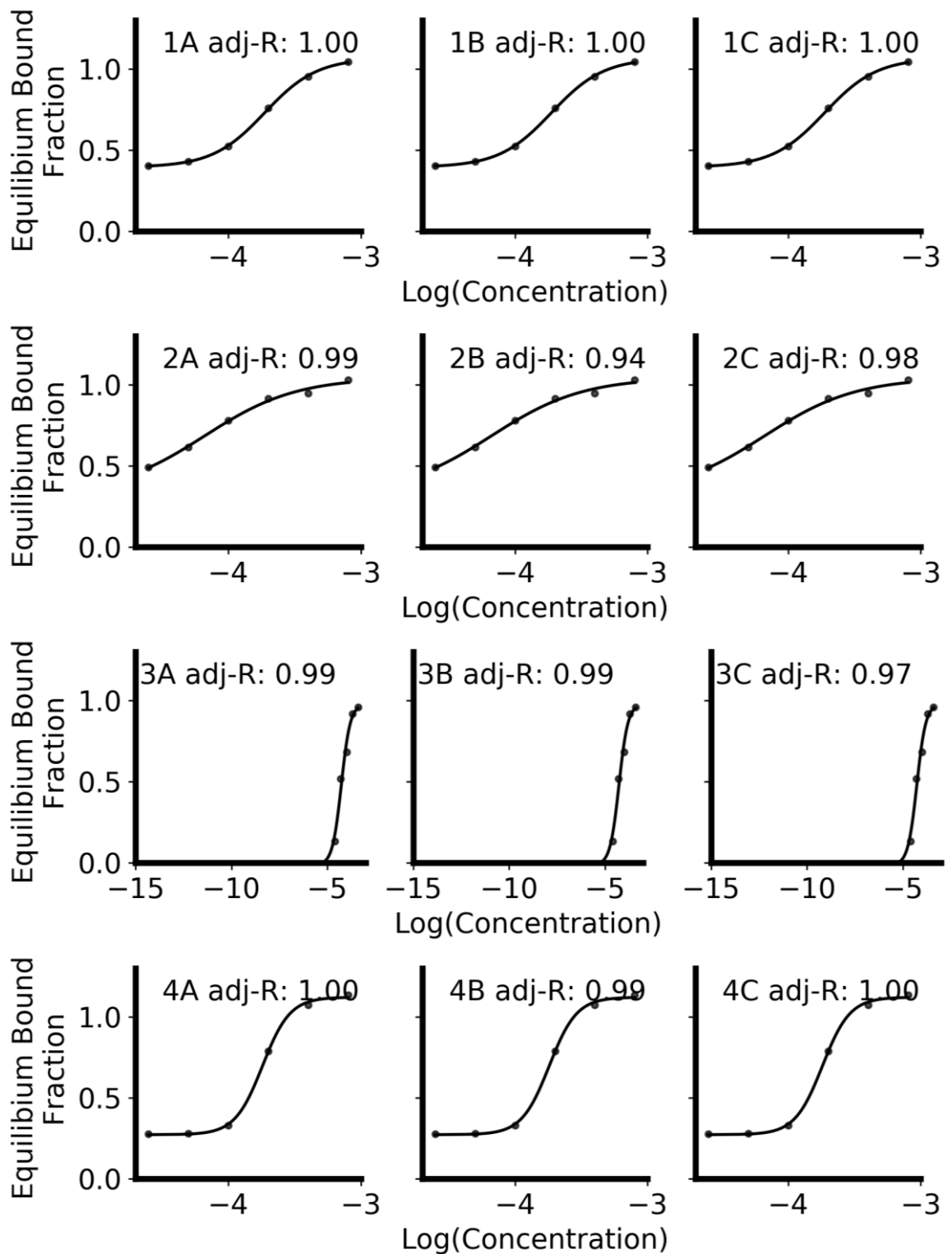


Figure 4.4 - Sigmoidal fits for the non-sulphur containing sequences from the peptide library studied with the associated averaged adjusted- $R^2$  values. The points represent the experimental data and the fittings are denoted by the solid line where A, B & C represent the equilibrium bound fraction determined by Langmuir, Kisliuk & Langmuir-Kisliuk fits respectively. The numbers represent the following peptides: 1) AuBP1, 2) AuBP2, 3) HRE & 4) Pd4.

Values for  $K_D$ , the hill slope (n) and  $\Delta G$  were determined for each sequence using the Langmuir-Kisliuk model, see table 4.5. All the sequences studied have a Hill slope (n) > 1, this indicates positive cooperativity takes place during binding and suggests there is preferential binding to our gold surface where peptides in the bound and unbound states are not in competition.

Table 4.5 - Thermodynamic constants determined from MP-SPR kinetic data of the known gold binding peptides interacting with Au<sub>(111)</sub> surfaces under a high concentration regime.  $K_D$  is the dissociative constant, n is the Hill slope and  $\Delta G$  is Gibbs free energy. Units stated as appropriate.

	AuBP1	AuBP2	HRE	Pd4	A3	A3s	A3sT2	A3sC8
$K_D$ ( $\mu M$ )	$188 \pm 4.87$	$71.7 \pm 27.8$	$54.5 \pm 10.2$	$181 \pm 4.98$	$78.9 \pm 7.43$	$135 \pm 11.5$	$127 \pm 28.8$	$64.5 \pm 3.09$
n	$2.19 \pm 0.12$	$1.26 \pm 0.51$	$1.86 \pm 0.58$	$4.18 \pm 0.55$	$4.21 \pm 1.19$	$1.83 \pm 0.31$	$1.43 \pm 0.60$	$2.31 \pm 0.20$
$\Delta G$ (kcal·mol <sup>-1</sup> )	$-7.33 \pm 0.02$	$-7.94 \pm 0.24$	$-8.07 \pm 0.11$	$-7.36 \pm 0.02$	$-7.84 \pm 0.06$	$-7.53 \pm 0.05$	$-7.58 \pm 0.13$	$-7.96 \pm 0.03$

Initially we predicted that the peptides that contained amino acids with sulphur containing R-groups (Cys & Met) would be the strongest binders, due to both these amino acids being classified as soft ligands using HSAB theory.<sup>233,234</sup> HSAB theory states that soft ligands will preferentially bind to soft metals with the inverse also being true, meaning that like preferentially binds to like. Practically this means that Cys and Met will preferentially bind to Au<sup>0</sup>, Ag<sup>0</sup> & ZnS. The Cys-Au interaction was expected to be particularly favourable due to R-group on the Cys residue being a primary thiol which are well known for gold binding applications due to the strong Au-S bonds formed.<sup>230-232</sup>

Surprisingly, the strongest binder determined from the kinetic studies contained neither Cys nor Met but instead contains 4 His residues. While His is not as soft in nature as Cys it is still classified as a soft ligand using HSAB theory,<sup>233,234</sup> and is known to form stable interactions with Au.<sup>9,10</sup> When multiple His groups (i.e. M-His<sub>2</sub>) bind, the resulting M-His<sub>2</sub> complex is generally softer than the initial M-His complex.<sup>235</sup> This drives the interaction of multiple His groups with the surface forming a stronger overall binding interaction between the peptide and the surface analogous to multidentate ligands binding to a metal centre.

The other non-sulphur residue containing peptides (AuBP1, AuBP2 & Pd4) can be separated into two groups: the weakest binders in this study (AuBP1 & Pd4) and AuBP2,

the third strongest binder in this study. The AuBP1 sequence does not contain any residues traditionally used in gold binding (Cys, Met, His). Instead this sequence binds via two residue pairs, Lys<sub>5</sub> Arg<sub>6</sub> and Arg<sub>10</sub> Arg<sub>11</sub>.<sup>96</sup> These residue pairs form a cationic motif which creates a charge based interaction with the Au<sub>111</sub> surface. Likewise, AuBP2 contains no Cys, Met or His residues and instead achieves binding via Arg<sub>4</sub> Arg<sub>5</sub> and Arg<sub>8</sub> and Arg<sub>9</sub> sequence diads forming similar cationic motifs.<sup>96</sup> This binding motif enables both AuBP1 and AuBP2 to strongly bind to the Au<sub>(111)</sub> surface with ΔG values of -8.9 ± 0.2 and -8.7 ± 0.2 kcal·mol<sup>-1</sup> for AuBP1 and AuBP2 respectively. These values were determined from low concentration (0.23, 0.46, 0.92, 2.00 μM) SPR measurements using a Langmuir fitting.<sup>96</sup> The values obtained for ΔG for the AuBP1 and AuBP2 sequences, see table 4.5, in our studies differ from those in the literature by 1.57 kcal·mol<sup>-1</sup> and 0.76 kcal·mol<sup>-1</sup> respectively. A reduction in the overall ΔG value was expected as the Langmuir-Kisliuk model does not account for peptide-peptide interactions which will have a greater contribution under higher concentrations due to an increased probability of peptide-peptide collisions. The binding affinity of both the AuBP1 and AuBP2 sequences were reported to be the same;<sup>96</sup> however, it appears as if the AuBP1 sequence experiences more peptide-peptide interactions in solution which are not detected by the MP-SPR spectrometer, this is potentially caused by the hydrophobic LVL motif in this sequence.<sup>96,236</sup>

The Pd4 sequence was originally identified using phage display as a palladium binder and was not tested on Au<sub>(111)</sub> surfaces in the original literature.<sup>98</sup> While it might be expected that this sequence would bind poorly to the Au<sub>(111)</sub> surface, palladium is also a soft metal like gold. Therefore, similar “soft” residues can be expected to bind to both the Au and Pd surfaces. The Pd4 sequence has a comparable binding affinity to the AuBP1 sequence with the His<sub>6</sub> and His<sub>11</sub> groups present facilitating favourable His-Au interactions<sup>235</sup> as in the HRE system there are multiple His residues available to interact with the gold surface with the resulting M-His<sub>2</sub> complex is generally softer than the M-His complex.<sup>235</sup>

The sulphur containing binding peptides (A3, A3s, A3sT2 & A3sC8) do not appear to form the expected strong Au-S interaction, expected to be very thermodynamically favourable. While the Cys-Au or Met-Au interactions are not the dominant interaction, this may be due to a steric issue where the Met/Cys R-group is not in the correct orientation to form a strong Au-S interaction. The Cys-Au<sub>(111)</sub> interaction appears to be preferred to the Met-Au<sub>(111)</sub> interaction; the author suggests this is caused by either the higher reactivity of the primary thiol or due to less steric hindrance around the sulphur group.

Computational studies of the A3 sequence in literature show that the Tyr-Au interaction is a strong binding interaction<sup>237</sup> and this residue is located between the Ala-1 and Ser-4 residues which have been determined to anchor the sequence<sup>215</sup> leading to a strong binding interaction holding the peptide to the surface. The same study reported the Tyr, Met & Phe groups were the strongest binders in the sequence and the aromaticity of Tyr assisted with its adsorption,<sup>215</sup> to test this experimentally the A3sT2 sequence was developed which replaced Tyr<sub>2</sub> with Thr. This substitution appears to make minimal impact in the binding performance of the A3sT2 ( $\Delta G -7.58 \pm 0.13$ ) sequence compared to A3s ( $\Delta G -7.53 \pm 0.05$ ) with the difference in  $\Delta G$  being within error.

The thiol chemistry afforded by Met and Cys groups is not as dominant as originally anticipated with peptide diads forming equally as strong if not stronger binding interactions. Multiple histidine residues in a sequence appear to have a high affinity for the gold surface with sequence diads such as His His, Lys Arg or Arg Arg facilitating the strongest binding mechanisms. The strongest overall binder from MP-SPR studies was the HRE sequence containing 2 His His diads in the primary sequence and the weakest overall binder was Pd4, which contained 2 His residues but no His diads. The AuBP1 and AuBP2 sequences differed in binding affinity, which was not reported in the original literature, this is likely a concentration based effect due to the 100 fold greater concentrations used in this study. The observed differences in behaviour are likely due to peptide-peptide interactions and peptide assembly/agglomeration which is not observed at the sensor surface but will impact the measured kinetics. To further study the agglomeration/assembly behaviour observed, isothermal titration calorimetry experiments were proposed.

#### 4.3.2 Isothermal Titration Calorimetry Binding Studies

The kinetic MP-SPR studies in section 4.3.1 suggested that the library of gold binders studied with the exception of AuBP1 all undergo peptide-assisted binding where peptides bound to the surface assist in the adsorption of peptides in the intrinsic layer onto the surface. Differences in binding affinity between the AuBP1 and AuBP2 sequences were not reported in the original literature<sup>96</sup> and were attributed to concentration dependent agglomeration/assembly behaviour; however such aggregation is undetectable by MP-SPR due to this process not occurring on the sensor surface.

Isothermal titration calorimetry (ITC) measures the overall thermal change in the sample cell and facilitates the precise addition of known quantities of titrant. Consequently this technique is sensitive to what occurs within the solvent in addition to the processes which are occurring at the AuNPs' surface. Thermodynamic ITC studies were used to investigate

the thermodynamics of both peptide solvation and peptide-Au binding, see figure 4.5 & figure 4.6 for the solvation isotherms and figure 4.7 & figure 4.8 for the peptide-Au isotherms. The peptide-Au study used uncapped  $17\pm3$  nm gold nanoparticles, which express the  $\text{Au}_{(111)}$ ,  $\text{Au}_{(110)}$  and  $\text{Au}_{(100)}$  crystal facets. The addition of  $\text{Au}_{(110)}$  and  $\text{Au}_{(100)}$  crystal facets was predicted to result in a difference in the values of  $\Delta G$  determined via MP-SPR and ITC.

The collected ITC isotherms were processed using a simplistic empirical approach where the  $\Delta H$  values are determined using the amplitude of the dataset, and a linear fitting of the slope is employed to determine  $K_D$ .<sup>107,109,238</sup> Unlike the MP-SPR spectrometer, the ITC instrument is highly sensitive to all thermodynamic processes within the sample cell. Consequently, developing an accurate analytical model for such a complex system is outside the scope of this study and a model developed with invalid assumptions would compromise the findings of this study. While a linear fitting approach is the most basic empirical fitting method, has been used by scientists for hundreds of years and was the first fitting model to be studied extensively,<sup>239</sup> this model assumes linearity of the dataset. If the dataset is non-linear, error can be introduced which is shown in the Anscombe's quartet where 4 different datasets return the same linear regression fit.<sup>240</sup> However, due to the ability of the experimentalist to judge linearity this model can be appropriately used in cases where more complex fittings may not be appropriate.

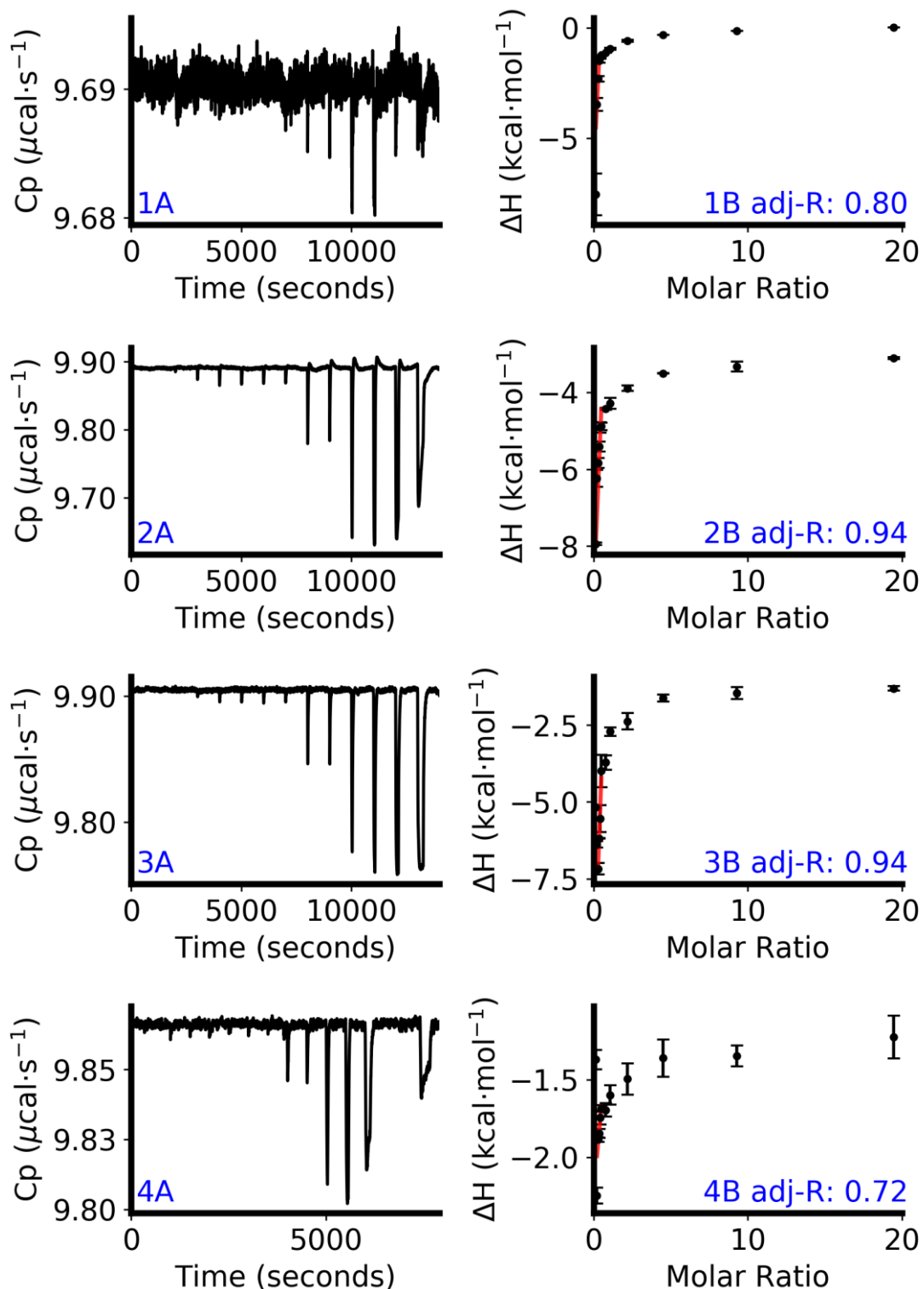


Figure 4.5 - Heat capacity plots (A) and isotherms (B) of peptide solvation for the A3 sequences from the peptide library studied with the associated adjusted- $R^2$  values. The isotherm shown in subplot B is an average of the 2 isotherms collected with the variance between datasets being shown as error bars. The red line shows the linear region fitted to determine  $K_A$  values for these systems. The numbers represent the following peptides: 1) A3, 2) A3s, 3) A3sC8 & 4) A3sT2.

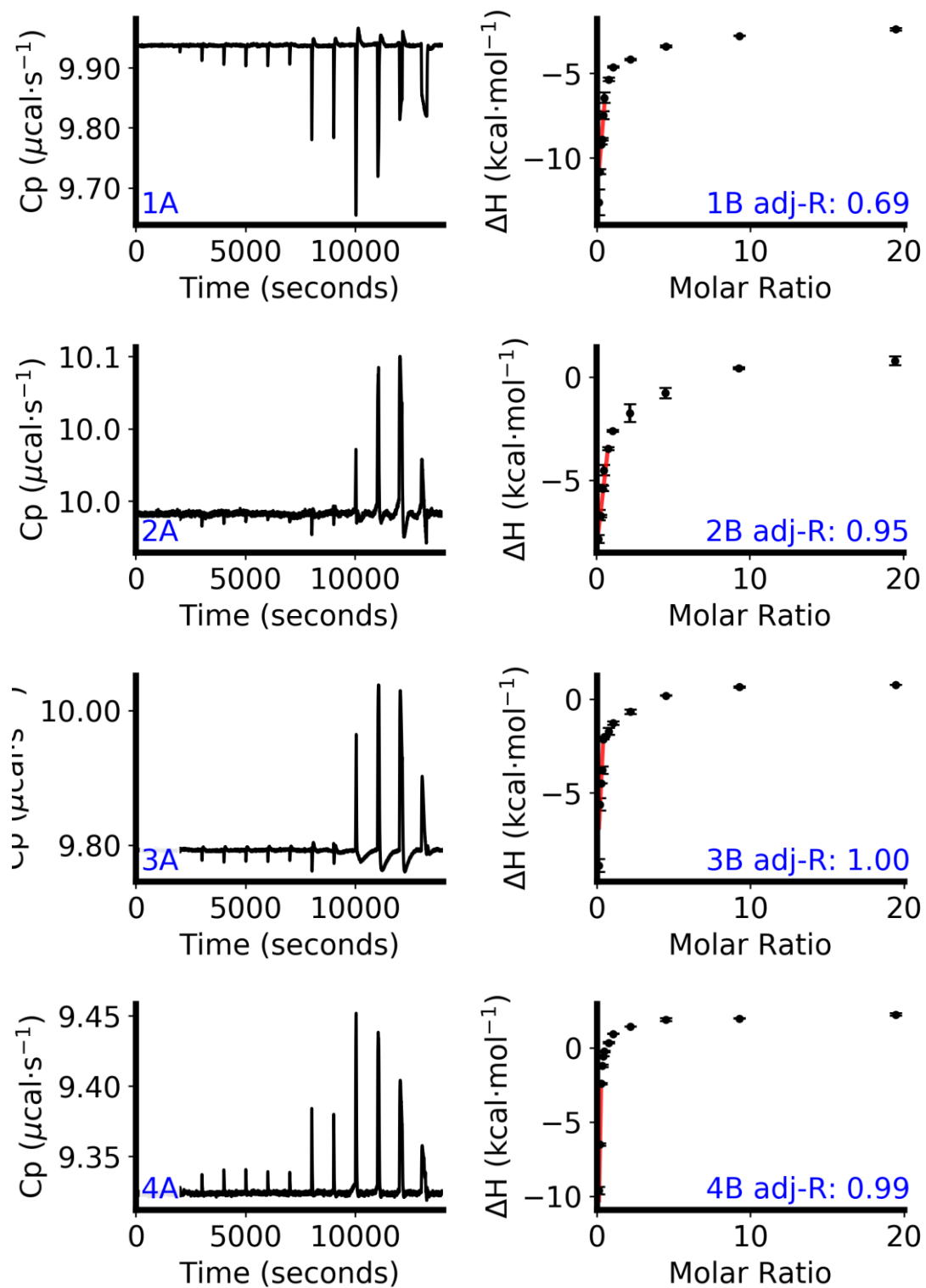


Figure 4.6 - Heat capacity plots (A) and isotherms (B) of peptide solvation for the non-sulphur containing sequences from the peptide library studied with the averaged adjusted- $R^2$  values. The isotherm shown in subplot B is an average of the 2 isotherms collected with the variance between datasets being shown as error bars. The red line shows the linear region fitted to determine  $K_A$  values for these systems. The numbers represent the following peptides: 1) AuBP1, 2) AuBP2, 3) HRE & 4) Pd4.

The thermodynamic constants for the solvation experiments were extracted from the isotherms, see figure 4.5 and figure 4.6, with numerical data presented in table 4.6. It was observed that the solvation of all the sequences in the studied library were enthalpically

driven; however, the entropic behaviour of the sequences could be divided into two distinct groups which were the A3 family of sequences and the non-sulphur containing sequences. The non-sulphur containing sequences all had negative values for  $T\Delta S$  which suggests that the system becomes more ordered upon solvation. This increase in order upon solvation indicates that peptide agglomeration/assembly could be occurring. This is supported by the presence of Arg and His residues in the primary sequence which are known to form favourable His-His, His-Arg and Arg-Arg interactions.<sup>241,242</sup>

Table 4.6: Tabulated thermodynamic constants determined from ITC peptide solvation datasets. Where the peptides tabulated in table 4.1 were dispersed into 18MΩ water.  $\Delta H$  is the enthalpy of solvation,  $T\Delta S$  is the temperature independent solvation entropy and  $\Delta G$  is the Gibbs free energy of solvation. Units stated where appropriate.

	AuBP1	AuBP2	HRE	Pd4	A3	A3s	A3sT2	A3sC8
$\Delta H$ (kcal·mol <sup>-1</sup> )	-10.24 ± 0.77	-8.64 ± 0.29	-9.62 ± 0.40	-11.85 ± 0.26	-7.57 ± 0.95	-4.83 ± 0.04	-1.02 ± 0.15	-5.87 ± 0.20
$T\Delta S$ (kcal·mol <sup>-1</sup> )	-2.36 ± 0.79	-1.06 ± 0.29	-1.48 ± 0.40	-2.99 ± 0.27	9.15 ± 0.97	2.99 ± 0.79	1.07 ± 0.23	7.43 ± 0.20
$\Delta G$ (kcal·mol <sup>-1</sup> )	-7.88 ± 1.10	-7.58 ± 0.41	-8.14 ± 0.57	-8.86 ± 0.37	-16.72 ± 1.36	-7.82 ± 0.79	-2.09 ± 0.27	-13.30 ± 0.37

The A3 family of sequences does not contain either the His or Arg residues and all had positive values for  $T\Delta S$  which suggests that the system becomes more disordered upon solvation indicating peptide agglomeration/assembly is not occurring. This supports the proposed hypothesis that the behaviour observed in the non-sulphur containing subset is due to the His and Arg residues. The A3 family of peptides has a lower enthalpic drive than the non-sulphur containing subset with the maximal  $\Delta H$  value of the A3 subsets being 1.07 kcal mol<sup>-1</sup> less exothermic than the minimum  $\Delta H$  value of the non-sulphur subset. However, due to the lack of entropic hindrance the  $\Delta G$  values of the A3 subset with the exception of A3sT2 are equal to or greater than that of the non-sulphur containing subset. This suggests that the Tyr<sub>2</sub> is important for the solvation for the A3 family of sequences and is why the A3sT2 was less favourable than the rest of the sequences tested. The most favourable sequences for solvation were the A3 and A3sC8 peptides which have  $\Delta G$  values of -16.72 and -13.30 kcal mol<sup>-1</sup> respectively which suggests that the thiol group (Met<sub>9</sub> or Cys<sub>8</sub>) are important for solvation.

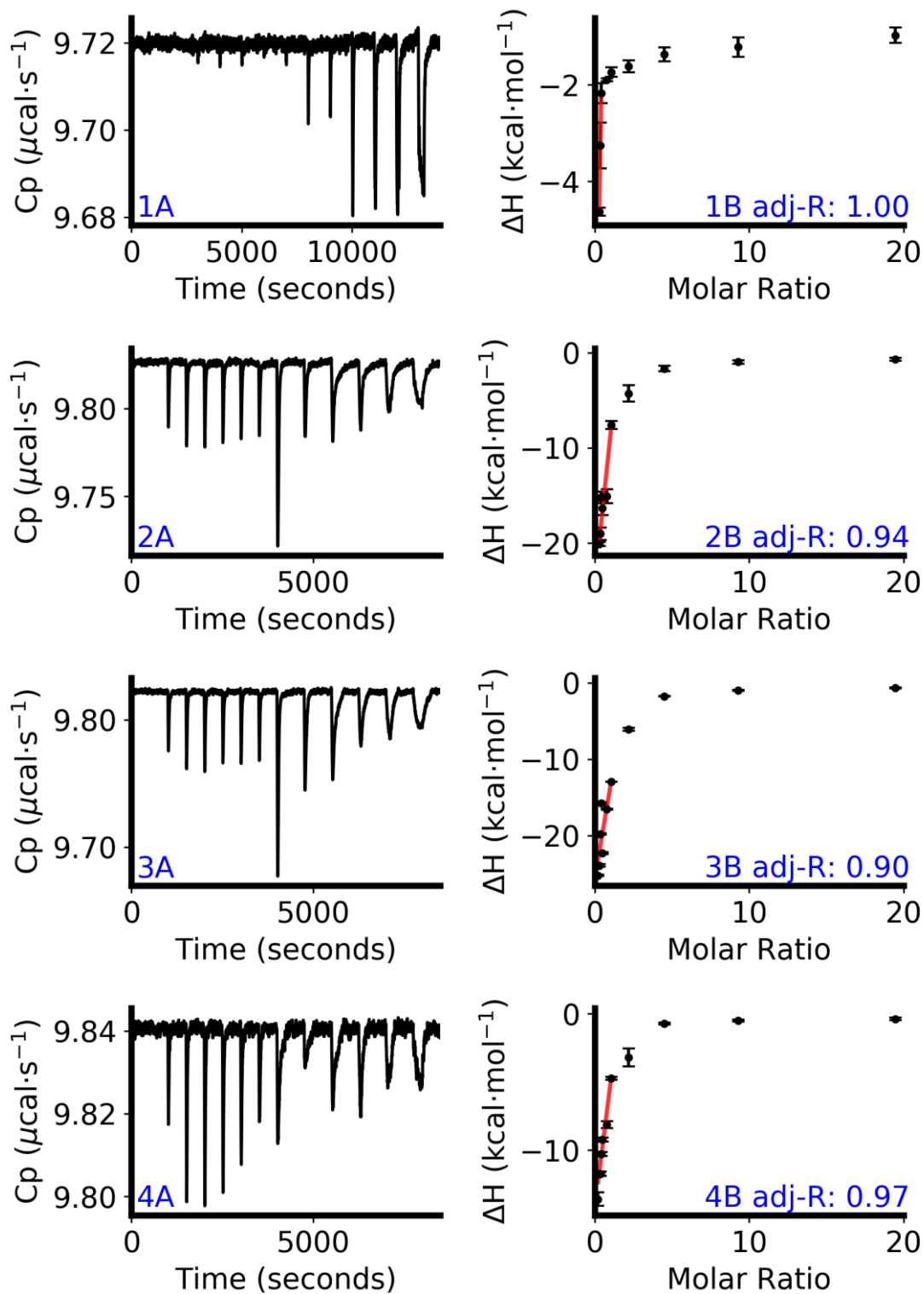


Figure 4.7 - Heat capacity plots (A) and isotherms (B) for the peptide-Au interactions of the A3 sequences from the peptide library studied with the associated adjusted- $R^2$  values. The isotherm shown in subplot B is an average of the 2 isotherms collected with the variance between datasets being shown as error bars. The red line shows the linear region fitted to determine  $K_A$  values for these systems. The numbers represent the following peptides: 1) A3, 2) A3s, 3) A3sC8 & 4) A3sT2.

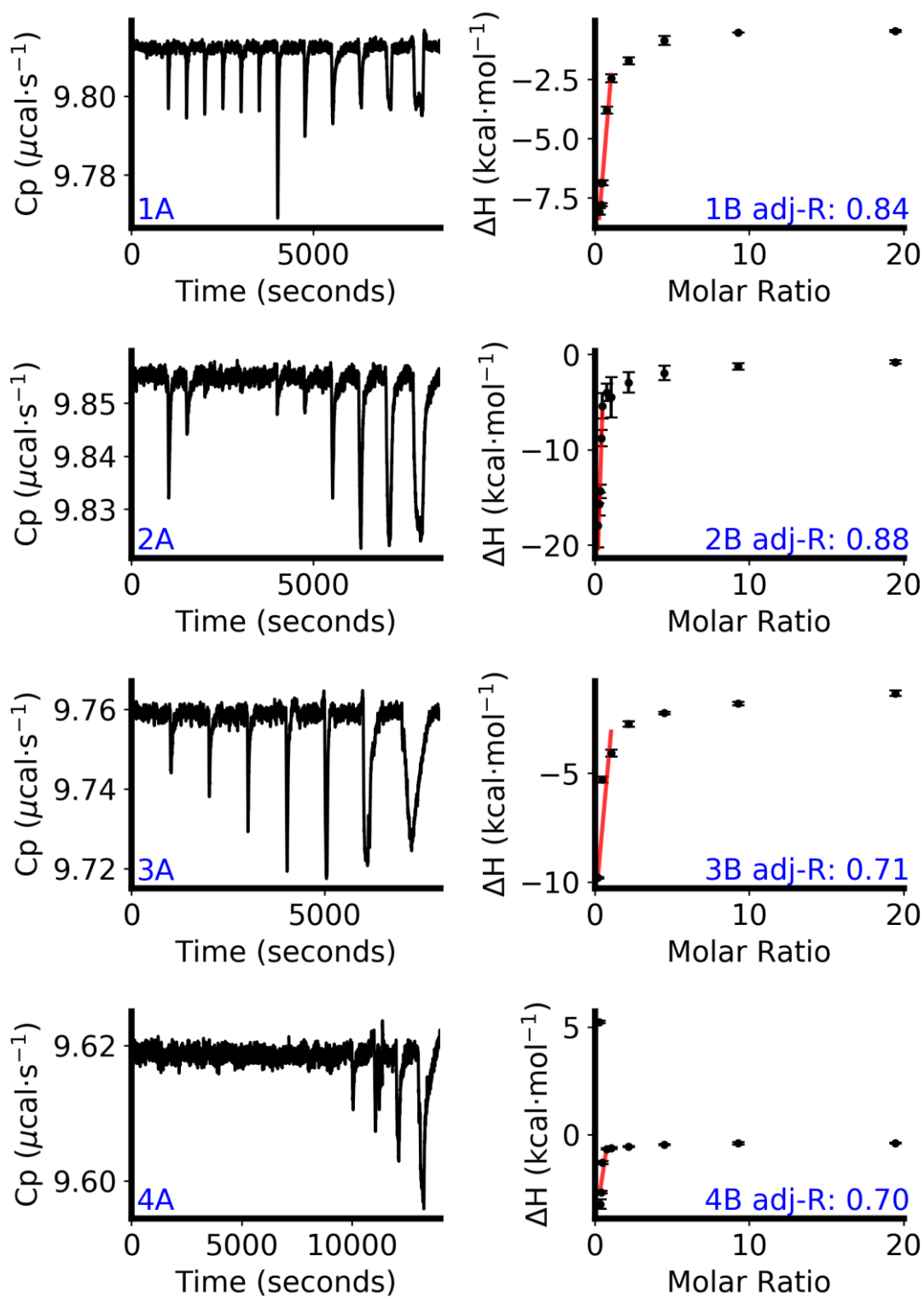


Figure 4.8 - Heat capacity plots (A) and isotherms (B) for the peptide-Au interactions of the non-sulphur containing sequences from the peptide library studied with the associated adjusted- $R^2$  values. The isotherm shown in subplot B is an average of the 2 isotherms collected with the variance between datasets being shown as error bars. The red line shows the linear region fitted to determine  $K_A$  values for these systems. The numbers represent the following peptides: 1) AuBP1, 2) AuBP2, 3) HRE & 4) Pd4.

The thermodynamic constants for peptide-Au binding experiments were extracted from the isotherms, see figure 4.7 and figure 4.8, with numerical data presented in table 4.7. It was observed that the peptide-Au binding of all the sequences in the studied library was enthalpically driven similar to the behaviour observed in the solvation experiments. However, the two subsets of entropic behaviour for the A3 family of sequences and the non-sulphur containing sequences were not observed. Instead the entropic behaviour of the studied library appeared to tend towards a reduced value of  $T\Delta S$  inferring the system was becoming more ordered with the exception of the AuBP1, Pd4 and A3 sequences which had increased values of  $T\Delta S$ . No clear correlation was observed between  $\Delta G$  values indicative of binding strength and entropic behaviour. The two strongest binders in this study AuBP2 and A3 had opposite entropic behaviour and  $\Delta G$  values of -8.55 and -8.17 kcal mol<sup>-1</sup> respectively.

Table 4.7: Tabulated thermodynamic constants determined from ITC peptide binding datasets. Where the peptides tabulated in table 4.1 were titrated into a suspension containing AuNPs in 18MΩ water.  $\Delta H$  is the enthalpy of interaction,  $T\Delta S$  is the temperature independent interaction entropy and  $\Delta G$  is Gibbs free energy of interaction. Units stated where appropriate.

	AuBP1	AuBP2	HRE	Pd4	A3	A3s	A3sT2	A3sC8
$\Delta H$ (kcal·mol <sup>-1</sup> )	-7.62 ± 0.14	-17.14 ± 2.33	-8.48 ± 0.14	-2.83 ± 0.22	-3.66 ± 0.18	-19.41 ± 0.25	-13.22 ± 0.58	-24.55 ± 0.13
$T\Delta S$ (kcal·mol <sup>-1</sup> )	0.02 ± 0.19	-8.59 ± 2.33	-0.90 ± 0.29	4.48 ± 0.31	4.51 ± 0.18	-11.48 ± 0.26	-5.45 ± 0.58	-16.61 ± 0.16
$\Delta G$ (kcal·mol <sup>-1</sup> )	-7.64 ± 0.24	-8.55 ± 3.30	-7.58 ± 0.32	-7.31 ± 0.38	-8.17 ± 0.25	-7.93 ± 0.36	-7.77 ± 0.82	-7.94 ± 0.21

The observed difference in entropic behaviour between the solvation and peptide-Au experiments suggests that between the competing peptide-peptide and peptide-Au interactions the peptide-Au is most favourable. This is in agreement with the MP-SPR studies where the Hill slope ( $n$ ) > 1 indicated that positive cooperativity occurs during binding and suggested there is preferential binding to the Au<sub>(111)</sub> surface when peptides in the bound and unbound states are not in competition. The ITC studies suggest that the peptide-peptide and peptide-Au interactions may compete with sequences such as HRE, AuBP1, Pd4, A3 and A3sC8 which all have lower  $\Delta G$  for the peptide-Au interaction than for solvation which could not be observed in the MP-SPR studies.

The strongest binder in this study is a sulphur containing sequence, A3, contrary to the findings in the MP-SPR studies. This suggests that either the Au<sub>(111)</sub>, Au<sub>(110)</sub> and Au<sub>(100)</sub> facets are important for maximising A3 binding strength or the presence of the other gold facets has a negative impact on the peptide diad binding strength. The second hypothesis is supported by HRE being the among weakest binders in the ITC studies while being the strongest binder in the MP-SPR studies. The HRE sequence binds to Au through two His His diads, which are soft ligands<sup>233,234</sup> known to form stable interactions with Au<sup>9,10</sup> and the interaction of two His residues is known to form a softer more favourable M-His<sub>2</sub> complex.<sup>235</sup> This suggests that the diad binding motif may have a lower efficacy when Au<sub>(110)</sub> and Au<sub>(100)</sub> facets are present.

The AuBP1 and AuBP2 sequences are known to bind to Au via peptide diads;<sup>96</sup> however, they show no significant change between MP-SPR and ITC studies with all the values observed being the same within the margins of error. The high uncertainty for the AuBP2 sequence suggests that two thermodynamic events may be competing such as a peptide-Au event and an assembly event leading to the formation of agglomerates inside the ITC sample vessel. This suggests that the Arg Arg and Lys Arg diads used by the AuBP1 and AuBP2 sequences are still effective when the Au<sub>(110)</sub> and Au<sub>(100)</sub> facets are present, meaning the reduced binding efficacy for the HRE sequence may be due to the His residues specifically.

The Pd4 sequence binds through two His residues which are not present as diads, His<sub>6</sub> and His<sub>11</sub>, with a small reduction in ΔG being observed; however, this was within error of the MP-SPR ΔG value. Studying the behavior observed in the HRE and Pd4 sequences the author proposes that the His interactions are less favourable with Au<sub>(100)</sub> and Au<sub>(110)</sub> facets. The proposed mechanism is that upon binding to the particles HRE forms an initial His-Au<sub>(111)</sub> binding interaction, but due to the orientation of the His groups the second His interaction would be with either the Au<sub>(100)</sub> or Au<sub>(110)</sub> facet which is non-preferred. Due to the unfavourable interaction a M-His complex is formed and the ‘multidentate’ behaviour observed in the MP-SPR studies does not occur. Testing this hypothesis by a computational simulation approach is outside the scope of this project; however, future work should look at modelling this interaction to determine the validity of the proposed hypothesis.

The sulphur containing binding peptides (A3, A3s, A3sT2 & A3sC8) do not appear to be forming the expected strong Au-S interaction; with the Met-Au and Cys-Au interactions appearing to not be the dominant interaction. Instead the presence of Pro<sub>8</sub>, which is

omitted from the A3s derived sequence appears to be key to the high binding affinity for A3.<sup>98</sup> This supports the hypothesis that the Met/Cys R-group is not in the correct orientation to form a strong Au-S interaction and that the Pro<sub>8</sub> anchoring is required to achieve effective Met/Cys R-group Au interaction. The Thr<sub>2</sub> substitution appears to not make a significant impact on the overall binding with ΔG values for A3s and A3sT2 being within error which is in agreement with the MP-SPR experiments.

The solvation ITC studies showed an increase in order upon solvation for the non-sulphur containing sequences which suggests peptide agglomeration/assembly could be occurring. The sequences' propensity to agglomerate or assemble can be attributed to the Arg and His residues present within these sequences which are known to form favourable His-His, His-Arg and Arg-Arg interactions.<sup>241,242</sup> The A3 family of sequences appear to become less ordered upon solvation suggesting these do not agglomerate or assemble when solvated; however, this behaviour was not observed in the peptide-Au studies suggesting that the peptide-Au interaction is more favourable than the peptide-peptide interaction. The peptide-Au studies supported the findings from the MP-SPR studies that the thiol chemistry afforded by Met and Cys groups is not as dominant as originally anticipated. The A3 peptide is the strongest overall binder due to the presence of Pro<sub>8</sub> which was omitted from the A3s sequences that facilitated anchoring to the Au facet.<sup>98</sup> Peptide diads formed equally as strong if not stronger binding interactions, especially in the case of AuBP2; however, the His residue appeared to have a lower affinity for the Au particles than in the MP-SPR studies. This is attributed to a lower affinity of His for the Au<sub>(100)</sub> and Au<sub>(110)</sub> facets present on the gold nanoparticles leading to both HRE and Pd4 being weaker binders in this study. Future work should focus on studying the His containing sequences (HRE & Pd4) to determine how they interact with Au<sub>(111)</sub>, Au<sub>(100)</sub> and Au<sub>(110)</sub> surfaces to determine if there are different preferences and test the proposed hypothesis of the His affinities; however, this is outside the scope of this study.

#### 4.3.3 Peptide Conformation & Assembly Studies

The peptide-Au studies discussed in section 4.3.2 showed that peptides have different entropic behaviour in solvation conditions compared to the Au bound condition. For solvation the non-sulphur containing sequences such as AuBP1 have a negative entropy change suggesting the system becomes more ordered upon solvation which could be explained by an increase in secondary structure or aggregation. The sulphur containing sequences have a positive entropy change upon solvation suggesting these systems become more disordered. Upon introducing gold into the system for peptide-Au binding studies the entropic behaviour for these systems changed with solely the AuBP1, Pd4 and A3 systems having a positive entropy change thus becoming more disordered. The

observed difference in entropic behaviour between the solvation and peptide-Au experiments suggests that between the competing peptide-peptide and peptide-Au interactions the peptide-Au is most favourable. In an attempt to elucidate the cause of the behaviour observed circular dichroism (CD) spectroscopy and transmission electron microscopy (TEM) studies were undertaken. The CD spectroscopy study was used to determine if the observed differences in entropic behaviour could be attributed to changes in the secondary structure of the peptide upon binding. To achieve this the study compared the spectral differences between peptides in the solvated and bound states, see figure 4.9.

The CD spectra, see figure 4.9, show that the secondary structure for all the solvated peptides is a random coil structure<sup>174</sup> which was attributed to the peptides being too short to develop defined secondary structures. While short peptide sequences containing between 9-17 amino acids have been reported to have defined secondary structures, these sequences were extracted from alpha-helical protein domains.<sup>243</sup> However, the peptide sequences explored in this study have been determined in previously published work using phage display. Phage display does not screen for secondary structure but instead screens sequences on their binding propensity to a target substrate, meaning the amino acid composition is not biased towards producing defined secondary structures.<sup>96,99</sup> The CD spectra for the studied sequences, see figure 4.9, show different spectral signature with some samples having two minima, see figure 4.9-1, while other samples had one minima, see figure 4.9-7. However, to the author's knowledge an in depth study into structural motifs for random coil structures has not been undertaken and further assignment of these spectra is outside the scope of this project. Upon the peptide-Au interaction some spectral changes were observed; however, the secondary structure for all sequences remained as a random coil structure. This suggests that the changes in entropy observed in the peptide-Au ITC studies, section 4.3.2, may not be related to a peptide conformation change.

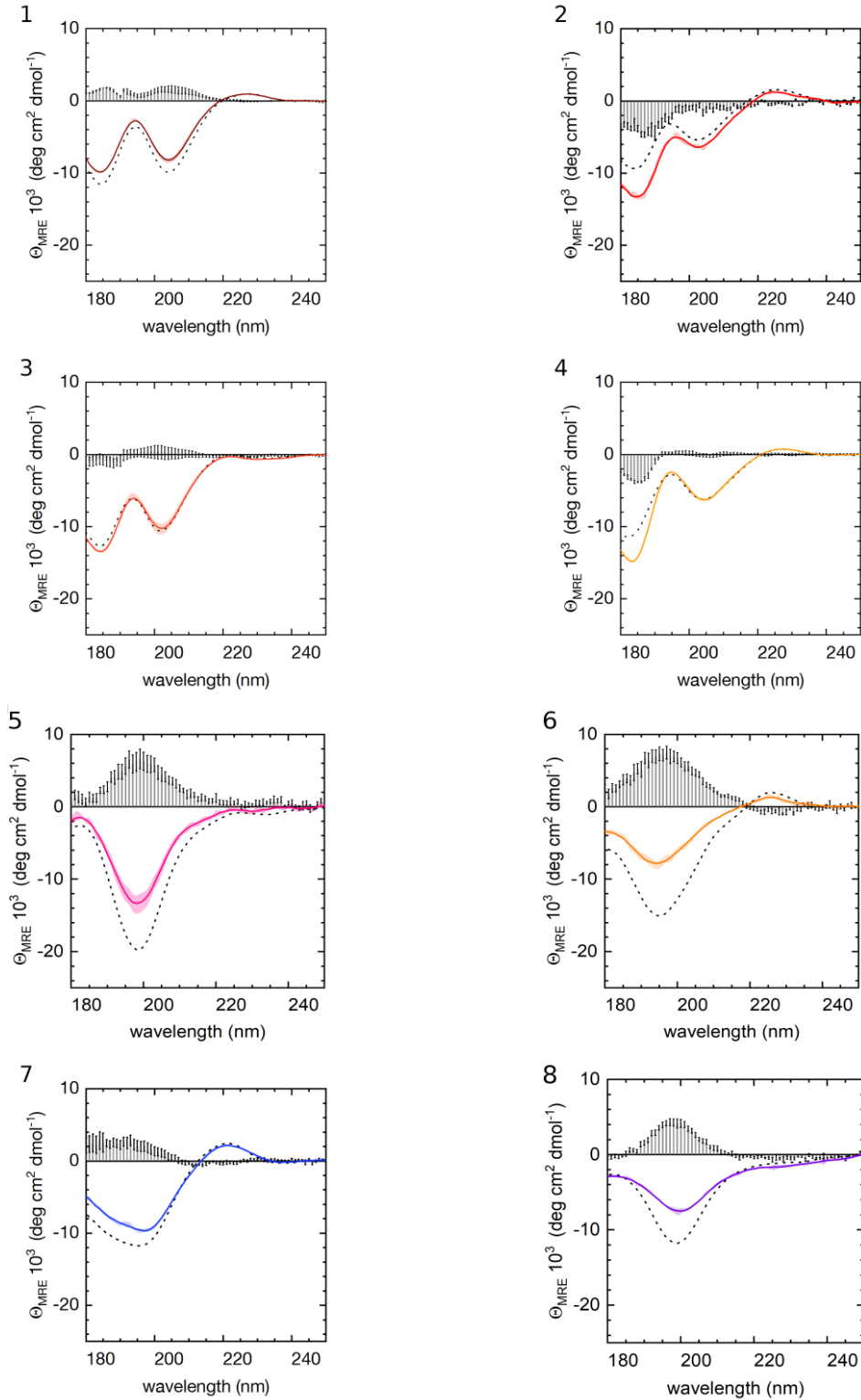


Figure 4.9: Plots showing the circular dichroism (CD) spectra for the studied peptide, see table 4.1, in the unbound state in aqueous media (dashed line) and in the gold-bound state (coloured line). The bars on the plots represent the difference between the unbound and bound spectra. The numbers represent the following peptides: 1) A3, 2) A3s, 3) A3sC8, 4) A3sT2, 5) AuBP1, 6) AuBP2, 7) HRE & 8) Pd4. Figures courtesy of Dr. M Michaelis.

Another possible cause of the entropic behaviour observed in the ITC studies is the agglomeration/assembly of peptide-coated AuNPs after the peptide-Au binding interaction has occurred. To assess the validity of this hypothesis a JEOL 2100 Plus TEM was used to image gold nanoparticles which had been treated with a 800  $\mu$ M peptide solution as well as a blank system which contained just the nanoparticles which had not been treated with any peptides or surface coatings, see figure 4.10. The samples were prepared using a dropcast preparation technique on quantifoil grids, see section 4.2.6, and imaged at 120kX magnification using a JEOL 2100 Plus TEM. The obtained TEM micrographs, see figure 4.10-nA, were binarized and converted into distance maps to determine the center of the imaged particles without human bias from local maxima in the distance map. Interparticle distance was determined by performing the delaunay triangulation<sup>225</sup> method in FIJI on the determined particle centers, see figure 4.10-nB, and an average value for interparticle distance obtained.

The peptide-Au ITC studies showed the entropy values for the AuBP1, Pd4 and A3 systems becoming more positive suggesting the system becomes more disordered upon peptide-Au interactions, while the remaining peptide systems entropy values became more negative suggesting the system became more ordered. This would suggest that we should observe greater average interparticle spacing with the AuBP1, Pd4 and A3 samples compared to the AuNPs sample. However, the AuBP1, Pd4 and A3 samples have average interparticle spacing values of  $26\pm2.6$ ,  $26\pm1.8$  &  $28\pm1.4$  nm respectively all of which are lower than the average interparticle spacing of the untreated AuNPs ( $35\pm5.4$  nm). The remaining systems (A3s, A3sC8, A3sT2, AuBP2 and HRE) all appeared to become more ordered in the peptide-ITC studies meaning the average interparticle spacing should be lower than the untreated AuNPs. This is reflected in the interparticle spacings determined for A3s, A3sC8, A3sT2 & HRE which are  $27\pm3.5$ ,  $28\pm5.4$ ,  $26\pm4.6$  &  $28\pm1.8$ nm respectively. However, the AuBP2 sample had an average interparticle spacing of  $47\pm4.1$  nm which is greater than the average interparticle spacing of the untreated AuNPs ( $35\pm5.4$  nm).

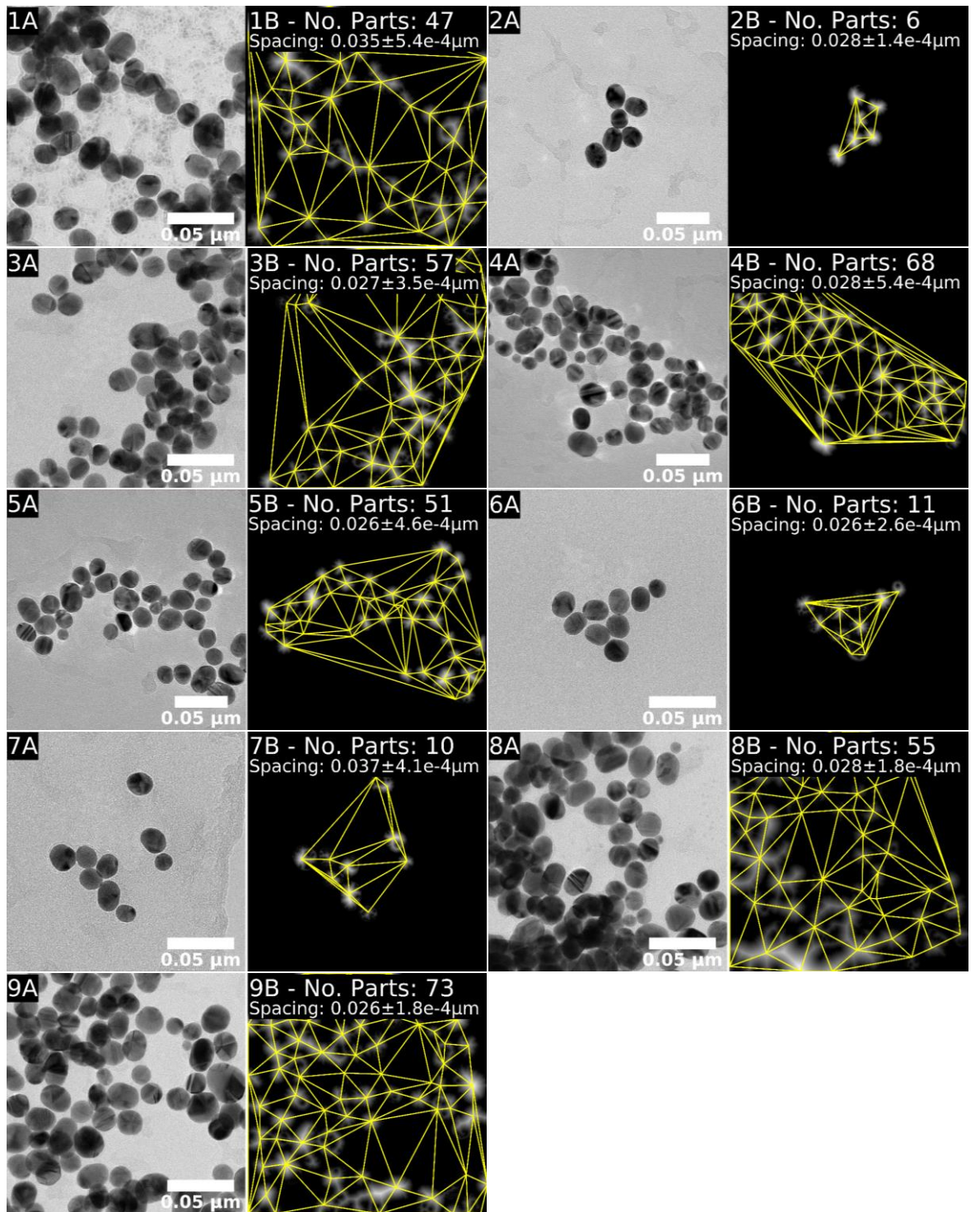


Figure 4.10: Representative transmission electron microscopy (TEM) micrographs (A) and their respective distance maps and delaunay triangulations (B) of AuNPs pre and post treatment with a peptide solution (800  $\mu\text{M}$ ). The numbers represent the following peptides: 1) No Peptide, 2) A3, 3) A3s, 4) A3sC8, 5) A3sT2, 6) AuBP1, 7) AuBP2, 8) HRE & 9) Pd4. The scale bar in each image represents 50nm.

Due to the small sample of particles present in the representative TEM micrographs for A3, AuBP1 & AuBP2 there is a low confidence in the determined average interparticle spacing for these samples. Although all samples were prepared in the same manner an even distribution of gold particles across the TEM grid does not appear to have occurred. Within the imaged 0.23 micron<sup>2</sup> area we appear to observe grouping for the A3, AuBP1 and AuBP2 sample; however, as there are so few particles present within this area the average interparticle spacing for a larger sample area is likely to be far greater. Therefore, the question can be posed at what length scale/magnification should these aggregation/agglomeration studies be used? Answering this question is outside the scope of this study; however, this initial data suggests this could be a useful way to observe peptide aggregation behaviour under fixed concentrations. Future studies should sample multiple areas of TEM grids and prepare 3 grids for each sample to ensure that any drying effects can be properly accounted for. Using the programmable features of the JEOL 2100 Plus, such a study could automate sampling after the experimentalist has aligned the microscope which would allow for the automated collection of a large micrograph dataset. Image processing could be automated using the scripting/macros features of FIJI to ensure each image is correctly processed and batch features used to compile image data. The processed images could be checked by the experimentalist and the compiled data reviewed.

Table 4.8: Investigating agglomeration/aggregation behaviour during peptide-Au interactions determined using transmission electron microscopy (TEM) micrographs (Average Interparticle distance) and dynamic light scattering (DLS) Z-Average diameter measurements. The solutions measured were AuNPs post treatment with a peptide solution (800 µM), as well as a blank system.

Peptide	TEM - Average Interparticle Spacing (nm)	DLS - Z-Average diameter (nm)
None	35 ± 5.4	23 ± 0.1
A3	28 ± 1.4	2044 ± 479
A3s	27 ± 3.5	263 ± 7
A3sC8	28 ± 5.4	173 ± 15
A3sT2	26 ± 4.6	379 ± 10
AuBP1	26 ± 2.6	303 ± 48
AuBP2	37 ± 4.1	526 ± 71
HRE	28 ± 1.8	348 ± 24
Pd4	26 ± 1.8	238 ± 66

The agglomerates/aggregates observed in the TEM studies, see figure 4.10, are made of multiple discrete gold particles. Dynamic light scattering (DLS) measurements were used to try to quantify the average size of the observed agglomerates/aggregates, see table 4.8. The DLS data does not appear to reflect the observations made in the TEM samples with A3 that appears to have small clusters of 6 particles in the TEM micrograph, having an average aggregate size of 2044nm when determined by DLS. The confidence in the data obtained from both techniques is low as the two techniques show opposing pictures. While further experiments are outside the scope of this study, future DLS experiments should focus on collecting DLS data using a real-time sampling titration method would be better suited to track the progress of agglomerate/aggregate formation. The proposed DLS titrations would be conducted using the same experimental protocol as the ITC titrations, ideally with stirring as this would allow for the particulate/aggregate sizes to be monitored in real-time which could then be related back to the existing ITC datasets. The proposed DLS titrations should investigate both the peptide-Au interaction and peptide solvation to understand if any aggregation is occurring and would facilitate the development of more representative analytical models.

Ultimately, the CD, TEM and DLS studies proved inconclusive in explaining the entropic behaviour observed in the ITC studies. TEM microscopy studies appear to be a promising method to observe the “end point” state for peptide-Au systems; however, a large micrograph dataset comprising multiple magnifications and sample grids prepared in triplicate would be required to ensure drying effects are mitigated. A further consideration is that the sample will have to be prepared the same day as imaged as any continued peptide-peptide or peptide-Au interactions may compromise the reliability of the collected data. Future TEM studies should be coupled with DLS titrations to enable the study of aggregation/agglomeration behaviour and directly relate it to the entropic behaviour observed in the ITC studies. Using both the ‘end point’ TEM measurements and the ‘real-time’ DLS measurements a more informative picture on the agglomeration/aggregation behaviour observed in these systems could be developed.

#### 4.4 Conclusions

The thiol chemistry afforded by Met and Cys groups was anticipated to form a strong Au-S interaction and expected to be very thermodynamically favourable; however, the MP-SPR and ITC studies show that this is not the case with peptide diads such as Lys Arg or Arg Arg, forming equally as strong if not stronger binding interactions. The designed A3s, A3sT2 and A3sC8 sequences all had a poorer binding efficacy than the original A3 sequence; this is attributed to the removal of the Pro<sub>8</sub> residue which is important for effective anchoring of the sequence onto a gold substrate.<sup>98</sup> Upon anchoring through the Pro<sub>8</sub> residue, the Met<sub>9</sub> residue becomes proximal to the Au substrate increasing the probability of a binding interaction. Future studies should explore substitution of Cys for Met in the original A3 sequence as this may facilitate a stronger binding interaction.

This study found that multiple histidine residues or diads in a sequence appear to have a high affinity for the Au<sub>(111)</sub> surface and a far lower affinity for the Au<sub>(110)</sub> and Au<sub>(100)</sub> surfaces. However, computational simulation of these binding interactions was beyond the scope of this study. Future studies should perform computational simulations to investigate the interaction between the His containing sequences (HRE & Pd4) and the Au<sub>(111)</sub>, Au<sub>(110)</sub> and Au<sub>(100)</sub> surfaces to determine binding preferences and elucidate the mechanism by which binding occurs. A separate study should also computationally investigate the amino acid interactions with Au<sub>(110)</sub> and Au<sub>(100)</sub> surfaces to complement the existing Au<sub>(111)</sub> study by Hoefling *et al.*<sup>216</sup> as such research would assist the development of bespoke binding peptides.

Peptide-peptide interaction behaviour was investigated through ITC solvation studies which showed an increase in order upon solvation for the non-sulphur containing sequences suggesting that peptide agglomeration/assembly has occurred. The propensity of these sequences to undergo agglomeration/assembly was attributed to the Arg and His residues present within the primary sequence.<sup>241,242</sup> This was supported by no agglomeration/assembly behaviour being observed for the A3 family of sequences which do not contain either His or Arg residues. Due to both the high binding efficacy observed in the ITC and MP-SPR studies as well as desirable solvation behaviour A3 was selected as the Au binding region for the bespoke ZA2 sequence.

These two subsets of entropic behaviour were not observed in the peptide-Au studies with solely A3, AuBP1 and Pd4 becoming more disordered upon interacting with the AuNPs. The difference in entropic behaviour between the solvation and peptide-Au ITC studies suggested that out of the competing peptide-peptide and peptide-Au interactions the peptide-Au interaction is most favourable. This is in agreement with the MP-SPR studies

where the Hill slope ( $n$ )  $> 1$ , indicated that positive cooperativity occurs during binding and suggested there is preferential binding to the  $\text{Au}_{111}$  surface where peptides in the bound and unbound states are not in competition.

In an attempt to elucidate the source of the entropic behaviour observed, circular dichroism (CD) spectroscopy, transmission electron microscopy (TEM) and dynamic light scattering (DLS) studies were undertaken. However, these proved inconclusive in explaining the entropic behaviour observed in the ITC studies. A future study should use a combination of dynamic light scattering (DLS) titrations to measure aggregate formation in 'real time' and TEM studies performed using 3 grids for each sample and analysing multiple areas of each grid under different magnifications to measure aggregation behaviour. The DLS studies will measure particulate/aggregate size during each addition of titrant using the same incubation periods as the ITC studies while the TEM studies will provide information on the 'final state' of these aggregates after the peptide-Au interaction. The DLS titrations should investigate both the peptide-Au interaction and peptide solvation to understand if any aggregation is occurring. Such data would facilitate the development of more representative analytical models.

The following chapter will move away from Au systems to discuss a novel technique developed to study the emissive defect states within semiconductors. This technique will be applied to ZnO systems to understand how peptide mediation affects defect states within the synthesised matter. These findings will assist in understanding the peptide's role in the target ZnO-Au system synthesised using a one-pot mediated synthesis. No kinetic or thermodynamic studies for ZnO binding peptides will be conducted as this has been extensively studied previously by the Perry group.<sup>42,94,95</sup>

# Chapter V: Two-Dimensional Fitting Approaches Towards An Understanding Of Semiconductor Fluorescent Behaviour

## 5.1 Introduction

In the 21<sup>st</sup> century electronic devices and microcontrollers have become commonplace with ca. 50% of the world utilising the internet according to the UN's International Telecommunications Union (ITU).<sup>244</sup> The internet enabled devices used to access the internet depend on semiconductors to form the logic gates,<sup>245</sup> resistors,<sup>246</sup> diodes,<sup>247</sup> light emitting diodes,<sup>248</sup> flat panel displays<sup>249</sup> and capacitors<sup>250</sup> which make up these devices. Therefore understanding the band structure and native and non-native defects/impurities within semiconductor materials is of fundamental importance to facilitate the development of novel electronic devices.

Optical spectroscopy is well suited for characterising the electronic, structural and dynamic properties of solids<sup>160</sup> making it a natural choice to explore the properties of semiconductors. This chapter will focus on fluorescence spectroscopy in particular as it directly measures the photons produced by radiative relaxation processes within the sample. These processes include radiative recombination, stimulated emission & relaxation to trap/defect states.<sup>161–163,251,252</sup>

When photons interact with semiconductors, electron-hole pairs are induced promoting the electrons from their ground state to an excited state. The electron is unlikely to remain in the excited state permanently and instead undergoes radiative recombination where the electron hole pair recombine through relaxation of an electron from the conductance band (CB) to the valence band (VB). Alternatively, radiative decay occurs where an electron relaxes to a lower energy in-band gap trap state within the material. Both these types of relaxation are forms of spontaneous emission where the energy absorbed by the material is released as photons.<sup>161,162</sup> The electrons which relax to an in-gap trap state primarily undergo non-radiative recombination with their respective holes, this trap-assisted recombination is referred to as Shockley-Read-Hall (SRH) recombination.<sup>163</sup>

Stimulated emission can also cause radiative recombination, where an electron in the excited state relaxes from CB->VB and is interfered with by the electromagnetic field of a photon, which we will refer to as photon-A. This then produces an additional photon upon relaxation with the same energy as photon-A.<sup>251,252</sup> This type of emission is observed in high-quality cavities where a strong field is applied and provides information on the

dynamics of the energy and momentum of the excited electron-hole pairs<sup>253</sup> according to their collisions and interactions with phonons.

This study focuses on the spontaneous emission regime because in the absence of interactions and accounting for the field states and their fluctuations:<sup>254</sup>

1. The system uniformly fills the  $4\pi$  sr solid angle, this means that there is uniform emission across the sample's surface
2. Coherence along the excitation time axis is lost
3. Both the matter and field induce onsets of polarizing effects in each other

These properties are useful for diagnostic and quality control (QC) techniques on semiconductor materials, with the interaction between the field and matter having a fundamental implication regardless of any degree of material isolation. The system will always undergo relaxation even when the field is at its lowest zero state. The uniform sample emission ( $4\pi$  sr solid angle) makes spontaneous emission spectroscopy (SES) both attractive and available for industrial and academic settings.

A two-dimensional approach to SES was reported by Marose *et al.* for molecular systems<sup>169</sup> with application for monitoring bioprocesses, further developed by Kovrigin.<sup>170</sup> Due to the nature of spontaneous emission in solid state materials with allowed and disallowed transitions due to symmetry effects, utilising 2D-SES has the potential to view the emission topology. This allows for observation of the emissive states present within a semiconductor with dependence on excitation energy.

The application of 2D-SES to semiconductors is a novel approach and in this chapter the viability and potential of this technique is explored using a library of widely studied semiconductors. The library of semiconductors selected are as follows: CdS, CdSe, ZnS, ZnSe, ZnO analytical standard, ZnO nanorods, anthracene, & TiO<sub>2</sub> anatase. The aim of this study is to determine if two-dimensional fluorescence spectroscopy can be used to analyse the states present, including in-band defect states, within semiconductors for potential academic and QC industrial applications.

## 5.2 Materials and Methods

Cadmium sulphide (CdS), zinc sulphide (ZnS) and zinc selenide (ZnSe) standard analytical references were purchased from Alfa Aesar (Haverhill, Massachusetts USA). Zinc oxide analytical standard (average particle size of 117 micron), cadmium selenide (CdSe), titanium dioxide anatase polymorph (TiO<sub>2</sub>), anthracene (C<sub>14</sub>H<sub>10</sub>) and 1,3-hexamethylenetetramine (HMTA, C<sub>6</sub>H<sub>12</sub>N<sub>4</sub>) were purchased from Sigma-Aldrich (St. Louis, Missouri USA). Finally, zinc nitrate hexahydrate (Zn(NO<sub>3</sub>)<sub>2</sub>·6H<sub>2</sub>O) was purchased from

fluka (Charlotte, North Carolina USA). All these materials were used without any further treatment. If required type 1 water was used with a resistance of  $18\text{M}\Omega$  at  $25^\circ\text{C}$ . Zinc oxide nanorods were synthesised in house using a protocol from the literature<sup>11,255</sup> detailed below in section 5.2.1.

All fluorescence measurements were performed on samples in the solid-state using black 96-well plates from Corning. The spectrometer used was a TECAN i-control M200 Pro spectrometer (Tecan Group Ltd. Switzerland) fitted with a monochromator and controlled by the i-control (version 1.9.17.0) software. Characterisation of the size, morphology and structure of the synthesised nanorods was done using both a JEOL JSM-7100F SEM microscope and a X'Pert PRO X-ray diffractometer (Malvern Panalytical, Malvern, UK) using Cu K $\alpha$  radiation operating at a wavelength of  $1.54056\text{\AA}$ .

### 5.2.1 Zinc Oxide Nanorods

Utilising a procedure documented in the literature,<sup>11,255</sup> ZnO nanorods were prepared using HMTA (0.42g, Sigma-Aldrich),  $\text{Zn}(\text{NO}_3)_2 \cdot 6\text{H}_2\text{O}$  (0.058g, Fluka) &  $18\text{M}\Omega \text{H}_2\text{O}$  (90mL) placed into a glass reaction vessel. The reaction mixture was incubated at  $20^\circ\text{C}$  using a water bath stirrer setup for the first 24hrs. Subsequently, the samples were incubated at  $68^\circ\text{C}$  using a water bath stirrer setup for a further 48hrs. Post incubation the precipitate was separated from the reaction medium using centrifugation (10 mins, rcf 15557) using a Centrifuge 5804 R (eppendorf) and washed with  $18\text{M}\Omega \text{H}_2\text{O}$  three times before being lyophilised. The twinned ZnO nanorods formed had a length of  $1.4 \pm 0.2 \mu\text{m}$  with a length to diameter ratio (L/D) of  $10.7 \pm 1.7$ , these parameters were determined from a sample of 62 nanorods.

## 5.3 Characterisation

### 5.3.1 Zinc Oxide Nanorods

The structural properties of the synthesised ZnO nanorods were determined using a JEOL JSM-7100F SEM microscope. The sample was mounted on an aluminium stub using carbon tape and was left uncoated. An accelerating voltage of 5 eV was used to image without observing large charging effects, SEI imaging was used to determine the size and morphology of the uncoated sample. A total of 62 nanorods were measured to determine the sample's average size.

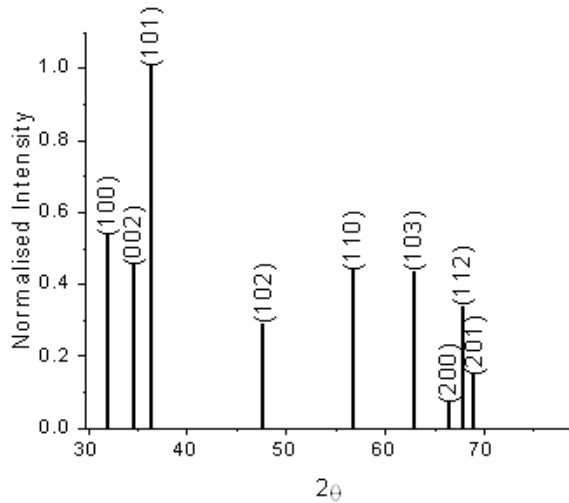


Figure 5.1 - Powder X-ray diffraction line spectra for ZnO nanorods

Further structural and composition based information was determined using a PANalytical X’Pert PRO X-ray diffractometer (Malvern Panalytical, Malvern, UK) having Cu K $\alpha$  radiation operating at a wavelength of 1.54056 $\text{\AA}$ . The samples were scanned over a range between 3° and 90° of 2 $\theta$  with a step size of 0.02°·s $^{-1}$ . Experiments were carried out at room temperature with an acceleration voltage of 45 kV and 40 mA filament current. The X’Pert-HighScore Plus (Version 4.5) program was used to analyse and identify peaks in the diffraction patterns, for the line spectra see figure 5.1. The XRD spectral profile obtained for the synthesised nanorods is in good agreement with those reported in the literature/previous studies within the group.<sup>95</sup>

### 5.3.2 Tecan i-Control M200 Pro

Understanding the instrumental setup of the Tecan i-Control M200 Pro is of fundamental importance when attempting to utilise the instrument to perform experiments not originally conceived by the manufacturers. The Tecan i-Control M200 Pro used in this study contains a xenon flash lamp with an arc size of 1.5mm that produces a 10W light output at a frequency of 40Hz. The output intensity of this source is heavily wavelength dependent, see figure 5.2, with the intensity fluctuating between different flashes. This means the maximal fluence of this source is ca.  $0.2 \times 10^{-6}$  W/cm $^2$ , not accounting for intensity losses due to the quality of transmission by lenses, mirrors, fibers, etc. and the quality of the adjustments to each other.<sup>256</sup> To account for the varying emission intensity from the source, the instrument uses a flash monitor system which monitors the energy of each flash using a photodiode. This measurement is used to correct the measured fluorescence values.<sup>257</sup>

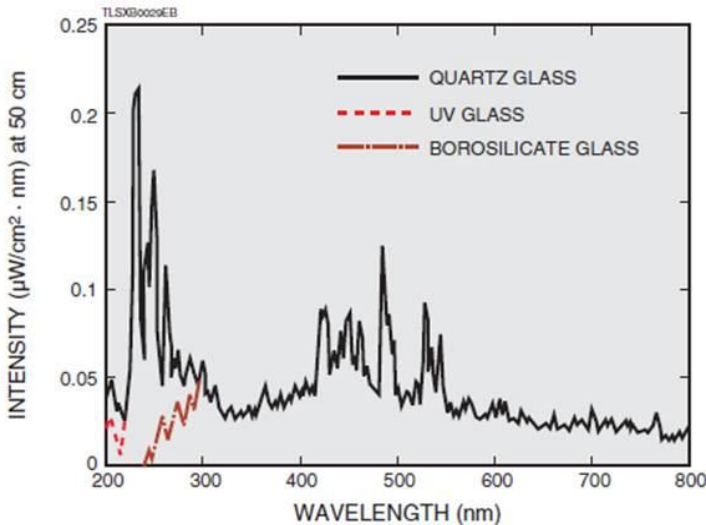


Figure 5.2 - Spectrum of the emission intensity of the flash lamp in an Infinite 200 pro, the UV Glass trace matches the emission profile of the InfiniteM200 Pro due to UV-glass being in the flash lamp windows.<sup>256</sup>

Double monochromators are employed as the wavelength selection system for this instrument. Both the excitation source and emission have independent double monochromators enabling the spectrometer to have a fluorescence excitation range of 230-850nm inclusive and an emission detection range of 280-850nm inclusive. A filter wheel is used between the light source and the excitation monochromator to block undesired diffraction orders produced by the optical gratings in the device.<sup>257</sup> The bandwidth of the excitation source is 5nm between 230-315nm inclusive and 9nm between 316-850nm; while the bandwidth of detected emission is 20nm between 280-850nm inclusive. The beam waist (spot size) of the excitation source using the top optics is ca. 3mm.<sup>257</sup>

## 5.4 Results and Discussion

### 5.4.1 Two-Dimensional Fluorescence Mapping (2DFM) Technique

The Tecan i-control M200 Pro has no option/setting within i-control (version 1.9.17.0) to perform two-dimensional fluorescence spectroscopy automatically. However, this sampling method can be achieved by collecting a series of one-dimensional spectra on any conventional plate reader or spectrometer. For one-dimensional emission spectra the excitation wavelength used will be incremented by a fixed amount herein referred to as the step (ie. 10nm). If one-dimensional excitation spectra are collected then the emission detection wavelength is incremented by a fixed step. These collected one-dimensional spectra can be arranged and compiled into a two-dimensional array where the columns and rows relate to the excitation and emission wavelengths respectively. To avoid measuring the excitation source in the fluorescence studies a 30nm gap between the excitation wavelength (ie. 300nm) and the first detected emission wavelength (ie. 330nm)

is always maintained to preserve instrument health. This means that the one-dimensional spectra will be of different lengths and will need to be correctly offset when compiling the 2D-array.

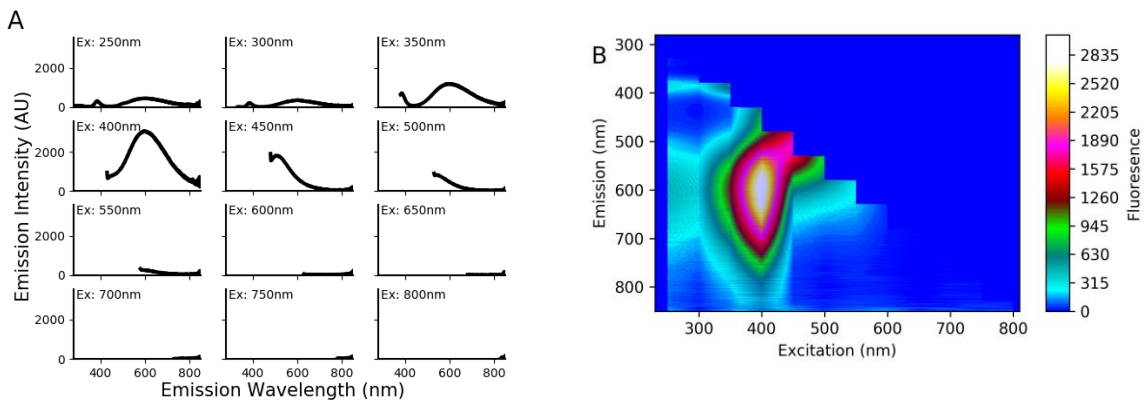


Figure 5.3 - Fluorescence spectral profiles of ZnO nanorods. A) The collection of 1D-emission spectra compiled to generate the 2D-array. B) The plot of the compiled 2D-array from 1D-emission spectra using a 50nm step.

To test the concept a test dataset was acquired by sampling ZnO nanorods 1D-emission spectra with a 50nm step, see figure 5.3. The collected spectra were compiled into the 2D-array by hand; however, this was a very time consuming process which was prone to human error. Any “missing” values where data was not collected were set to zero and any negative values were also set to zero as they are non-physical.



Figure 5.4 - The structure of a i-control “script” file where it is composed of a total of 60 actions divided into 6 blocks.

The compiled spectra, figure 5.3B, shows a coarse topology of the emissive states present within the ZnO nanorod sample with the near band edge emission being observed at ca. 380nm. This presentation also suggests that the emissive center for the 570 nm emission has a different physical nature depending on whether the sample is excited above or below 300 nm. However, the step used in figure 5.3B was too coarse to provide sufficient resolution for a first approximation of the exact states present within the sample. To develop the technique beyond the realms of qualitative measurements the limitations of the instrumentation had to be explored. The i-control software used to set up experiments on the Tecan i-control M200 Pro spectrometer is of particular interest as within i-control software “script” files are used to set up experiments that can include temperature ramping, absorbance spectra and fluorescence emission or excitation spectra. Multiple different “actions” (i.e. acquiring a fluorescence spectra) can be sequentially executed; however, each “script file” is limited to containing 6 blocks, each of

which can contain 10 actions, see figure 5.4. When a script file is created the first “action” is consumed by setting up instrument parameters leaving 59 available “actions”. Therefore, with no “actions” being used for other functions (i.e. temperature control) a total of 59 spectra are acquirable per script. To the author’s knowledge there is no simple way to bypass this software limit in the i-control software, and to open up the saved “script” files within a text editor to attempt to reverse engineer them is non-trivial and outside the scope of this project. Utilisation of 2 or more scripts to allow for a greater number of steps while covering a large spectral range is a sub-optimal approach as it is unknown if the instrumental constant ( $Z$ ) will remain consistent between two scripts. Simple scaling attempts using an overlapping region (i.e. 390-405nm) could not be used with confidence as it is unknown if any photo-induced degradation has occurred within the sample leading to different emissive properties of defect states or impurities within the sample.

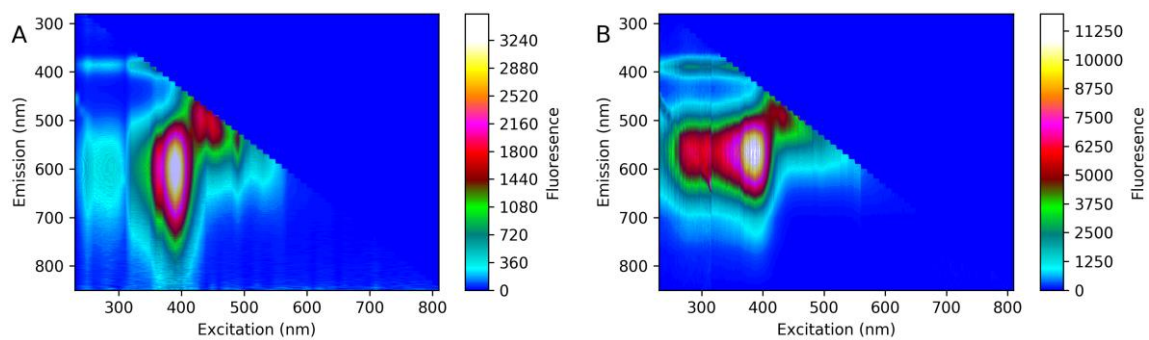


Figure 5.5 - 2D-Fluorescence spectra of ZnO nanorods. A) 2D-spectrum compiled from 1D-emission spectra with a 10nm step along the excitation axis. B) 2D-spectrum compiled from 1D-excitation spectra with a 10nm step along the emission axis.

With these limitations in mind a second dataset was acquired using the ZnO nanorods sample scanning from 230-810nm with a 10nm step, this uses the full 59 spectra available within the software. Due to the greater number of spectra to compile and the high probability for human error a python (Python 3.7.5) script using the pandas and numpy libraries, see script A5.1, was developed inhouse to facilitate the formation of these 2D-arrays. The script takes the raw excel (.xlsx) file produced by the spectrometer, extracts the relevant spectra and subsequently arranges the spectra with the correct zero padded offsets while setting negative values to zero. Once the script has finished it produces a discrete comma separated value (.csv) file for each well measured. Comparing both 2D-spectra with the 50nm (figure 5.3B) and 10nm (figure 5.5A) steps it can be observed that this is a vast improvement in the overall spectral resolution. However, the resolution of this data is still below the Rayleigh criterion, but can be used as a first approximation for the emissive states within such samples. Further enhancement of the spectral resolution could be achieved by selecting a smaller region of interest (ROI) along the stepped axis (i.e. 290-590 nm) then using a smaller step (i.e. 5nm).

Theoretically whether the experimentalist chooses to collect 1D-excitation or 1D-emission data, it should have minimal impact on the 2D-spectra produced. In practice the three different bandwidths for this instrument, discussed in Section 5.3.2, mean that while the overall spectral features should be similar it would not be expected for them to be identical. To determine how comparable the two methods for forming the 2D-spectra are, 1D-excitation spectra were acquired for the ZnO nanorods sample and compiled, see figure 5.5B. Upon inspection of both spectra the overall spectral profile for both spectra is similar; however in the emission spectra the change in bandwidth at 315nm is noticeable with a vertical discontinuation in the 2d-spectral plot. A diagonal line is also observable in both spectra, see circled region figure 5.6, starting around 460nm. Tecan was consulted about this issue, confirming this spectral feature is a high order diffraction of the monochromated excitation source.<sup>258</sup> This spectral contribution has a low intensity just being slightly above the background. Therefore, this is not removed during data processing to avoid the introduction of additional artifacts to the data.

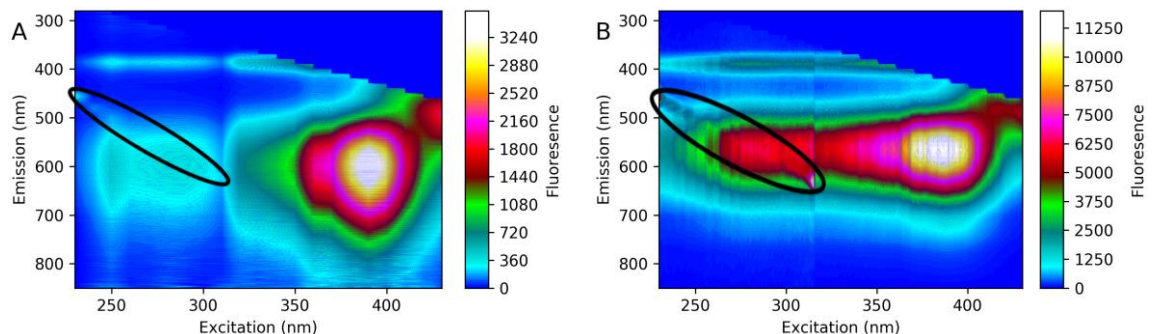


Figure 5.6 - 2D-Fluorescence spectra of ZnO nanorods zoomed in on the diagonalisation in the spectra. A) 2D-spectrum compiled from 1D-emission spectra with a 10nm step along the excitation axis. B) 2D-spectrum compiled from 1D-excitation spectra with a 10nm step along the emission axis.

Due to the discontinuation in bandwidth being more apparent in the 2D-spectra assembled from 1D-excitation spectra, the studies within this thesis acquire 1D-emission spectra and assemble 2D-spectra from them. The 1D-emission spectra were collected using excitation wavelengths between 230-810nm inclusive using a 10nm step, emission is collected from 30nm above the excitation wavelength (i.e. ex:300nm em:330nm) unless otherwise stated.

This is the first time 2D-fluorescence spectroscopy has been reported as a method to analyse semiconductor materials. Through use of this technique we obtain a topological view of the emissive states within a sample, these two-dimensional spectra shall herein be referred to as two-dimensional fluorescence maps (2DFM). 2DFM is viable on spectrometers designed solely for one-dimensional operation which allows for experimentation on existing fluorescence spectrometers equipped with a monochromator and could be deployed in a variety of settings.

Further improvements to the processing script could be done to remove the weak high-order excitation signal from the dataset; although, this would be instrument specific. Options for after-market modifications to existing instruments are possible where a microprocessor or single board computer (SBC) such as a raspberry Pi could be used to execute the compiling code with minimal user input. Furthermore, bespoke instrumentation could be developed equipped with an integrating sphere, photon counting detector, controlled atmosphere and a monochromator and should be able to perform low temperature measurements. This instrument would be able to directly measure the quantum yield of emissive states, determine the effect of the gaseous environment on emission behaviour, and reduced temperature conditions would sharpen peak line shapes. Such a device should be designed to measure emission over a larger detection range (i.e. 250 - 3300nm) as this would allow exploration of the traps states within low band-gap materials (i.e. CdSe).

The current, qualitative implementation is useful for rapid visual inspection of the quality of semiconductors as it provides information on all the emissive states present. However, more information is obtainable through fitting with 2d-line-shapes to account for each state. In the next section (Section 5.4.2) such fitting approaches will be addressed.

#### 5.4.2 Two-Dimensional Fluorescence Fitting Methods (2DFMtd)

Developing a robust fitting approach for the 2DFMs while maintaining both a high quality of fit and physical relevance is non-trivial. The extra dimension greatly adds to the complexity as each line-shape can interact with each other within the x-y plane. Before developing fitting algorithms/methodologies, several key criteria were established:

1. All line-shapes have physical relevance
2. Good quality of fit measurable by adjusted  $R^2$  (adj.  $R^2$ ) values
3. Process is user friendly.

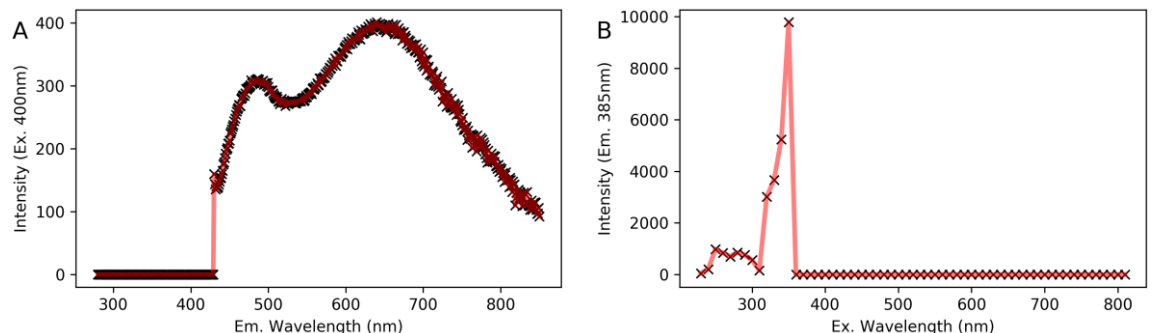


Figure 5.7 - 1D-slices from ZnO analytical standard 2DFM. A) 1D-slice vertical slice, which is an emission spectrum for 400nm excitation. B) 1D-slice horizontal slice, which is an excitation spectrum for 385nm emission.

Comparing representative 1D-spectral samples of the emission and excitation spectra from ZnO Analytical standard, see figure 5.7, it is apparent that there is a difference in spectral resolution between the two spectral slices. As discussed previously in section 5.4.1, the excitation spectral slice is below the Rayleigh criterion due to the coarse 10nm stepping along the excitation axis. However, due to the extra dimension afforded by the 2DFM, the resolution is still high enough to begin to resolve the surface and volume contributions.

$$f(x, y) = \frac{A}{2\pi\sigma_x\sigma_y} \cdot e^{-\left(\frac{(x-x_c)^2}{2\sigma_x^2} + \frac{(y-y_c)^2}{2\sigma_y^2}\right)} \quad 5.1$$

The reduced resolution along the excitation axis meant 2D-Gaussian line-shapes, see equation 5.1, were the natural choice to model the peaks. The population of 2D-Lorentzians which reside within the 2D-Gaussian peak area were not modelled as the resolution of the data was too low to assign these line-shapes with a high level of confidence. Two types of 2D-Gaussian line-shapes can be considered when fitting: the first is the homogeneous case where ( $\sigma_x = \sigma_y$ ), the second is the inhomogeneous case where ( $\sigma_x \neq \sigma_y$ ). The inhomogeneous case is formed from discrete homogeneous Gaussian line-shapes which are not resolved. Due to the limited resolution along the excitation axis both types of 2D-Gaussians were permitted during fitting. Ultimately, this should have minimal impact as the 2D-Gaussian line-shapes themselves are composed of discrete lorentzian line-shapes as previously discussed.

Once the line-shape had been selected, development focused on designing the fitting algorithm. The initial ideology was to develop a universal fitting system which could detect, initialise and fit the 2DFM datasets with minimum human input, reducing the possibility for human error and freeing up human time for data collection and analysis of results and other non-automatable tasks. A five step process was outlined, see figure 5.8, where initially peak detection was performed on the dataset, line-shapes were initialised using the parameters suggested from the peak detection before Levenberg-Marquardt optimisation<sup>209,210</sup> and extraction of the fitted line-shape properties. However, due to the complexity the second dimension adds to the data compounded with the poor excitation spectral resolution, the peaks detected were either sharp high-frequency noise or the maxima of a peak which is formed from multiple discrete gaussians. This meant the

outlined process could not reliably pass the peak detection step, see figure 5.8, thus this step was scrapped and the algorithm was revised.

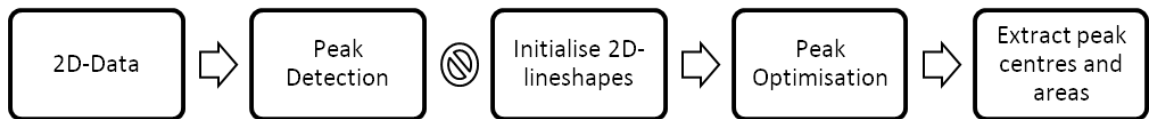
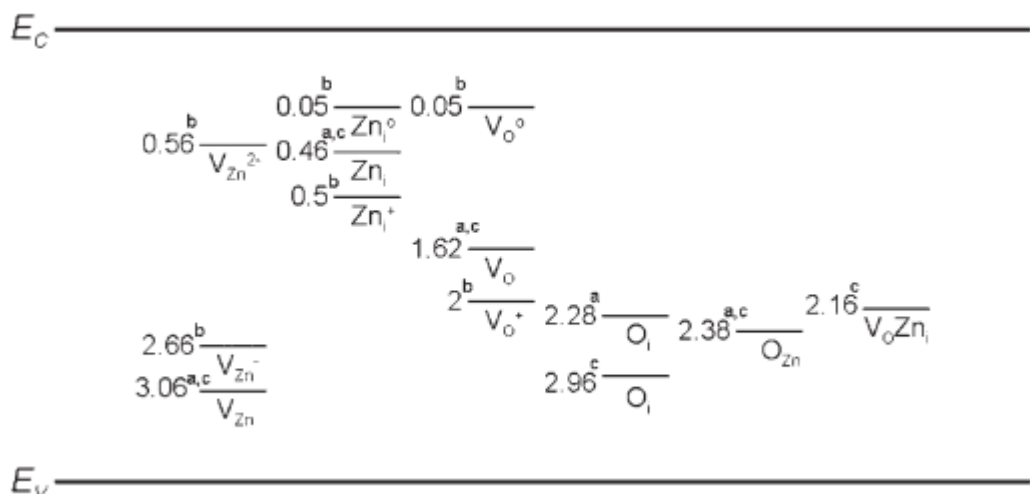


Figure 5.8 - Initial proposed fitting procedure, the stop symbol indicates where the method fails

While revising the algorithm and reflecting on the resolution issues encountered, techniques used by companies in the early days of digital printing technology were studied as the reliable reproduction of text at varying sizes was an open question. Ultimately, this led to reading about Adobe's approach to early printing technology with their Type 1 font format.<sup>259</sup> The unique element in their approach was the use of a "hint" system on how to draw characters correctly without having all the sizes hard coded in memory. It was conceived that a "hint" system would also be applicable here as there are known spectral peaks and defect energies available for these systems in the literature, see figure 5.9.



Using these as the initial start point allowed for the peak centres to be correctly identified; however, upon running a Levenberg-Marquardt optimisation where the peak centre was fixed but the peak amplitude and  $\sigma_x$ ,  $\sigma_y$  widths were allowed to vary resulted in a mixture of very broad and very narrow non-physical peaks. This meant the revised outlined process could not reliably pass the peak optimisation step, the reason for this failure is

likely due to the lower-resolution of the excitation spectra as there are solely 59 points spaced at 10nm intervals between 230-810 nm inclusive. Thus once again the algorithm had to be revised.

The current version of the algorithm, see figure 5.10, functions within the outlined criteria where a good quality of fit must be obtained while the fit has to retain physical relevance. Although admittedly this iteration is not as simple to use. Peak identification via the “hints” system proved very efficient and this technique was retained again for this algorithm. However, instead of allowing the Levenberg-Marquardt(LM) algorithm to optimise  $\sigma_x$ ,  $\sigma_y$  & amplitude, the experimentalist optimises the  $\sigma_x, \sigma_y$  and provides an initial estimation on amplitude guided by both visual inspection and the adjusted-R<sup>2</sup> (adj-R<sup>2</sup>) value of the fitting. It was found the initial estimates can reach very good agreements with the data prior to LM optimisation with an adj-R<sup>2</sup>  $\geq 0.88$ . Once a good estimate (adj-R<sup>2</sup>  $\geq 0.85$ ) has been obtained the LM optimisation is performed solely varying the peak amplitudes of the 2D-Gaussian line-shapes leading to physical fits with and adj-R<sup>2</sup>  $\geq 0.92$ .

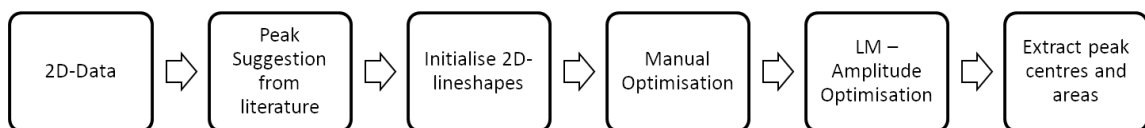


Figure 5.10 - The current algorithm/process used to approach fittings for 2DFMs

In an effort to improve the ease of use of this fitting approach and to better satisfy criterion 3, software was developed in-house to assist with fitting, see script A5.2. When developing the software it was deemed that 4 spectra were required to be visible to the experimentalist to facilitate fitting. These were a 1d-emission slice, 1d-excitation slice, experimental 2DFM and recreated 2DFM from the proposed model. These 4 spectra would assist the experimentalist in suggesting these 2D-line shapes allowing for the corresponding excitation and emission slices to be evaluated while viewing the 2D experimental data. The python program (Python 3.7.5) used the matplotlib,<sup>204,262</sup> lmfit,<sup>263</sup> numpy<sup>264</sup> and pandas<sup>265</sup> libraries.

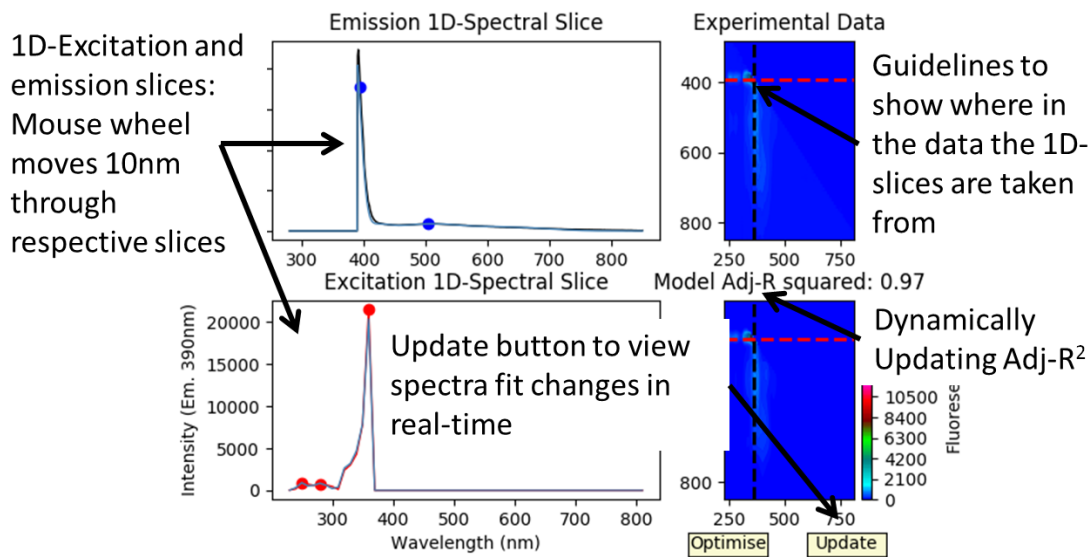


Figure 5.11 - The current algorithm/process used to approach fittings for 2DFMs

The program enables the user to view the 2DFMs of both the experimental data and the model, see figure 5.11, as well as “move” through 1d-slices along the emission and excitation axes independently with a 10nm step via scrolling the mouse wheel in real time. Through editing the loaded csv file, saving and pressing the “update” button, changes to the modelled spectra can be viewed in real time. While this is not a perfect solution, this system is simpler for the experimentalist as there is constant visual feedback to the changes being made. The tools developed in this section were applied to the selected library of semiconductors to study their emissive state topography.

#### 5.4.3 2DFMtd Fittings

The methods and tools developed in the previous sections were applied to the library of semiconductors studied, producing a 2DFM for each sample with their corresponding fitting, see figure 5.12. The fitting approach was able to successfully fit almost all of the samples with adjusted- $R^2$  (adj- $R^2$ ) values of 0.92 or greater with all the line shapes used remaining physically relevant. When comparing the 2DFMs to the fittings some spectral differences are observed; however, with each additional line-shape the complexity of the model increases dramatically making two-dimensional optimisation of such models non-trivial. Cadmium selenide (CdSe) was the sole sample that could not be fitted reliably due to the horizontal band-gap transition spectral signature as the resolution along the excitation axis (horizontal axis) is too low to assign peak centers with confidence. The blue emission at ca. 320 nm observed in CdS, CdSe, TiO<sub>2</sub>, Anthracene, ZnS, ZnSe is assigned to the emission from the plastic well plate. Future studies should use a glass-bottomed well plate to avoid well plate fluorescence.

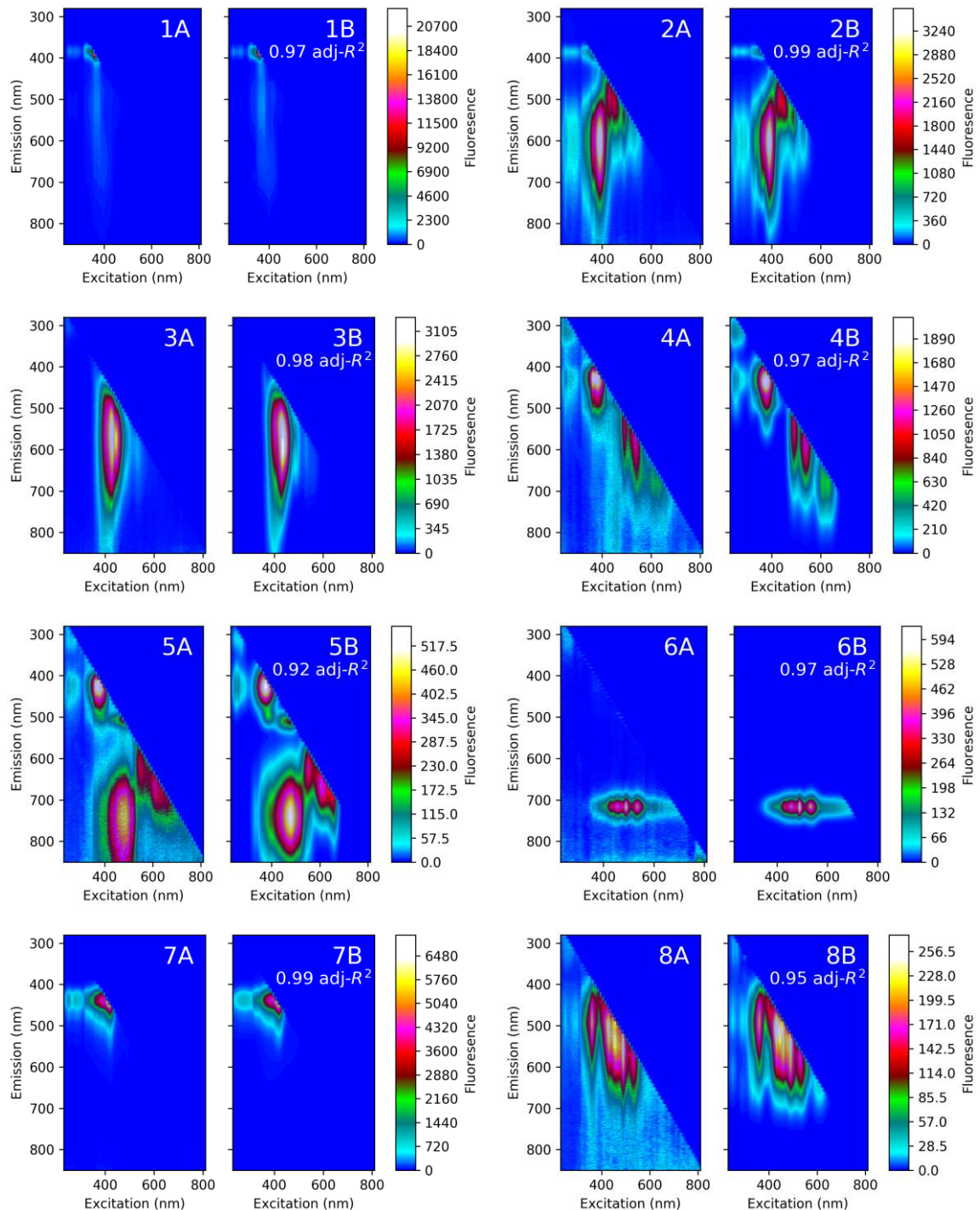


Figure 5.12 - 2DFMs of the library of semiconductors explored and their respective fits with the adj- $R^2$  value reported. Where: 'A' denotes the experimental data and 'B' denotes the proposed model. The numbers denote: 1) ZnO analytical standard, 2) ZnO nanorods, 3) ZnS, 4) ZnSe, 5) CdS, 6) CdSe, 7) anthracene, 8) TiO<sub>2</sub> anatase. The colorbar bar shown on the right of each figure is for the experimental data plot 'A' and is representative of the colorbar of plot 'B'. This omission was chosen for layout reasons.

The metal oxides, ZnO and TiO<sub>2</sub>, in the semiconductor library are both n-type with comparable band-gaps (3.2-3.4 eV). The wurtzite polymorph of ZnO was chosen for these studies and is known for its structural plasticity. Depending upon preparation technique single crystals, thin films, wires, nanocrystals and nanobelts can be formed each with different electronic and optical properties. The tunable optical and luminescence

characteristics of ZnO make the II-VI semiconductor suitable for a range of applications which include medicine,<sup>130,131</sup> engineering novel electronics<sup>132–134</sup> and sensing devices.<sup>137,138</sup>

Generally, ZnO spectral emission can be divided into two subsets: ultraviolet (UV) emission and visible emission. The ultraviolet emission is a subset of discrete narrow emissions generated by band gap transitions.<sup>164,165</sup> While the visible emission can emit over a broad spectral range with discrete emission often categorised as ‘green’, ‘yellow’ and ‘red’.<sup>159</sup> Comparing the 2DFMs of the ZnO analytical standard and the nano-rods, figure 5.12-1A and figure 5.12-2A respectively, provides an insight into the role of the surface in the energy relaxation processes within ZnO nanorods. It should be noted that the 2DFM presentation helps the experimentalist to understand that while exciting the sample using a wavelength of 200, 400 and 500 nm an emission at 570 nm may be observed, the physical nature of the emitting centers for these 570 nm emissions is different. Furthermore, if solely the 1D-spectra was viewed a peak would be observed at 570nm which is a superposition of the different 570nm peaks with different weightings whereas the 2DFM presentation allows quantitative deconvolution of the bands as discrete 2D-line-shapes.

The anatase polymorph of TiO<sub>2</sub> was the other metal oxide in the studied library, this material is commonly studied in energy and environmental research.<sup>266–268</sup> 2DFM of the sample, see figure 5.12-8, allows for clear resolution of two bands at 430 and 490 nm, two bands at 530 and 560nm and two low energy emission transitions at 600 and 640 nm, all as separate two-dimensional line shapes. The observed states at 430 and 490 nm may be attributed to various indirect X-Γ and V<sub>O</sub>-Γ electron-hole recombination relaxation pathways.<sup>269</sup> The bands at 530 and 560 nm were assigned to the recombination of free electrons with trapped holes in different defect states which are likely at the surface of the sample.<sup>270</sup> Finally the low energy transition subset observed was assigned to the radiative recombination of free holes and electrons whose relaxation pathway has gone from CB -> shallow traps -> deep traps -> recombination,<sup>270</sup> with each transition the electron loses a quanta of energy equivalent to the energy level of the specific trap state.

The semiconductor library explored contains ZnS, CdS, ZnSe and CdSe; these metal sulphides and selenides have a range of optoelectronic applications including: sensors,<sup>271</sup> solar cells, lasers<sup>272–274</sup> and flat panel displays.<sup>249</sup> Both ZnS and ZnSe are cubic zinc blende semiconductors with a band gap energy of 3.6 eV<sup>275</sup> and 2.8 eV<sup>276</sup> respectively. The materials have both a high refractive index and transmittance from UV to far IR<sup>277,278</sup> meaning these materials are well suited for optoelectronic applications. Both ZnS and

ZnSe have applications in the engineering of lasers with ZnS used for UV lasers<sup>274</sup> while ZnSe is used for visible/near IR lasers.<sup>272,273</sup> Zinc sulphide finds additional applications in: sensors,<sup>271</sup> electroluminescence devices<sup>279</sup> and flat panel displays.<sup>249</sup> The 2DFM of ZnS, see figure 5.12-3, shows two emissions: the main ‘violet’ emission at 430 nm and two weak “green” emissions as a shoulder at 520 and 580 nm. The emission at 430 nm is reported to be sensitive to thermal annealing under an oxygen containing environment and is assigned to either Zn<sup>2+</sup> vacancies or to oxygen impurities within the sample.<sup>280</sup> The shoulder observed at 530 nm and 580 nm may be caused by Mn impurities within this sample.<sup>281</sup> Comparing the 2DFM of ZnSe, see figure 5.12-4, with that of ZnS it is observed that the ZnSe has a different emission behaviour with a prominent peak at 435 nm and a collection of red-shifted peaks at 520 nm, 540 nm and 580 nm. The emission at 435 nm is due to the band gap recombination<sup>282</sup> while the red-shifted emission can be assigned to Zn vacancies (V<sub>Zn</sub>).<sup>283</sup>

The other sulphide and selenide material in the studied library, CdS and CdSe, are extensively studied with reported band gaps of 2.4 eV<sup>284</sup> and 1.7 eV<sup>285</sup> respectively. The optical properties of these materials make them suited for biological applications such as photo-stable luminescent biological labelling<sup>286,287</sup> and optoelectronic applications including solar cell engineering<sup>288,289</sup> and development of light-emitting devices with orange-red emission.<sup>290,291</sup> The current understanding of the electronic properties of these materials has been developed by exploring the dependence of emission on temperature,<sup>284,292</sup> surface<sup>293–296</sup> and composition.<sup>297,298</sup> The proposed 2DFM technique is a complementary technique to these historical studies with the 2DFM for CdS, see figure 5.12-5, resolving the complex superpositioning of emission for this semiconductor. The resolved emissions include a ‘cyan’ emission at 500 nm, a ‘green’ emission at 510 nm, a subset of orange emissions at 620 nm and a subset of red emissions at 670, 680 and 690 nm. The emissions at 500 nm and 510 nm can be assigned to exciton decay and radiative recombination of a free electron with a hole trapped on a sulphur vacancy,<sup>284,292</sup> while the orange and red subsets are assigned to specific relaxation pathways via either deep trap states or the surface.<sup>284,299</sup> For the CdSe sample the 2DFM, see figure 5.12-6, shows the characteristic semiconductor edge emission at 718 nm.<sup>299</sup>

The final sample in the semiconductor library to address is anthracene, which is a highly conjugated planar organic semiconductor with a low C-H ratio which was selected as a representative sample of the acenes family of compounds.<sup>300</sup> The high purity and ordered packing of these molecules make them highly attractive for developing organic electronics.<sup>301</sup> The 2DFM for anthracene, see figure 5.12-7, shows a subset of overlapped blue emissions and a weak green emission. The blue subset consists of overlapping

discrete emissions at 423, 445 and 480 nm these are assigned to the 0-1, 0-2 and 0-3 transitions of the vibronic envelope for excited molecules<sup>302</sup> at exciton trapping sites.<sup>303,304</sup> For these transitions 0 represents the lowest excited singlet state and 4 represents the ground state of excited molecules.<sup>302</sup> The weak green emission at 545 nm is assigned to trace impurities.<sup>305</sup>

Using a library of semiconductors the resolving power of the 2DFM technique has been showcased with the ability to resolve spectral signatures that would have been superimposed in a 1D-presentation. An excellent example of the aforementioned resolving power is the ability to separate the 570 nm emission within ZnO into the emissive states of different physical nature dependent upon excitation wavelength. The power of this deconvolving approach steps beyond resolving intrinsic states within a sample and is able to detect trace impurities such as Mn in the ZnS sample studied.<sup>281</sup> This technique is very applicable to semiconductor studies and quality control (QC) applications in both academic and industrial settings.

## 5.5 Conclusion

Within this chapter a novel methodologic approach to the analysis of emissive states in semiconductors is proposed. Through use of this technique we obtain a topological view of the emissive states within a sample, these two-dimensional spectra shall herein be referred to as two-dimensional fluorescence maps (2DFM). 2DFM is viable on spectrometers designed solely for one-dimensional operation which allows for experimentation on existing fluorescence spectrometers equipped with a monochromator and could be deployed in a variety of settings. Bespoke instrumentation could be developed to assist this avenue of research; these spectrometers would ideally be equipped with an integrating sphere, photon counting detector, controlled atmosphere and a monochromator and would be able to perform low temperature measurements. This instrument would be able to directly measure the quantum yield of emissive states, determine the effect of the gaseous environment on emission behaviour and reduced temperature conditions would sharpen peak line-shapes. Such a device should be designed to measure emission over a larger detection range (i.e. 250- 3300nm) as this would allow exploration of the traps states within low band-gap materials (i.e. CdSe).

The proposed fitting algorithm performs within the outlined criteria where a good quality of fit must be obtained while retaining physical relevance. Through use of bespoke in-house software the author has attempted to make this process as simple to use as possible. The “hints” system, inspired by the early font work by Adobe,<sup>259</sup> is fundamental to retaining physical relevance in the suggested peaks. Currently, the experimentalist optimises the

$\sigma_x$ ,  $\sigma_y$  and provides an initial estimation on amplitude guided by both visual inspection and the adjusted-R<sup>2</sup> (adj-R<sup>2</sup>) value of the fitting. The LM optimisation is performed solely varying the peak amplitudes of the 2D-Gaussian line-shapes leading to physical fits with an adj-R<sup>2</sup>≥0.9<sup>2</sup>. Future work on this technique would facilitate collection of higher resolution data enabling more of the fitting process to be automated.

The software developed during this study could be further optimised including features such as: removal of the weak high-order excitation signal from the dataset. Such software could be deployed on a microprocessor enabling compiling of 2D-arrays before the data reaches the pc. This could be implemented either by the manufacturer or as an after-market add-on through use of single board computers (SBCs).

Using a library of semiconductors the resolving power of the 2DFM technique has been showcased with the ability to resolve spectral signatures that would have been superimposed in a 1D-presentation. An excellent example of the aforementioned resolving power is the ability to separate the 570 nm emission within ZnO into the emissive states of different physical nature dependent upon excitation wavelength. The power of this deconvolving approach steps beyond resolving intrinsic states within a sample and is able to detect trace impurities such as Mn in the ZnS sample studied.<sup>281</sup> This technique is very applicable to semiconductor studies and quality control (QC) applications in both academic and industrial settings.

# Chapter VI: Quantification and Engineering of Trap State Emission using Two-Dimensional Fluorescence Mapping for Solid State Zinc Oxide micro/nano structures

Research presented in section 6.4.4 in this chapter is included in “Polariton condensation and surface enhanced Raman in spherical ZnO microcrystals” (doi: 10.1038/s41467-020-18666-4).

## 6.1 Introduction

As previously discussed in Chapter V, ZnO is a naturally occurring II-VI semiconductor with a band gap of ca. 3.2eV, whose properties have been widely studied for the past 6 decades.<sup>114–118</sup> The wurtzite polymorph is of particular interest as it is known for its structural diversity with respect to native defect states. Depending upon the preparation technique selected single crystals,<sup>122</sup> thin films,<sup>123</sup> wires,<sup>124</sup> nanocrystals<sup>125</sup> and nanobelts<sup>126</sup> can be formed each with different electronic and optical properties. The tunable optical and luminescence characteristics<sup>127–129</sup> of ZnO make the II-VI semiconductor suitable for a range of applications which include: medicine,<sup>130,131</sup> engineering novel electronics,<sup>132–134</sup> flat-panel displays<sup>129</sup> and sensing devices.<sup>137,138</sup>

Generally, ZnO spectral emission can be divided into two regions: ultraviolet (UV) emission and visible emission, for wavelengths see table 4.9. The ultraviolet emission is a subset of discrete narrow emissions generated by band gap transitions,<sup>164,165</sup> while the visible emission can emit over a broad spectral range with discrete emission often categorised as ‘green’,<sup>129,136</sup> ‘blue’,<sup>166</sup> ‘yellow’<sup>166,167</sup> and ‘red’.<sup>159</sup> Visible emissions can be attributed to native trap states within ZnO (i.e. V<sub>Zn</sub>), where conduction band (CB)->trap state transitions produce spontaneous fluorescence emission. The ability to tune the spectral emission of ZnO with no additional dopants solely through controlling defect/trap state populations within the matter is attractive for a range of optoelectronic applications including solar cells<sup>306</sup> and light emitting diodes (LEDs).<sup>307</sup> While most of the tunable emission resides within the visible range, low energy transitions have been reported to produce emission in the near infrared region.<sup>168</sup>

Table 4.9 - Wavelengths and corresponding energies for ZnO emission

	Colour	Wavelength (nm)	Energy (eV)
Visible	UV <sup>164,165</sup>	387	3.20
	Blue <sup>166</sup>	440	2.82
	Green <sup>129,136</sup>	510	2.43
	Yellow <sup>166,167</sup>	640	1.94
	Red <sup>159</sup>	708	1.75

In Chapter V, the resolving power of the 2D-Fluorescence map (2DFM) technique was showcased. This highlighted the resolving power of the technique where spectral signatures that would have been superimposed in a 1D-presentation are resolved in 2DFM. The ‘green’ emission at 570nm for the ZnO samples studied in Chapter V (ZnO nanorods and ZnO analytical standard) is of particular interest as the 2DFMs showed the 570 nm emissive center having a different physical nature dependent upon the excitation wavelength used. Additionally, when comparing the maps for the ZnO analytical stand and the nano-rods the role of trap state relaxations within the nano-rod sample was apparent.

This preliminary study highlights the different emissive states between the two wurtzite ZnO samples formed using different synthetic conditions. Further, to determine if there are any trends in emissive state topology for ZnOs formed using different synthetic conditions this study will use 2DFMs of each sample to extract the transitions and relaxation pathways the excited electrons in these materials undergo. The “hints” required to perform the 2DFM analysis will be generated using known trap state energies from literature.<sup>129,166,260</sup>

The application of 2DFM to semiconductors is a novel and powerful approach allowing for deconvolution of emissive states. In this chapter the differences in emissive states within different ZnOs will be explored using a representative library of ZnOs obtained by hydrothermal wet chemical synthesis. The library of ZnOs selected are as follows: an analytical standard, microspheres, nanorods, nanoplatelets, nanoflowers & a ZnO-Au nanocomposite. The nanoplatelet and nanoflowers samples were selected to explore the effect peptide mediated synthesis has on native defects in the synthesised matter. The ZnO-Au sample uses a novel ZnO/Au hybrid binding sequence engineered from G12 and

A3, a known ZnO and Au binder respectively. The emissive state topology of this library will be investigated under 3 different conditions:

1. Untreated sample in its native solid state with no surface treatment
2. Sample treated with 0.5% PVA surface passivation reported to reduce ‘green’ emission originating at the surface and increase near band edge (NBE) emission.<sup>199</sup>
3. Sample treated with 1M NaBH<sub>4</sub> surface activation reported to increase oxygen vacancies (V<sub>O</sub>) at the surface.<sup>200</sup>

The aim of this study is to use 2DFM to determine the emissive topology, transitions and relaxation pathways in different ZnOs. Two surface treatments that are reported in the literature will be used to observe the effects of state passivation or induction within these materials. The observed behaviour with and without treatment will be compared between different ZnOs within the studied library to determine if any information can be obtained about how to control state populations through modulating the wet chemical synthetic conditions.

## 6.2 Materials and Methods

Sodium citrate (Na<sub>3</sub>C<sub>6</sub>H<sub>5</sub>O<sub>7</sub>), 1,3-hexamethylenetetramine (HMTA, C<sub>6</sub>H<sub>12</sub>N<sub>4</sub>), and zinc oxide analytical standard material (average particle size of 117 µm determined from a sample of 50 particles, for representative SEM image and histogram of particle sizes see figure A6.1-1) were purchased from Sigma-Aldrich (St. Louis, Missouri USA). Zinc nitrate hexahydrate (Zn(NO<sub>3</sub>)<sub>2</sub>·6H<sub>2</sub>O) was purchased from fluka (Charlotte, North Carolina USA). All these materials were used without any further treatment. If required type 1 water was used with a resistance of 18MΩ at 25°C. The ZA2 peptide used in this study was synthesised in house using the protocol detailed below while the GT-16 peptide was purchased from Pepceuticals (Leicester, UK), for purity see table A6.1. All samples except the ZnO analytical standard were synthesised in house using either a protocol from the literature or novel synthetic route, the protocols for each sample are detailed below.

All fluorescence measurements were performed on all the samples in the solid-state using black 96-well plates from Corning. The spectrometer used was a TECAN i-control M200 Pro spectrometer (Tecan Group Ltd. Switzerland) fitted with a monochromator and controlled by the i-control (version 1.9.17.0) software. The 2DFM technique was performed as discussed in Chapter V. Characterisation of the size, morphology and structure of the synthesised nanorods was done using both a JEOL JSM-7100F SEM microscope and a X’Pert PRO X-ray diffractometer (Malvern Panalytical, Malvern, UK) using Cu Kα radiation operating at a wavelength of 1.54056 Å. For the ZnO-Au sample a JEOL 2100 Plus TEM/STEM microscope fitted with a JEOL EX-24200M1G2T EDX

system and a LaB<sub>6</sub> source was used to study the nanoscale gold inclusions. Confocal emission microscopy studies were conducted using a Leica TCS SP5 (Leica, Milton Keynes, UK). Instrumental parameters that were kept constant throughout the experiments were the numerical aperture (0.5 NA), objectives (63x), step size of 0.5 µm and PMT gain of 1000 V.

### 6.2.1 Zinc Oxide Microspheres

The ZnO polycrystalline microspheres were synthesised by Professor C. Perry based on a protocol from the literature.<sup>308</sup> A reaction mixture (10ml) containing 50 mM Zn(NO<sub>3</sub>)<sub>2</sub>, 50 mM HMTA and 38 mM sodium citrate was prepared and mixed at room temperature. The solution was heated to 90°C for 1.5 hrs and the precipitate formed was collected by centrifugation using Centrifuge 5904R M (Eppendorf, Hamburg, Germany) at 5000 rpm for 5 minutes. The pellet was washed with 2x 10ml Type-I water, 1x 10ml absolute EtOH before being suspended in 500µL Type-I water and immediately lyophilised. The formed ZnO microspheres had a diameter of 1.9±0.4 µm determined from a sample of 55 particles, for representative SEM image and histogram of particle sizes see figure A6.1-2.

### 6.2.2 Zinc Oxide Nanorods

Utilising a procedure documented in the literature,<sup>11,255</sup> ZnO nanorods were prepared using HMTA (0.42g, Sigma-Aldrich), Zn(NO<sub>3</sub>)<sub>2</sub>·6H<sub>2</sub>O (0.058g, Fluka) & 18mΩ H<sub>2</sub>O (90mL) placed into a glass reaction vessel. The reaction mixture was incubated at 20°C using a water bath stirrer setup for 24hrs. Subsequently, the samples were incubated at 68°C using a water bath stirrer setup for a further 48hrs. Post incubation the precipitate was separated from the reaction medium using centrifugation (10 mins, rcf 15557) using a Centrifuge 5804 R (eppendorf) and washed with 18MΩ H<sub>2</sub>O three times before being lyophilised. The twinned ZnO nanorods formed had a length of 1.4±0.2 µm with a length to diameter ratio (L/D) of 10.7±1.7, these parameters were determined from a sample of 62 nanorods, for representative SEM image and histogram of particle sizes see figure A6.1-3.

### 6.2.3 Solid Phase Synthesis of the ZA2 Binding Peptide

The ZA2 peptide (GLHVMHKVAYSSGAPPMPFF) was synthesized using Fmoc-protective group chemistry leveraging the microwave-assisted solid-phase peptide synthesis technique (Liberty Blue Peptide Synthesizer CEM Corp). Peptide purity and the molecular weight of the sequence were determined using high-performance liquid chromatography (Dionex RP-HPLC equipped with phenomenex peptide C18 column) and matrix-assisted laser desorption/ionisation time-of-flight mass spectrometry (Bruker Ultraflex III MALDI-TOF), see table A6.1.

#### 6.2.4 Peptide Mediated Zinc Oxide Synthesis

Utilising a procedure documented in the literature,<sup>11,255</sup> ZnO platelets/nanoflowers were prepared using the GT16/ZA2 peptide respectively (2.82mM, 1mL, sequences in table 6.1), HMTA (0.42g, Sigma-Aldrich), Zn(NO<sub>3</sub>)<sub>2</sub>·6H<sub>2</sub>O (0.058g, Fluka) & 18mΩ H<sub>2</sub>O (89mL) placed into a glass reaction vessel. The reaction mixture was incubated at 20°C using a water bath stirrer setup for 24hrs. Subsequently, the samples were incubated at 68°C using a water bath stirrer setup for a further 48hrs. Post incubation the precipitate was separated from the reaction medium using centrifugation (10 mins, rcf 15557) using a Centrifuge 5804 R (eppendorf) and washed with 18mΩ H<sub>2</sub>O three times before being lyophilised. Using the GT16 sequence nanoplatelets were formed with a diameter of 0.8±0.1 μm and a L/D of 0.2±0.1 μm, while the ZA2 sequence formed nanoflowers with a diameter of 5.4±0.3 μm; these flowers had individual rods originating from the center of the structure with a length of 1.7±0.1 μm and a L/D ratio of 3.7±0.4. These parameters were determined from a sample of; 51 nanoplatelets and 59 nanoflowers, for representative SEM image and histogram of particle sizes see figure A6.1-4 and figure A6.1-5 respectively.

Table 6.1 - Biomineralisation peptides used in this study with their corresponding one-letter sequence and the respective morphologies of ZnO generated through the sequence mediated synthesis.

Peptide Name	ZnO morphology	Sequence
GT16 <sup>11</sup>	Nanoplatelets	GLHVMHKVAPPRGGGC
ZA2	Nanoflowers	GLHVMHKVAYSSGAPPMPFF

#### 6.2.5 Zinc Oxide - Peptide - Au composite one-pot synthetic route

This synthesis utilises a novel peptide sequence, herein referred to as ZA2, which was engineered from regions of G12 (a known ZnO binder and parent peptide of GT-16<sup>42</sup>) and A3 (a known and well studied Au binder).<sup>39</sup> Utilising the novel ZA2 sequence and a modification to a procedure documented in the literature,<sup>11,94,255</sup> ZnO-ZA2-Au nanocomposite materials were prepared using HAuCl<sub>4</sub> (10 mM, 9 ml, Sigma), ZA2 Peptide (GLHVMHKVAYSSGAPPMPFF, 2.82mM, 1mL), HMTA (0.42g, Sigma-Aldrich), Zn(NO<sub>3</sub>)<sub>2</sub>·6H<sub>2</sub>O (0.058g, Fluka) & 18mΩ H<sub>2</sub>O (80mL) placed into a glass reaction vessel. The reaction mixture was incubated at 20°C using a water bath stirrer setup for 24hrs. Subsequently, the samples were incubated at 68°C using a water bath stirrer setup for a further 48hrs. Post incubation the precipitate was separated from the reaction medium using centrifugation (10 mins, rcf 15557) using a Centrifuge 5804 R (eppendorf) and washed with 18mΩ H<sub>2</sub>O three times before being lyophilised. The pseudo spherical ZnO particles formed were 5.0±0.3 μm determined from a sample of 50 particles, for representative SEM image and histogram of particle sizes see figure A6.1-6, with discrete

nanoscale gold inclusions distributed throughout the sample, as shown by the TEM studies below.

### 6.3 Characterisation

Structural properties of the ZnO samples were determined using SEM microscopy. The microscope used was a JEOL JSM-7100F at an accelerating voltage of 5 keV. SEM SEI imaging was used to determine the size and morphology of uncoated samples with a sample size of at least 50 particles being measured for each sample, the number of particles measured for each sample are available in section 6.2. Determined particle sizes are available in table 6.2.

Further structural and composition based information was determined using a PANalytical X'Pert PRO X-ray diffractometer (Malvern Panalytical, Malvern, UK) having Cu K $\alpha$  radiation operating at a wavelength of 1.54056 $\text{\AA}$ . The samples were scanned over a range between 3° and 90° of 2 $\theta$  with a step size of 0.02°·s $^{-1}$ . Experiments were carried out at room temperature with an acceleration voltage of 45 kV and 40 mA filament current. The X'Pert-HighScore Plus (Version 4.5) program was used to analyse and identify peaks in the diffraction patterns, for the line spectra see figure A6.2. The presence of gold in ZnO-ZA2-Au was confirmed by the Au<sub>(111)</sub>, Au<sub>(200)</sub> & Au<sub>(220)</sub> peaks being present in the samples' diffractograms. The crystallite domain size was determined according to the Scherrer formula<sup>309</sup> with the following constants: x-ray wavelength 0.15406 nm & shape factor (K) of 0.9, while B was determined at the full width half maximum. Domain size of ZnO for each sample is tabulated in table 6.2 and the domain size of Au in the ZnO-ZA2-Au sample was determined to be 19±6 nm, for TEM image of the gold inclusions and a histogram of the particle sizes see figure A6.3.

Table 6.2 - ZnO & Au domain sizes calculated using the Scherrer equation<sup>309</sup> with corresponding particle size for each sample.

ZnO Sample Name	ZnO		Au (nm)	
	Domain Size (nm)	Particle Size ( $\mu\text{m}$ )	Domain Size	Particle Size
Standard	52 $\pm$ 9	117 $\pm$ 38	-	-
Microspheres	18 $\pm$ 5	1.9 $\pm$ 0.4	-	-
NanoRods	23 $\pm$ 7	1.4 $\pm$ 0.2	-	-
NanoPlatelets (GT16)	18 $\pm$ 2	0.8 $\pm$ 0.1	-	-
NanoFlowers (ZA2)	46 $\pm$ 6	5.4 $\pm$ 0.3	-	-
ZnO-ZA2-Au	45 $\pm$ 4	5.0 $\pm$ 0.3	19 $\pm$ 6	18.6 $\pm$ 6.9

TEM and STEM microscopic techniques were used to identify the presence and size of gold inclusions in the ZnO-ZA2-Au sample. The ZnO-ZA2 was also imaged using these techniques as this is the analogous material with no gold inclusions. The microscope used was a JEOL 2100 Plus TEM/STEM microscope fitted with a JEOL EX-24200M1G2T EDX system and a LaB<sub>6</sub> source. An accelerating voltage of 200kV was used for both TEM and STEM imaging. TEM imaging was used for initial screening of the nanocomposites to determine which synthetic routes yielded a desirable product. Upon passing the initial screening TEM, STEM and semi-quantitative EDX mapping were performed on the sample to determine the morphology of the nanostructure as well as the size and localisation of any gold inclusions present in the sample. Due to the ZnO structure in ZnO-ZA2-Au being on the micrometer scale which is a thousand fold greater than the usual nanometer imagine scale of TEM imaging, several TEM micrographs were carefully stitched together to achieve an informative image of the sample while taking care to avoid artifacts.

The optical absorbance behaviour of ZnO-ZA2-Au and ZnO-ZA2 samples were explored using a Cary-50 UV-Vis-NIR spectrometer with a 200 - 800nm data collection window using a collection interval of 1 nm. The sample was held in a 1mm pathlength quartz cuvette in aqueous medium to reduce any scattering caused by the internal quartz air interface. Assignment of the adsorption contributions within the ZnO-ZA2-Au sample was achieved by modelling the contribution of discrete gold inclusions using Mie theory and summing the modelled contribution with the ZnO-ZA2 spectral response. This method

allowed for the differences in absorption behaviour of ZnO to be observed between when discrete gold inclusions are or are not present. A python script was developed inhouse to perform the Mie theory modelling, this script leveraged the matplotlib<sup>203,204</sup>, mpmath<sup>310</sup>, pandas and SciPy<sup>311</sup> modules. The mpmath package is vital to these calculations as during the computation of the Mie scattering the values tend to explode towards infinity, going beyond the normal double computable range which python uses, before the values collapse back towards zero. The computable range for double precision calculations is from  $\pm 2.23 \times 10^{-308}$  to  $\pm 1.80 \times 10^{308}$  numbers outside this range are assigned an arbitrary inf term if the mpmath package is not used.<sup>312</sup> Mpmath avoids this issue by using a higher internal precision during calculation before returning the answer in double float precision for python to use, which is suitable for these calculations.

## 6.4 Results and Discussion

### 6.4.1 ZnO 2DFM Emissive State Topology & Fitting

The methods and tools developed in Chapter V were applied to the library of ZnOs studied, producing a 2DFM for each sample with their corresponding fitting, see figure 6.1. The “hints” required for this fitting were all the possible transitions between the band gap and in-band gap states. Literature values for the energies of ZnO native defect states<sup>127,128,260,261</sup> were used to calculate a table of possible transitions used as the hints for these fittings, see table 6.3.

Table 6.3 - Tabulated energy values for photons in electron volts (eV) emitted during radiative relaxation of excited electrons in ZnO.<sup>129,166,260</sup> Values with a red background are outside of the detection range for the Tecan i-control M200 Pro. The following symbol representation is adopted: CB denotes conduction band, VB denotes valence band,  $V_O$  &  $V_{Zn}$  represent vacancies for oxygen and zinc respectively,  $O_i$  &  $Zn_i$  represent interstitials for oxygen and zinc respectively,  $V_OZn_i$  represents a complex of an oxygen vacancy and zinc interstitial,  $V_{O0}/Zn_{i0}$  denotes a neutral oxygen vacancy or neutral zinc interstitial and  $O_{Zn}$  is an oxygen antisite. The signs present denote the charge of the defect, no sign or 0 means neutral and + or - denote a positive or negative charge respectively. All charges are single charges unless preceded by a number.

Energy of photon (eV)	CB	$V_{O0}/Zn_{i0}$	$Zn_i$	$Zn_{i+}$	$V_{Zn2-}$	$V_O$	$V_{O+}$	$V_OZn_i$	$O_i$	$O_{Zn}$	$V_{Zn-}$	$O_i$	$V_{Zn}$
$V_{O0}/Zn_{i0}$	0.05												
$Zn_i$	0.46	0.41											
$Zn_{i+}$	0.50	0.45	0.04										
$V_{Zn2-}$	0.56	0.51	0.10	0.06									
$V_O$	1.62	1.57	1.16	1.12	1.06								
$V_{O+}$	2.00	1.95	1.54	1.50	1.44	0.38							
$V_OZn_i$	2.10	2.05	1.64	1.60	1.54	0.48	0.10						
$O_i$	2.28	2.23	1.82	1.78	1.72	0.66	0.28	0.18					
$O_{Zn}$	2.38	2.33	1.92	1.88	1.82	0.76	0.38	0.28	0.10				
$V_{Zn-}$	2.66	2.61	2.20	2.16	2.10	1.04	0.66	0.56	0.38	0.28			
$O_i$	2.96	2.91	2.50	2.46	2.40	1.34	0.96	0.86	0.68	0.58	0.30		
$V_{Zn}$	3.06	3.01	2.60	2.56	2.50	1.44	1.06	0.96	0.78	0.68	0.40	0.10	
VB	3.20	3.15	2.74	2.70	2.64	1.58	1.20	1.10	0.92	0.82	0.54	0.24	0.14

Out of the 91 different possible emissions generated by these transitions only emissions with an energy between ca. 4.42 - 1.45 eV (280-850 nm) can be detected by the Tecan i-control M200 Pro spectrometer. Applying this restriction on the 91 possible transitions yields 42 observable transitions, any transitions which are outside the detection range have been assigned a shaded background in table 6.3. Using these known transitions as “hints” the fitting approach outlined in Chapter V was able to successfully fit all of the

samples with adjusted- $R^2$  (adj- $R^2$ ) values of 0.93 or greater with all the line shapes used remaining physically relevant.

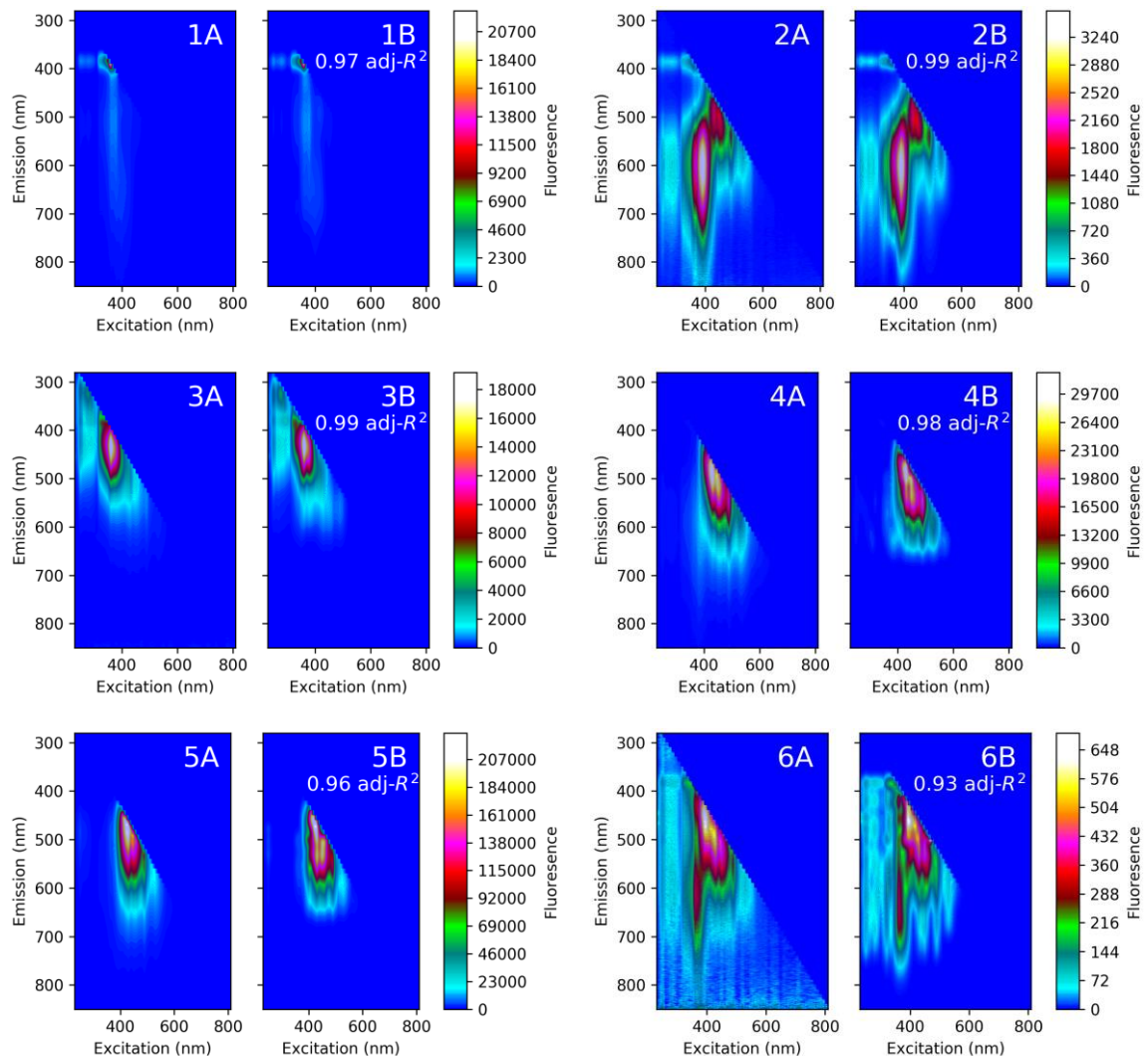


Figure 6.1 - 2DFMs of the ZnO library explored and their respective fits with the adj- $R^2$  value reported. Where: 'A' denotes the experimental data and 'B' denotes the proposed model. The numbers denote: 1) analytical standard, 2) nanorods, 3) microspheres, 4) nanoplatelets, 5) nanoflowers & 6) ZnO-Au composite. The colorbar bar shown on the right of each figure is for the experimental data plot 'A' and is representative of the colorbar of plot 'B'. This omission was chosen for layout reasons.

When comparing the 2DFMs to the fittings, see figure 6.1, some spectral differences are observed; however, as previously discussed in chapter V, each additional line-shape added increases the complexity of the model meaning two-dimensional optimisation of such models is non-trivial. The most complex case to fit was the ZnO-Au material as there does not appear to be a preferred/dominant transition for this material. The blue emission at ca. 320 nm observed in microspheres and ZnO-Au is assigned to the emission from the plastic well plate. Future studies should use a glass-bottomed well plate to avoid well plate fluorescence.

Generally, ZnO spectral emission can be divided into two subsets: ultraviolet (UV) emission and visible emission. The ultraviolet emission is a subset of discrete narrow emissions generated by band gap transitions,<sup>164,165</sup> while the visible emission can emit over a broad spectral range with discrete emission often categorised as ‘green’, ‘yellow’ and ‘red’.<sup>159</sup> Comparing the 2DFMs of the ZnO library, see figure 6.1, it was observed that the UV emission at ca. 335nm (3.7 eV) was dominant in the analytical standard and microsphere samples. The other samples in the studied library were dominated by visible emission, in particular ‘red’ and ‘green’ emissions at 650 and 510 nm respectively, which are attributed to surface associated traps in ZnO.<sup>121</sup> This provides an insight into the role of the surface in the energy relaxation processes within ZnO nanostructures.

The semi-quantitative approach for looking at dominant emissive states within the emissive state topology for different samples is useful and provides an insight into the material characteristics. However, to compare subtle differences between ZnOs a quantitative approach must be adopted where each transition modelled is accounted for. To achieve this the parameters for each individual 2D-line-shape within the model is reviewed and grouped into groups of the same transition (i.e. CB → VB). Grouping of the 2D-line-shapes is possible due to the “hints” system used as it directly relates the peaks to 42 known observable transitions, see table 6.3. Once grouped, the percentile emission contribution of that transition in respect to the total modelled emission is calculated and a Jablonski diagram created, see figure 6.2. While Jablonski diagrams cannot be used for band structure related transitions, defect states can be considered as discrete ‘molecules’ within the ZnO matter meaning the use of Jablonski plots is appropriate. For diagrammatic purposes the conduction and valence bands are represented as a straight line corresponding to the direct band gap distance between the maximum of the valence band and the minimum of the conduction band.

Qualitative observations of the generated Jablonski diagrams, see figure 6.2, uncovered two subsets of relaxation transition emission behaviour within the library studied. The first subset, containing the analytical standard, microspheres and nanorods, has 8 observable transitions. The second subset is formed of the peptide mediated samples, which includes the nanoplatelets, nanoflowers and ZnO-Au, each with 16 observable transitions. This divide between the behaviour of ZnOs manufactured under peptide mediated and non-peptide mediated conditions suggested that peptide presence introduces additional defect states into the lattice structure during synthesis. This theory is supported by the mechanism by which peptide mediation controls the substrate growth through binding to specific facets in the developing crystal.

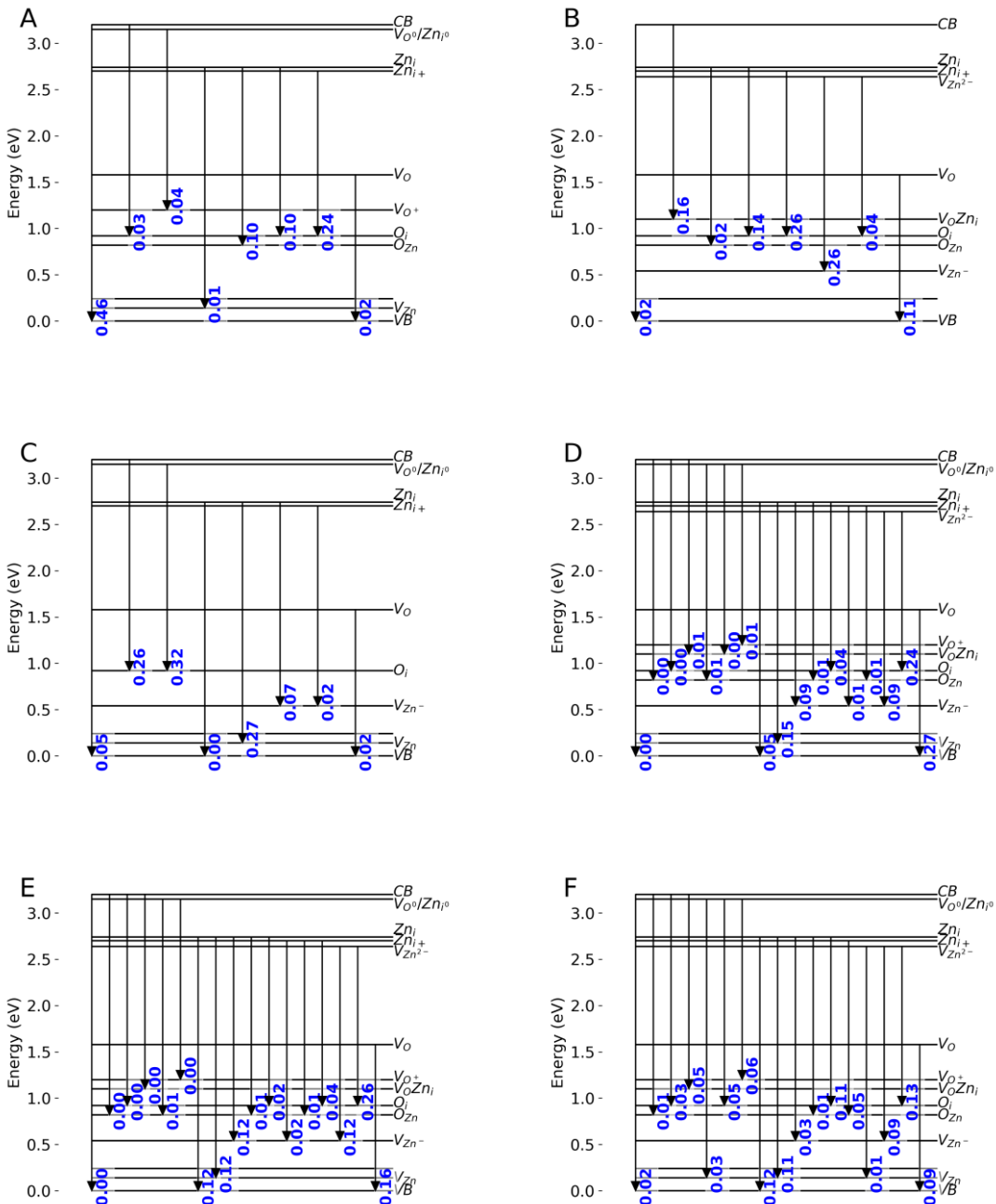


Figure 6.2 - Jablonski diagrams of the ZnO library explored generated from their respective fitted models with the percentile emission contribution for each transition. The letters denote: A) analytical standard, B) nanorods, C) microspheres, D) nanoplatelets, E) nanoflowers & F) ZnO-Au composite. The following symbol representation is adopted: CB denotes conduction band, VB denotes valence band,  $V_O$  &  $V_{Zn}$  represent vacancies for oxygen and zinc respectively,  $O_i$  &  $Zn_i$  represent interstitials for oxygen and zinc respectively,  $V_OZn_i$  represents a complex of an oxygen vacancy and zinc interstitial,  $V_O^0/Zn_i^0$  denotes a neutral oxygen vacancy or neutral zinc interstitial and  $O_{Zn}$  is an oxygen antisite. The signs present denote the charge of the defect, no sign or 0 means neutral and + or - denote a positive or negative charge respectively. All charges are single charges unless preceded by a number. This data is presented in a tabulated form in table A6.2.

The peptides used in this study, GT-16 (GLHVMHKVAPPRGGGC)<sup>11,42</sup> and ZA2 (GLHVMHKVAYSSGAPPMPFF), are derived from the G-12 (GLHVMHKVAPPR)<sup>11</sup> sequence which is a known ZnO binding peptide. Both the G-12 and GT-16 sequences

bind to the (0001) and (1010) facets in the developing crystal mediating growth along the *a* and *c* axes respectively.<sup>42</sup> However, the GT-16 sequence preferentially binds to the (0001) plane restricting growth along the *c*-axis.<sup>42</sup> The facet preference of the ZA2 sequence is unknown as binding studies were not conducted; although the author predicts the binding behaviour to be similar to the parent peptide G-12 binding to both the (0001) and (1010) facets. The (0001) facet of ZnO is a Zn<sup>2+</sup> terminated surface and the (1010) facet is a Zn<sup>2+</sup> and O<sup>2-</sup> mixed terminated surface meaning interactions with these surfaces may produce higher populations of Zn and O vacancies ( $V_{Zn}$  and  $V_O$ ).

Looking at the percentile contributions of the different transitions it was observed that  $V_{Zn(2-)} \rightarrow O_i$  was a dominant transition in the nanoplatelets, nanoflowers and ZnO-Au materials contributing to 25, 26 & 14% of the total emission respectively. This transition is not observed in either the analytical standard or the microspheres and is a 4% contribution in the nanorod sample, supporting the theory that peptide mediation is influencing defect states within these materials. The other dominant transition for the peptide mediated subset was the  $V_O \rightarrow VB$  transition contributing 27, 16 & 9% to the total emission respectively for the nanoplatelets, nanoflowers and ZnO-Au materials. In comparison, the  $V_O \rightarrow VB$  transition contributed 2% to the total emission for both the analytical standard and microspheres. However, for the nanorods the  $V_O \rightarrow VB$  transition contributed for 11% of the total emission this suggested the HMTA hydrothermal synthesis method introduces  $V_O$  defect states into the ZnO lattice during synthesis. This theory is supported by the HMTA synthesis forming nanorods with a preferred direction of growth along the *c*-axis,<sup>94</sup> growth along this axis means the (1010) facet becomes larger and due to its mixed terminated nature increases the chance of surface based  $V_O$ .<sup>129,166</sup>

Comparing the relative contributions of the near band edge (NBE) emission generated by the CB  $\rightarrow$  VB transition, it is observed that the non-peptide mediated subset all have band-gap exciton emission, which is centered at ca. 335 nm (3.7 eV). The relative contributions for the analytical standard, microspheres and nanorods are 46, 4.6 & 2% respectively. Both the microspheres and analytical standard have low populations of  $V_{Zn}$  and  $V_O$  defects. Therefore, it was predicted that the NBE emission for both materials would be comparable; however, the microsphere sample is dominated by two transitions (26% CB- $\rightarrow O_i$  and 31%  $V_O/Zn_i \rightarrow O_i$ ) both of which are related to oxygen interstitial ( $O_i$ ) defects. This suggests the citrate mediated synthesis may introduce  $O_i$  defects to the lattice during synthesis. The author proposes that these observations may be due to the charged nature of the citrate molecule which complexes with the free Zn<sup>2+</sup> ions and interacts with the (1010) facet of the developing ZnO crystal through electrostatic interactions causing free O<sup>2-</sup> ion to be trapped in between the lattice. A future study could

focus on developing an in-depth mechanistic understanding of the citrate mediated synthetic route; however, this is outside the scope of this study.

For the peptide mediated sample the NBE emission is below 1% for both the nanoplatelets and nanoflowers while the ZnO-Au composite has a NBE emission of 2.4% of the total emission. The ZnO-Au composite is an interesting case as the sample does not appear to have a preferred or dominant emission, with all 16 of the observable contributions contributing at least 1% to the overall emission. This study proposes this unusual behaviour is due to the discrete Au inclusions where electrons at the ZnO-Au boundary feel the metallic environment of Au.

The Zn interstitial ( $Zn_i$ ) defect state appears in every sample studied and is usually attributed to the volume of ZnO structures.<sup>313,314</sup> The transitions which relax from this state account for 44, 36, 42, 36, 77 & 52% of total overall emissions for the analytical standard, microspheres, nanorods, nanoplatelets, nanoflowers & ZnO-Au respectively. Due to the complex nature of relaxations within these samples where the emission of a given transition is codependent on the two states involved, the relative concentrations of  $Zn_i$  defects in these materials is beyond the scope of this study.

The aforementioned complex interplay between defects states and resultant emissive transitions have been harnessed with a range of surface coatings reported in literature targeting passivation or introduction of defect states.<sup>199–201,315</sup> From these reported surface treatments two are of particular interest: 0.5% PVA surface passivation is reported to reduce ‘green’ emission originating at the surface and increase near band edge (NBE) emission<sup>199</sup> and 1M NaBH<sub>4</sub> surface activation is reported to increase oxygen vacancies ( $V_O$ ) at the surface.<sup>200</sup> The impact of each treatment on the relaxation pathways within the ZnO samples will be explored through 2DFM data and Jablonski diagrams determined from the obtained data.

The 2DFMs of the 0.5% PVA treated samples, see figure 6.3, were fitted using the approach outlined in Chapter V using the known transitions in table 6.3 as the required “hints”. The method successfully fitted all the samples with adjusted-R<sup>2</sup> (adj-R<sup>2</sup>) values of 0.91 or greater with all the line shapes used remaining physically relevant.

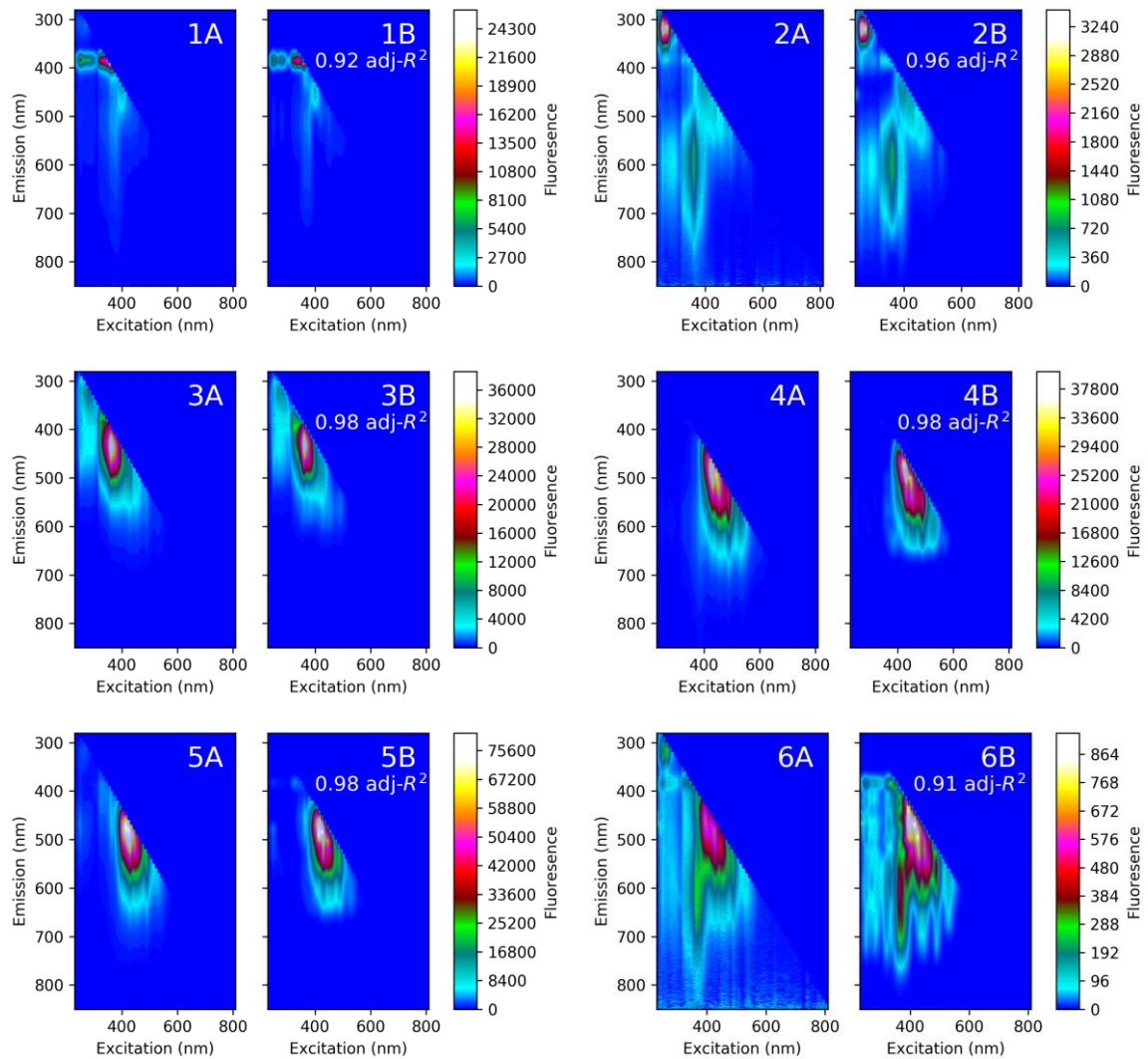


Figure 6.3 - 2DFMs of the 0.5% PVA treated ZnO library explored and their respective fits with the adj- $R^2$  value reported. Where: 'A' denotes the experimental data and 'B' denotes the proposed model. The numbers denote: 1) analytical standard, 2) nanorods, 3) microspheres, 4) nanoplatelets, 5) nanoflowers & 6) ZnO-Au composite. The colorbar bar shown on the right of each figure is for the experimental data plot 'A' and is representative of the colorbar of plot 'B'. This omission was chosen for layout reasons.

When comparing the 2DFMs to the fittings, see figure 6.3, some spectral differences are observed; however, as previously discussed in Chapter V, each additional line-shape added increases the complexity of the model meaning two-dimensional optimisation of such models is non-trivial. The blue emission at ca. 320 nm observed in the analytical standard, nanorods, microspheres, nanoflowers and ZnO-Au is assigned to the emission from the plastic well plate. Future studies should use a glass-bottomed well plate to avoid well plate fluorescence.

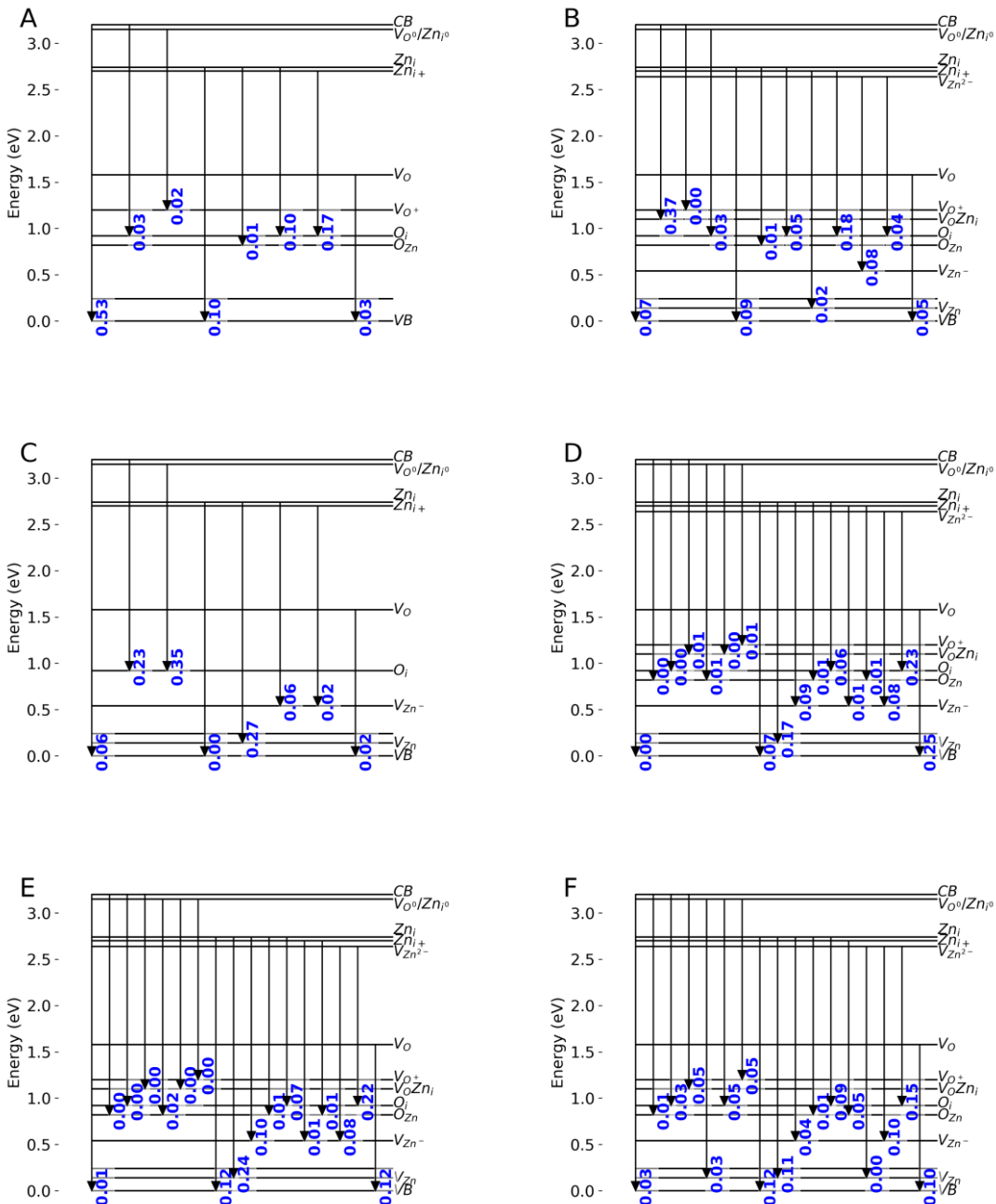


Figure 6.4 - Jablonski diagrams of the 0.5% PVA treated ZnO library explored generated from their respective fitted models with the percentile emission contribution for each transition. The letters denote: A) analytical standard, B) nanorods, C) microspheres, D) nanoplatelets, E) nanoflowers & F) ZnO-Au composite. The following symbol representation is adopted: CB denotes conduction band, VB denotes valence band,  $V_O$  &  $V_{Zn}$  represent vacancies for oxygen and zinc respectively,  $O_i$  &  $Zn_i$  represent interstitials for oxygen and zinc respectively,  $V_{O/Zn}^+$  represents a complex of an oxygen vacancy and zinc interstitial,  $V_{O/Zn}^0$  denotes a neutral oxygen vacancy or neutral zinc interstitial and  $O_{Zn}^0$  is an oxygen antisite. The signs present denote the charge of the defect, no sign or 0 means neutral and + or - denote a positive or negative charge respectively. All charges are single charges unless preceded by a number. This data is presented in a tabulated form in table A6.3.

The PVA treatment is reported to enhance the NBE emission in  $V_O$  trap dominated ZnOs meaning a decrease in 'green' emission should be observed.<sup>199</sup> Comparing the emissive

state topology of the studied ZnO library between the untreated and treated cases, see figure 6.1 and figure 6.3 respectively, there is a noticeable change in 2d spectral features for the analytical standard, nanorods and ZnO-Au with a reduction of 'green' emission around 510nm. The nanoflower sample shows slight variations between the treated and untreated states while the microspheres and nanoplatelets appear to be unaffected by the treatment. Jablonski diagrams were generated for the PVA treated library to facilitate the discussion of the underlying transitions which occur post treatment, see figure 6.4.

The untreated library discussed earlier, see figure 6.2, had two subsets of emissive transition behaviour where the analytical standard, nanorods and microspheres have 8 observable transitions while the nanoplatelets, nanoflowers and ZnO-Au have 16 observable transitions. For the PVA treated library, see figure 6.4, the peptide-mediated subset with 16 observable transitions is still observed; however, the nanorods sample now has 12 observable emissive transitions placing it into a new subset which is intermediate between the original two subsets. The new third subset of emissive transition behaviour observed in the nanorod sample is caused by the passivation of surface  $V_O$  defects affecting a preferred relaxation pathway,  $V_O \rightarrow VB$ , in the untreated sample which contributed to 11% to the total emission. Post PVA treatment the  $V_O \rightarrow VB$  transition total emission contribution decreased to 5%, this suggests that over half the  $V_O$  states observed in the  $V_O \rightarrow VB$  transition were at the surface with the remaining 5% of  $V_O$  states observed being located in the volume of the material.

The passivation of the  $V_O$  surface defects restricts relaxation cascades which require these surface  $V_O$  defects. This leads to previously unfavourable relaxation cascades being used for relaxation and new emissive transitions being observed. Four new transitions are observed for the PVA treated nanorod sample these are:  $CB \rightarrow V_{O(+)}$ ,  $V_O/Zn_i \rightarrow O_i$ ,  $Zn_i \rightarrow VB$  and  $Zn_{i(+)} \rightarrow V_{Zn}$ . In total these new transitions account for 14% of the total emission of the PVA treated nanorods.

The  $V_O \rightarrow VB$  transition contribution for the peptide mediated samples are 25, 12, 10% for the nanoplatelets, nanoflowers and ZnO-Au respectively. All these contributions have decreased by ca. 1-2% due to passivation of surface  $V_O$ . The  $V_O \rightarrow VB$  transition contribution for the remaining subset are 3 & 2% for the analytical standard and microspheres respectively. These values for the final subset are approximately the same as pre-treatment, suggesting that the  $V_O \rightarrow VB$  transition is generated from  $V_O$  located within the volume of the sample. However, while the differences in emission contribution of the  $V_O \rightarrow VB$  transition are negligible, comparison of the observed emissive transitions between the pre and post treated samples proves more interesting. Both the analytical

standard and nanoflowers have replaced emissive transitions: these are  $Zn_i \rightarrow V_{Zn}$  replaced by  $Zn_i \rightarrow VB$  for the analytical standard and  $Zn_{i(+)} \rightarrow O_i$  replaced by  $V_O/Zn_i \rightarrow V_O Zn_i$  for the nanoflowers. This suggests that the  $V_O$  defects residing at the surface of these samples were part of these replaced relaxation cascades in the untreated samples and when passivated alternate relaxation pathways were used. This implies that surface  $V_O$  defects play an important role in the relaxation cascades within the analytical standard, nanorod and nanoflower samples through non-observable transitions (i.e.  $V_{Zn} \rightarrow V_O$ ). While for the microspheres, nanoplatelets & ZnO-Au there were no changes in the observed emissive transitions suggesting the preferred relaxation cascades are not dependent on surface  $V_O$  for these materials. It is important to highlight the ‘new’ emissive states observed were previously present inside the matter but were unfavourable when the surface  $V_O$  defects were not passivated.

Both the  $V_O \rightarrow VB$  and  $V_{Zn(2-)} \rightarrow O_i$  transitions were dominant for the peptide mediated subset identified in the untreated samples. The emissive contribution of the  $V_{Zn(2-)} \rightarrow O_i$  transition is 23, 22 & 15% for the PVA treated nanoplatelets, nanoflowers and ZnO-Au materials respectively. The total emission contribution of this transition appears to alter negligibly between the pre and post-treatment states. This behaviour is consistent with the other samples showing no change from the untreated samples.

The PVA surface treatment is reported to increase NBE emission through passivation of the surface  $V_O$  defects.<sup>199</sup> When comparing the relative contributions of the near band edge (NBE) emission generated by the  $CB \rightarrow VB$  transition post PVA treatment, it is observed that the non-peptide mediated subset all still have band-gap exciton emission, which is centered at ca. 335 nm (3.7 eV); the relative contributions for the analytical standard, microspheres and nanorods being 53, 6 & 7% respectively. Both the analytical standard and nanorods see an increase in NBE emission while the microspheres remain approximately the same. As previously discussed the microsphere sample is dominated by two transitions (23%  $CB \rightarrow O_i$  and 35%  $V_O/Zn_i \rightarrow O_i$ ) which are both related to  $O_i$  defects. The emission contribution of these transitions has varied slightly when comparing pre and post treatment contributions. However, the differences are negligible which was expected as  $O_i$  defects are attributed to the volume while the surface treatment used solely works on states attributed to the surface.

For the peptide mediated subset the NBE emission remains below 1% for both the nanoplatelets post-PVA treatment while the nanoflowers and ZnO-Au composite have increased NBE emissions of 1 & 3% respectively. Post-PVA treatment the ZnO-Au composite still does not appear to have a preferred or dominant emission.

The Zn interstitial ( $Zn_i$ ) defect state still appears in every sample studied post PVA treatment and is usually attributed to the volume of ZnO structures.<sup>313,314</sup> The transitions which relax from this state account for 39, 36, 36, 42, 55 & 42% of total overall emissions for the analytical standard, microspheres, nanorods, nanoplatelets, nanoflowers & ZnO-Au respectively. The overall trend for these emissive transitions is a decrease in total emission contribution post PVA treatment, this is likely due to the alternative competing relaxation cascades when the preferred cascade requiring surface  $V_O$  is passivated.

As reported in the original literature the 0.5% PVA surface treatment is an effective method to reduce emissions relating to surface based  $V_O$ ;<sup>199</sup> however, the impact of passivating surface  $V_O$  defect states on the overall emissive state topology is difficult to predict. While an increase in NBE emission was observed for both the analytical standard and nanorods, there were other unexpected changes such as 4 new transitions in the nanorod sample and the  $Zn_i \rightarrow V_{Zn}$  transition replaced by  $Zn_i \rightarrow VB$  for the analytical standard. To effectively use this surface treatment on ZnO used for a device, such as a low voltage luminescence flat panel display,<sup>129,135</sup> the behaviour pre and post treatment of the given ZnO must be studied as this is not a ‘one case fits all’ type of treatment and is dependent on both the observable and unobservable transitions which surface  $V_O$  is involved in.

The other surface treatment explored in this study is 1M NaBH<sub>4</sub> which introduces surface based  $V_O$  defects to the sample,<sup>200</sup> the effect of this treatment is the antithesis of the 0.5% PVA treatment previously discussed. The 2DFMs of the 1M NaBH<sub>4</sub> treated samples, see figure 6.5, were fitted using the approach outlined in Chapter V using the known transitions in table 6.3 as the required “hints”. The method successfully fitted all the samples with adjusted-R<sup>2</sup> (adj-R<sup>2</sup>) values of 0.93 or greater with all the line shapes used remaining physically relevant. When comparing the 2DFMs to the fittings, see figure 6.5, some spectral differences are observed; however, as previously discussed in Chapter V, each additional line-shape added increases the complexity of the model meaning two-dimensional optimisation of such models is non-trivial. The blue emission at ca. 320 nm observed in the nanorods, microspheres and ZnO-Au is assigned to the emission from the plastic well plate. Future studies should use a glass-bottomed well plate to avoid well plate fluorescence.

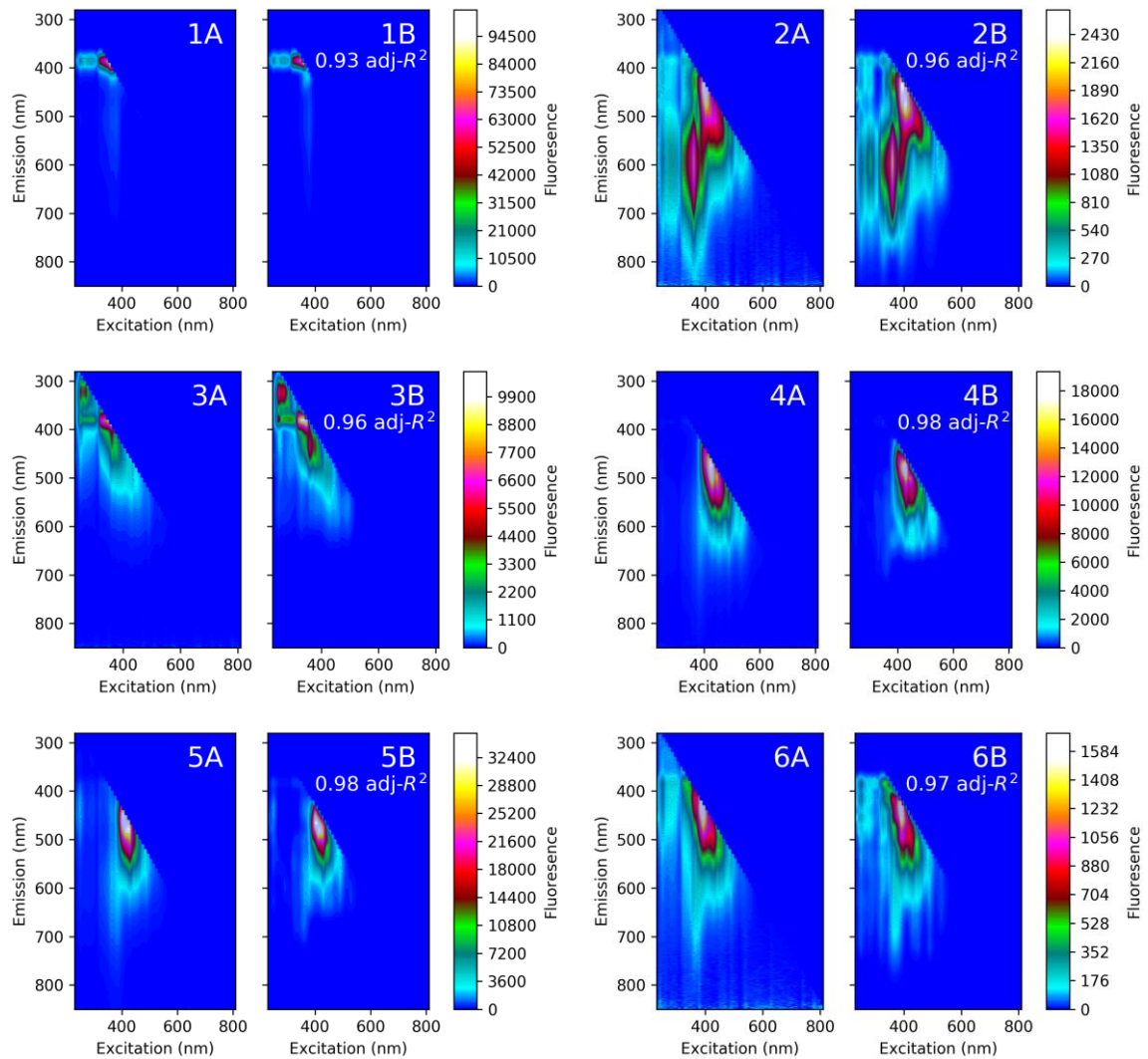


Figure 6.5 - 2DFMs of the 1M NaBH<sub>4</sub> treated ZnO library explored and their respective fits with the adj-R<sup>2</sup> value reported. Where: 'A' denotes the experimental data and 'B' denotes the proposed model. The numbers denote: 1) analytical standard, 2) nanorods, 3) microspheres, 4) nanoplatelets, 5) nanoflowers & 6) ZnO-Au composite. The colorbar bar shown on the right of each figure is for the experimental data plot 'A' and is representative of the colorbar of plot 'B'. This omission was chosen for layout reasons.

The 1M NaBH<sub>4</sub> treatment is reported to increase the number of V<sub>O</sub> surface trap states in ZnOs meaning an increase in 'green' emission should be observed.<sup>200</sup> Comparing the emissive state topology of the studied ZnO library between the untreated and treated cases, see figure 6.1 and figure 6.5 respectively, there is a noticeable change for whole library post treatment where emission is observed at lower excitation wavelength. However, while there are some notable differences with the 2D-spectral features being blue-shifted with respect to the excitation axis, the overall topology appears to only vary slightly between pre and post treatment. Jablonski diagrams were generated for the NaBH<sub>4</sub> treated library to facilitate the discussion of the underlying transitions which occur post treatment, see figure 6.6.

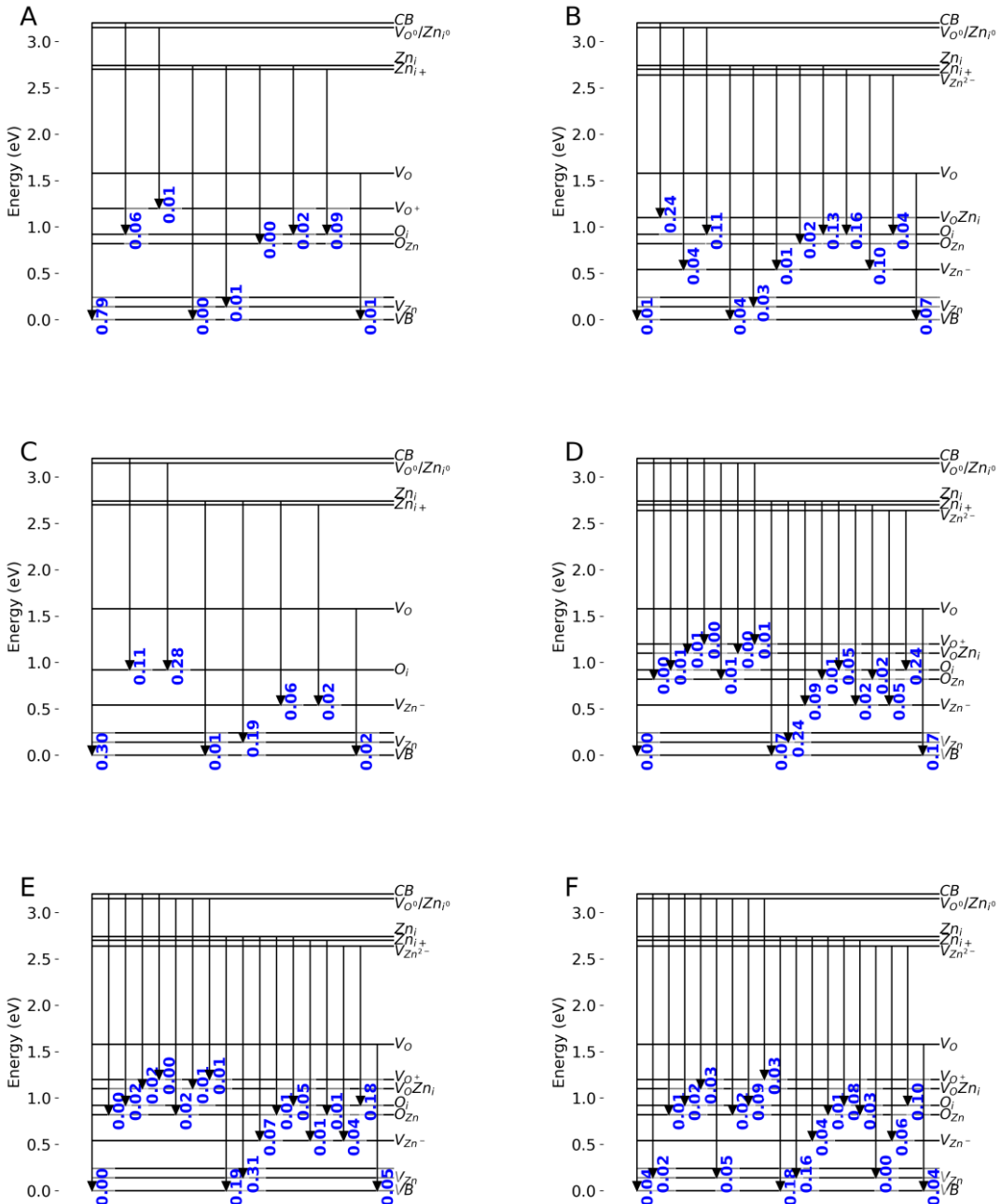


Figure 6.6 - Jablonski diagrams of the 1M NaBH<sub>4</sub> treated ZnO library explored generated from their respective fitted models with the percentile emission contribution for each transition. The letters denote: A) analytical standard, B) nanorods, C) microspheres, D) nanoplatelets, E) nanoflowers & F) ZnO-Au composite. The following symbol representation is adopted: CB denotes conduction band, VB denotes valence band, V<sub>O</sub> & V<sub>Zn</sub> represent vacancies for oxygen and zinc respectively, O<sub>i</sub> & Zn<sub>i</sub> represent interstitials for oxygen and zinc respectively, V<sub>OZni</sub> represents a complex of an oxygen vacancy and zinc interstitial, V<sub>O<sup>0</sup>Zn<sub>i<sup>0</sup></sub></sub> denotes a neutral oxygen vacancy or neutral zinc interstitial and O<sub>Zn</sub> is an oxygen antisite. The signs present denote the charge of the defect, no sign or 0 means neutral and + or - denote a positive or negative charge respectively. All charges are single charges unless preceded by a number. This data is presented in a tabulated form in table A6.4.

The untreated library discussed earlier, see figure 6.2, had two subsets of emissive transition behaviour where the analytical standard, nanorods and microspheres have 8 observable transitions while the nanoplatelets, nanoflowers and ZnO-Au have 16

observable transitions. The PVA treated library, see figure 6.4, has 3 subsets of emissive transition behaviour with the nanorods forming a new 12 transition subset. For the NaBH<sub>4</sub> treated library, see figure 6.6, the peptide-mediated subset has 18 observable transitions and is still observed for the nanoplatelets and nanoflowers with 19 observable transitions for the ZnO-Au sample. The nanorod sample has 13 observable emissions while the analytical standard and microspheres subset have 9 and 8 observable emissions respectively. The subset behaviour observed for the PVA treatment still applies here and it appears that the peptide-mediated samples still behave similarly in both treatment conditions. The nanorods form the third subset which is consistent with the PVA treatment and this is due to the large (1010) facet present in these nanocrystals due to preferred growth along the c-axis.<sup>94</sup> The (1010) facet has a mixed terminated surface formed of Zn<sup>2+</sup> and O<sup>2-</sup>; the author proposes that this surface is susceptible to V<sub>O</sub> defect formation. Post NaBH<sub>4</sub> treatment the V<sub>O</sub> → VB transition total emission contribution changes negligibly to 10%; however, additional V<sub>O</sub> defects on the surface of the sample appear to make alternate relaxation pathways accessible including V<sub>O</sub>/Zn<sub>i</sub> → V<sub>Zn(-)</sub>, V<sub>O</sub>/Zn<sub>i</sub> → O<sub>i</sub>, Zn<sub>i</sub> → VB, Zn<sub>i</sub> → V<sub>Zn</sub> and Zn<sub>i</sub> → V<sub>Zn(-)</sub>. Quantitative discussion on defect concentration and the subsequent relaxation cascades is beyond the scope of this technique and study. This would, however, prove an interesting follow up investigation.

The V<sub>O</sub> → VB transition contribution was one of two dominant transitions in the peptide mediated subset, post-NaBH<sub>4</sub> treatment the emission contribution was 17, 5, 4% for the nanoplatelets, nanoflowers and ZnO-Au respectively. All these contributions have decreased by at least 5%, though this is unexpected due to NaBH<sub>4</sub> treatment creating more surface V<sub>O</sub> defects. The behaviour suggests that the surface V<sub>O</sub> defects are key for unlocking alternate relaxation pathways within these materials. Both the nanoplatelet and nanoflower samples have a new transition which is CB → V<sub>O(+)</sub> transition, where electrons are relaxing from the conduction band to the newly formed V<sub>O(+)</sub> defects located at the surface. The nanoflower sample also has one relaxation pathway replaced where Zn<sub>i(+)</sub> → O<sub>i</sub> was replaced by V<sub>O</sub>/Zn<sub>i</sub> → V<sub>O</sub>Zn<sub>i</sub>, this is likely due to the V<sub>O</sub>Zn<sub>i</sub> cascade being preferred when more V<sub>O</sub> defects are present. The final member of the peptide mediated subset ZnO-Au has two new emissive transitions, these are CB → V<sub>Zn</sub> and V<sub>O</sub>Zn<sub>i</sub> → O<sub>Zn</sub>. Similarly to the nanorods case, while none of these are an emissive transition to the surface V<sub>O</sub> states the new defects play an important role in these cascades.

Comparing the V<sub>O</sub> → VB transition for the remaining subset shows a total emission contribution of 1 and 2% for the analytical standard and microspheres respectively. These changes again are negligible between pre and post treatment with the treatment not introducing any new transitions for the microsphere sample. However, the analytical

standard has a new transition  $Zn_i \rightarrow VB$ , which, as previously discussed, is part of a relaxation cascade involving  $V_o$  defects. An important differentiation between the observations made for the PVA treatment compared to the  $NaBH_4$  treatment is while states such as  $O_i$  existed in the sample pretreatment and were unfavourable transitions, the  $V_o$  concentration between pre and post  $NaBH_4$  treatment conditions are different due to the  $NaBH_4$  creating new  $V_o$  defects.

Both the  $V_o \rightarrow VB$  and  $V_{Zn(2-)} \rightarrow O_i$  transitions were dominant for the peptide mediated subset identified in the untreated samples. The emissive contribution of the  $V_{Zn(2-)} \rightarrow O_i$  transition is 24, 18 & 10% for the PVA treated nanoplatelets, nanoflowers and ZnO-Au materials respectively. The total emission contribution of this transition appears to alter slightly between the pre and post-treatment states with the ZnO-Au sample showing the greatest change of 5%. No change is observed in the other samples when comparing between the pre and post treated states.

Comparing the relative contributions of the near band edge (NBE) emission generated by the  $CB \rightarrow VB$  transition post  $NaBH_4$  treatment, it is observed that the non-peptide mediated subset still all have band-gap exciton emissions centered at ca. 335 nm (3.7 eV), where the relative contributions for the analytical standard, microspheres and nanorods are 80, 30 & 1% respectively. Both the analytical standard and microspheres see an increase in NBE emission while the nanorods show a reduced emission. As previously discussed the untreated microspheres sample was dominated by two transitions which are  $CB \rightarrow O_i$  and  $V_o/Zn_i \rightarrow O_i$  with total emission contributions of 11 and 28% respectively. The emission contribution of the  $CB \rightarrow O_i$  has halved post treatment while the  $V_o/Zn_i \rightarrow O_i$  transition has decreased slightly when comparing pre and post treatment contributions. It would appear that the  $CB \rightarrow O_i$  is now less favoured compared to other transitions due to the increased  $V_o$  concentration.

For the peptide mediated subset the NBE emission remains below 1% for both the nanoplatelets and nanoflowers while the ZnO-Au composite has increased NBE emissions of 4%. Post- $NaBH_4$  treatment the ZnO-Au composite appears to prefer  $Zn_i \rightarrow V_{Zn}$  and  $Zn_i \rightarrow V_{Zn(-)}$  transitions post treatment although there is still no dominant transition.

The Zn interstitial ( $Zn_i$ ) defect state still appears in every sample studied post PVA treatment and is usually attributed to the volume of ZnO structures.<sup>313,314</sup> The transitions which relax from this state accounts for 13, 28, 39, 49, 65 & 50% of total overall emissions for the analytical standard, microspheres, nanorods, nanoplatelets, nanoflowers & ZnO-Au respectively. Both the analytical standard and microspheres show a decrease in the

total emission contribution from these states, this may be due to the CB  $\rightarrow$  VB transition being a competing relaxation pathway which is more favourable post treatment. The rest of the samples show an increase in emission from these states.

The 1M NaBH<sub>4</sub> surface treatment is an effective method to increase NBE emission for both the analytical standard and microspheres which are both microscale samples. However, this behaviour is not observed in the nanoscale samples, this may be a surface area to volume effect. The NaBH<sub>4</sub> treatment appears to be successful at reducing the emission from the V<sub>O</sub>  $\rightarrow$  VB transition; however, it was observed that increased V<sub>O</sub> defect concentrations were required to make some transitions preferred, i.e. the 5 new transitions in the nanorods V<sub>O/Zn<sub>i</sub></sub>  $\rightarrow$  V<sub>Zn(-)</sub>, V<sub>O/Zn<sub>i</sub></sub>  $\rightarrow$  O<sub>i</sub>, Zn<sub>i</sub>  $\rightarrow$  VB, Zn<sub>i</sub>  $\rightarrow$  V<sub>Zn</sub> and Zn<sub>i</sub>  $\rightarrow$  V<sub>Zn(-)</sub>. Similar to the PVA surface treatment this is not a ‘one case fits all’ treatment and to effectively use it the effects on the selected ZnO sample must be studied as two systems can behave very differently. The results of this treatment like the PVA treatment is dependent on both the observable and unobservable transitions which surface V<sub>O</sub> is involved in.

Using a library of ZnOs the resolving power of the 2DFM technique has been showcased again, with the fitted 2D-line-shapes used to determine a Jablonski diagram for the transitions occurring within the samples. Through studying the Jablonski diagrams of the untreated sample it became clear that synthesis conditions strongly affect the defect concentrations within the synthesised matter. An excellent example of this is the peptide mediated subset, where the emission behaviours of all 3 samples synthesised using peptides had the same dominant transitions and number of emissions. Upon applying a surface treatment to these samples, either NaBH<sub>4</sub> or PVA, the same trend in behaviour was observed across all 3 samples supporting the theory that the synthesis conditions are of vital importance. The 2DFM technique is sensitive to the synthetic conditions therefore future studies could explore different synthetic routes with a goal to develop a systematic understanding of the interplay between synthetic conditions and defect population.

The efficacy of the two surface treatments used is highly sample dependent, while 0.5% PVA does passivate surface V<sub>O</sub> and 1M NaBH<sub>4</sub> introduces new V<sub>O</sub> surface defects the overall effect on a given sample is hard to predict due to the complex interplay between states. To effectively use either treatment, pre and post treatment 2DFMs would have to be collected for the sample and the differences in the desired transition compared. If the intended outcome is to increase NBE for the analytical standard or microspheres, the NaBH<sub>4</sub> treatment is superior causing a dramatic increase in NBE emission while for nanorods the PVA treatment is more effective.

When discussing the emissive contribution of different states it would be useful to convert these values to a quantum yield (QY) for each transition. This would allow for easier comparison of this data with future studies which may use different spectrometers or have a different experimental setup. However, the Tecan i-control M200 Pro plate reader is not equipped with a photon counting detector and/or an integrating sphere meaning direct determination of quantum yield is not possible. To overcome this limitation the relative quantum yield was determined against a rhodamine 6G<sup>316</sup> to attempt to approach a first approximation of the quantum yield values. The determination of relative quantum yield is addressed in section 6.4.2 below.

#### 6.4.2 First Approximation of the Quantum Yield of ZnO 2DFM Emissive Transitions

As a first approximation of the quantum yield (QY) of the emissive transitions in ZnOs determined through the 2DFM technique, the relative QY of each emission was determined. Calculation of the relative QY, equation 6.1, requires a reference material with known QY. For this study, rhodamine 6G (R6G) was selected as its fluorescence behaviour is well documented.<sup>317-319</sup>

$$Q_s = Q_r \left( \frac{A_r}{A_s} \right) \left( \frac{E_s}{E_r} \right) \quad 6.1$$

Equation 6.1 is the equation used to determine relative QY where s & r represent sample and reference respectively, Q is the QY, A is the absorbance at a given wavelength and E is the integral of the emission per mol. To calculate a first approximation of the relative QY of the states inside the samples several assumptions are made:

1. The emission intensity of maxima of R6G is consistent regardless of where it is excited, as it is in the molecular regime.<sup>169</sup>
2. Taking the integral of the one dimensional emission along the emission axis at the x-center of the gaussian will yield a representative emission intensity for that state.
3. Absorbance values for ZnO samples will be approximately equal at 515nm.
4. The absorbance and QY of R6G dye in the aqueous and solid states are comparable under infinite dilution where only monomers of dye are fluorescing.

For the calculation of Q<sub>s</sub> (the quantum yield of the sample), the parameters for the R6G reference material must be obtained; however, though widely studied, to the knowledge of the author no reports exist on the QY of R6G in air. Therefore, as previously stated we will assume the QY of R6G dye in the solid state is equal to that of the aqueous solution when the dye is infinitely diluted leaving just monomer fluorescence. Using the same plate reader configuration as used to obtain the ZnO 2DFM datasets, fluorescence data was collected for R6G in the aqueous state performing serial dilutions until the emission peak

was within detection range, see figure 6.7A. The final R6G<sub>(aq)</sub> concentration after dilution was 0.69 μM, this dye solution concentration was also used to collect the A<sub>515nm</sub> value for this sample which was 0.1357.

Fluorescence spectra were collected for the R6G<sub>(s)</sub> sample where solid state “dilutions” were performed by mixing the R6G dye with spectroscopic grade KBr, which does not absorb or fluoresce in the range of interest. Initial concentrations (14.8 - 30 μmol·g<sup>-1</sup>) of R6G<sub>(s)</sub> show signature J-aggregate characteristics<sup>320,321</sup> where the emission of the R6G has been red shifted, see figure 6.7B, likely due to head to tail packing of dye molecules.<sup>322</sup> Further ‘dilution’ results in the destruction of the J-aggregates and the molecular emission behaviour of R6G is observed when the concentration is at 14.8 nmol·g<sup>-1</sup>.

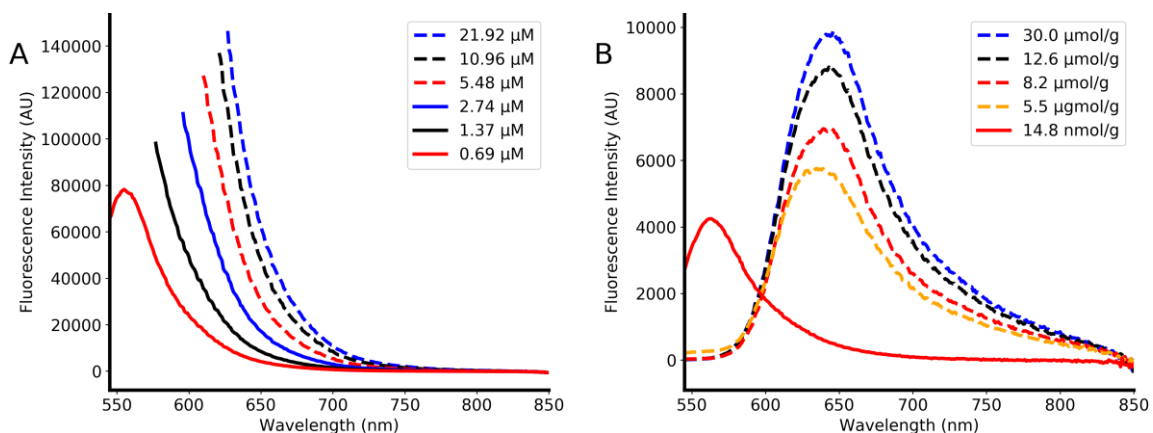


Figure 6.7 - One-dimensional fluorescence spectra for rhodamine 6G fluorescent dye. A) Fluorescence spectra for different concentrations of aqueous rhodamine 6G. B) Fluorescence spectra for different concentrations of rhodamine 6G in the solid state “diluted” in spectroscopic grade KBr.

While the fluorescence maxima differs, with maximal intensity values being 78246 and 4248 for the aqueous and solid state R6G respectively, between the two dye samples this is suggested to be attributed to the number of emissive dye molecules present as in the solid state only the molecules at the surface will be detected.

After obtaining the E<sub>R</sub> and A<sub>R</sub> (integral of the emission per mole and absorbance respectively for the reference) values the samples' A<sub>S</sub> and E<sub>S</sub> (integral of the emission per mole and absorbance respectively for the sample) values must be obtained using the value of 0.004184711 for A<sub>S</sub>, determined from UV-vis spectroscopy of the analytical standard in good agreement with literature data.<sup>323</sup> The individual 2D-line-shapes which form the modelled emissive state topology were represented as 1D-line-shapes at the excitation center (x<sub>c</sub>). The definite integral for each 1D-representation was collected with the lower and upper limit being x<sub>c</sub>+30 and 850nm respectively, this range is equivalent to the 1D-spectra collected on the plate reader. Using the assigned transitions of the 2D-

line-shapes, see figure 6.2, the first approximation of QY contribution of each state can be determined, as shown in figure 6.8.

The discussion on the determined QY values, see figure 6.8, focuses on the NBE emission and the dominant emissive state for each sample. However, the discussion will not address the individual transitions for each material as this was covered previously in section 6.4.1. Comparing the QY of the NBE emission the values are: 1.5e-3, 1.5e-5, 1.8e-3, 7.3e-3, 1.0e-5, 4.8e-6 for the analytical standard, nanorods, microspheres, nanoplatelets, nanoflowers and ZnO-Au respectively. The microspheres were observed to have the highest yield with a value 3e-4 greater than the analytical standard. This was unexpected as the NBE emission is very dominant in the emissive state topology of the analytical standard, while the CB  $\rightarrow$  O<sub>i</sub> and V<sub>O/Zn</sub>  $\rightarrow$  O<sub>i</sub> were the dominant transitions for the microspheres with a QY of 6.5e-3 each. The highest QY value was 2.3e-4 for the nanorod sample was for the Zn<sub>i(+)</sub>  $\rightarrow$  O<sub>i</sub> a transition which accounts for 26% of the total emission. These findings are in good agreement with the observations made in section 6.4.1 suggesting this approximation is representative of the true QY values for this system.

The dominant transition for the peptide mediated subset was the V<sub>Zn(2-)</sub>  $\rightarrow$  O<sub>i</sub> transition, this is reflected in the QY values obtained which were: 2.0e-3, 6.9e-3 and 2.4e-5 for the nanoplatelets, nanoflowers and ZnO-Au nanocomposite respectively which were the highest values for relative QY for these samples. The QY of the ZnO-Au sample is far lower than the other two peptide mediated samples with all QY values for each transition being in the 1e-5 or 1e-6 range. These low values may be caused by the discrete gold inclusions having a ‘parasitic’ effect on the ZnO fluorescence. The determined values for QY of these materials is well below a useful value for lasing applications. For comparison R6G can be used as a lasing material in dye lasers<sup>324</sup> and has a QY of 0.9-0.98 depending on the solvent system the dye is dissolved in.<sup>317</sup>

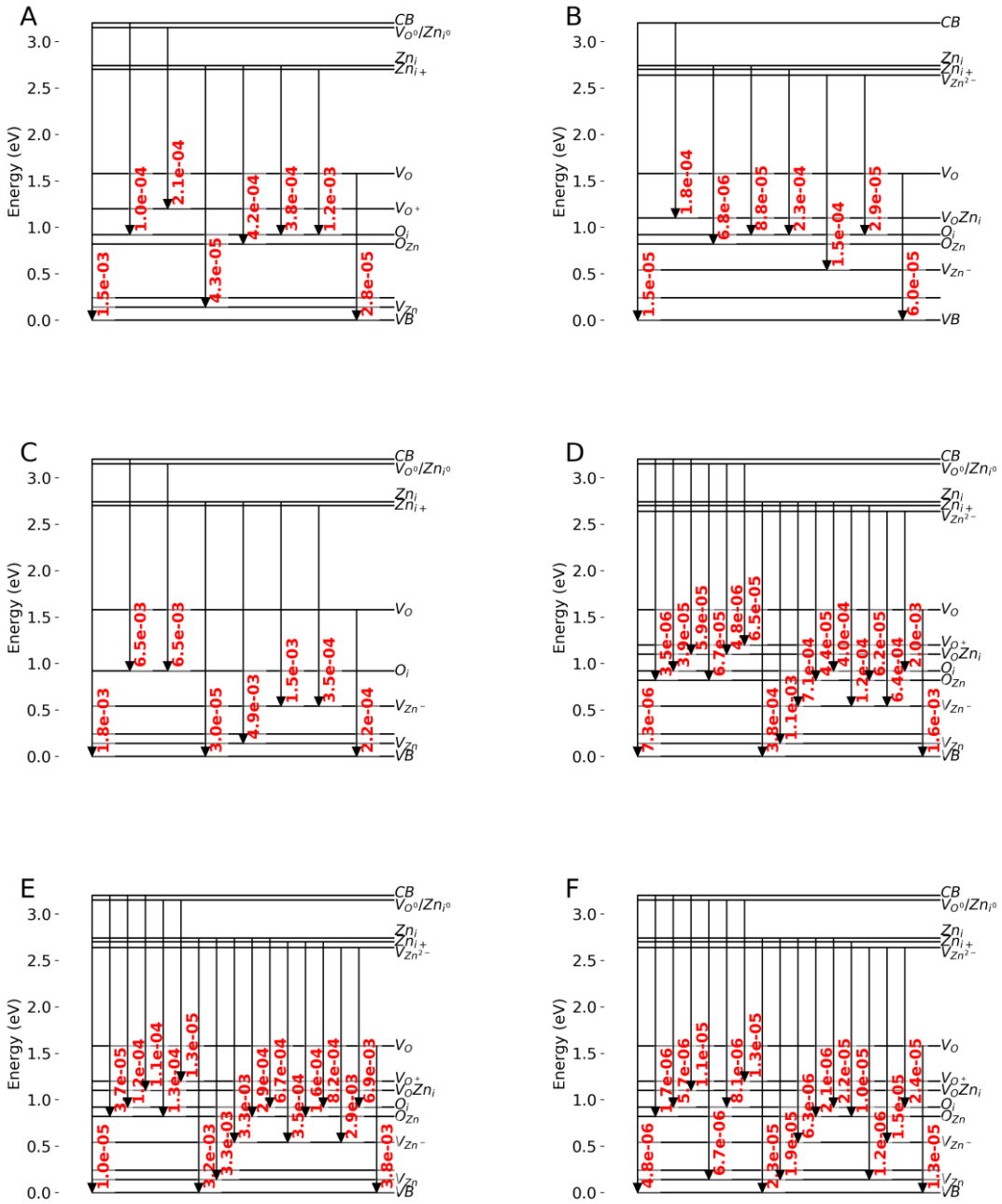


Figure 6.8 - Jablonski diagrams of the ZnO library explored generated from their respective fitted models with the relative quantum yield for each transition. The letters denote: A) analytical standard, B) nanorods, C) microspheres, D) nanoplatelets, E) nanoflowers & F) ZnO-Au composite. The following symbol representation is adopted: CB denotes conduction band, VB denotes valence band,  $V_O$  &  $V_{Zn}$  represent vacancies for oxygen and zinc respectively,  $O_i$  &  $Zn_i$  represent interstitials for oxygen and zinc respectively,  $V_{O^+}Zn_i$  represents a complex of an oxygen vacancy and zinc interstitial,  $V_{O^0}/Zn_{i^0}$  denotes a neutral oxygen vacancy or neutral zinc interstitial and  $O_{Zn}^-$  is an oxygen antisite. The signs present denote the charge of the defect, no sign or 0 means neutral and + or - denote a positive or negative charge respectively. All charges are single charges unless preceded by a number. This data is presented in a tabulated form in table A6.5.

Using the first approximation of the QY for each emissive transition the effect of two studied surface treatments, 0.5% PVA<sup>199</sup> and 1M NaBH<sub>4</sub>,<sup>200</sup> can be investigated to

determine if the QY of the NBE emission has been increased or if the surface coatings have reduced the QY of other transitions, see figure 6.9 and figure 6.10 for the PVA and NaBH<sub>4</sub> treatments respectively.

First focusing on the 0.5% PVA surface coating passivates surface V<sub>O</sub> defect states and is reported to increase NBE emission.<sup>199</sup> As previously discussed in section 6.4.1, while an increase in NBE emission was observed for both the analytical standard and nanorods, there were other unexpected changes such as 4 new transitions in the nanorod sample and the Zn<sub>i</sub> -> V<sub>Zn</sub> transition replaced by Zn<sub>i</sub> ->VB for the analytical standard. This is indicative that the impact of a given surface treatment on the overall emissive state topology is difficult to predict.

Comparing the determined QYs for the 0.5% PVA treated library, see figure 6.9, an increase in NBE emission is observed for all samples. The values are: 5.0e-3, 1.1e-4, 5.8e-3, 9.3e-6, 5.7e-5 and 5.2e-6 for the analytical standard, nanorods, microspheres, nanoplatelets, nanoflowers and ZnO-Au respectively. Similarly to the untreated samples the microsphere sample has the highest overall quantum yield for the NBE emission. However, as discussed for the previous sample the NBE emission is not the dominant state for the microspheres, instead the CB -> O<sub>i</sub> and V<sub>O/Zn<sub>i</sub></sub> -> O<sub>i</sub> were the dominant transitions for the microspheres with a QY of 1.2e-2 and 1.6e-2 respectively. The highest QY value was 1.2e-4 for the nanorod sample for the CB -> V<sub>O/Zn<sub>i</sub></sub>, while the Zn<sub>i(+)</sub> -> O<sub>i</sub> which was the dominant transition pretreatment has a QY of 5.0e-5. The difference in the QY for the Zn<sub>i(+)</sub> -> O<sub>i</sub> transition pre and post PVA treatment is in agreement with the percentile contribution differences observed where the contribution decreases from 26% to 18% of the total overall emission. This suggests that the PVA treatment is enhancing the NBE emission and not simply quenching emission from the surface V<sub>O</sub> defects.

The dominant transition for the peptide mediated subset was the V<sub>Zn(2-)</sub> -> O<sub>i</sub> transition, this is reflected in the QY values obtained which were: 2.1e-3, 2.1e-3 and 2.3e-5 for the nanoplatelets, nanoflowers and ZnO-Au nanocomposite respectively, which were the highest values for relative QY for these samples. Post-treatment the QY of the ZnO-Au sample remains far lower than the other two peptide mediated samples with all QY values for each transition being in the 1e-5 or 1e-6 range. This is to be expected as the discrete gold inclusions are located within the volume of the sample and if they are having a 'parasitic' effect on the ZnO fluorescence, the PVA treatment would not affect them.

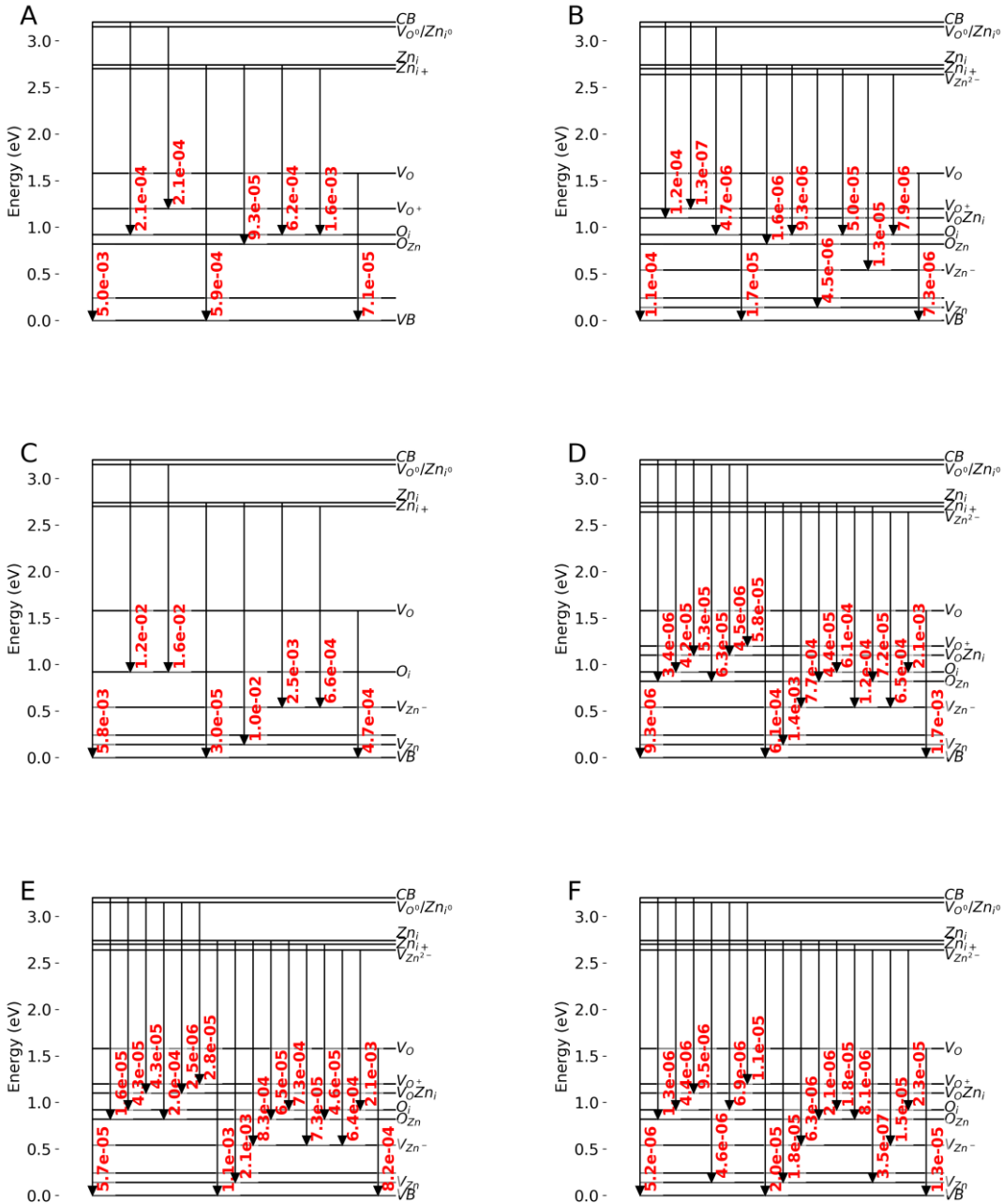


Figure 6.9 - Jablonski diagrams of the 0.5% PVA treated ZnO library explored generated from their respective fitted models with the relative quantum yield for each transition. The letters denote: A) analytical standard, B) nanorods, C) microspheres, D) nanoplatelets, E) nanoflowers & F) ZnO-Au composite. The following symbol representation is adopted: CB denotes conduction band, VB denotes valence band,  $V_O$  &  $V_{Zn}$  represent vacancies for oxygen and zinc respectively,  $O_i$  &  $Zn_i$  represent interstitials for oxygen and zinc respectively,  $V_{O/Zn_i}$  represents a complex of an oxygen vacancy and zinc interstitial,  $V_{O^0/Zn_{i^0}}$  denotes a neutral oxygen vacancy or neutral zinc interstitial and  $O_{Zn}$  is an oxygen antisite. The signs present denote the charge of the defect, no sign or 0 means neutral and + or - denote a positive or negative charge respectively. All charges are single charges unless preceded by a number. This data is presented in a tabulated form in table A6.6.

The second surface treatment explored was 1M NaBH<sub>4</sub>, see figure 6.10, which is reported to increase V<sub>O</sub> defects at the surface of ZnO.<sup>200</sup> As previously discussed in section 6.4.1, an increase in NBE emission for both the microscale samples, analytical standard and microspheres was observed. However, this behaviour was not observed in the nanoscale sample which may have been due to the surface to volume ratio of these samples. The NaBH<sub>4</sub> treatment appears to be successful at reducing the emission from the V<sub>O</sub> → VB transition; however, it was observed that increased V<sub>O</sub> defect concentrations were required to make some transitions preferred i.e. the 5 new transitions in the nanorods V<sub>O/Zn<sub>i</sub></sub> → V<sub>Zn(-)</sub>, V<sub>O/Zn<sub>i</sub></sub> → O<sub>i</sub>, Zn<sub>i</sub> → VB, Zn<sub>i</sub> → V<sub>Zn</sub> and Zn<sub>i</sub> → V<sub>Zn(-)</sub>. Similarly to the PVA treatment this is indicative that the impact of a given surface treatment on the overall emissive state topology is difficult to predict.

Comparing the determined QYs for the 1M NaBH<sub>4</sub> treated library, see figure 6.10, an increase in NBE emission is observed for all samples. The values are: 2.0e-2, 6.8e-6, 4.3e-3, 8.9e-6, 2.1e-5 and 1.2e-5 for the analytical standard, nanorods, microspheres, nanoplatelets, nanoflowers and ZnO-Au respectively. The analytical standard has the highest QY from the NBE emission out of all the samples both in the NaBH<sub>4</sub> treated library and other two libraries (untreated and PVA treated). The dominant transitions in the untreated microsphere samples were CB → O<sub>i</sub> and V<sub>O/Zn<sub>i</sub></sub> → O<sub>i</sub> with a QY of 9.9e-4 and 2.1e-3 respectively. These values have both decreased when compared to both the untreated and PVA treated samples suggesting the large increase in NBE for the NaBH<sub>4</sub> treated microspheres is due to a reduction in dominant state emission and in turn a lower overall quantum yield. The highest QY value was 2.2e-4 for the nanorod sample for the CB → V<sub>O/Zn<sub>i</sub></sub>, while the Zn<sub>i(+)</sub> → O<sub>i</sub>, which was the dominant transition pretreatment, has a QY of 6.7e-5. The differences observed are similar to those observed for the PVA treatment difference in the QY for the Zn<sub>i(+)</sub> → O<sub>i</sub> transition pre and post PVA treatment. Similarly to the PVA treatment the observed change is in agreement with the percentile contribution differences observed where the contribution decreases from 26% to 16% of the total overall emission. The observed changes suggest that the NaBH<sub>4</sub> does enhance the NBE emission in a similar process to the PVA treatment. However, the introduction of V<sub>O</sub> surface defects appears to passivate other dominant emissions in the treated matter, therefore the percentile contribution of the NBE emission may be greater as the overall emission intensity of the sample is reduced.

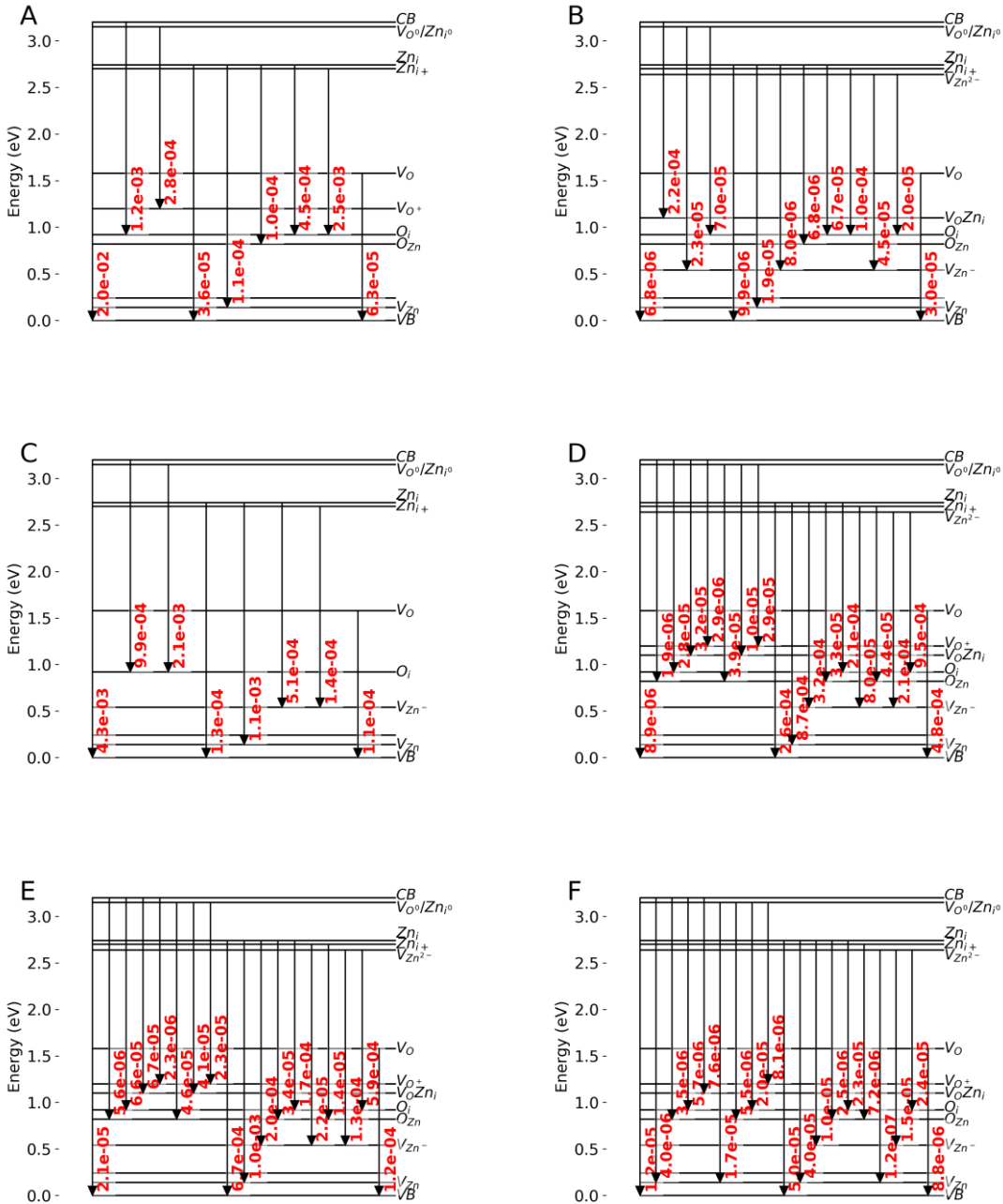


Figure 6.10 - Jablonski diagrams of the 1M NaBH<sub>4</sub> treated ZnO library explored generated from their respective fitted models with the relative quantum yield for each transition. The letters denote: A) analytical standard, B) nanorods, C) microspheres, D) nanoplatelets, E) nanoflowers & F) ZnO-Au composite. The following symbol representation is adopted: CB denotes conduction band, VB denotes valence band, VO & V<sub>Zn</sub> represent vacancies for oxygen and zinc respectively, O<sub>i</sub> & Zni represent interstitials for oxygen and zinc respectively, VO/Zni<sub>0</sub> represents a complex of an oxygen vacancy and zinc interstitial, VO/Zni<sub>0</sub> denotes a neutral oxygen vacancy or neutral zinc interstitial and O<sub>Zn</sub> is an oxygen antisite. The signs present denote the charge of the defect, no sign or 0 means neutral and + or - denote a positive or negative charge respectively. All charges are single charges unless preceded by a number. This data is presented in a tabulated form in table A6.7.

The dominant transition for the untreated peptide mediated subset was the  $V_{Zn(2-)} \rightarrow O_i$  transition, a decrease in the QY for this transition was observed for both the nanoplatelets and nanoflower samples with a QY of 9.5e-4 and 5.9e-4 respectively. The  $V_{Zn(2-)} \rightarrow O_i$  transition remains the dominant transition for the nanoplatelets while the  $Zn_i \rightarrow V_{Zn}$  is now the dominant transition for the nanoflowers with a QY of 1e-3. While both the other two samples in the peptide mediated subset have shown a decrease in the QY for the  $V_{Zn(2-)} \rightarrow O_i$  transition there is no change in the QY for the ZnO-Au sample post treatment. However, the dominant transition is now  $Zn_i \rightarrow VB$  with a QY of 5e-5, the similarity in the dominant transitions for the treated nanoflowers and ZnO-Au sample can be explained by the similarity in synthetic route. It appears that the nanoflower matter which does not have discrete gold inclusions may have a greater population of  $V_{Zn}$  states when compared to the ZnO-Au sample. However, this is purely speculative as the concentrations of defect states can not be quantified using this method.

Using the R6G fluorescent dye a first approximation of the QY was determined using the relative quantum yield approach for the three libraries studied. This technique appears to be a robust method to approximate the QY of different emissive states and has good agreement with the percentile emission findings. However, there are potential cases such as CdSe investigated in Chapter V where the current approach would not be suitable as assumption 2 requires the y-width ( $\sigma_y$ )  $\gg$  x-width ( $\sigma_x$ ). In the case of CdSe  $\sigma_y \ll \sigma_x$  for the NBE emission which dominates the collected 2DFM meaning the approximation of QY will be very inaccurate.

Future experimental work should collect a 2DFM for the R6G dye in both the liquid state (0.69  $\mu M$ ) and solid state (14.8  $nmol \cdot g^{-1}$ ), it would be expected to see diagonalisation in the emissive topology for both the liquid and solid R6G 2DFM, due to the R6G behaving like a molecular system.<sup>169,202</sup> The emissive states within the 2DFM for the liquid and solid R6G 2DFM should be fitted using the same approach used for the semiconductors studied in both Chapter V and Chapter VI, this will allow for deconvolution of the diagonalised spectral response of R6G. The deconvolved line-shapes can then be integrated to obtain the emission of the 2D-line-shape which will be the value for  $E_R$ . Likewise, integrals for the 2D-line-shapes for the transitions can be obtained and used as the  $E_S$  values. Using this approach would overcome the error introduced when the y-width ( $\sigma_y$ )  $\gg$  x-width ( $\sigma_x$ ) criterion is not satisfied.

While more robust values of QY can be obtained using a spectrometer equipped with an integrating sphere and photon counting detector, the technique proposed within this section provides a method to obtain a first approximation of QY using a plate reader

setup. The ability to obtain this an approximation of QY from existing spectrometers not equipped with either an integrating sphere or photon counting detector makes it particularly attractive for screening semiconductor samples and quality control applications in both academic and industrial settings.

#### 6.4.3 Discrete Au inclusion SPR absorbance within a ZnO Matrix

The surface plasmon resonance (SPR) of gold nanoparticles is in the visible range and is dependent on both the medium the particles are in and as well as the size and morphology of these particles. The correlation between size and colour has led to methods being developed utilising the visible absorbance of AuNPs in water to identify particle size.<sup>206</sup> The ZnO-Au sample in the library of ZnOs studied had a distinctive reddish-purple hue instead of the white colouration of ZnO, see figure 6.11, this colouration was attributed to the  $\text{Au}_{\text{SPR}}$  absorbance of the discrete gold inclusions in this matter.

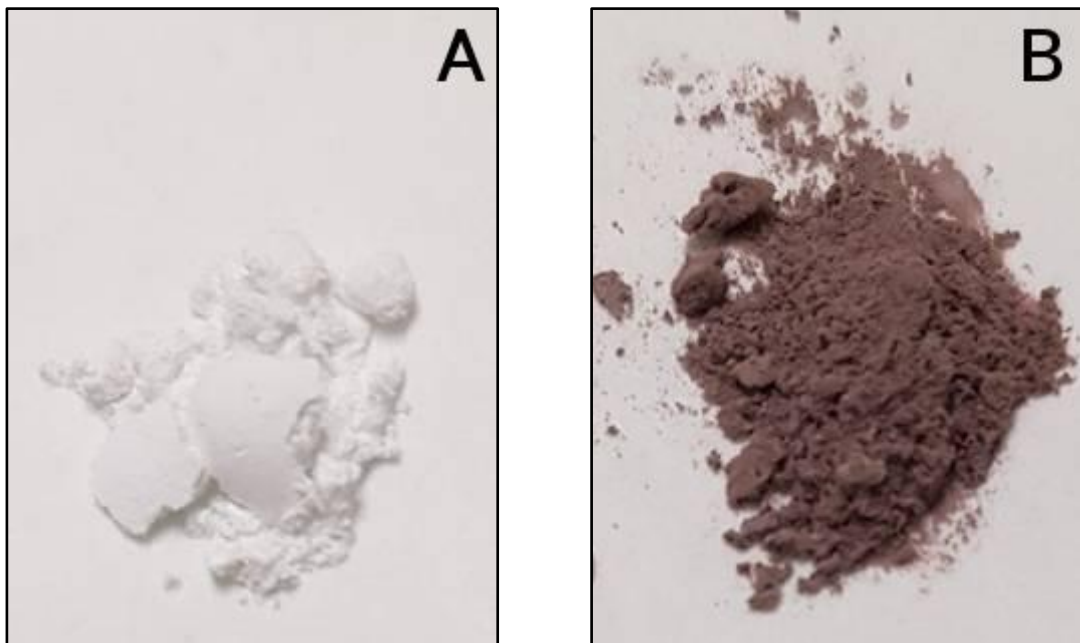


Figure 6.11 - Comparison of the hue of the ZnO-ZA2 and ZnO-Au samples where the ZnO-ZA2 has a white colouration similar to ZnO while the ZnO-Au has a distinct reddish-purple hue. The letters denote the two different samples: A) ZnO-ZA2 and B) ZnO-Au.

During the emissive state topology studies, section 6.4.1, it was observed that ZnO-Au had no dominant state with all states appearing to be equally preferred. This behaviour was suggested to be due to the discrete Au inclusions where electrons at the ZnO-Au boundary feel the metallic environment of Au. Conceptualising the discrete gold inclusions in ZnO-Au as gold nanoparticles within a ZnO medium allows for the calculation of a Mie theory spectra. These spectra will be used to compare the theoretical absorbance of the

$\text{Au}_{\text{SPR}}$  with the actual absorbance of the  $\text{Au}_{\text{SPR}}$  of the Au inclusions. This will provide information on whether the ZnO-Au boundary is distinct or there is a region where ZnO/Au behaviour becomes hybridised.

To deconvolve the Au inclusion contribution from the spectral features of ZnO, optical absorbance spectra were collected for the nanoflowers and the ZnO-Au samples over a spectral range of 200-800 nm inclusive, see figure 6.12A. The nanoflower sample was selected to represent the ZnO spectral contribution as both the nanoflowers and ZnO-Au samples used the ZA2 peptide (GLHVMHKVAYSSGAPPMPFF) in the peptide-mediated synthesis. Comparing the nanoflower and ZnO-Au spectra there is a blue shift of the ZnO in gap transition, see figure 6.12A peaks a & a\* for nanoflower and ZnO-Au respectively. ZnO-Au has 4 addition spectral features b\*, c\*, d\* and e\* out of these c\* or d\* might be the  $\text{Au}_{\text{SPR}}$  peak.

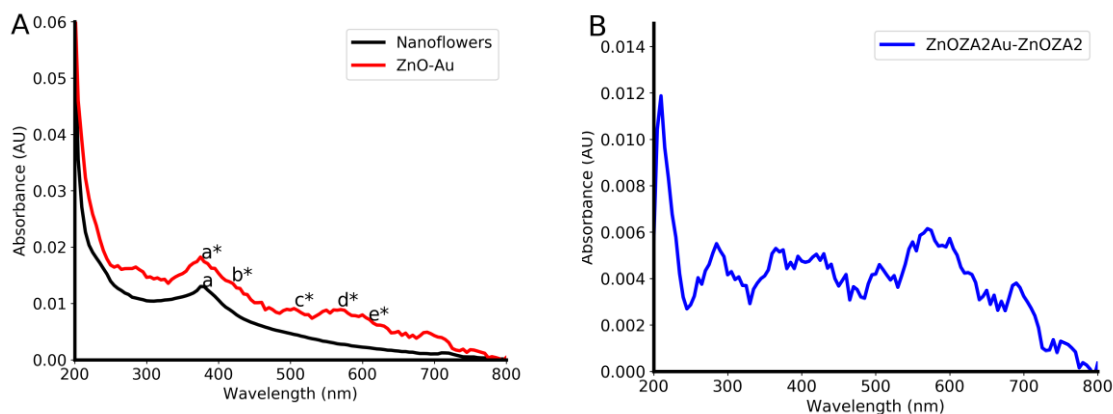


Figure 6.12 - Absorbance spectra for ZnO-ZA2 and ZnO-ZA2-Au samples collected using UV-vis spectroscopy. A) Experimentally collected optical absorbance data for both the nanoflowers and ZnO-Au, the letters denote different spectral features and the asterisk denotes spectral features relating to ZnO-Au B) Subtraction of the ZnO-ZA2 spectrum from ZnO-ZA2-Au spectrum to highlight spectral differences.

To ensure the differences observed are not due to different scattering effects, scanning electron microscopy (SEM) was used to determine the size and morphology of both samples, see figure 6.13. The ZnO particles in both nanoflowers and the ZnO-Au sample being 5.4 and 5 micron respectively, this size difference is minimal compared to the overall size of the ZnO matter therefore the scattering effects for both samples was approximated to be the same. Due to the large diameter of the ZnO particles, small amounts of sample were placed in an aqueous environment to minimise scattering effects while ensuring the  $\text{Au}_{\text{SPR}}$  peak was still observed in collected spectra. Water was selected to minimise the scattering arising from the quartz/sample interface in the cuvette. While nanoscale ZnO is soluble in water, due to the ionic nature of this compound, the ca. 5 - 5.5  $\mu\text{m}$  structures are stable in water for the 10 minutes collection time required for the

UV-vis studies. This is supported by the 1.9  $\mu\text{m}$  ZnO structures reported in the literature to only dissolve by ca. 1% under exposure to nanopure aqueous environments for 100 hours.<sup>325</sup> Therefore the amount of the ca. 5-5.5  $\mu\text{m}$  ZnO particle dissolved over a 10 minute period will be negligible.



Figure 6.13 - Secondary electron image scanning electron micrographs for: A) ZnO nanoflowers synthesised in the presence of the ZA2 sequence, B) ZnO-ZA2-Au nanocomposite synthesised in the presence of the ZA2 sequence and HAuCl<sub>4</sub>.

To determine if there are any spectral differences between the gold inclusions within the ZnO-Au sample and a calculated spectra of AuNPs in a ZnO medium the size of the gold inclusion must be determined. Although SEM is suitable for studying the size and morphology of the ZnO the size of the teardrop formed in the SEM is too large to obtain with high resolution (single nanometers) while being able to detect the L emission from Au by EDX. Transmission electron microscopy (TEM) and scanning TEM (STEM) are better suited to imaging the small Au inclusions, through use of STEM and EDX mapping the location of the gold inclusions can be determined with nanometer resolution. To study the gold inclusions using both TEM and STEM a thin section of the ZnO-Au specimen was selected as in thicker regions the TEM beam is attenuated by the time it reaches the detector. Using an accelerating voltage of 200kV a series of TEM images were obtained of this thinner section of the ZnO-Au, see figure 6.14A. The dark regions in figure 6.14A are due to the gold inclusions with their high electron density whereas the ZnO appears as light grey in colour.

EDX mapping was used to confirm the presence of the Au inclusions which are observed as bright areas on the Au EDX map, see figure 6.14B, which correspond to the dark regions attributed to gold inclusions in the TEM image, see figure 6.14A. To confirm the presence of these dark regions was unique to ZnO-Au and could not be attributed to any other source, the nanoflower sample was studied using the same conditions and no dark spots were observed, see figure A6.4. To determine if the gold inclusions were located on the surface of the ZnO-Au sample EDX maps for both Zn and O were obtained, see figure 6.14C for Zn map and figure A6.4 for O map, both maps appeared identical and no dark regions were observed suggesting the gold inclusions were distributed throughout

the sample. Using the collected data the diameter of the gold inclusions was determined to be  $18.6 \pm 6.9$  nm (52 inclusions measured, see figure A6.3) pseudo-elliptical inclusions which are distributed throughout the sample. This is in good agreement with the values previously calculated using the Scherrer equation, see table 6.2.

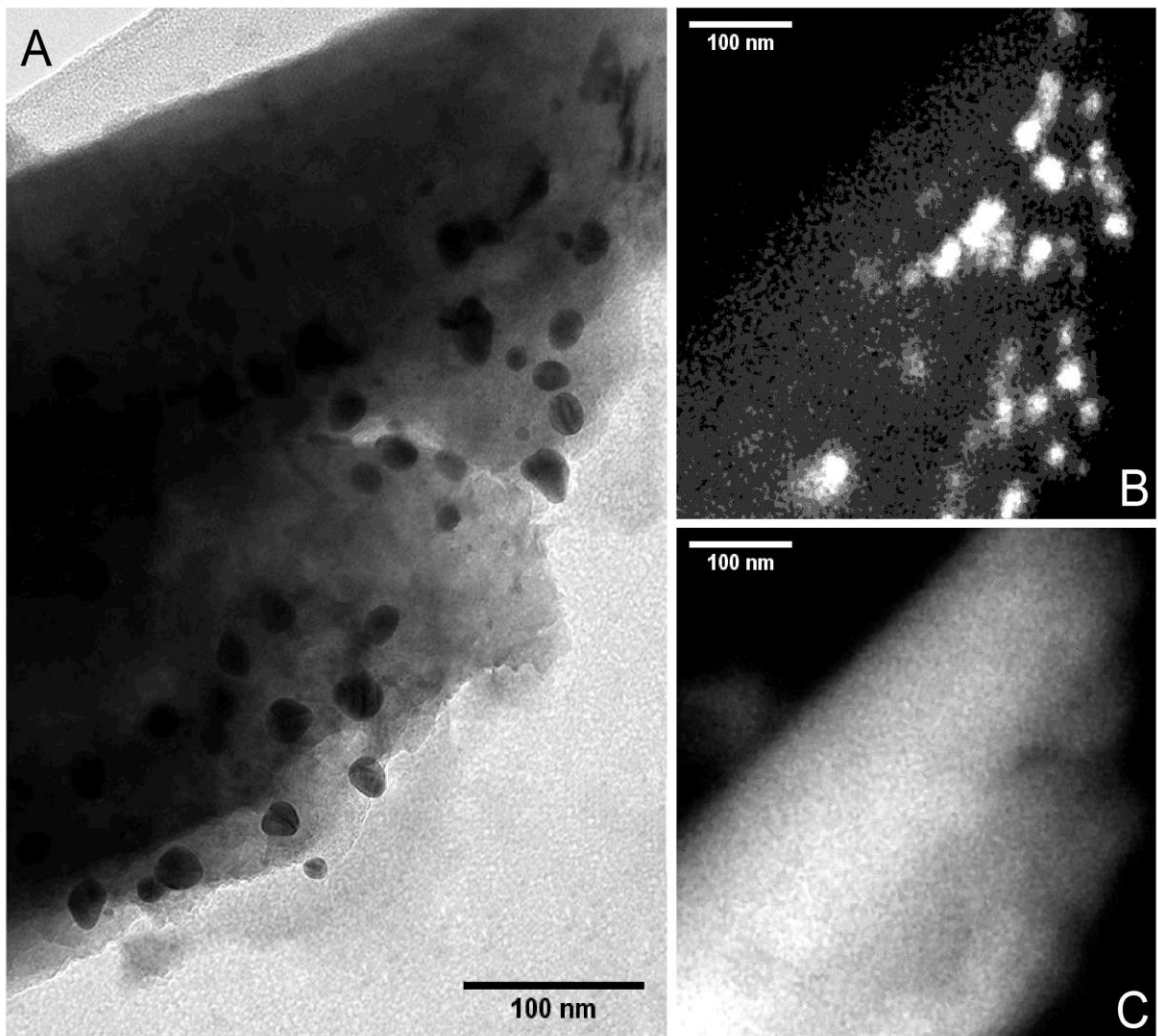


Figure 6.14: Transmission Electron Microscopy and EDX imaging of ZnO-Au nanocomposite A: Stitched transmission electron micrograph of ZnO-Au from multiple different micrographs to obtain a high resolution image of the microscale sample taking care to avoid artifacting the image. The dark regions in A correspond to embedded gold clusters in the ZnO matrix. B: Au EDX map of the nanocomposite which has good agreement with the dark regions in A. C: Zn EDX map of the nanocomposite indicating the gold clusters are embedded inside the ZnO matrix. The Zn EDX map is representative of the O EDX map as localisation was the same.

Modelling the optical properties of gold using Mie theory is well studied in the literature with methods being developed to determine the size of gold nanoparticles from UV-vis spectra<sup>206,326</sup> and tune the extinction peak of graphene coated gold nanoparticles for antitumor applications.<sup>327</sup> Taking inspiration from the work of Amendola *et al.* an inhouse python script was developed, see script A6.1, to model the contribution of the gold

inclusions to the overall spectrum. The environments the gold inclusions experience can be accounted for by taking the refractive index of each environment into consideration.<sup>328</sup> Both H<sub>2</sub>O and ZnO environments were considered in this study to account for environments both within the volume and at the surface of the ZnO.

To save computation time Mie scattering spectra were precalculated for particles with diameters ranging between 8-100nm in both ZnO and H<sub>2</sub>O environments using a 1nm step in diameter. The precalculated spectra were then weighted and summed to match the spectral features observed in the ZnO-Au sample. Each calculated Mie scattering spectra used an x-axis step of 5nm, which is consistent with the reference used for the complex relative permeability values for Au.<sup>329</sup> While the 5nm step must be used it limits the resolving power of the calculated Mie spectra, as multiple particle sizes have the same wavelength for the Au<sub>SPR</sub> peak, see figure 6.15.

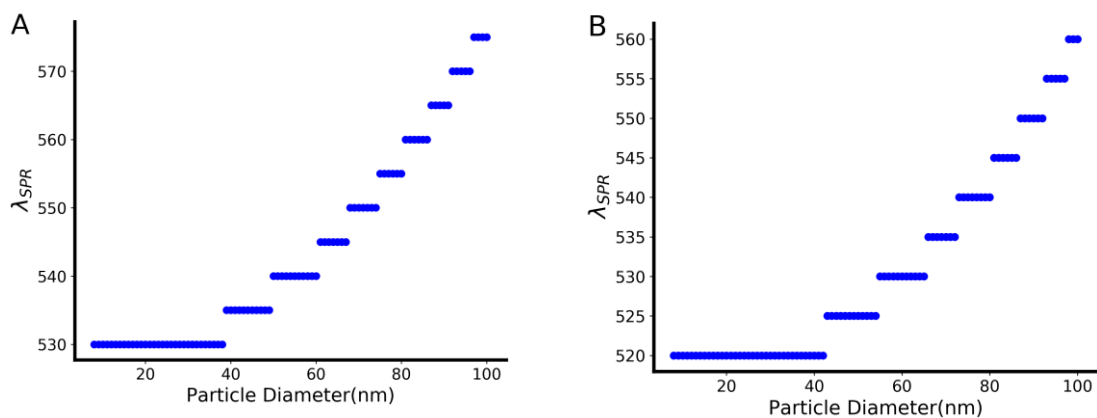


Figure 6.15 - Plots showing the wavelength at which the Au<sub>SPR</sub> maxima is observed when 5 nm stepping is used in the Mie theory spectra for particle diameters between 8-100nm. The letters represent: A) Spectra calculated using a ZnO environment B) Spectra calculated using a H<sub>2</sub>O environment

Due to multiple particle diameters returning the same  $\lambda_{SPR}$  value, a high level of confidence cannot be given to discussion on a single particle size; instead the discussion will be built upon the range of particle sizes which return the same  $\lambda_{SPR}$  value. Returning to the collected optical absorbance spectra for ZnO-Au, see figure 6.12A, peaks c\* and d\* located at 505 and 570nm respectively were attributed to Au<sub>SPR</sub> absorbance. Consulting figure 6.15, a peak with a  $\lambda_{SPR}$  value is not possible with a spherical geometry in either ZnO or H<sub>2</sub>O environments. However this blueshifted Au<sub>SPR</sub> peak could be accounted for by non-spherical gold inclusions as nanostructures with edges such as nanostars are known to have a blueshifted SPR peak.<sup>330-332</sup> Calculation of Mie scattering of gold inclusions with a non-spherical geometry is outside the scope of this project but is a potential area for future work.

The  $d^*$  peak, see figure 6.12A, located at 570nm is asymmetrical and is skewed towards the blue side of the spectrum. Subtracting the nanoflower spectra from the ZnO-Au spectra removes the ZnO spectral contributions, see figure 6.12B, while leaving any unique spectral features in the ZnO-Au sample. The peak  $d^*$  at 570nm can be observed in figure 6.12B and has a distinct asymmetry suggesting that there are several Au<sub>SPR</sub> peaks present generated by different sized gold inclusions. Consulting figure 6.15, the peak observed at 570nm is attributed to large Au inclusions which are sized between 92-96 nm in a ZnO environment. Large gold inclusions between 92-96 nm were not observed in the initial processing of the STEM/TEM data. However, upon increasing the brightness of this image these ca. 96nm inclusions can be observed, see figure 6.16. The inclusions inside the ZnO matrix are likely polycrystalline with each domain being formed from discrete seeds. The size of these domains was determined to be 19nm using the values calculated using the Scherrer equation earlier.

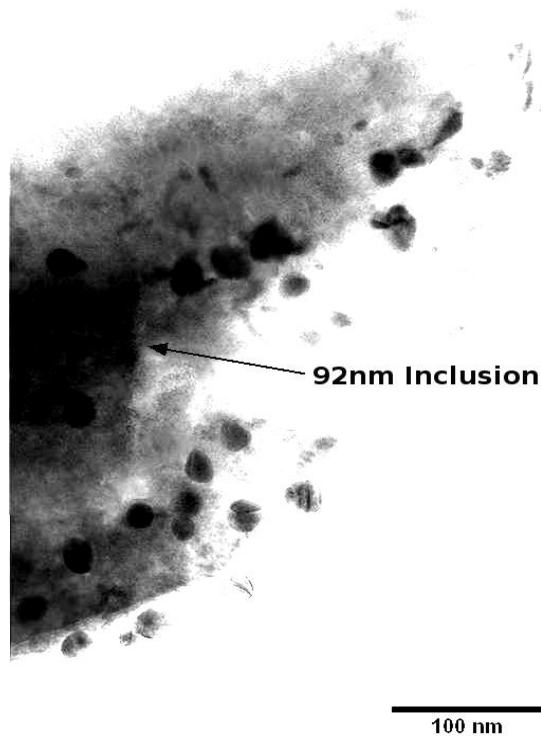


Figure 6.16: Transmission Electron Microscopy of ZnO-Au nanocomposite A: Transmission Electron Image of ZnO-Au with the dark regions corresponding to embedded gold clusters in the ZnO matrix, brightness has been increased by 80% to show the large dark mass inside the ZnO, which is ca. 95nm. This dark spot is a gold inclusion but is too deep within the ZnO matrix to be detected by STEM.

The asymmetry on the blue side of the peak at 570nm suggests a spectral contribution of smaller Au inclusions which may be sized between 8-34 nm in either a ZnO or H<sub>2</sub>O environment. Using the subtracted spectra, see figure 6.12B, the peak at 570nm was

fitted using Levenberg-Marquardt optimisation to alter the weighting for the 92-96 nm and 8-34nm spectra in the ZnO environment and the 8-34nm spectra in the H<sub>2</sub>O environment.

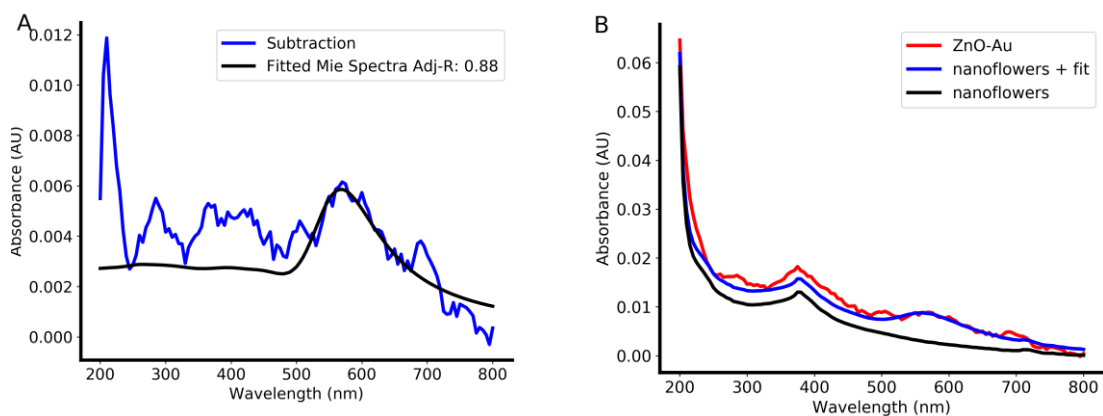


Figure 6.17 - Fitted Absorbance spectra for ZnO-Au samples collected using UV-vis spectroscopy. A) Showing the subtracted data. Fitted using Mie spectra using least squares fitting for the region fitted between 530-800nm B) The suggested fit of ZnO-Au data with the Mie spectra and nanoflowers summed.

The fitted Mie spectra, see figure 6.17A, has a good quality of fit with an adjusted- $R^2$  value of 0.88. However, it appears the spectral contribution on the red side ca. 720nm over estimates the Au inclusion contribution suggesting there might be a separate spectral feature at 690nm which is convolved with the peak observed at 570nm. The spectral contribution of the 92-96nm Au inclusion in the ZnO environment dominates the overall Au<sub>SPR</sub> scattering modelled. This suggests that the 92-96nm inclusions are responsible for the sample's distinctive reddish-purple hue. The contribution of 8-34 nm Au inclusions in the H<sub>2</sub>O environment make a small contribution while the contribution of these particles in the ZnO environment is negligible. This suggests that the 8-34nm Au inclusions are located at the surface while the larger 92-96nm Au inclusions are located within the volume of the sample. Summing the fitted Mie spectra and the nanoflower spectra, see figure 6.17B, produces a spectra which is representative of the ZnO-ZA2 sample suggesting the Au<sub>SPR</sub> contribution can be accounted for. However, spectral differences on the blue side of the spectra are still observed suggesting that there is a difference between the two ZnOs in these samples which supports the theory that electrons at the ZnO-Au boundary feel the metallic environment of Au.

In this section Mie theory was used to model Au inclusions within the ZnO-Au sample under the assumption of spherical geometry. The modelled spectra had a good quality of fit (adj- $R^2$  0.88) and the modelled contributions were predominantly 92-96 nm Au inclusions which were located within the ZnO volume of the sample. There was also a small contribution of 8-34nm Au inclusions which are located at the surface of the sample. The assumption of a spherical geometry of the gold inclusions when performing the Mie

theory calculations was valid for the peak at 570 nm; however, the peak at 505 nm was unable to be fit under these assumptions. A future study could address this by performing Mie calculations using complex non-spherical geometries as it is known that Au particles with edges have a blue shifted Au<sub>SPR</sub> peak.<sup>330-332</sup> Summing the fitted Mie and nanoflower spectra forms a close approximation of the spectral features observed for the ZnO-Au sample. However, spectral differences on the blue side of the spectra are still observed suggesting that there is a difference between the two ZnOs in these samples which supports the theory that electrons at the ZnO-Au boundary feel the metallic environment of Au.

#### 6.4.4 Nonlinear Fluorescence Behaviour in ZnO

The collected 2DFMs for the microspheres and analytical standard, see figure 6.18, both showed a relatively high quantum yield for the NBE emission using a low power excitation source with a maximal fluence of ca.  $0.2 \cdot 10^{-6}$  W/cm<sup>2</sup>. Both these samples have microscale particle sizes which makes them well suited to imaging using optical microscopy. In collaboration with Dr V. Volkov, confocal microscopy studies were performed to investigate the localisation and nature of emissive centers within the analytical standard and microspheres.

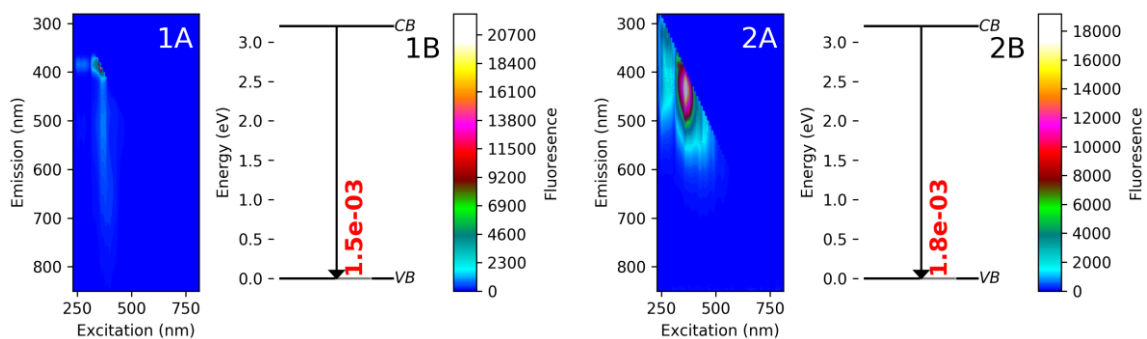


Figure 6.18 - 2DFMs of the ZnO analytical standard and microspheres and the approximated quantum yield for the NBE transition. Where : 'A' denotes the 2DFM collected for the matter and 'B' denotes the Jablonski diagram showing the CB->VB transition with the approximated quantum yield value. The number represents: 1) analytical standard and 2) microspheres.

Confocal images were collected for both samples using a 405 nm diode laser as the excitation source and the response of each sample was collected at 430 and 510 nm, see figure 6.19. The emissive centers at 430 nm are attributed to the NBE emission and distributed evenly over the analytical standard shape with a slight increase in emission density towards the edge of crystal, which is attributed to the increase in curvature. The microspheres appear to have a greater emissive centres at the edge likely due to the increased curvature of the microspheres compared to the analytical standard. Slight spatial broadening is observed for the microspheres sample at 430 nm which correlates to the internal crystal domains (ca. 18 nm). The emission at 510 nm tends to localise at the

surface for the analytical standard while a greater spatial spreading is observed for the microspheres.

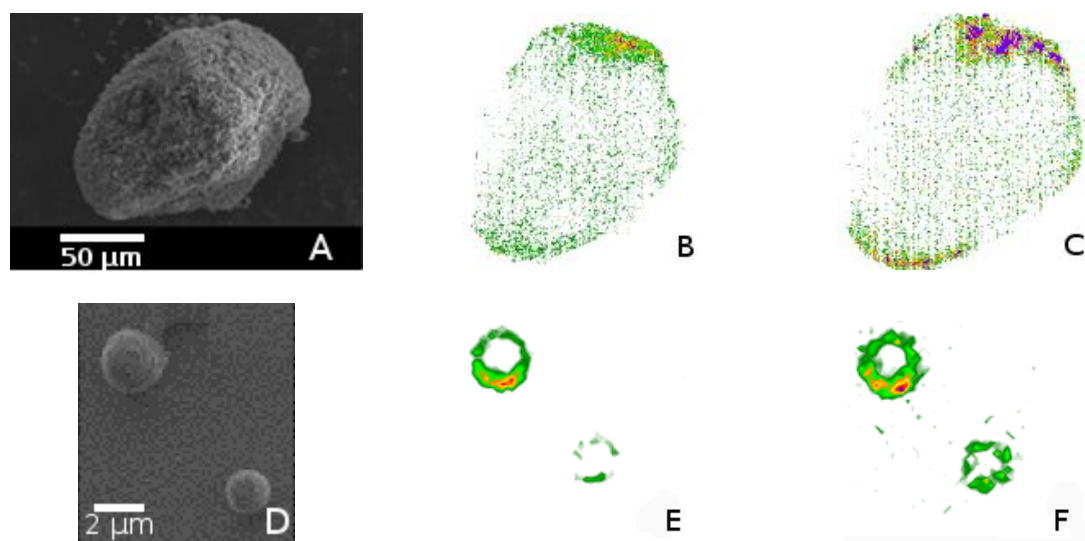


Figure 6.19 - Fluorescence emission localisation of ZnOs under microscopic resolution. A) SEM image of selected analytical standard crystal. B and C) confocal images scanned at the equatorial plane of the analytical standard crystal using 405nm excitation and collected at 430 and 510nm respectively. D) SEM image of selected microspheres. E and F) confocal images scanned at the equatorial plane of the microspheres using 405nm excitation and collected at 430 and 510nm respectively.

In both samples it was observed that the curvature at the boundary of the particles appears to affect the emission behaviour of the matter, leading to more emissive centers being located at the boundary. This suggests that the boundary of the ZnO matter could be behaving as a low quality cavity which is of particular interest as high quality cavities are used to study the formation of polaritons.<sup>253</sup> To determine if polariton formation is occurring within these samples, power dependent emission studies were performed, see figure 6.20, to determine whether the relationship between power and emission is linear or nonlinear.

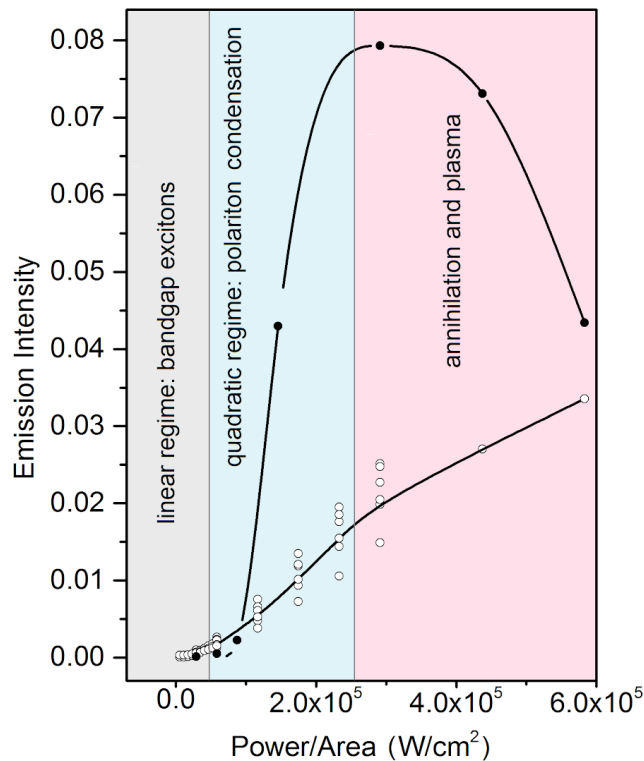


Figure 6.20 - The power dependent behaviour of the emission intensity for the ZnO analytical standard and microspheres. The plot of the dependence of emission intensity on fluence of excitation radiation (405nm) for ZnO analytical standard (line with non-filled circular markers) & microspheres (line with filled circular markers).

The behaviour observed in figure 6.20 for these microstructures under high power coherent radiation with a tight focusing regime using a confocal emission microscope resembles the physics that occurs in high-quality cavities. Initially, a quadratic power dependence is observed upon imaging excited band-gap carriers in the ZnO microscystal. However, above a threshold value the quadratic behaviour observed begins to break down which is assigned to quasi-particle annihilation and potentially ionisation. Previous studies reported on electron-hole plasma upon excitation of ZnO films;<sup>333,334</sup> however, no spectral signatures characteristic of this were observed. We propose the nonlinear behaviour observed is due to polariton formation where the coupling of radiation to the material response forms the lower polariton branch<sup>335,336</sup> as observed in high quality cavities. Dr V. Volkov has continued to explore this behaviour in greater depth using confocal spectral scanning, spatial filtering of confocal images and lumerical modelling to develop an understanding of the nature of these emissive centers.

## 6.5 Conclusion

Within this chapter the resolving power of the 2DFM technique has enabled the transitions occurring in these samples under photoexcitation to be assigned. Jablonski diagrams were created where each assigned transition and its emissive contribution were compiled to assist the experimentalist. Studying the Jablonski diagrams for the untreated ZnO library, observations were made that the synthetic conditions used have a strong impact on the defect concentrations within the synthesised material. An excellent example of this is a peptide mediated subset, where the emission behaviours of all 3 samples synthesised using peptide mediated conditions had the same dominant transitions and number of emissions. Upon applying a surface treatment to these samples, either NaBH<sub>4</sub> or PVA, the same trend in behaviour was observed across all 3 samples supporting the theory that the synthesis conditions are of vital importance. The 2DFM technique is sensitive to the synthetic conditions therefore future studies could explore different synthetic routes with a goal to develop a systematic understanding of the interplay between synthetic conditions and defect population.

Studying the ZnO library post two separate surface treatments 0.5% PVA and 1M NaBH<sub>4</sub> it was concluded that the efficacy of the two surface treatments used in this study is highly sample dependent. The 0.5% PVA does passivate surface V<sub>O</sub> defects and 1M NaBH<sub>4</sub> introduces new V<sub>O</sub> surface defects; the overall effect on a given sample is hard to predict due to the complex interplay between states. To effectively use either treatment, pre and post treatment 2DFMs would have to be collected for the sample and the differences in the desired transition compared. If the intended outcome is to increase NBE for the analytical standard or microspheres the NaBH<sub>4</sub> treatment is superior, causing a dramatic increase in NBE emission, while for nanorods the PVA treatment is more effective. Future studies could focus on investigating the relationship between synthetic conditions/defect population and treatment behaviour to develop a better understanding of this interplay allowing for the surface treatments to be used with predictable outcomes in an industrial setting.

To ensure easy comparison of emissive data between datasets collected on different instruments and from different studies, the determination of the quantum yield (QY) is of fundamental importance. The plate reader spectrometer used in this study, Tecan i-control M200 Pro, was not equipped with a photon counting detector or integrating sphere meaning this type of device can not directly determine QY. However, the determination of the relative quantum yield using R6G which has a known QY is possible. This study proposes a method for determining a first approximation of the QY for each emissive transition observed within the studied matter from the collected 2DFM. This method was

applied to all three ZnO libraries studied: untreated, 0.5% PVA treated and 1M NaBH<sub>4</sub> treated. This approach is a robust method to approximate the QY of different emissive states and has good agreement with the percentile emission findings. The ability to obtain an approximation of QY from existing spectrometers not equipped with either an integrating sphere or photon counting detector makes it particularly attractive for screening semiconductor samples and quality control applications in both academic and industrial settings.

While this first approximation of QY has been robust for the studied samples, it currently relies on 1d slices along the emission axis, which assumes that y-width ( $\sigma_y$ ) >> x-width ( $\sigma_x$ ). However, for samples such as CdSe, studied in Chapter V, where  $\sigma_y \ll \sigma_x$  the approximation of QY will be very inaccurate. Future studies should collect a 2DFM for the R6G dye in both the liquid state (0.69  $\mu\text{M}$ ) and solid state (14.8  $\text{nmol}\cdot\text{g}^{-1}$ ), it would be expected to see diagonalisation in the emissive topology for both the liquid and solid R6G 2DFM, due to the R6G behaving like a molecular system.<sup>169,202</sup> The emissive states within the 2DFM for the liquid and solid R6G 2DFM should be fitted using the same approach used for the semiconductors studied in both Chapter V and Chapter VI, this will allow for deconvolution of the diagonalised spectral response of R6G. The deconvolved line-shapes can then be integrated to obtain the emission of the 2D-line-shape which will be the value for  $E_R$ . Likewise, integrals for the 2D-line-shapes for the transitions can be obtained and used as the  $E_S$  values. Using this approach would overcome the error introduced when the y-width ( $\sigma_y$ ) >> x-width ( $\sigma_x$ ) criterion is not satisfied.

The studied ZnO library contained ZnO-Au which was a ZnO sample with discrete gold inclusions within the matter which are responsible for the sample's distinctive reddish-purple hue instead of the white colouration of wurtzite ZnOs. The spectral response of the Au inclusions was modelled using Mie theory under the assumption that the inclusions had a spherical geometry. The modelled spectra had a good quality of fit (adj-R<sup>2</sup> 0.88) and the modelled contributions were predominantly 92-96 nm Au inclusions which were located within the ZnO volume of the sample. There was also a small contribution of 8-34nm Au inclusions which are located at the surface of the sample. The assumption of a spherical geometry of the gold inclusions when performing the Mie theory calculations was valid for the peak at 570 nm; however, the peak at 505 nm was unable to be fit under these assumptions. A future study could address this by performing Mie calculations using complex non-spherical geometries as it is known that Au particles with edges have a blue shifted Au<sub>SPR</sub> peak.<sup>330-332</sup> Summing the fitted Mie and nanoflower spectra forms a close approximation of the spectral features observed for the ZnO-Au sample. However, spectral differences on the blue side of the spectra are still observed suggesting that there

is a difference between the two ZnOs in these samples which supports the theory that electrons at the ZnO-Au boundary feel the metallic environment of Au.

The 2DFMs and approximated QY values for the NBE emission of the microspheres and analytical standard which are both microscale samples were of particular interest for fluorescence studies under microscopic resolution. In collaboration with Dr V. Volkov confocal microscopy studies were performed to investigate the localisation and nature of emissive centers within the analytical standard and microspheres. A quadratic relationship between emission intensity and excitation power was observed for these microstructures under high power coherent radiation with a tight focusing regime using a confocal emission microscope, which resembles the physics that occurs in high-quality cavities. Initially, a quadratic power dependence is observed upon imaging excited band-gap carriers in the ZnO microscystal. We propose the nonlinear behaviour observed is due to polariton formation where the coupling of radiation to the material response forms the lower polariton branch<sup>335,336</sup> as observed in high quality cavities. Above a threshold value the quadratic behaviour observed begins to break down which is assigned to quasi-particle annihilation and potentially ionisation. Dr V. Volkov has continued to explore this behaviour in greater depth using confocal spectral scanning, spatial filtering of confocal images and lumerical modelling to develop an understanding of the nature of these emissive centers.

# Chapter VII: Conclusions & Future Work

## 7.1 Findings

The digital age has brought an unprecedented rate of human advancement in the past half-century, bringing with it new questions about the world around us and also where humanity fits into this new paradigm. This relentless development and progression since the industrial revolution has led to environmental pollution and destruction to keep up with humanity's ever-growing requirements. Using the biomimetic approach chemists have begun to look to nature for inspiration and learn how nature performs chemistry with high yield and minimal pollution.

Following the principles of biomimetics, scientists inspired by biomimetic mineralisation have investigated peptide-mediated synthesis routes to control the size and morphology of the synthesised inorganic matter. Computational studies have measured the ability of individual amino acids, peptides and proteins to understand the requirements for engineering the primary structure of sequence to bind selectively to a given target. Experimental techniques such as phage display have been used to screen ca.  $10^7$  possible binding sequences can elucidate the strongest binders.

This study set out to determine the applicability of 2D spontaneous emission spectroscopy as a tool capable of analysing the states present, including in-band defect states, within semiconductors for potential academic and QC industrial applications. ZnO matter was of particular interest as it is known for its structural diversity with respect to native defect states. Multiple different ZnO samples synthesised using different synthetic routes were tested, as well as a ZnO-Au nanocomposite material which has been synthesised using a one-pot peptide-mediated synthetic route. The discrete gold inclusions in ZnO-Au composites have been reported to enhance catalytic performance compared to ZnO matter.<sup>72-74</sup> Therefore, understanding the effect of the synthetic route used and/or the presence of gold inclusions on the defect states present in ZnO matter would enable the engineering of new devices for optoelectronic or catalytic applications.

The one-pot synthetic method required a bespoke peptide sequence with discrete ZnO and Au binding regions, herein referred to as ZA2. Leveraging the previous ZnO binding studies performed within the research group<sup>42,94,95</sup> the ZnO binding region was developed from the G12 (GLHVMHKVAPPR) sequence.<sup>42</sup> For the gold binding region of the ZA2 sequences kinetic and thermodynamic peptide-Au binding studies were undertaken, investigating known binding sequences such as A3<sup>39</sup>, AuBP1<sup>96</sup>, AuBP2<sup>96</sup> and Pd4.<sup>97</sup>

Isothermal titration calorimetry was selected for the thermodynamic studies as it allowed for investigations using AuNPs as the gold substrate and multiparametric surface plasmon resonance (MP-SPR) was chosen for the kinetic studies and used  $\text{Au}_{(111)}$  surfaces. During the kinetics studies the efficacy of the langmuir and kisliuk models to model and fit peptide binding interactions at the  $\text{Au}_{(111)}$  surface in the biominerallisation (25-800  $\mu\text{M}$ ) concentration range was assessed. This study found that while Langmuirian assumptions are valid for low concentration binding studies (0.1-2.5  $\mu\text{M}$ ) they are no longer valid in the biominerallisation concentration range, with the Kisliuk model offering a better fit. Using the A3 peptide as a model system this study proposed the unified Langmuir-Kisliuk kinetic model as a way to model the kinetics of peptide adsorption onto surfaces, specifically  $\text{Au}_{(111)}$  surfaces in this study's case.

The Langmuir-Kisliuk model is able to relate back to the traditional Langmuirian kinetic models for comparison with historic data, as well as being suited to process data collected at both the high and low concentration regimes. Fitting of the data using a dose-response curve allowed for the determination of both  $K_D$  and the Hill slope ( $n$ ), the latter being useful to predict what state the peptide prefers to be in and whether or not peptide assistive adsorption would occur. Finally, introducing the partial molar volume of the solvent in the calculation of  $\Delta G$  allowed us to closely approximate the thermodynamic constants for a system even under higher concentrations. The Langmuir-Kisliuk model was compared against the existing Langmuir and Kisliuk model for the rest of the studied peptides and offered the highest quality of fit. Consequently, all kinetic and derived thermodynamic terms for the MP-SPR studies used the Langmuir-Kisliuk kinetics.

The thiol chemistry afforded by Met and Cys groups was anticipated to form a strong Au-S interaction and expected to be very thermodynamically favourable; however, the MP-SPR and ITC studies show that this is not the case with peptide diads such as Lys Arg or Arg Arg, forming equally as strong if not stronger binding interactions. The designed A3s, A3sT2 and A3sC8 sequences all had a poorer binding efficacy than the original A3 sequence; this is suggested to be due to the removal of the  $\text{Pro}_8$  residue which these studies suggest is important for effective anchoring of the sequence onto a gold substrate.<sup>98</sup> Upon anchoring through the  $\text{Pro}_8$  residue, the  $\text{Met}_9$  residue becomes proximal to the Au substrate increasing the probability of a binding interaction.

While the MP-SPR and ITC studies showed that diads in the peptide sequence such as Lys Arg, Arg Arg formed equally as strong if not stronger binding interactions with gold substrates, His His diads appear to solely have a high binding affinity for the  $\text{Au}_{(111)}$  surface. In the MP-SPR studies using  $\text{Au}_{(111)}$  surfaces, both His His diads and His residue

containing sequences (HRE & Pd4) had a high affinity for the gold substrate while in the ITC studies which uses gold nanoparticles which present Au<sub>(111)</sub>, Au<sub>(110)</sub> & Au<sub>(100)</sub> showed a low affinity for the gold substrate. This suggests that the Histidine residue preferentially binds to the Au<sub>(111)</sub> plane/facet but the interaction with Au<sub>(110)</sub> & Au<sub>(100)</sub> planes/facets are not favourable. An indepth computational simulation of these binding interactions was beyond the scope of this study; however, this observation presents an interesting avenue for future study.

Peptide-peptide interaction behaviour was investigated through ITC solvation studies which showed an increase in order upon solvation for the non-sulphur containing sequences, suggesting that peptide agglomeration/assembly had occurred. The propensity of these sequences to undergo agglomeration/assembly was attributed to the Arg and His residues present within the primary sequence.<sup>241,242</sup> This was supported by no agglomeration/assembly behaviour being observed for the A3 family of sequences which do not contain either His or Arg residues. Due to both the high binding efficacy observed in the ITC and MP-SPR studies as well as desirable solvation behaviour A3 was selected as the Au binding region for the bespoke ZA2 sequence.

Leveraging previous ZnO binding studies performed within the Perry research group<sup>42,94,95</sup> the ZnO binding region was developed from the G12<sup>42</sup> (GLHVMHKVAPPR) sequence - a known ZnO binder with ability to control the growth of ZnO during hydrothermal synthesis.<sup>42</sup> Previous studies have shown that the N-terminus of G12 is important for ZnO binding; however, the APPR motif at the C-terminus was shown to be not required.<sup>42</sup> Consequently, GLHVMHKV was chosen as the ZnO binding region of the bespoke ZA2 sequence.

To study the relationship between defect states and synthetic route for ZnOs, including ZA2 mediated synthesis, this study proposes two-dimensional spontaneous emission spectroscopy as a novel methodologic approach to the analysis of emissive states in semiconductors. Through use of this technique we obtain a topological view of the emissive states within a sample, these two-dimensional spectra shall herein be referred to as two-dimensional fluorescence maps (2DFM). 2DFM is viable on spectrometers designed solely for one-dimensional operation which allows for experimentation on existing fluorescence spectrometers equipped with a monochromator and could be deployed in a variety of settings.

The proposed fitting algorithm performs within the outlined criteria where a good quality of fit must be obtained while retaining physical relevance. Through use of bespoke in-house

software the author has attempted to make this process as simple to use as possible. The “hints” system, inspired by the early font work by Adobe,<sup>259</sup> is fundamental to retaining physical relevance in the suggested peaks. Currently, the experimentalist optimises the  $\sigma_x$ ,  $\sigma_y$  and provides an initial estimation on amplitude guided by both visual inspection and the adjusted-R<sup>2</sup> (adj-R<sup>2</sup>) value of the fitting. The LM optimisation is performed solely varying the peak amplitudes of the 2D-Gaussian line-shapes leading to physical fits with an adj-R<sup>2</sup> $\geq 0.92$ .

A library of widely used and studied semiconductors were used to validate this approach and demonstrate the resolving power of the 2DFM technique which is capable of resolving spectral signatures that would have been superimposed in a 1D-presentation. An excellent example of the aforementioned resolving power is the ability to separate the 570 nm emission within ZnO into the emissive states of different physical nature dependent upon excitation wavelength. The power of this deconvolving approach steps beyond resolving intrinsic states within a sample and is able to detect trace impurities such as Mn in the ZnS sample studied.<sup>281</sup> This technique is very applicable to semiconductor studies and quality control (QC) applications in both academic and industrial settings.

The proposed 2DFM technique facilitated the assignment of the transitions occurring in ZnO samples under photoexcitation. The assigned transitions were compiled with their corresponding emission contribution and presented as Jablonski diagrams; the author observed that the synthetic conditions used have a strong impact on the defect concentrations within the synthesised ZnO matter. An excellent example of this is the peptide mediated subset, where the emission behaviours of all 3 samples synthesised using peptide mediated conditions had the same dominant transitions and number of emissions. Upon applying a surface treatment to these samples, either NaBH<sub>4</sub> or PVA, the same trend in behaviour was observed across all 3 samples. This supports the theory that the synthesis conditions are of vital importance for defect formation.

Surface treatments were reported in literature to enhance the NBE emission of ZnO, this study found that the efficacy of the two separate surface treatments used in this study (0.5% PVA and 1M NaBH<sub>4</sub>) was highly sample dependent. The 0.5% PVA does passivate surface V<sub>O</sub> defects, and 1M NaBH<sub>4</sub> introduces new V<sub>O</sub> surface defects. The overall effect on a given sample is hard to predict due to the complex interplay between states. To effectively use either treatment, pre and post treatment 2DFMs would have to be collected for the sample and the differences in the desired transition compared. If the intended outcome is to increase NBE for the analytical standard or microspheres, the NaBH<sub>4</sub>

treatment is superior causing a dramatic increase in NBE emission while for nanorods the PVA treatment is more effective.

To ensure that the results collected in this study would be comparable with future 2DFM studies, which may use different experimental setups, the determination of the quantum yield (QY) was of fundamental importance. The plate reader spectrometer used in this study, Tecan i-control M200 Pro, was not equipped with a photon counting detector or integrating sphere, meaning this type of device cannot directly determine QY. However, the determination of the relative quantum yield using R6G which has a known QY is possible. This study proposed a method for determining a first approximation of the QY for each emissive transition observed within the studied matter from the collected 2DFM. This method was applied to all three ZnO libraries studied: untreated, 0.5% PVA treated and 1M NaBH<sub>4</sub> treated. This approach is a robust method to approximate the QY of different emissive states and has good agreement with the percentile emission findings. The ability to obtain an approximation of QY from existing spectrometers not equipped with either an integrating sphere or photon counting detector makes it particularly attractive for screening semiconductor samples and quality control applications in both academic and industrial settings.

The observed emission behaviour of the ZnO-Au samples suggested that the ZnO matter surrounding the discrete gold inclusions in ZnO-Au feels the metallic environment of Au. This hypothesis was tested by modelling the spectral response of Au inclusions using Mie theory under the assumption that the inclusions had a spherical geometry. The modelled spectra had a good quality of fit adj-R<sup>2</sup> 0.88 and the modelled contributions were predominantly 92-96 nm Au inclusions, which were located within the ZnO volume of the sample. There was also a small contribution of 8-34nm Au inclusions which were located at the surface of the sample. The assumption of a spherical geometry of the gold inclusions when performing the Mie theory calculations was valid for the peak at 570 nm; however, the peak at 505 nm was unable to be fit under these assumptions. A future study could address this by performing Mie calculations using complex non-spherical geometries as it is known that Au particles with edges have a blue shifted Au<sub>SPR</sub> peak.<sup>330-332</sup> Summing the fitted Mie and nanoflower spectra formed a close approximation of the spectral features observed for the ZnO-Au sample. However, spectral differences on the blue side of the spectra were still observed suggesting that there is a difference between the two ZnOs in these samples. This supports the theory that electrons at the ZnO-Au boundary feel the metallic environment of Au.

The 2DFMs and approximated QY values for the NBE emission of the microspheres and analytical standard which are both microscale samples were of particular interest for fluorescence studies under microscopic resolution. In collaboration with Dr V. Volkov, confocal microscopy studies were performed to investigate the localisation and nature of emissive centers within the analytical standard and microspheres. A quadratic relationship between emission intensity and excitation power was observed for these microstructures under high power coherent radiation with a tight focusing regime using a confocal emission microscope, which resembles the physics that occurs in high-quality cavities. Initially, a quadratic power dependence was observed upon imaging excited band-gap carriers in the ZnO microcrystal. We propose the nonlinear behaviour observed was due to polariton formation where the coupling of radiation to the material response formed the lower polariton branch<sup>335,336</sup> as observed in high quality cavities. Above a threshold value the quadratic behaviour observed begins to break down which is assigned to quasi-particle annihilation and potentially ionisation. Dr V. Volkov has continued to explore this behaviour in greater depth using confocal spectral scanning, spatial filtering of confocal images and numerical modelling to develop an understanding of the nature of these emissive centers.

## 7.2 Future work

This study has generated several promising avenues for future study in the gold binding, 2DFM and ZnO/ZnO-Au studies and each area will be addressed in turn below. The gold binding studies highlighted the complexity of peptide binding interactions; to facilitate the development of engineered peptide sequences ‘from scratch’ a broader understanding of these systems is required. The sequences derived from A3 were developed in this study with the intent to improve on the binding efficacy of A3; however, all A3s sequences were worse binders due to the deletion of the Pro<sub>8</sub> residue from the A3 sequence. The A3s-C8 peptide sequence had the most comparable binding efficacy to the original A3 sequence suggesting that substitution of Cys<sub>9</sub> for Met<sub>9</sub> in the original A3 sequence could facilitate a stronger binding interaction.

The proposed preference of His for the Au<sub>(111)</sub> crystal facet over the Au<sub>(100)</sub> & Au<sub>(110)</sub> facets needs to be computationally validated in a future study where computational simulations are used to investigate the interaction between the His containing sequences (HRE & Pd4) and the Au<sub>(111)</sub>, Au<sub>(110)</sub> and Au<sub>(100)</sub> surfaces to determine binding preferences and elucidate the mechanism by which binding occurs. Additionally, a separate study should also computationally investigate the amino acid interactions with Au<sub>(110)</sub> and Au<sub>(100)</sub> surfaces to complement the existing Au<sub>111</sub> study by Hoefling *et al.*<sup>216</sup> as such research would assist the development of bespoke binding peptides.

During the ITC studies the entropic behaviour observed for the solvation vs peptide-Au binding studies could not be experimentally determined. The author proposes a future study using dynamic light scattering (DLS) titrations to measure particulate/aggregate size during each addition of titrant using the same incubation periods as the ITC studies. The DLS titrations should investigate both the peptide-Au interaction and peptide solvation to understand if any aggregation is occurring. Such data would facilitate the development of more representative analytical models.

The 2DFM technique is capable of working on existing instrumentation. However, through use of bespoke instrumentation direct measurement of the quantum yield of emissive states/transitions is possible, as well as measuring the effects of the gaseous environment on emission behaviour with increased sharpness of peak lineshapes through reduced temperature conditions. The bespoke instrumentation described would require an integrating sphere, photon counting detector, controlled atmosphere and a monochromator and would be able to perform low temperature measurements. Such a device should be designed to measure emission over a larger detection range (i.e. 250-3300nm) as this would allow exploration of the trap states within low band-gap materials (i.e. CdSe).

Future 2DFM studies should collect higher resolution datasets along the excitation axis as this would facilitate a higher quality of fitting and enable the software to be further developed to facilitate automation. Additional software improvements would focus mainly on the introduction of ‘quality of life’ features such as: removal of the weak high-order excitation signal from the dataset. The series of 1d-spectra to 2d-matrix compilation code and the removal of the weak high-order excitation signal could be developed on a microprocessor enabling compiling of 2D-arrays before the data reaches the pc. This could be implemented either by the manufacturer or as an after-market addon through use of single board computers (SBCs).

The first approximation of QY for the 2DFMs proposed in this study is robust for the studied ZnO samples. However, it currently relies on 1d slices along the emission axis, which assumes that  $y$ -width ( $\sigma_y$ )  $\gg$   $x$ -width ( $\sigma_x$ ) which is not always valid - for example for CdSe, studied in Chapter V,  $\sigma_y \ll \sigma_x$  meaning the approximation of QY will be very inaccurate. To avoid this potential error, future studies should collect a 2DFM for the R6G dye in both the liquid state (0.69  $\mu\text{M}$ ) and solid state (14.8  $\text{nmol}\cdot\text{g}^{-1}$ ). It would be expected to see diagonalisation in the emissive topology for both the liquid and solid R6G 2DFM, due to the R6G behaving like a molecular system.<sup>169,202</sup> The emissive states within the

2DFM for the liquid and solid R6G 2DFM should be fitted using the same approach used for the semiconductors studied in both Chapter V and Chapter VI, this will allow for deconvolution of the diagonalised spectral response of R6G. The deconvolved line-shapes can then be integrated to obtain the emission of the 2D-line-shape which will be the value for  $E_R$ . Likewise, integrals for the 2D-line-shapes for the transitions can be obtained and used as the  $E_S$  values. Using this approach would overcome the error introduced when the y-width ( $\sigma_y$ )  $\gg$  x-width ( $\sigma_x$ ) criterion is not satisfied.

Finally, during this study it was determined that the 2DFM technique is sensitive to the synthetic conditions used to synthesise ZnO matter, leading to a subset of emissive behaviour which could be attributed to the sample synthesised using a peptide -mediated synthetic route. Future studies could explore a wider variety of synthetic routes for ZnO and ZnOs with known/quantified defect populations to develop a systematic understanding of the interplay between synthetic conditions and defect population for ZnO. Such an understanding would facilitate the use of ZnO surface treatments with predictable outcomes which would be well suited to industrial settings. Exploration of other semiconductors such as TiO<sub>2</sub> which have been synthesised using different conditions including peptide-mediated synthesis to determine if similar synthetic route dependent emissive subsets are observed in other matter.

### 7.3 Conclusion

To conclude, this study has investigated the binding kinetics of peptide-Au at high concentrations and reviewed the kinetic models applied to these systems. This investigation led to the proposal of the Langmuir-Kisliuk kinetic model which is capable of fitting both high and low concentration kinetic datasets. The A3 sequence was determined as the strongest gold binder overall from the peptide-Au binding studies and was used as the gold binding region of the bespoke hybrid binding sequence, ZA2, which was developed in house. The ZA2 sequence was used as the peptide in the one-pot peptide-mediated synthetic route to synthesise ZnO-Au. Finally, 2DFM which is a novel technique for analysing the emissive states and transitions present within semiconductor matter was developed during this study and is sensitive to trace impurities and the synthetic route by which the sample was formed. The 2DFM technique is very applicable to semiconductor studies and quality control (QC) applications in both academic and industrial settings.

## References

- 1 N. Kröger, R. Deutzmann and M. Sumper, *Science*, 1999, **286**, 1129–1132.
- 2 W. Stöber, A. Fink and E. Bohn, *Journal of Colloid and Interface Science*, 1968, **26**, 62–69.
- 3 I. J. Lovette and J. W. Fitzpatrick, *Handbook of Bird Biology*, John Wiley & Sons, 2016.
- 4 B. Bhushan, *Philos. Trans. A Math. Phys. Eng. Sci.*, 2009, **367**, 1445–1486.
- 5 N. F. Lepora, P. Verschure and T. J. Prescott, *Bioinspir. Biomim.*, 2013, **8**, 013001.
- 6 U. G. K. Wegst, H. Bai, E. Saiz, A. P. Tomsia and R. O. Ritchie, *Nature Materials*, 2015, **14**, 23–36.
- 7 M. Eggermont, *Proceedings of the Canadian Engineering Education Association*, 2011.
- 8 L. Cooper, A. Gullane, J. Harvey, A. Hills, M. Zemura, J. Martindale, A. Rennie and D. Cheneler, *Comput. Methods Biomed. Engin.*, 2019, **22**, 1163–1173.
- 9 J. M. Slocik, J. T. Moore and D. W. Wright, *Nano Letters*, 2002, **2**, 169–173.
- 10 J. M. Slocik and D. W. Wright, *Biomacromolecules*, 2003, **4**, 1135–1141.
- 11 M. M. Tomczak, M. K. Gupta, L. F. Drummy, S. M. Rozenzhak and R. R. Naik, *Acta Biomater.*, 2009, **5**, 876–882.
- 12 S. Krüger, M. Schwarze, O. Baumann, C. Günter, M. Bruns, C. Kübel, D. V. Szabó, R. Meinusch, V. de Z. Bermudez and A. Taubert, *Beilstein J. Nanotechnol.*, 2018, **9**, 187–204.
- 13 L. Addadi, D. Joester, F. Nudelman and S. Weiner, *Chemistry*, 2006, **12**, 980–987.
- 14 K. Liu and L. Jiang, *Annu. Rev. Mater. Res.*, 2012, **42**, 231–263.
- 15 E. Dujardin and S. Mann, *Advanced Materials*, 2002, **14**, 775.
- 16 Z. Xia, 2016.
- 17 S. Mann, *J. Mater. Chem.*, 1995, **5**, 935.
- 18 C. M. Niemeyer, *Angew. Chem. Int. Ed Engl.*, 2001, **40**, 4128–4158.
- 19 A. Sanchez, S. Abbet, U. Heiz, W.-D. Schneider, H. Häkkinen, R. N. Barnett and U. Landman, *J. Phys. Chem. A*, 1999, **103**, 9573–9578.
- 20 E. Roduner, *Chem. Soc. Rev.*, 2006, **35**, 583–592.
- 21 T. Castro, R. Reifenberger, E. Choi and R. P. Andres, *Phys. Rev. B Condens. Matter*, 1990, **42**, 8548–8556.
- 22 G. Schmid and B. Corain, *Eur. J. Inorg. Chem.*, 2003, **2003**, 3081–3098.
- 23 B. D. Briggs and M. R. Knecht, *J. Phys. Chem. Lett.*, 2012, **3**, 405–418.
- 24 H. Kato, K. Asakura and A. Kudo, *J. Am. Chem. Soc.*, 2003, **125**, 3082–3089.
- 25 R. A. Wogelius and D. J. Vaughan, in *Environmental Mineralogy*, eds. G. Papp, T. G. Weiszburg, D. J. Vaughan and R. A. Wogelius, Mineralogical Society of Great Britain and Ireland, Budapest, 2000, pp. 7–87.
- 26 E. R. Dumont, *Proc. Biol. Sci.*, 2010, **277**, 2193–2198.
- 27 M. H. Ross, G. I. Kaye and W. Pawlina, *Histology: A Text and Atlas with Cell and Molecular Biology*, 2003.
- 28 R. O. Ritchie, M. J. Buehler and P. Hansma, *Physics Today*, 2009, **62**, 41–47.
- 29 A. Nanci, *Ten Cate's Oral Histology - E-Book: Development, Structure, and Function*, Elsevier Health Sciences, 2017.
- 30 S. Mann, *Biomineratization: Principles and Concepts in Bioinorganic Materials Chemistry*, Oxford University Press on Demand, 2001.
- 31 P. B. Kaufman, P. Dayanandan, Y. Takeoka, W. C. Bigelow, J. D. Jones and R. Iler, *Silicon and Siliceous Structures in Biological Systems*, 1981, 409–449.
- 32 R. B. Frankel, D. A. Bazylinski, M. S. Johnson and B. L. Taylor, *Biophysical Journal*, 1997, **73**, 994–1000.
- 33 R. M. Crawford, *Silicon and Siliceous Structures in Biological Systems*, 1981, 129–156.
- 34 S. Mann, *Nature*, 1988, **332**, 119–124.
- 35 A. Veis and A. Perry, *Biochemistry*, 1967, **6**, 2409–2416.
- 36 K. Sanford and M. Kumar, *Curr. Opin. Biotechnol.*, 2005, **16**, 416–421.

- 37 R. T. Knapp, C.-H. Wu, K. C. Mobilia and D. Joester, *J. Am. Chem. Soc.*, 2012, **134**, 17908–17911.
- 38 V. A. Hughes and D. E. Dunstan, in *Modern Biopolymer Science*, Elsevier, 2009, pp. 559–594.
- 39 J. M. Slocik, M. O. Stone and R. R. Naik, *Small*, 2005, **1**, 1048–1052.
- 40 I. Sóvágó, C. Kállay and K. Várnagy, *Coord. Chem. Rev.*, 2012, **256**, 2225–2233.
- 41 S. S. Krishna, I. Majumdar and N. V. Grishin, *Nucleic Acids Res.*, 2003, **31**, 532–550.
- 42 M.-K. Liang, O. Deschaume, S. V. Patwardhan and C. C. Perry, *J. Mater. Chem.*, 2011, **21**, 80–89.
- 43 C.-Y. Chiu, Y. Li, L. Ruan, X. Ye, C. B. Murray and Y. Huang, *Nat. Chem.*, 2011, **3**, 393–399.
- 44 Y. Li, Z. Tang, P. N. Prasad, M. R. Knecht and M. T. Swihart, *Nanoscale*, 2014, **6**, 3165–3172.
- 45 M. J. Limo, A. Sola-Rabada, E. Boix, V. Thota, Z. C. Westcott, V. Puddu and C. C. Perry, *Chem. Rev.*, 2018, **118**, 11118–11193.
- 46 M. J. Limo, C. C. Perry, A. A. Thyparambil, Y. Wei and R. A. Latour, *Bio-Inspired Nanotechnology*, 2014, 37–94.
- 47 C. Sanchez, H. Arribart and M. M. G. Guille, *Nat. Mater.*, 2005, **4**, 277–288.
- 48 T. Sun, G. Qing, B. Su and L. Jiang, *Chem. Soc. Rev.*, 2011, **40**, 2909–2921.
- 49 C. Tamerler and M. Sarikaya, *Acta Biomater.*, 2007, **3**, 289–299.
- 50 H. Dai, W.-S. Choe, C. K. Thai, M. Sarikaya, B. A. Traxler, F. Baneyx and D. T. Schwartz, *J. Am. Chem. Soc.*, 2005, **127**, 15637–15643.
- 51 M. Brune, J. L. Hunter, S. A. Howell, S. R. Martin, T. L. Hazlett, J. E. Corrie and M. R. Webb, *Biochemistry*, 1998, **37**, 10370–10380.
- 52 F. Marin and G. Luquet, in *Handbook of Biomineralization*, ed. E. Buerlein, Wiley-VCH Verlag GmbH, Weinheim, Germany, 2007, pp. 273–290.
- 53 S. Weiner, *J. Struct. Biol.*, 2008, **163**, 229–234.
- 54 J. W. Kehoe and B. K. Kay, *Chem. Rev.*, 2005, **105**, 4056–4072.
- 55 The Nobel Prize in Chemistry 2018,  
<https://www.nobelprize.org/prizes/chemistry/2018/press-release/>, (accessed 8 October 2019).
- 56 G. P. Whyburn, Y. Li and Y. Huang, *J. Mater. Chem.*, 2008, **18**, 3755.
- 57 V. Thota and C. C. Perry, *Recent Pat. Nanotechnol.*, 2017, **11**, 168–180.
- 58 S. Donatan, H. Yazici, H. Bermek, M. Sarikaya, C. Tamerler and M. Urgen, *Materials Science and Engineering: C*, 2009, **29**, 14–19.
- 59 J. Mao, X. Shi, Y.-B. Wu and S.-Q. Gong, *Materials* , DOI:10.3390/ma9080700.
- 60 C. Li, G. D. Botsaris and D. L. Kaplan, *Cryst. Growth Des.*, 2002, **2**, 387–393.
- 61 W. Wang, C. F. Anderson, Z. Wang, W. Wu, H. Cui and C.-J. Liu, *Chem. Sci.*, 2017, **8**, 3310–3324.
- 62 J. P. Palafox-Hernandez, Z. Tang, Z. E. Hughes, Y. Li, M. T. Swihart, P. N. Prasad, T. R. Walsh and M. R. Knecht, *Chem. Mater.*, 2014, **26**, 4960–4969.
- 63 S. Anu Mary Ealia and M. P. Saravanakumar, *IOP Conf. Ser.: Mater. Sci. Eng.*, 2017, **263**, 032019.
- 64 P. T.c., L. Mathew, N. Chandrasekaran, A. M. and A. Mukherjee, in *Biomimetics Learning from Nature*, ed. A. Mukherjee, InTech, 2010.
- 65 R. Bhandari, R. Coppage and M. R. Knecht, *Catal. Sci. Technol.*, 2012, **2**, 256–266.
- 66 Y. Suzumoto, M. Okuda and I. Yamashita, *Cryst. Growth Des.*, 2012, **12**, 4130–4134.
- 67 P. Ghosh, G. Han, M. De, C. K. Kim and V. M. Rotello, *Adv. Drug Deliv. Rev.*, 2008, **60**, 1307–1315.
- 68 M.-C. Daniel and D. Astruc, *Chem. Rev.*, 2004, **104**, 293–346.
- 69 V. Puddu, J. M. Slocik, R. R. Naik and C. C. Perry, *Langmuir*, 2013, **29**, 9464–9472.
- 70 C.-L. Chen, P. Zhang and N. L. Rosi, *J. Am. Chem. Soc.*, 2008, **130**, 13555–13557.
- 71 C. Song, M. G. Blaber, G. Zhao, P. Zhang, H. C. Fry, G. C. Schatz and N. L. Rosi, *Nano Lett.*, 2013, **13**, 3256–3261.
- 72 F. Xiao, F. Wang, X. Fu and Y. Zheng, *J. Mater. Chem.*, 2012, **22**, 2868.
- 73 K.-J. Kim, P. B. Kreider, C.-H. Chang, C.-M. Park and H.-G. Ahn, *J. Nanopart. Res.*, 2013, **15**, 14937.

- 74 F.-X. Xiao and B. Liu, *Nanoscale*, 2017, **9**, 17118–17132.
- 75 S. W. Boettcher, N. C. Strandwitz, M. Schierhorn, N. Lock, M. C. Lonergan and G. D. Stucky, *Nat. Mater.*, 2007, **6**, 592–596.
- 76 S. Bala, R. K. Aithal, P. Derosa, D. Janes and D. Kuila, *J. Phys. Chem. C*, 2010, **114**, 20877–20884.
- 77 G. Zhang, H. Fang, H. Yang, L. A. Jauregui, Y. P. Chen and Y. Wu, *Nano Lett.*, 2012, **12**, 3627–3633.
- 78 W.-Y. Lee, N.-W. Park, S.-Y. Kang, G.-S. Kim, J.-H. Koh, E. Saitoh and S.-K. Lee, *J. Phys. Chem. C*, 2019, **123**, 14187–14194.
- 79 A. Som, A. K. Samal, T. Udayabhaskararao, M. S. Bootharaju and T. Pradeep, *Chem. Mater.*, 2014, **26**, 3049–3056.
- 80 L. Wang, J. Wang, S. Zhang, Y. Sun, X. Zhu, Y. Cao, X. Wang, H. Zhang and D. Song, *Anal. Chim. Acta*, 2009, **653**, 109–115.
- 81 R. K. Joshi, Q. Hu, F. Alvi, N. Joshi and A. Kumar, *J. Phys. Chem. C*, 2009, **113**, 16199–16202.
- 82 E. Wongrat, P. Pimpang and S. Choopun, *Appl. Surf. Sci.*, 2009, **256**, 968–971.
- 83 T. Ning, Y. Zhou, H. Shen, H. Lu, Z. Sun, L. Cao, D. Guan, D. Zhang and G. Yang, *J. Phys. D Appl. Phys.*, 2007, **40**, 6705–6708.
- 84 K. Ozga, T. Kawaharamura, A. Ali Umar, M. Oyama, K. Nouneh, A. Slezak, S. Fujita, M. Piasecki, A. H. Reshak and I. V. Kityk, *Nanotechnology*, 2008, **19**, 185709.
- 85 V. Subramanian, E. E. Wolf and P. V. Kamat, *J. Phys. Chem. B*, 2003, **107**, 7479–7485.
- 86 N. Zheng and G. D. Stucky, *J. Am. Chem. Soc.*, 2006, **128**, 14278–14280.
- 87 J. W. Chiou, S. C. Ray, H. M. Tsai, C. W. Pao, F. Z. Chien, W. F. Pong, M.-H. Tsai, J. J. Wu, C. H. Tseng, C.-H. Chen, J. F. Lee and J.-H. Guo, *Appl. Phys. Lett.*, 2007, **90**, 192112.
- 88 Z. H. Chen, Y. B. Tang, C. P. Liu, Y. H. Leung, G. D. Yuan, L. M. Chen, Y. Q. Wang, I. Bello, J. A. Zapien, W. J. Zhang, C. S. Lee and S. T. Lee, *J. Phys. Chem. C*, 2009, **113**, 13433–13437.
- 89 Y. Nishijima, K. Ueno, Y. Yokota, K. Murakoshi and H. Misawa, *J. Phys. Chem. Lett.*, 2010, **1**, 2031–2036.
- 90 Z. Sun, C. Wang, J. Yang, B. Zhao and J. R. Lombardi, *J. Phys. Chem. C*, 2008, **112**, 6093–6098.
- 91 T. Sakano, Y. Tanaka, R. Nishimura, N. N. Nedyalkov, P. A. Atanasov, T. Saiki and M. Obara, *J. Phys. D Appl. Phys.*, 2008, **41**, 235304.
- 92 J. Im, J. Singh, J. W. Soares, D. M. Steeves and J. E. Whitten, *J. Phys. Chem. C*, 2011, **115**, 10518–10523.
- 93 X. Wang, X. Kong, Y. Yu and H. Zhang, *The Journal of Physical Chemistry C*, 2007, **111**, 3836–3841.
- 94 M. J. Limo and C. C. Perry, *Langmuir*, 2015, **31**, 6814–6822.
- 95 M. J. Limo, PhD, Nottingham Trent University, 09 October, 2015.
- 96 M. Hnilova, E. E. Oren, U. O. S. Seker, B. R. Wilson, S. Collino, J. S. Evans, C. Tamerler and M. Sarikaya, *Langmuir*, 2008, **24**, 12440–12445.
- 97 D. B. Pacardo, M. Sethi, S. E. Jones, R. R. Naik and M. R. Knecht, *ACS Nano*, 2009, **3**, 1288–1296.
- 98 H. Heinz, B. L. Farmer, R. B. Pandey, J. M. Slocik, S. S. Patnaik, R. Pachter and R. R. Naik, *J. Am. Chem. Soc.*, 2009, **131**, 9704–9714.
- 99 R. R. Naik, S. J. Stringer, G. Agarwal, S. E. Jones and M. O. Stone, *Nat. Mater.*, 2002, **1**, 169–172.
- 100 B. Hammer and J. K. Norskov, *Nature*, 1995, **376**, 238–240.
- 101 M. Duckenfield, *The Monetary History of Gold: A Documentary History, 1660-1999*, Routledge, 2016.
- 102 I. Freestone, N. Meeks, M. Sax and C. Higgitt, *Gold Bulletin*, 2007, **40**, 270–277.
- 103 M. Faraday, *The Bakerian Lecture: Experimental relations of gold (and other metals) to light*, 1857.
- 104 R. Sardar, A. M. Funston, P. Mulvaney and R. W. Murray, *Langmuir*, 2009, **25**, 13840–13851.

- 105 A. Gole and C. J. Murphy, *Chemistry of Materials*, 2004, **16**, 3633–3640.
- 106 M. Wuithschick, A. Birnbaum, S. Witte, M. Sztucki, U. Vainio, N. Pinna, K. Rademann, F. Emmerling, R. Krahnert and J. Polte, *ACS Nano*, 2015, **9**, 7052–7071.
- 107 D. Oliver, M. Michaelis, H. Heinz, V. V. Volkov and C. C. Perry, *Phys. Chem. Chem. Phys.*, 2019, **21**, 4663–4672.
- 108 T. R. Walsh, *Acc. Chem. Res.*, 2017, **50**, 1617–1624.
- 109 A. Sola-Rabada, M. Michaelis, D. J. Oliver, M. J. Roe, L. Colombi Ciacchi, H. Heinz and C. C. Perry, *Langmuir*, 2018, **34**, 8255–8263.
- 110 Q. Shao and C. K. Hall, *Langmuir*, 2016, **32**, 7888–7896.
- 111 A. K. Samal, T. S. Sreeprasad and T. Pradeep, *Journal of Nanoparticle Research*, 2010, **12**, 1777–1786.
- 112 I. Langmuir, *Journal of the American Chemical Society*, 1918, **40**, 1361–1403.
- 113 P. Kisliuk, *Journal of Physics and Chemistry of Solids*, 1957, **3**, 95–101.
- 114 R. B. Heller, J. McGannon and A. H. Weber, *Journal of Applied Physics*, 1950, **21**, 1283–1284.
- 115 A. Cimino, M. Marezio and A. Santoro, *Die Naturwissenschaften*, 1957, **44**, 348–349.
- 116 R. A. Powell, W. E. Spicer and J. C. McMenamin, *Physical Review B*, 1972, **6**, 3056–3065.
- 117 V. Srikanth and D. R. Clarke, *Journal of Applied Physics*, 1998, **83**, 5447–5451.
- 118 G. Heiland, E. Mollwo and F. Stöckmann, Elsevier, 1959, vol. 8, pp. 191–323.
- 119 J. W. Anthony, *Handbook of Mineralogy*, Mineral Data Pub, 1995.
- 120 Wiley-VCH Verlag GmbH & Co. KGaA, Ed., in *Ullmann's Encyclopedia of Industrial Chemistry*, Wiley-VCH Verlag GmbH & Co. KGaA, Weinheim, Germany, 2000, vol. 5, p. 27.
- 121 H. Morkoç and Ü. Özgür, *Zinc Oxide: Fundamentals, Materials and Device Technology*, John Wiley & Sons, 2008.
- 122 L. Yin, L. Zhang, F. Li and M. Yu, *Materials Research Bulletin*, 2005, **40**, 2219–2224.
- 123 A. R. Nimbalkar and M. G. Patil, *Physica B: Condensed Matter*, 2017, **527**, 7–15.
- 124 Y. Zhang, M. K. Ram, E. K. Stefanakos and D. Yogi Goswami, *Journal of Nanomaterials*, 2012, **2012**, 1–22.
- 125 J.-J. Dong, J. Wu, H.-Y. Hao, J. Xing, H. Liu and H. Gao, *Nanoscale Res. Lett.*, 2017, **12**, 529.
- 126 Y. Xi, C. G. Hu, X. Y. Han, Y. F. Xiong, P. X. Gao and G. B. Liu, *Solid State Communications*, 2007, **141**, 506–509.
- 127 B. Lin, Z. Fu and Y. Jia, *Applied Physics Letters*, 2001, **79**, 943–945.
- 128 S. A. M. Lima, F. A. Sigoli, M. Jafelicci Jr and M. R. Davolos, *International Journal of Inorganic Materials*, 2001, **3**, 749–754.
- 129 S. A. Studenikin, N. Golego and M. Cocivera, *J. Appl. Phys.*, 1998, **84**, 2287–2294.
- 130 Q. Li, S.-L. Chen and W.-C. Jiang, *J. Appl. Polym. Sci.*, 2007, **103**, 412–416.
- 131 H. Hong, F. Wang, Y. Zhang, S. A. Graves, S. B. Z. Eddine, Y. Yang, C. P. Theuer, R. J. Nickles, X. Wang and W. Cai, *ACS Appl. Mater. Interfaces*, 2015, **7**, 3373–3381.
- 132 K. Nomura, H. Ohta, K. Ueda, T. Kamiya, M. Hirano and H. Hosono, *Science*, 2003, **300**, 1269–1272.
- 133 B.-Y. Oh, M.-C. Jeong, T.-H. Moon, W. Lee, J.-M. Myoung, J.-Y. Hwang and D.-S. Seo, *Journal of Applied Physics*, 2006, **99**, 124505.
- 134 Z. L. Wang and J. Song, *Science*, 2006, **312**, 242–246.
- 135 C. T. Troy, New Phosphor View Promises Display Advances, [https://www.photonics.com/Articles/New\\_Phosphor\\_View\\_Promises\\_Display\\_Advances/a122](https://www.photonics.com/Articles/New_Phosphor_View_Promises_Display_Advances/a122), (accessed 29 February 2020).
- 136 K. Vanheusden, C. H. Seager, W. L. Warren, D. R. Tallant, J. Caruso, M. J. Hampden-Smith and T. T. Kodas, *J. Lumin.*, 1997, **75**, 11–16.
- 137 S. Xu, Y. Qin, C. Xu, Y. Wei, R. Yang and Z. L. Wang, *Nature Nanotechnology*, 2010, **5**, 366–373.
- 138 X. Wang, C. J. Summers and Z. L. Wang, *Nano Lett.*, 2004, **4**, 423–426.
- 139 H. Karzel, W. Potzel, M. Köfferlein, W. Schiessl, M. Steiner, U. Hiller, G. M. Kalvius, D. W. Mitchell, T. P. Das, P. Blaha, K. Schwarz and M. P. Pasternak, *Physical*

- Review B*, 1996, **53**, 11425–11438.
- 140 E. H. Kisi and M. M. Elcombe, *Acta Crystallographica Section C Crystal Structure Communications*, 1989, **45**, 1867–1870.
- 141 M. Catti, Y. Noel and R. Dovesi, *Journal of Physics and Chemistry of Solids*, 2003, **64**, 2183–2190.
- 142 S. Desgreniers, *Physical Review B*, 1998, **58**, 14102–14105.
- 143 L. Gerward and J. S. Olsen, *J. Synchrotron Radiat.*, 1995, **2**, 233–235.
- 144 R. R. Reeber, *Journal of Applied Physics*, 1970, **41**, 5063–5066.
- 145 W. P. Davey, *Physical Review*, 1925, **25**, 753–761.
- 146 A. Maeland and T. B. Flanagan, *Canadian Journal of Physics*, 1964, **42**, 2364–2366.
- 147 U. Rössler, *Physical Review*, 1969, **184**, 733–738.
- 148 S. Bloom and I. Ortenburger, *Phys. Stat. Sol. (b)*, 1973, **58**, 561–566.
- 149 J. R. Chelikowsky, *Solid State Commun.*, 1977, **22**, 351–354.
- 150 P. Schröer, P. Krüger and J. Pollmann, *Phys. Rev. B Condens. Matter*, 1994, **49**, 17092–17101.
- 151 R. A. Powell, W. E. Spicer and J. C. McMenamin, *Physical Review Letters*, 1971, **27**, 97–100.
- 152 L. Ley, R. A. Pollak, F. R. McFeely, S. P. Kowalczyk and D. A. Shirley, *Physical Review B*, 1974, **9**, 600–621.
- 153 D. W. Langer and C. J. Vesely, *Physical Review B*, 1970, **2**, 4885–4892.
- 154 I. Ivanov and J. Pollmann, *Phys. Rev. B Condens. Matter*, 1981, **24**, 7275–7296.
- 155 D. H. Lee and J. D. Joannopoulos, *Phys. Rev. B Condens. Matter*, 1981, **24**, 6899–6907.
- 156 P. Schröer, P. Krüger and J. Pollmann, *Phys. Rev. B Condens. Matter*, 1993, **47**, 6971–6980.
- 157 S. Massidda, R. Resta, M. Posternak and A. Baldereschi, *Phys. Rev. B Condens. Matter*, 1995, **52**, 16977–16980.
- 158 D. Vogel, P. Krüger and J. Pollmann, *Phys. Rev. B Condens. Matter*, 1995, **52**, 14316–14319.
- 159 Ü. Özgür, Y. I. Alivov, C. Liu, A. Teke, M. A. Reshchikov, S. Doğan, V. Avrutin, S.-J. Cho and H. Morkoç, *J. Appl. Phys.*, 2005, **98**, 041301.
- 160 M. Cardona and G. Güntherodt, Eds., *Light Scattering in Solids VI*, Springer Berlin Heidelberg, Berlin, Heidelberg, 1991, vol. 68.
- 161 *Proc. R. Soc. Lond. A Math. Phys. Sci.*, 1927, **114**, 243–265.
- 162 Libretexts, 12.8: Spontaneous Emission,  
[https://phys.libretexts.org/Bookshelves/Quantum\\_Mechanics/Book%3A\\_Introductory\\_Quantum\\_Mechanics\\_\(Fitzpatrick\)/12%3A\\_Time-Dependent\\_Perturbation\\_Theory/12.08%3A\\_Spontaneous\\_Emission](https://phys.libretexts.org/Bookshelves/Quantum_Mechanics/Book%3A_Introductory_Quantum_Mechanics_(Fitzpatrick)/12%3A_Time-Dependent_Perturbation_Theory/12.08%3A_Spontaneous_Emission), (accessed 12 May 2020).
- 163 Libretexts, 4. Recombination with Defect Levels (Shockley-Read-Hall),  
[https://eng.libretexts.org/Bookshelves/Materials\\_Science/Supplemental\\_Modules\\_\(Materials\\_Science\)/Solar\\_Basics/C.\\_Semiconductors\\_and\\_Solar\\_Interactions/IV.\\_Recombination\\_of\\_Charge\\_Carriers/4.\\_Recombination\\_with\\_Defect\\_Levels\\_\(Shockley-Read-Hall\)](https://eng.libretexts.org/Bookshelves/Materials_Science/Supplemental_Modules_(Materials_Science)/Solar_Basics/C._Semiconductors_and_Solar_Interactions/IV._Recombination_of_Charge_Carriers/4._Recombination_with_Defect_Levels_(Shockley-Read-Hall)), (accessed 12 May 2020).
- 164 J. Ewles and R. Whiddington, *Proceedings of the Royal Society A: Mathematical, Physical and Engineering Sciences*, 1938, **167**, 34–52.
- 165 J. T. Randall, *Transactions of the Faraday Society*, 1939, **35**, 2.
- 166 H. Zeng, G. Duan, Y. Li, S. Yang, X. Xu and W. Cai, *Adv. Funct. Mater.*, 2010, **20**, 561–572.
- 167 R. Raji and K. G. Gopchandran, *Journal of Science: Advanced Materials and Devices*, 2017, **2**, 51–58.
- 168 R. K. Biroju and P. K. Giri, *Journal of Applied Physics*, 2017, **122**, 044302.
- 169 S. Marose, C. Lindemann and T. Scheper, *Biotechnol. Prog.*, 1998, **14**, 63–74.
- 170 E. L. Kovrigin, *PLoS One*, 2014, **9**, e101227.
- 171 R. W. Woody, *Circular Dichroism and the Conformational Analysis of Biomolecules*, 1996, 25–67.
- 172 J. L. S. Lopes, A. J. Miles, L. Whitmore and B. A. Wallace, *Protein Sci.*, 2014, **23**,

- 1765–1772.
- 173 G. H. Wagnière, *Comprehensive Chiroptical Spectroscopy*, 2012, 1–34.
- 174 N. J. Greenfield, *Nat. Protoc.*, 2006, **1**, 2876–2890.
- 175 A. Micsonai, F. Wien, L. Kerna, Y.-H. Lee, Y. Goto, M. Réfrégiers and J. Kardos, *Proc. Natl. Acad. Sci. U. S. A.*, 2015, **112**, E3095–103.
- 176 A. Micsonai, F. Wien, É. Bulyáki, J. Kun, É. Moussong, Y.-H. Lee, Y. Goto, M. Réfrégiers and J. Kardos, *Nucleic Acids Res.*, 2018, **46**, W315–W322.
- 177 J. Pawley, *Handbook of Biological Confocal Microscopy*, Springer Science & Business Media, 2006.
- 178 E. Abbe, *Archiv für Mikroskopische Anatomie*, 1873, **9**, 413–468.
- 179 L. De Broglie, *Annales de Physique*, 1925, **10**, 22–128.
- 180 B. Michen, C. Geers, D. Vanhecke, C. Endes, B. Rothen-Rutishauser, S. Balog and A. Petri-Fink, *Sci. Rep.*, 2015, **5**, 9793.
- 181 E. Freire, O. L. Mayorga and M. Straume, *Analytical Chemistry*, 1990, **62**, 950A–959A.
- 182 M. M. Pierce, C. S. Raman and B. T. Nall, *Methods*, 1999, **19**, 213–221.
- 183 M. W. Freyer and E. A. Lewis, *Methods Cell Biol.*, 2008, **84**, 79–113.
- 184 M. J. Cliff, A. Gutierrez and J. E. Ladbury, *J. Mol. Recognit.*, 2004, **17**, 513–523.
- 185 S. Milev, *General Electric*.
- 186 H. M. Hiep, T. Endo, K. Kerman, M. Chikae, D.-K. Kim, S. Yamamura, Y. Takamura and E. Tamiya, *Sci. Technol. Adv. Mater.*, 2007, **8**, 331–338.
- 187 K. Korhonen, N. Granqvist, J. Ketolainen and R. Laitinen, *Int. J. Pharm.*, 2015, **494**, 531–536.
- 188 H. Ju, X. Zhang and J. Wang, *NanoBiosensing: Principles, Development and Application*, Springer Science & Business Media, 2011.
- 189 W. L. Bragg, *Science*, 1934, **79**, 237–240.
- 190 B. D. Cullity, *Elements of X Ray Diffraction*, Nabu Press, 2011.
- 191 C. Whiston, *X-Ray Methods*, Wiley, 1987.
- 192 H. P. Klug and L. E. Alexander, *X-Ray Diffraction Procedures: For Polycrystalline and Amorphous Materials*, Wiley-Interscience, 1974.
- 193 J. H. Crawford and L. M. Slifkin, *Point Defects in Solids: General and Ionic Crystals*, Springer Science & Business Media, 2013.
- 194 W. Böllmann, 1970.
- 195 A. Kelly, G. W. Groves and P. Kidd, *Crystallography and Crystal Defects*, John Wiley & Sons, 2000.
- 196 R. B. Merrifield, *Journal of the American Chemical Society*, 1963, **85**, 2149–2154.
- 197 F. Albericio and S. A. Kates, *Solid-Phase Synthesis: A Practical Guide*, CRC Press, 2000.
- 198 USPTO, -20070090104-A1, *US Patent*, 2007.
- 199 L. Qin, C. Shing, S. Sawyer and P. S. Dutta, *Optical Materials*, 2011, **33**, 359–362.
- 200 X.-F. Su, J.-B. Chen, R.-M. He, Y. Li, J. Wang and C.-W. Wang, *Materials Science in Semiconductor Processing*, 2017, **67**, 55–61.
- 201 T. Hu, F. Li, K. Yuan and Y. Chen, *ACS Appl. Mater. Interfaces*, 2013, **5**, 5763–5770.
- 202 C. Lindemann, S. Marose, H. O. Nielsen and T. Scheper, *Sensors and Actuators B: Chemical*, 1998, **51**, 273–277.
- 203 T. A. Caswell, M. Droettboom, J. Hunter, A. Lee, E. Firing, D. Stansby, J. Klymak, E. S. de Andrade, J. H. Nielsen, N. Varoquaux, T. Hoffmann, B. Root, P. Elson, R. May, D. Dale, J.-J. Lee, J. K. Seppänen, D. McDougall, A. Straw, P. Hobson, C. Gohlke, T. S. Yu, E. Ma, A. F. Vincent, S. Silvester, C. Moad, J. Katins, N. Kniazev, F. Ariza and E. Ernest, , DOI:10.5281/zenodo.3264781.
- 204 J. D. Hunter, *Computing in Science & Engineering*, 2007, **9**, 90–95.
- 205 S. John, *Phys. Rev. Lett.*, 1987, **58**, 2486–2489.
- 206 W. Haiss, N. T. K. Thanh, J. Aveyard and D. G. Fernig, *Anal. Chem.*, 2007, **79**, 4215–4221.
- 207 H. Freundlich, *Zeitschrift für Physikalische Chemie*, , DOI:10.1515/zpch-1907-5723.
- 208 W. Rudzinski and T. Panczyk, *The Journal of Physical Chemistry B*, 2001, **105**, 6858–6866.

- 209 K. Levenberg, *Quarterly of Applied Mathematics*, 1944, 2, 164–168.
- 210 D. W. Marquardt, *Journal of the Society for Industrial and Applied Mathematics*, 1963, 11, 431–441.
- 211 P. Das and M. Reches, *Biopolymers*, 2015, 104, 480–494.
- 212 P. Das, T. Duanias-Assaf and M. Reches, *Journal of Visualized Experiments*, 2017.
- 213 M. P. Ramírez, M. Rivera, D. Quiroga-Roger, A. Bustamante, M. Vega, M. Baez, E. M. Puchner and C. A. M. Wilson, *Protein Sci.*, 2017, **26**, 1404–1412.
- 214 R. B. Pandey, H. Heinz, J. Feng, B. L. Farmer, J. M. Slocik, L. F. Drummy and R. R. Naik, *Phys. Chem. Chem. Phys.*, 2009, **11**, 1989–2001.
- 215 J. Yu, M. L. Becker and G. A. Carri, *Langmuir*, 2012, **28**, 1408–1417.
- 216 M. Hoefling, F. Iori, S. Corni and K.-E. Gottschalk, *Langmuir*, 2010, **26**, 8347–8351.
- 217 V. F. Gallucci and T. J. Quinn, *Transactions of the American Fisheries Society*, 1979, 108, 14–25.
- 218 T. M. Swannack, *Encyclopedia of Ecology*, 2008, 1799–1805.
- 219 I. Mills, T. Cvitas, K. Homann, N. Kallay and K. Kuchitsu, *Quantities, Units and Symbols in Physical Chemistry*, Blackwell Scientific Publications, Oxford, 1993.
- 220 J. A. Tullman, W. F. Finney, Y.-J. Lin and S. W. Bishnoi, *Plasmonics*, 2007, 2, 119–127.
- 221 K. L. Zapadka, F. J. Becher, A. L. Gomes Dos Santos and S. E. Jackson, *Interface Focus*, 2017, **7**, 20170030.
- 222 K. Oura, V. G. Lifshits, A. A. Saranin, A. V. Zотов and M. Katayama, *Surface Science: An Introduction*, Springer Science & Business Media, 2013.
- 223 C. N. R. Rao, G. U. Kulkarni, P. John Thomas and P. P. Edwards, *Trends in Chemistry of Materials*, 2008, 435–441.
- 224 J. G. Lees, B. R. Smith, F. Wien, A. J. Miles and B. A. Wallace, *Anal. Biochem.*, 2004, **332**, 285–289.
- 225 B. Delaunay, *Bulletin de l'Académie des Sciences de l'URSS. Classe des sciences mathématiques et na*, 1934, 793–800.
- 226 G. Yang, C. Cecconi, W. A. Baase, I. R. Vetter, W. A. Breyer, J. A. Haack, B. W. Matthews, F. W. Dahlquist and C. Bustamante, *Proc. Natl. Acad. Sci. U. S. A.*, 2000, **97**, 139–144.
- 227 H. Dietz and M. Rief, *Proc. Natl. Acad. Sci. U. S. A.*, 2006, **103**, 1244–1247.
- 228 M. Carrion-Vazquez, H. Li, H. Lu, P. E. Marszalek, A. F. Oberhauser and J. M. Fernandez, *Nat. Struct. Biol.*, 2003, **10**, 738–743.
- 229 F. Oesterhelt, D. Oesterhelt, M. Pfeiffer, A. Engel, H. E. Gaub and D. J. Müller, *Science*, 2000, **288**, 143–146.
- 230 E. Pensa, E. Cortés, G. Corthey, P. Carro, C. Vericat, M. H. Fonticelli, G. Benítez, A. A. Rubert and R. C. Salvarezza, *Accounts of Chemical Research*, 2012, 45, 1183–1192.
- 231 S. Moon, S.-I. Tanaka and T. Sekino, *Nanoscale Res. Lett.*, 2010, **5**, 813–817.
- 232 M. K. Corbierre and R. Bruce Lennox, *Chemistry of Materials*, 2005, 17, 5691–5696.
- 233 T.-L. Ho and T. -L. Ho, *Chemischer Informationsdienst*, 1975, 6, no–no.
- 234 R. G. Parr and R. G. Pearson, *Journal of the American Chemical Society*, 1983, 105, 7512–7516.
- 235 H. Xu, D. C. Xu and Y. Wang, *ACS Omega*, 2017, **2**, 7185–7193.
- 236 C. Zhu, Y. Gao, H. Li, S. Meng, L. Li, J. S. Francisco and X. C. Zeng, *Proceedings of the National Academy of Sciences*, 2016, 113, 12946–12951.
- 237 J. Feng, J. M. Slocik, M. Sarikaya, R. R. Naik, B. L. Farmer and H. Heinz, *Small*, 2012, **8**, 1049–1059.
- 238 Malvern Panalytical, Isothermal Titration Calorimetry (ITC), <https://www.malvernpanalytical.com/en/products/technology/microcalorimetry/isothermal-titration-calorimetry/>, (accessed 4 July 2020).
- 239 X. Yan, *Linear Regression Analysis: Theory and Computing*, World Scientific, 2009.
- 240 F. J. Anscombe, *Am. Stat.*, 1973, **27**, 17–21.
- 241 J. Vondrásek, P. E. Mason, J. Heyda, K. D. Collins and P. Jungwirth, *J. Phys. Chem. B*, 2009, **113**, 9041–9045.
- 242 J. Heyda, P. E. Mason and P. Jungwirth, *J. Phys. Chem. B*, 2010, **114**, 8744–8749.

- 243 Z. Qin, A. Fabre and M. J. Buehler, *The European Physical Journal E*, 2013, 36.
- 244 International Telecommunications Union, 2019.
- 245 US, 7256622B2, *Patent*, 14 August, 2007.
- 246 US, 4005471A, *Patent*, 25 January, 1977.
- 247 US, 3067485A, *Patent*, 11 December, 1962.
- 248 US, 3293513, *Patent*, 20 December, 1966.
- 249 M. Bredol and J. Merikhi, *J. Mater. Sci.*, 1998, **33**, 471–476.
- 250 US, 3102230A, *Patent*, 27 August, 1963.
- 251 A. Einstein, *Strahlungs-Emission und -Absorption nach der Quantentheorie*, 1916.
- 252 A. Einstein, *Zur Quantentheorie der Strahlung*, 1917.
- 253 J. Kasprzak, M. Richard, S. Kundermann, A. Baas, P. Jeambrun, J. M. J. Keeling, F. M. Marchetti, M. H. Szymańska, R. André, J. L. Staehli, V. Savona, P. B. Littlewood, B. Deveaud and L. S. Dang, *Nature*, 2006, **443**, 409–414.
- 254 M. Donaire, *Physical Review A*, 2011, 83.
- 255 M. K. Liang, PhD, Nottingham Trent University, 2010.
- 256 helpdesk-uk@tecan.com, 2019.
- 257 Tecan, *Tecan Instructions For Use For infinite 200*, Tecan, 2008.
- 258 helpdesk-uk@tecan.com, 03 April, 2019.
- 259 Adobe Systems Incorporated, *Adobe Type 1 Font Format*, Adobe Systems Incorporated, 1990.
- 260 A. B. Djurisić and Y. H. Leung, *Small*, 2006, **2**, 944–961.
- 261 P. S. Xu, Y. M. Sun, C. S. Shi, F. Q. Xu and H. B. Pan, *Nuclear Instruments and Methods in Physics Research Section B: Beam Interactions with Materials and Atoms*, 2003, 199, 286–290.
- 262 T. A. Caswell, M. Droettboom, A. Lee, J. Hunter, E. Firing, D. Stansby, J. Klymak, T. Hoffmann, E. S. de Andrade, N. Varoquaux, J. H. Nielsen, B. Root, P. Elson, R. May, D. Dale, J.-J. Lee, J. K. Seppänen, D. McDougall, A. Straw, P. Hobson, C. Gohlke, T. S. Yu, E. Ma, A. F. Vincent, S. Silvester, C. Moad, N. Kniazev, P. Ivanov, E. Ernest and J. Katins, , DOI:10.5281/zenodo.3714460.
- 263 M. Newville, T. Stensitzki, D. B. Allen and A. Ingargiola, , DOI:10.5281/zenodo.11813.
- 264 S. van der Walt, S. C. Colbert and G. Varoquaux, *Comput. Sci. Eng.*, 2011, **13**, 22–30.
- 265 W. McKinney, in *Proceedings of the 9th Python in Science Conference*, SciPy, 2010, pp. 56–61.
- 266 B. O'Regan and M. Grätzel, *Nature*, 1991, 353, 737–740.
- 267 M. Wagemaker, A. P. M. Kentgens and F. M. Mulder, *Nature*, 2002, 418, 397–399.
- 268 R. Wang, K. Hashimoto, A. Fujishima, M. Chikuni, E. Kojima, A. Kitamura, M. Shimohigoshi and T. Watanabe, *Nature*, 1997, 388, 431–432.
- 269 N. Daude, C. Gout and C. Jouanin, *Physical Review B*, 1977, 15, 3229–3235.
- 270 D. K. Pallotti, L. Passoni, P. Maddalena, F. Di Fonzo and S. Lettieri, *The Journal of Physical Chemistry C*, 2017, 121, 9011–9021.
- 271 P. T. Snee, R. C. Somers, G. Nair, J. P. Zimmer, M. G. Bawendi and D. G. Nocera, *J. Am. Chem. Soc.*, 2006, **128**, 13320–13321.
- 272 K. Ando, H. Ishikura, Y. Fukunaga, T. Kubota, H. Maeta, T. Abe and H. Kasada, *physica status solidi (b)*, 2002, 229, 1065–1071.
- 273 C. Ma, D. Moore, Y. Ding, J. Li and Z. L. Wang, *International Journal of Nanotechnology*, 2004, 1, 431.
- 274 Y. Jiang, W. J. Zhang, J. S. Jie, X. M. Meng, J. A. Zapien and S.-T. Lee, *Advanced Materials*, 2006, 18, 1527–1532.
- 275 N. R. Pawaskar, S. D. Sathaye, M. M. Bhadbhade and K. R. Patil, *Materials Research Bulletin*, 2002, 37, 1539–1546.
- 276 K. Lischka, *physica status solidi (b)*, 1997, 202, 673–681.
- 277 T. Hattori, Y. Homma, A. Mitsuishi and M. Tacke, *Optics Communications*, 1973, 7, 229–232.
- 278 L. Thamizhmani, A. K. Azad, J. Dai and W. Zhang, *Applied Physics Letters*, 2005, 86, 131111.

- 279 P. Calandra, M. Goffredi and V. Turco Liveri, *Colloids and Surfaces A: Physicochemical and Engineering Aspects*, 1999, **160**, 9–13.
- 280 S. Park, C. Jin, H. Kim, C. Hong and C. Lee, *Journal of Luminescence*, 2012, **132**, 231–235.
- 281 D. Denzler, M. Olschewski and K. Sattler, *Journal of Applied Physics*, 1998, **84**, 2841–2845.
- 282 D. C. Reynolds, L. S. Pedrotti and O. W. Larson, *Journal of Applied Physics*, 1961, **32**, 2250–2254.
- 283 D. D. Nedeoglo and A. V. Simashkevich, *Shtiintsa, Kishinev*, 1984, 150.
- 284 R. J. Collins, *Journal of Applied Physics*, 1959, **30**, 1135–1140.
- 285 R. G. Wheeler and J. O. Dimmock, *Physical Review*, 1962, **125**, 1805–1815.
- 286 M. Bruchez, M. Moronne, P. Gin, S. Weiss and A. Paul Alivisatos, *Science*, 1998, **281**, 2013–2016.
- 287 W. C. W. Chan and S. Nie, *Science*, 1998, **281**, 2016–2018.
- 288 W. U. Huynh, J. J. Dittmer and A. P. Alivisatos, *Science*, 2002, **295**, 2425–2427.
- 289 T. Ablekim, J. N. Duenow, X. Zheng, H. Moutinho, J. Moseley, C. L. Perkins, S. W. Johnston, P. O’Keefe, E. Colegrave, D. S. Albin, M. O. Reese and W. K. Metzger, *ACS Energy Letters*, 2020, **5**, 892–896.
- 290 M. C. Schlamp, X. Peng and A. P. Alivisatos, *Journal of Applied Physics*, 1997, **82**, 5837–5842.
- 291 S. Coe, W.-K. Woo, M. Bawendi and V. Bulović, *Nature*, 2002, **420**, 800–803.
- 292 F. A. Kröger, *Physica*, 1940, **7**, 1–12.
- 293 M. Hamity and R. H. Lema, *Journal of Photochemistry and Photobiology A: Chemistry*, 1996, **99**, 177–183.
- 294 S. A. Ivanov, A. Piryatinski, J. Nanda, S. Tretiak, K. R. Zavadil, W. O. Wallace, D. Werder and V. I. Klimov, *J. Am. Chem. Soc.*, 2007, **129**, 11708–11719.
- 295 K. Wu, Y. Du, H. Tang, Z. Chen and T. Lian, *J. Am. Chem. Soc.*, 2015, **137**, 10224–10230.
- 296 C. Pu and X. Peng, *J. Am. Chem. Soc.*, 2016, **138**, 8134–8142.
- 297 B. O. Dabbousi, J. Rodriguez-Viejo, F. V. Mikulec, J. R. Heine, H. Mattoussi, R. Ober, K. F. Jensen and M. G. Bawendi, *The Journal of Physical Chemistry B*, 1997, **101**, 9463–9475.
- 298 O. Chen, J. Zhao, V. P. Chauhan, J. Cui, C. Wong, D. K. Harris, H. Wei, H.-S. Han, D. Fukumura, R. K. Jain and M. G. Bawendi, *Nat. Mater.*, 2013, **12**, 445–451.
- 299 M. Aven and J. S. Prener, *Physics and chemistry of II-VI compounds*, 1967.
- 300 M. Chen, L. Yan, Y. Zhao, I. Murtaza, H. Meng and W. Huang, *Journal of Materials Chemistry C*, 2018, **6**, 7416–7444.
- 301 G. Giri, E. Verploegen, S. C. B. Mannsfeld, S. Atahan-Evrenk, D. H. Kim, S. Y. Lee, H. A. Becerril, A. Aspuru-Guzik, M. F. Toney and Z. Bao, *Nature*, 2011, **480**, 504–508.
- 302 Z. A. Dreger, H. Lucas and Y. M. Gupta, *The Journal of Physical Chemistry B*, 2003, **107**, 9268–9274.
- 303 S. D. Khan-Magometova, *Luminescence and Nonlinear Optics*, 1973, 233–285.
- 304 M. D. Galanin, M. I. Demchuk, S. D. Khan-Magometova, A. F. Chernyavskii and Z. A. Chizhikova, *JETPL*, 1974, **20**, 115.
- 305 E. Glöckner and H. C. Wolf, *Zeitschrift für Naturforschung A*, 1969, **24**.
- 306 A. B. Djurišić, X. Liu and Y. H. Leung, *physica status solidi (RRL) - Rapid Research Letters*, 2014, **8**, 123–132.
- 307 S. J. Pearton and F. Ren, *Curr. Opin. Chem. Eng.*, 2014, **3**, 51–55.
- 308 R. S. Moirangthem, P.-J. Cheng, P. C.-H. Chien, B. T. H. Ngo, S.-W. Chang, C.-H. Tien and Y.-C. Chang, *Opt. Express*, 2013, **21**, 3010–3020.
- 309 A. L. Patterson, *Physical Review*, 1939, **56**, 978–982.
- 310 F. Johansson, P. Peterson, M. Pernici, O. Certik, V. Steinberg, N. Telang, M. Taschuk, C. Van Horsen, J. Baayen, C. Smith, J. Arias de Reyna, I. Tziakos, A. Meurer, S. Krastanov, K. Allen, T. Hartmann, S. B. Kirpichev, K. Kuhlman, P. Masson, M. Kagalenko and J. Warner, *mpmath: a Python library for arbitrary-precision floating-point arithmetic (version 1.10)*, 2018.

- 311 SciPy 1.0 Contributors, P. Virtanen, R. Gommers, T. E. Oliphant, M. Haberland, T. Reddy, D. Cournapeau, E. Burovski, P. Peterson, W. Weckesser, J. Bright, S. J. van der Walt, M. Brett, J. Wilson, K. J. Millman, N. Mayorov, A. R. J. Nelson, E. Jones, R. Kern, E. Larson, C. J. Carey, İ. Polat, Y. Feng, E. W. Moore, J. VanderPlas, D. Laxalde, J. Perktold, R. Cimrman, I. Henriksen, E. A. Quintero, C. R. Harris, A. M. Archibald, A. H. Ribeiro, F. Pedregosa and P. van Mulbregt, *Nat. Methods*, 2020, **13**, 22.
- 312 *IEEE Standard for Binary Floating-Point Arithmetic*, IEEE, Piscataway, NJ, USA, 1985.
- 313 A. Janotti and C. G. Van de Walle, *Phys. Rev. B Condens. Matter*, 2007, **76**, 869.
- 314 P. Erhart and K. Albe, *Appl. Phys. Lett.*, 2006, **88**, 201918.
- 315 A. Ali, G. Rahman, T. Ali, M. Nadeem, S. K. Hasanain and M. Sultan, *Physica E: Low-dimensional Systems and Nanostructures*, 2018, **103**, 329–337.
- 316 K. Lawson-Wood, S. Upstone and K. Evans, *Determination of Relative Fluorescence Quantum Yields using the FL6500 Fluorescence Spectrometer*, PerkinElmer Inc, 2018.
- 317 D. Magde, R. Wong and P. G. Seybold, *Photochemistry and Photobiology*, 2007, **75**, 327–334.
- 318 Sabnis, *Handbook of Fluorescent Dyes and Probes*, John Wiley & Sons, 2015.
- 319 D. G. Kuroda and V. D. Kleiman, *Frontiers in Optics*, 2006.
- 320 E. E. Jelley, *Nature*, 1936, **138**, 1009–1010.
- 321 E. E. Jelley, *Nature*, 1937, **139**, 631–631.
- 322 T. Kikteva, D. Star, Z. Zhao, T. L. Baisley and G. W. Leach, *J. Phys. Chem. B*, 1999, **103**, 1124–1133.
- 323 N. B. Khelladi and N. E. C. Sari, *Advances in Materials Sciences*, , DOI:10.2478/adms-2013-0003.
- 324 F. J. Duarte and L. W. Hillman, *Dye Laser Principles: With Applications*, Elsevier, 2012.
- 325 R. B. Reed, D. A. Ladner, C. P. Higgins, P. Westerhoff and J. F. Ranville, *Environ. Toxicol. Chem.*, 2012, **31**, 93–99.
- 326 V. Amendola and M. Meneghetti, *J. Phys. Chem. C*, 2009, **113**, 4277–4285.
- 327 M. Farokhnezhad and M. Esmaeilzadeh, *Phys. Chem. Chem. Phys.*, 2019, **21**, 18352–18362.
- 328 C. F. Bohren and D. R. Huffman, 1998.
- 329 R. L. Olmon, B. Slovick, T. W. Johnson, D. Shelton, S.-H. Oh, G. D. Boreman and M. B. Raschke, *Phys. Rev. B Condens. Matter*, 2012, **86**, 285.
- 330 A. Kedia and P. S. Kumar, AIP, 2013, pp. 232–233.
- 331 F. Liebig, R. Henning, R. M. Sarhan, C. Prietzel, C. N. Z. Schmitt, M. Bargheer and J. Koetz, *RSC Adv.*, 2019, **9**, 23633–23641.
- 332 M. M. Phiri, D. W. Mulder and B. C. Vorster, *R Soc Open Sci*, 2019, **6**, 181971.
- 333 D. M. Bagnall, Y. F. Chen, M. Y. Shen, Z. Zhu, T. Goto and T. Yao, *Journal of Crystal Growth*, 1998, 184–185, 605–609.
- 334 K. Suzuki, M. Inoguchi, K. Fujita, S. Murai, K. Tanaka, N. Tanaka, A. Ando and H. Takagi, *Journal of Applied Physics*, 2010, **107**, 124311.
- 335 S. I. Pekar, *Journal of Physics and Chemistry of Solids*, 1958, **5**, 11–22.
- 336 J. J. Hopfield, *Physical Review*, 1958, **112**, 1555–1567.
- 337 F. J. Richards, *Journal of Experimental Botany*, 1959, **10**, 290–301.
- 338 J. McMurry and R. C. Fay, *Chemistry*, Pearson Prentice Hall, 2008.
- 339 nanoComposix, Nanoparticle Volume, Mass and Concentration, <https://nanocompositix.com/pages/nanoparticle-volume-mass-and-concentration>, (accessed 8 July 2020).

# Appendix

## A3: Peptide Binding Kinetics

In order to understand what is occurring in time and/or concentration dependent data obtained from different binding studies, mathematical models must be used. The choice of mathematical model depends upon what interactions are considered and can have a large impact on the findings. This section takes a detailed look at routinely used models to determine their applicability for the peptide-Au binding data.

### A3.1 Linear Regression

Linear regression is the most basic empirical fitting method which has been used by scientists for hundreds of years and was the first fitting model to be studied extensively.<sup>239</sup> This model can be expressed as:

$$y = mx + c \quad \text{A3.1}$$

Where  $m$  is the gradient and  $c$  is the  $y$ -intercept. This model does not theoretically account for any events occurring and is solely an empirical technique. This model assumes linearity of the dataset, if the dataset is non-linear error can be introduced which is shown in the Anscombe's quartet where 4 different datasets return the same linear regression fit.<sup>240</sup> However, due to the ability of the experimentalist to judge linearity this model can be appropriately used in cases where more complex fittings may not be appropriate.

### A3.2 Freundlich Fitting

The Freundlich isotherm was proposed in 1909 by Herbert Freundlich.<sup>207</sup> Unlike the Langmuir isotherm which is a theoretical model, the Freundlich isotherm is determined empirically. However, due to the relationship being entirely empirical it is preferred to use a theoretical model such as the Langmuir or Kisliuk Isotherm. The final concentration dependent form of the Freundlich isotherm can be expressed as:

$$\frac{x}{m} = Kc^{\frac{1}{n}} \quad \text{A3.2}$$

Where  $n$  and  $K$  are constants,  $c$  is concentration,  $x$  is the mass of adsorbate and  $m$  is the mass of adsorbent. This model requires  $K$  and  $n$  to be empirically determined and fails under high concentrations. As this model does not theoretically model binding events it has not been selected for further investigation in this study.

### A3.3 Langmuir Isotherm

The Langmuir isotherm was published by Irving Langmuir in 1918, this model is the standard method for describing surface interactions due to its robust nature and simplicity. This isotherm requires three assumptions:<sup>112</sup>

1. The surface has a specific number of binding sites where the analyte can be adsorbed.
2. The surface of the adsorbent is in contact with a solution containing the analyte which is strongly attracted to the surface.
3. The adsorption solely involves the formation of a monolayer no further adsorption occurs.

These assumptions can be used to generate the following reaction equilibrium for binding interactions between the analyte (A) and the surface (S):



The equilibrium constant for the binding interaction above can be expressed as:

$$K_A = \frac{[AS]}{[A][S]} \quad A3.4$$

Where [A] denotes the concentration of analyte, while [S] and [AS] are 2D analogues of concentration expressed in mol·cm<sup>-2</sup>. The complete form of the Langmuir isotherm considers binding interaction in terms of the total surface coverage, θ denotes the fraction of adsorption sites where a molecule of analyte is adsorbed. Due to the initial assumptions of there being a finite number of sites, the concentration of [S] during the binding process can be denoted as (1-θ). Therefore we can rewrite [AS]/[S] as follows:

$$\frac{[AS]}{[S]} = \frac{\theta}{1 - \theta} \quad A3.5$$

Let [A] = c:

$$K_A = \frac{\theta}{c(1 - \theta)} \quad A3.6$$

Rearranging to find θ:

$$\theta = \frac{K_A c}{1 + K_A c} \quad A3.7$$

This is the final form of the concentration-dependent Langmuir adsorption isotherm assuming constant pressure. However, this isotherm is only suitable for concentration-dependent experiments. A different derivation is required to utilise this isotherm in kinetic studies such as MP-SPR experiments. Due to the assumptions made in this model, there are limitations to what systems this can be applied to. For instance, any peptide systems which form multilayers are not suitable for modelling with this isotherm. Also, pressure

changes and phase transition must not occur for this version of the model. Peptide-peptide interactions are not accounted for in this model.

### A3.4 Von Bertalanffy/Monomolecular growth model

This model was originally proposed by Gallucci and Quinn in 1979 under the name Von Bertalanffy model.<sup>217</sup> However, due to this name more commonly being attributed to another model, this model is now referred to as the monomolecular growth model.<sup>218</sup> This model when applied to binding interactions is a 1:1 Langmuir type model so can be considered a kinetic version of the Langmuir isotherm with time dependent terms. Using the concentration dependent Langmuir isotherm the time dependent form can be derived. The change in the fraction of adsorption sites where a molecule of analyte is adsorbed ( $\theta$ ) over time can be expressed as:

$$\frac{d\theta}{dt} = k\theta \quad \text{A3.8}$$

Where t is time and k is the rate of reaction. Therefore, the binding rate is proportional to the current amount of filled binding sites ( $\theta$ ). However, when  $k > 0$ , the total amount of binding will be unlimited which due to the assumptions made in the Langmuir isotherm is not possible. Instead, the binding rate should be proportional to the remaining free sites. Thus:

$$t \rightarrow \infty, \frac{d\theta}{dt} \rightarrow 0 \quad \text{A3.9}$$

$$\therefore \frac{d\theta}{dt} = k(\alpha - \theta) \quad \text{A3.10}$$

Where  $\alpha$  is the equilibrium bound fraction. The solution for  $\theta$  can be expressed as:

$$\therefore \theta_t = \alpha - (\alpha - \beta) e^{-kt} \quad \text{A3.11}$$

Where  $\beta$  is the initial size, if it is assumed that all available sites are free upon the start of a binding study,  $\beta = 0$  and the solution for  $\theta$  can be simplified to:

$$\therefore \theta_t = \alpha(1 - e^{-kt}) \quad \text{A3.12}$$

This is the final form of the time-dependent Monomolecular growth model and due to the assumptions made during its derivation it is equivalent to the time-dependent Langmuir model. Therefore, this model is limited to investigating systems where solely monolayer formation occurs as multilayer formation is not accounted for and no peptide-peptide interactions are considered.

### A3.5 Double First-Order Model (DFO Model)

The Monomolecular growth model assumes one first order process is occurring during the binding process. However, due to the complex nature of interactions at the abiotic-biotic

interfaces, a second first-order term can be proposed to account for the peptide-peptide interactions, as both processes are first order and effect the change in the fraction of adsorption sites where a molecule of the analyte is adsorbed ( $\theta$ ). This model in its simplest form can be expressed as:

$$\theta_t = a \left\{ \left( 1 - e^{-k_1 t} \right) + \left( 1 - e^{-k_2 t} \right) \right\} \quad \text{A3.13}$$

Where  $k_1$  is a rate term for adsorption and  $k_2$  is the rate term for peptide-peptide interactions. The assumption is made that  $k_1 \gg k_2$ . However, the assumption that both of these factors equally contribute to the adsorption is not necessarily correct, instead we can separate the scaling factors and express the function as:

$$\theta_t = \alpha \left( 1 - e^{-k_1 t} \right) + \beta \left( 1 - e^{-k_2 t} \right) \quad \text{A3.14}$$

Where  $\alpha$  and  $\beta$  represent the contribution of each first order process to the overall binding event. This model currently assumes that both events occur immediately. However, assuming that the affinity of the analyte for the surface is high and the previous assumption that  $k_1 \gg k_2$  it is more logical to allow the second event to occur after a delay. This leads us to the final form of the DFO model:

$$\theta_t = \alpha \left( 1 - e^{-k_1 t} \right) + \beta \left( 1 - e^{-k_2(t-t_0)} \right) \quad \text{A3.15}$$

This model is different from the Langmuir model as it accounts for a second interaction between the peptides. However, it still suffers from many of the assumptions made in the Langmuir model such as no multi-layer formation and the peptide-peptide interactions and surface-peptide interactions are considered separately with all binding interactions being permanent.

### A3.6 Kisliuk Isotherm

The kisliuk isotherm was proposed by Paul Kisliuk in 1957.<sup>113</sup> This model is more complex than the Langmuir model as it accounts for an adsorbate in both the interfacial and adsorbed states. This model is unique as it considers that peptides already adsorbed to the adsorbent can assist in further adsorption through peptide-peptide interactions. This model makes several assumptions which are:

1. The adsorption involves the formation of a monolayer and no further adsorption occurs.
2. The surface has a specific number of chemically identical binding sites where the analyte can be adsorbed.
3. The adsorbate is above the binding site in an interfacial state before either desorbing or adsorbing.
4. The surface of the absorbent is in contact with a solution containing the analyte which is strongly attracted to the surface.

A schematic showing the modelled parameters is below:

If we utilise the differential form of the monomolecular model as a starting point we can derive the kinetic form of the Kisliuk isotherm.

$$\frac{d\theta}{dt} = k(\alpha - \theta) \quad \text{A3.16}$$

Where  $\alpha$  is the maxima of the curve as the Kisliuk isotherm is a probabilistic model we can let this be 1, denoting 100% adsorption.

$$\frac{d\theta}{dt} = k(1 - \theta) \quad \text{A3.17}$$

Currently we are solely accounting for Langmuir type adsorption events, a second term needs to be introduced to account for the adsorption due to peptide-peptide interactions. Looking at the schematic of adsorption modelled by the Kisliuk isotherm we can see there are  $S_D$ ,  $S_E$  representing the probabilities of Langmuir adsorption and peptide assisted adsorption respectively.

Due to this being a probabilistic model:  $S_E + S_D = 1$ , therefore  $S_E$  and  $S_D$  are co-dependent. The last two terms  $K_{ES}$  and  $K_{EC}$  represent the rate of desorption and adsorption from the interfacial state respectively. Considering all these terms we can generate a new term called the “Sticking Coefficient” denoted as  $K_E$  to model the contributions of these other effects.  $K_E$  can be expressed as:

$$K_E = \frac{S_E}{k_{ES} S_D} \quad \text{A3.18}$$

Using  $K_E$  we can rewrite the differential form of the Kisliuk model as:

$$\frac{d\theta}{dt} = k(1 - \theta)(1 + K_E) \quad \text{A3.19}$$

The rate constant  $k$  is not proportional to the binding of the peptide but proportional to the overall mass diffusivity of the system so can be represented as  $R'$ .

$$\frac{d\theta}{dt} = R'(1 - \theta)(1 + K_E) \quad \text{A3.20}$$

If the equation is rearranged to solve for the  $\theta$  the following expression is obtained:

$$\theta_t = \frac{1 - e^{-R'(1 + K_E)t}}{1 + K_E e^{-R'(1 + K_E)t}} \quad \text{A3.21}$$

This is the final form of the time-dependent kisliuk isotherm, it is more robust than the Langmuir isotherm due to accounting for both Langmuir type interactions as well as peptide assisted adsorption. However, it suffers from the same limitation as the Langmuir isotherm through not considering multilayer formation. The advantage this model presents over the DFO model is that the two interaction types are considered simultaneously with any impact they will have on one another. However, no desorption is considered upon adsorption of the molecule thus this model will not give the entire picture of what is occurring.

### A3.7 Richards' Curve/Generalized Logistic Function

The generalized logistic function was originally proposed by F.J. Richards as a method for growth modelling for applications in botany.<sup>337</sup> Unlike the previous models, which attempt to model the interactions occurring, the generalized logistic function instead makes no assumptions about what interactions are occurring. Solely an empirical fitting of the instrumental response is performed. The generalized logistic function can be expressed as:

$$y = A_2 + \frac{A_1 - A_2}{1 + 10^{-(x - \log(x_0))n}} \Rightarrow \frac{B}{B_0} = \frac{1}{1 + 10^{-(x - \log(x_0))n}} \quad \text{A3.22}$$

Where A<sub>1</sub> and A<sub>2</sub> describe the asymptotes, x<sub>0</sub> is the midpoint of the sigmoid and n corresponds to the gradient of the slope, under the conditions where n=1 then the hill regime is adopted.

The concentration at the central point can be determined as follows:

$$EC_{50} = 10^{x_0} \quad \text{A3.23}$$

The obtained EC<sub>50</sub> value can be used to calculate the dissociative constant K<sub>D</sub>.

$$K_D = \frac{k_{off}}{k_{on}} = (EC_{50})^n \quad \text{A3.24}$$

While this model is solely empirical it can be used in cases where more complex fittings may not be appropriate as the model reflects the instrument response as the limits of detection are being approached. Such a model is well suited for experiments which push the limits of detection on instrumentation.

## A4: Towards an understanding of engineering binding sequences for Au systems through kinetic and thermodynamic studies

### A4.1 Calculation of gold nanoparticle concentration

To theoretically determine the concentration of gold nanoparticles formed in the reaction medium the radius of a gold atom must be determined. This is achieved by calculating its volume ( $V_{AuAtom}$ ), see equation A4.1, where  $m$  is molecular weight,  $\rho$  is the density,  $N_A$  is avogadro's constant and  $\pi/(3\sqrt{2})$  is the packing efficiency for face-centered cubic (FCC) systems. Due to an atom's spherical shape once the volume has been determined the radius of that atom ( $r_{AuAtom}$ ) can be calculated, see equation A4.2. The determined value of 144.1 pm is in agreement with the literature value.<sup>338</sup>

$$V_{AuAtom} = \frac{m}{\rho \cdot N_A} \cdot \frac{\pi}{3\sqrt{2}} = 1.254 \cdot 10^{-23} \text{ cm}^3 \quad \text{A4.1}$$

$$r_{AuAtom} = \sqrt[3]{\frac{3}{4\pi} \cdot V_{AuAtom}} = 1.441 \cdot 10^{-8} \text{ cm} = 144.1 \text{ pm} \quad \text{A4.2}$$

Next the number of atoms per particle ( $N_{AtomsPP}$ ) must be determined, this is calculated using the ratio between the radius of the particle ( $r_{Particle}$ ) and the radius of a gold atom ( $r_{AuAtom}$ ), see equation A4.3. In equation A4.3 we assume that the particle has spherical geometry.

$$N_{AtomsPP} = \frac{\frac{4}{3}\pi r_{Particle}^3 \cdot \frac{\pi}{3\sqrt{2}}}{\frac{4}{3}\pi r_{Atom}^3} = \frac{r_{Particle}^3 \cdot \frac{\pi}{3\sqrt{2}}}{r_{Atom}^3} = 1.619 \cdot 10^5 \quad \text{A4.3}$$

Knowing the number of atoms present per particle ( $N_{AtomsPP}$ ) and the number of Au atoms present in the reaction vessel, the number of particles ( $N_{Particles}$ ) formed can be theoretically determined, see equation A4.4, where  $c_{Au}$  is the concentration of Au precursor used (i.e. HAuCl<sub>4</sub>),  $V_{Au}$  is the volume of Au precursor used and  $N_A$  is avogadro's constant.

A4.4

$$N_{Particles} = \frac{c_{Au} \cdot V_{Au} \cdot N_A}{N_{AtomPP}} = \frac{0.16 \cdot 50 \cdot 10^{-3} \cdot N_A}{1.619 \cdot 10^5} = 2.976 \cdot 10^{16}$$

Finally the number of particles ( $N_{Particles}$ ) can be converted to the concentration of gold nanoparticles ( $c_{AuNPs}$ ) using equation A4.5.

A4.5

$$c_{AuNPs} = \frac{N_{Particles}}{N_A \cdot V_R} = \frac{4.649 \cdot 10^{13}}{50.25 \cdot 10^{-3} \cdot N_A} = 1.54 \cdot 10^{-9} M \approx 2 \text{ nM}$$

This yields a concentration of ca. 2 nM for the gold nanoparticle solution which is in agreement with the reported concentration ranges for nanoparticle synthesis.<sup>339</sup>

#### A4.2 Calculation of gold Binding site concentration

To determine the concentration of gold binding sites present in the ITC studies, the maximum possible number of binding sites available on the 17 nm gold nanoparticles must be determined. This was calculated by working out the surface area of the nanoparticle ( $S_{Particle}$ ) multiplied by the face-centred cubic (FCC) packing efficiency constant, see equation A4.6.

A4.6

$$S_{Particles} = 4 \cdot \frac{\pi}{3\sqrt{2}} \cdot \pi \cdot r_{Particles}^2 = 672.3 \text{ nm}^2$$

From the MP-SPR binding studies, see Chapter IV Section 4.3.1, it appears that multiple residues interact with the gold surface upon peptide binding. Therefore, if we simplify the peptide to a cylinder with the diameter of an amino acid which is  $3.5 \pm 0.1 \text{ \AA}$ <sup>226-229</sup> and length of 9 amino acids (ca. 31.5 Å) corresponding to the smallest peptide studied, we may approximate the maximum number of available binding sites. Calculating the area of a rectangle in the axial plane for the peptide cylinder yields an approximate value for the area the bound peptide would occupy on the gold surface, which was determined to be 1.1025 nm<sup>2</sup>. Dividing the area occupied by each bound peptide from the surface area of the particle multiplied by the concentration of gold nanoparticles used ( $c_{AuNPs}$ ) allows for the determination of the gold binding site concentration ( $c_{AuBindingSites}$ ), see equation A4.7, which was 1 μM.

$$c_{AuBindingSites} = \frac{672.3}{1.1} \cdot c_{AuNPs} = 611.2 \cdot 2 \cdot 10^{-3} = 1.2 \mu M \approx 1 \mu M$$

### A4.3 Appendix Tables and Figures

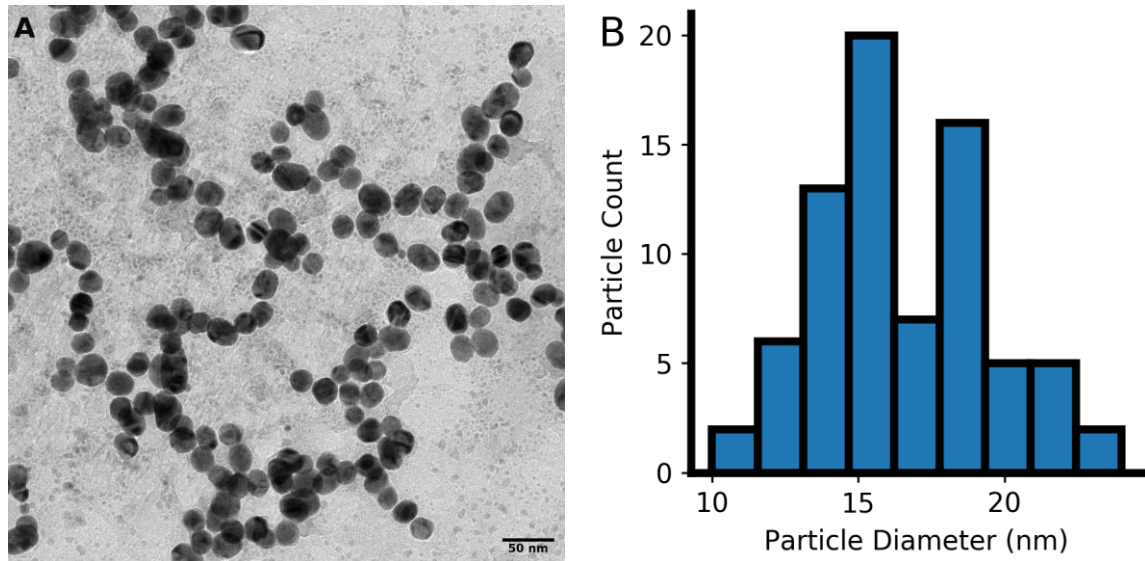


Figure A4.1 - Representative Transmission Electron Microscopy (TEM) micrograph (A) of uncoated gold nanoparticles taken using an accelerating voltage of 200 keV presented with size distribution data (B) determined from multiple imaging areas.

Table A4.1 - Purity and molecular weights of gold binding peptides used in this study.

Peptide Name	Sequence	Purity (%)	$M_r$	
			Expected	Actual
A3	AYSSGAPPMPFF	82	1221.382	1221.695
A3s	AYSSGAPMPPF	86	1124.267	1124.560
A3sC8	AYSSGAPCPPF	80	1096.214	1096.509
A3sT2	ATSSGAPMPPF	80	1062.198	1062.525
AuBP1	WAGAKRLVLRRE	84	1427.650	1427.431
AuBP2	WALRRSIRRQSY	84	1591.819	1591.782
HRE	AHHAHHAAD	85	965.971	965.402
Pd4	TSNAVHPTLRHL	81	1345.507	1345.950

## A5: Two-Dimensional Fitting Approaches Towards Of Semiconductor Fluorescent Behaviour

Script A5.1 - Python script developed in house to compile 1D-spectra into 2D fluorescence map. This script extracts multiple one-dimensional fluorescence spectra from a raw plate reader fluorescence datafile and assembles two-dimensional matrices of fluorescence intensity for each sampled well with appropriate offsetting for emission, excitation parameters used. The extracted two-dimensional matrices are saved as individual csv files with the filename set to the well name. These can then be opened using the 'plot\_from\_csv' function in this script to plot the 2D-FM with a consistent percentile based colour gradient

```
#####Made by Daniel Oliver#####
#####Nottingham Trent University#####
#####Author Provides Code As Is#####
from datetime import datetime
import pandas as pd
import numpy as np
import os
from matplotlib import pyplot as plt
from matplotlib.colors import LinearSegmentedColormap

#Setting up colour dictionary for the 2D maps

cdict = {'red': ((0.0, 0.0, 0.0),
                 (0.075, 0.0, 0.0),
                 (0.2, 0.0, 0.0),
                 (0.3, 0.0, 0.0),
                 (0.4, 0.5, 0.5),
                 (0.5, 1.0, 1.0),
                 (0.6, 1.0, 1.0),
                 (0.7, 1.0, 1.0),
                 (0.8, 1.0, 1.0),
                 (0.9, 1.0, 1.0),
                 (1.0, 1.0, 1.0)),
          'green': ((0.0, 0.0, 0.0),
                     (0.075, 1.0, 1.0),
                     (0.2, 0.5, 0.5),
                     (0.3, 1.0, 1.0),
                     (0.4, 0.0, 0.0),
                     (0.5, 0.0, 0.0),
                     (0.6, 0.0, 0.0),
                     (0.7, 0.5, 0.5),
                     (0.8, 1.0, 1.0),
                     (0.9, 1.0, 1.0),
                     (1.0, 1.0, 1.0)),
          'blue': ((0.0, 1.0, 1.0),
                    (0.075, 1.0, 1.0),
                    (0.2, 0.5, 0.5),
                    (0.3, 0.0, 0.0))}
```

```

        (0.4,  0.0,  0.0),
        (0.5,  0.0,  0.0),
        (0.6,  1.0,  1.0),
        (0.7,  0.0,  0.0),
        (0.8,  0.0,  0.0),
        (0.9,  1.0,  1.0),
        (1.0,  1.0,  1.0))}

newcmp = LinearSegmentedColormap('newcmp',cdict)

def nm_to_eV(x):
    return 1240/x

def extract_fluorescence(filename,debug=False,drop_wavelengths = True):
    if debug:
        startTime = datetime.now()
    #Arrays
    excitation = [np.nan]
    remove_rows = []
    well_names = [] #length of this array is equivalent to the number of samples

    #Dictionaries
    spectra = {}
    samples = {}

    i = 1
    j = 0

    init = True
    ##scanning file and determining values#####
    file = pd.read_excel(filename,header=None)

    spectra_index = file.loc[file[0]=="Wavel."]
    dead_rows = spectra_index.index[0]

    for x in file.loc[file[0]=="Excitation Wavelength"].index:
        excitation.append(file.iloc[x][4])

    while not pd.isna(file.iloc[dead_rows+i][0]):
        well_names.append(file.iloc[dead_rows+i][0])
        i+=1

    #####
    #listing rows to remove#####
    for x in range(0,file.shape[0]):
        if j == len(spectra_index.index):

```

```

        break
    if x == spectra_index.index[j] or x > spectra_index.index[j]
and x<= spectra_index.index[j]+len(well_names):
        if x == spectra_index.index[j]+len(well_names):
            j+=1
        else:
            pass
    else:
        remove_rows.append(x)
#####
#Modifying Dataset#####
file.drop(remove_rows,0,inplace=True)
trans_file = file.transpose()# can you use inplace with this
function check this Later
trans_file.drop(0,0,inplace=True)
## Replacing over values and empty cells with not a number (blank
space)
trans_file.fillna(np.nan,inplace=True)
trans_file.replace("OVER",np.nan,inplace=True)
#####

for x in range(0,j):
    cols = []
    for y in range(0,len(well_names)+1):
        cols.append(spectra_index.index[x]+y)
    spectra["spectrum{0}".format(x)] =
trans_file.filter(cols,axis=1).sort_values(spectra_index.index[x],ascen
ding=False).reset_index(drop=True)
    i+=1

for key, value in spectra.items():
    if init:
        df = pd.DataFrame(spectra[key])
        init = False
    else:
        df = pd.concat([df,spectra[key]],axis=1)

if drop_wavelengths:
    df.drop(spectra_index.iloc[1:,:].index,1,inplace=True)

for x in range (1, len(well_names)+1):
    columns = [dead_rows,dead_rows+x]
    for i in spectra_index.iloc[1:,:].index:
        columns.append(i+x)
    samples["well_{0}".format(well_names[x-1])] =
df.filter(columns,axis=1)
    samples["well_{0}".format(well_names[x-1])].loc[-1] =

```

```

excitation
    samples["well_{0}".format(well_names[x-1])].index =
samples["well_{0}".format(well_names[x-1])].index+1
    samples["well_{0}".format(well_names[x-
1])].sort_index(inplace=True)

    for key, value in samples.items():
        csv_filename = str(key)+(".csv")
        samples[key].to_csv(csv_filename,header=False,index=False)

    if debug:
        print(datetime.now()-startTime)

def
plot_from_csv(filename,cmp,level=250,dpi_setting=300,eV=False,debug=False,log=False,allowNeg=False):
    #eV plots axes in Electron Volts
    #debug prints execution time
    #log plots log of fluorescence intensity
    #allowNeg allows for negative intensity values, if false sets -ve
values to zero
    if debug:
        startTime = datetime.now()
    data = pd.read_csv(filename,header=None)
    fname = os.path.splitext(filename)[0]
    if not allowNeg:
        data[data<0]=0
    if eV:
        jpg_filename = str(fname)+"_ev.jpg"
        ex_wavelengths = data.loc[0].apply(nm_to_eV).values.tolist()
    else:
        jpg_filename = str(fname)+".jpg"
        ex_wavelengths = data.loc[0].values.tolist()
    del ex_wavelengths[0]
    data.drop(0,0,inplace=True)
    if eV:
        em_wavelengths = data.iloc[:,0].apply(nm_to_eV).values.tolist()
    else:
        em_wavelengths = data.iloc[:,0].values.tolist()
    data.drop(0,1,inplace=True)
    data.reset_index(drop=True,inplace=True)
    if log:
        Z = data.astype("float64").apply(np.log).values
    else:
        Z = data.astype("float64").values
    fig, ax = plt.subplots(1,figsize=(5,3),constrained_layout=True)
    psm =
ax.contourf(ex_wavelengths,em_wavelengths,Z,level,antialiased=True,cmap

```

```

=cmp,alpha=1)
    ax.set_facecolor((0,0,1))
    if log:
        fig.colorbar(psm,ax=ax).set_label("Log(Fluoresence)")
    else:
        fig.colorbar(psm,ax=ax).set_label("Fluoresence")
    if eV:
        plt.xlabel("Excitation Energy (eV)") #Label the x axis
        plt.ylabel("Emission Energy (eV)") # Label the y axis
    else:
        plt.xlabel("Excitation (nm)") #Label the x axis
        plt.ylabel("Emission (nm)") # Label the y axis
    plt.gca().set_xlim(230,600)
    plt.gca().set_ylim(790,300)
    plt.savefig(jpg_filename,dpi=dpi_setting)

    if debug:
        print(datetime.now()-startTime)

#Example of extracting spectral data for each well from raw
extract_fluorescence("200302_Anu_ZnS_B2_B3_Plate2.xlsx",debug=True)
#If more than one well needs to be plotted
plot_from_csv("well_B2.csv",newcmp,debug=True)
plot_from_csv("well_B3.csv",newcmp,debug=True)

```

Script A5.2 - Python script developed in house to assist with fitting fit multiple 2D-gaussian line shapes to 2D-fluorescence data with real time feedback.

```
#####Made by Daniel Oliver#####
#####Nottingham Trent University#####
#####Author Provides Code As Is#####
from matplotlib.patches import Rectangle
from lmfit.model import ModelResult
from matplotlib.widgets import Slider, Button
from matplotlib.colors import LinearSegmentedColormap
from numbers import Number
from time import strftime
import lmfit
import Logging
import matplotlib.pyplot as plt
import numpy as np
import pandas as pd

class _1d_slice:
    """This class handles all operations to do with the plotting of the
    1d spectral slices"""
    def __init__(self, ax, contour_ax, data2d_ax, em_wav, ex_wav,
array, model, emission=True):
        self.sp = signalProcessing()
        self.ax = ax
        self.contour_ax = contour_ax
        self.data2d_ax = data2d_ax
        self.emission = emission

        self.in_thres = 1 #instrumental noise threshold
        if self.emission:
            self.step = 1 #stepping through each emission spectra
        else:
            self.step = 10 #stepping through each row/excitation
spectra

        self.em_wav = em_wav
        self.ex_wav = ex_wav

        self.model = model
        self.fit = self.model.Lmfit_eval
        self.array = array
        if emission:
            rows, self.spectra = array.shape
        else:
            self.spectra, cols = array.shape
```

```

    self.ind = 0

    if self.emission:
        self.ax.set_title("Emission 1D-Spectral Slice")
        self.data =
    self.ax.plot(em_wav,self.array.iloc[:,self.ind],color="k",Linewidth=1)
        self.fitting =
    self.ax.plot(em_wav,self.fit[:,self.ind],color="steelblue",Linewidth=1)
        self.indicator =
    self.contour_ax.axvline(x=self.ex_wav[self.ind],color="k",Linewidth=2,L
inestyle="--")
        self.datindicator =
    self.data2d_ax.axvline(x=self.ex_wav[self.ind],color="k",Linewidth=2,L
inestyle="--")
        self.ax.set_ylabel("Intensity (Ex.
{0}nm)".format(self.ex_wav[self.ind]))
    else:
        self.ax.set_title("Excitation 1D-Spectral Slice")
        self.data =
    self.ax.plot(ex_wav,self.array.iloc[self.ind,:],color="r",Linewidth=1)
        self.fitting =
    self.ax.plot(ex_wav,self.fit[self.ind,:],color="steelblue",Linewidth=1)
        self.indicator =
    self.contour_ax.axhline(y=self.em_wav[self.ind],color="r",Linewidth=2,L
inestyle="--")
        self.datindicator =
    self.data2d_ax.axhline(y=self.em_wav[self.ind],color="r",Linewidth=2,L
inestyle="--")
        self.ax.set_xlabel("Wavelength (nm)")
        self.ax.set_ylabel("Intensity (Em.
{0}nm)".format(self.em_wav[self.ind]))

    self.update()

def onscroll(self, event):#need to find other event maybe?
    if event.inaxes == self.ax:
        Logging.debug('enter_axes', event.inaxes)
        if event.button == "up":
            self.ind = (self.ind +1*self.step) % self.spectra
            Logging.debug("%s %s" % (event.button, event.step))
        else:
            self.ind = (self.ind -1*self.step) % self.spectra
            Logging.debug("%s %s" % (event.button, event.step))
    self.update()

def find_peak(self,data:np.ndarray)->np.ndarray:

```

```

gradient = np.gradient(data)
indexes = np.argwhere(gradient==0)
return indexes

def SMA(self,data:np.ndarray, window = 10)->np.ndarray:
    """A simple moving average algorithm.
    averaged_val[i] =
    sum(val[i]+val[i+1]+...+val[i+window])/window
    """
    filtered = np.empty([len(data)-window])
    for i in range(0,len(data)-window):
        upper = data[i]
        for j in range(1, window):
            upper += data[i+j]
        filtered[i]= upper/window
    return filtered

def fit_update(self):
    self.fit = self.model.lmfit_eval
    self.update()

def update(self):
    if self.emission:
        self.data[0].set_ydata(self.array.iloc[:,self.ind])
        self.fitting[0].set_ydata(self.fit[:,self.ind])
        self.indicator.set_xdata(self.ex_wav[self.ind])
        self.datindicator.set_xdata(self.ex_wav[self.ind])
        self.ax.set_ylabel("Intensity (Ex.
{0}nm)".format(self.ex_wav[self.ind]))
    else:
        self.data[0].set_ydata(self.array.iloc[self.ind,:])
        self.fitting[0].set_ydata(self.fit[self.ind,:])
        self.indicator.set_ydata(self.em_wav[self.ind])
        self.datindicator.set_ydata(self.em_wav[self.ind])
        self.ax.set_ylabel("Intensity (Em.
{0}nm)".format(self.em_wav[self.ind]))

    self.ax.relim()
    self.ax.autoscale_view()

#self.plot[0].axes.figure.canvas.draw()
self.ax.figure.canvas.draw()
self.ax.figure.canvas.flush_events()

class _2d_fitting:

```

```

def __init__(self):
    self.lmfit_eval = None
    self.update = None
    #Setting up permitted variances
    self.xc_variance = 10
    self.yc_variance = 5
    self.xwidth_variance = 3
    self.ywidth_variance = 3

##      def
suggest_lineshapes(self,data,ex_wavelengths:np.ndarray,em_wavelengths:n
p.ndarray):

    def
amp_Lorentzian_2d(self,xy_mesh,mask,amp,xc:Number,yc:Number,xwidth:
Number,ywidth: Number)-> np.ndarray:
        """A two dimensional Lorentzian distribution.
        =amp*1/(1+4/3*((ex_wav[ex]-
xc)/sigma_x)**2)*1/(1+4/3*((em_wav-yc)/sigma_y)**2)
        """
        (x,y) = xy_mesh
        Lorentz = amp*1/(1+4/3*((x-xc)/xwidth)**2)*1/(1+4/3*((y-
yc)/ywidth)**2)
        Lorentz*=mask
        return np.ravel(Lorentz)

    def
amp_gaussian_2d(self,xy_mesh,mask,amp:Number,xc:Number,yc:Number,xwidth
: Number,ywidth: Number)-> np.ndarray:
        """A two dimensional gaussian distribution.
        =amp*np.exp(-((x-xc)**2/(2*sigma_x**2)+(y-
yc)**2/(2*sigma_y**2)))/(2*np.pi*sigma_x*sigma_y)
        """
        (x,y) = xy_mesh
        gauss = amp*np.exp(-((x-xc)**2/(2*xwidth**2)+(y-
yc)**2/(2*ywidth**2)))/(2*np.pi*xwidth*ywidth)
        gauss*=mask
        return np.ravel(gauss)

def _params_from_csv(self, filename):
    try:
        par = pd.read_csv(filename)
    except:
        raise Exception("Parameter file not found")
        exit()
    amp = par.iloc[:,0].tolist()
    xc = par.iloc[:,1].tolist()

```

```

yc = par.iloc[:,2].tolist()
xwidth = par.iloc[:,3].tolist()
ywidth = par.iloc[:,4].tolist()
lineshape = par.iloc[:,5].tolist()
draw = par.iloc[:,6].tolist()
return amp, xc, yc, xwidth, ywidth, lineshape, draw

def
evaluate(self,data,param_file,matrix,ex_wavelengths:np.ndarray,em_wavelengths:np.ndarray):
    try:
        mask = pd.read_csv(matrix,header=None)
    except:
        raise Exception("Mask not found")
        exit()

        amp,xc,yc,xwidth,ywidth,lineshape,draw =
self._params_from_csv(param_file)
        if Len(amp)!= Len(xc) or Len(amp) != Len(yc) or Len(amp) != Len(xwidth) or Len(amp) != Len(ywidth) or Len(amp) != Len(lineshape) or Len(amp) != Len(draw):
            raise Exception("Variable lists at different lengths, amp: {0}, xc: {0}, yc: {0}, x width: {0}, y width: {0}, lineshape: {0}, draw: {0}".format(Len(amp),Len(xc),Len(yc),len(sigma_x),len(sigma_y),len(lineshape),len(draw)))
            exit()

xy_mesh = np.meshgrid(ex_wavelengths,em_wavelengths)

Lmfit_model = self.generate_Model(lineshape,amp,draw)

params = Lmfit.Parameters()
for i in range(0,len(amp)):
    if draw[i] == "yes":
        params.add("Ls{0}_amp".format(i+1),value = amp[i],vary=False)
        params.add("Ls{0}_xc".format(i+1),value = xc[i],vary=False)
        params.add("Ls{0}_yc".format(i+1),value = yc[i],vary=False)
        params.add("Ls{0}_xwidth".format(i+1),value = xwidth[i],vary=False)
        params.add("Ls{0}_ywidth".format(i+1),value = ywidth[i],vary=False)

    raw_eval =
Lmfit_model.fit(np.ravel(data),params,xy_mesh=xy_mesh,mask=mask)

```

```

        self.r2 = self.adj_rsquared(raw_eval)
        self.lmfit_eval =
raw_eval.best_fit.reshape(np.outer(em_wavelengths,ex_wavelengths).shape
)

    def generate_Model(self,lineshape,amp,draw):
        for i in range(0,len(draw)):
            if draw[i] == "yes":
                first_lineshape = i
                if lineshape[i] == "Lorentzian":
                    lmfit_model =
Lmfit.Model(self.amp_Lorentzian_2d,prefix="ls{0}_".format(i+1),independ
ent_vars=["xy_mesh","mask"])
                elif lineshape[i] == "gaussian":
                    lmfit_model =
Lmfit.Model(self.amp_gaussian_2d,prefix="ls{0}_".format(i+1),independen
t_vars=["xy_mesh","mask"])
            else:
                raise Exception("Unsupported Lineshape, defaulting
to Gaussian")
                lmfit_model =
Lmfit.Model(self.amp_gaussian_2d,prefix="ls{0}_".format(i+1),independen
t_vars=["xy_mesh","mask"])
            break

        if len(amp)>1:
            for i in range(first_lineshape+1,len(amp)):
                if draw[i] == "yes":
                    if lineshape[i] == "Lorentzian":
                        lmfit_model +=
Lmfit.Model(self.amp_Lorentzian_2d,prefix="ls{0}_".format(i+1),independ
ent_vars=["xy_mesh","mask"])
                    elif lineshape[i] == "gaussian":
                        lmfit_model +=
Lmfit.Model(self.amp_gaussian_2d,prefix="ls{0}_".format(i+1),independen
t_vars=["xy_mesh","mask"])
                else:
                    raise Exception("Unsupported Lineshape,
defaulting to Gaussian")
                    lmfit_model +=
Lmfit.Model(self.amp_gaussian_2d,prefix="ls{0}_".format(i+1),independen
t_vars=["xy_mesh","mask"])
                else:
                    if lineshape[i] != np.nan:
                        logging.info("{0} Lineshape (ls{1}) turned
off".format(lineshape[i],i+1))

    return lmfit_model

```

```

    def
fit(self,data,param_file,matrix,ex_wavelengths:np.ndarray,em_wavelength
s:np.ndarray):
    try:
        mask = pd.read_csv(matrix,header=None)
    except:
        raise Exception("Mask not found")
    exit()

        amp,xc,yc,xwidth,ywidth,lineshape,draw =
self._params_from_csv(param_file)
        if Len(amp)!= Len(xc) or Len(amp) != Len(yc) or Len(amp) !=
Len(xwidth) or Len(amp) != Len(ywidth) or Len(amp) != Len(lineshape) or
Len(amp) != Len(draw):
            raise Exception("Variable lists at different lengths, amp:
{0}, xc: {0}, yc: {0}, x width: {0}, y width: {0}, lineshape: {0},
draw:
{0}".format(Len(amp),Len(xc),Len(yc),Len(sigma_x),Len(sigma_y),Len(line
shape),Len(draw)))
        exit()

xy_mesh = np.meshgrid(ex_wavelengths,em_wavelengths)

Lmfit_model = self.generate_Model(lineshape,amp,draw)

params = Lmfit.Parameters()
for i in range(0,Len(amp)):
    if draw[i] == "yes":
        params.add("Ls{0}_amp".format(i+1),value = amp[i],min =
1,max=amp[i]+10000)
        params.add("Ls{0}_xc".format(i+1),value =
xc[i],vary=False)#need to edit this
        params.add("Ls{0}_yc".format(i+1),value =
yc[i],vary=False)
        params.add("Ls{0}_xwidth".format(i+1),value =
xwidth[i],vary=False,min=5)
        params.add("Ls{0}_ywidth".format(i+1),value =
ywidth[i],vary=False,min=5)

Lmfit_result =
Lmfit_model.fit(np.ravel(data),params,xy_mesh=xy_mesh,mask=mask)
with
open("{0}_optimisation_report.txt".format(strftime("%y%m%d-%H%M")), "w")
as f:
    f.write(Lmfit_result.fit_report())
    calc = Lmfit_result.best_fit.reshape(np.outer(em_wavelengths,
ex_wavelengths).shape)

```

```

df_calc = pd.DataFrame(calc)
df_calc.to_csv("fitted.csv",header=False,index=False)

def adj_rsquared(self,results:ModelResult)->Number:
    """Function to determine the adjusted R-squared value from an
    LMFit fitting
        1-(1-'r-squared')[('sample size'-1)/('sample size'-('no.
    independent vars'+1))]
    """
    #Using len as these fitting algorithms only work with 1d-data
    k = 0
    for i in results.params:
        if results.params[i].vary == True:
            k+=1
    return 1-(1-self.rsquared(results))*((len(results.data)-
1)/(len(results.data)-(k+1)))

def rsquared(self,results:ModelResult)->Number:
    """Function to determine the R-squared value from an LMFit
    fitting
        1-'residual variability'/'population variability'
    """
    return 1-results.residual.var()/np.var(results.data)

class contourMap:
    def __init__(self,data_ax,model_ax,ex_wav,em_wav,data,model):
        self.data_ax = data_ax
        self.model_ax = model_ax
        self.data = data.astype("float64").values
        self.model = model

        self.a = 1 #Alpha value
        self.aa = True #Antialiasing
        self.lvl = 250

        self.ex_wav = ex_wav
        self.em_wav = em_wav

        self._cdict = {'red': ((0.0, 0.0, 0.0),
                               (0.075, 0.0, 0.0),
                               (0.2, 0.0, 0.0),
                               (0.3, 0.0, 0.0),
                               (0.4, 0.5, 0.5),
                               (0.5, 1.0, 1.0),
                               (0.6, 1.0, 1.0),
                               (0.7, 1.0, 1.0),
                               (0.8, 1.0, 1.0)),
                      'green': ((0.0, 0.0, 0.0),
                               (0.075, 0.0, 0.0),
                               (0.2, 0.0, 0.0),
                               (0.3, 0.0, 0.0),
                               (0.4, 0.5, 0.5),
                               (0.5, 1.0, 1.0),
                               (0.6, 1.0, 1.0),
                               (0.7, 1.0, 1.0),
                               (0.8, 1.0, 1.0)),
                      'blue': ((0.0, 0.0, 0.0),
                               (0.075, 0.0, 0.0),
                               (0.2, 0.0, 0.0),
                               (0.3, 0.0, 0.0),
                               (0.4, 0.5, 0.5),
                               (0.5, 1.0, 1.0),
                               (0.6, 1.0, 1.0),
                               (0.7, 1.0, 1.0),
                               (0.8, 1.0, 1.0))}


```

```

        (0.9, 1.0, 1.0),
        (1.0, 1.0, 1.0)),
'green': ((0.0, 0.0, 0.0),
            (0.075, 1.0, 1.0),
            (0.2, 0.5, 0.5),
            (0.3, 1.0, 1.0),
            (0.4, 0.0, 0.0),
            (0.5, 0.0, 0.0),
            (0.6, 0.0, 0.0),
            (0.7, 0.5, 0.5),
            (0.8, 1.0, 1.0),
            (0.9, 1.0, 1.0),
            (1.0, 1.0, 1.0)),
'blue': ((0.0, 1.0, 1.0),
          (0.075, 1.0, 1.0),
          (0.2, 0.5, 0.5),
          (0.3, 0.0, 0.0),
          (0.4, 0.0, 0.0),
          (0.5, 0.0, 0.0),
          (0.6, 1.0, 1.0),
          (0.7, 0.0, 0.0),
          (0.8, 0.0, 0.0),
          (0.9, 1.0, 1.0),
          (1.0, 1.0, 1.0))}

self.newcmp = LinearSegmentedColormap('newcmp',self._cdict)

self.dataMap =
self._generateMap(self.data_ax,self.data,"Experimental Data")
self.modelMap =
self._generateMap(self.model_ax,self.model.lmfit_eval,"Model Adj-R
squared: {0:.2f}".format(self.model.r2))

def _generateMap(self,ax,z,title):
    psm =
ax.contourf(self.ex_wav,self.em_wav,z,self.lvl,antialiased=self.aa,cmap
= self.newcmp,alpha=self.a)
    ax.set_facecolor((0,0,1))
    ax.set_xlim(230,810)
    ax.set_ylim(850,280)
    ax.figure.colorbar(psm,ax=ax).set_label("Fluorescence")
    ax.set_title(title)
    return psm

def update(self):
    for old in self.modelMap.collections:
        old.remove()
    self.modelMap =

```

```

self.model_ax.contourf(self.ex_wav, self.em_wav, self.model.lmfit_eval, se
lf.lvl, antialiased=self.aa, cmap=self.newcmp, alpha=self.a)
    self.model_ax.set_title("Model Adj-R squared:
{0:.2f}".format(self.model.r2))

#Unused at the moment
class UpdatingRect(Rectangle):
    """Subclass of Rectangle so that it can be called with an Axes
instance,
    causing the rectangle to update its shape to match the bounds
of the
    Axes"""
    def __call__(self, ax):
        self.set_bounds(*ax.viewLim.bounds)
        ax.figure.canvas.draw_idle()

class signalProcessing():
    #Not sure if this needs to be its own class
    def __init__(self):
        None

    def SMA(self,data:np.ndarray, window = 10)->np.ndarray:
        """A simple moving average algorithm.
        averaged_val[i] =
sum(val[i]+val[i+1]+....+val[i+window])/window
        """
        filtered = np.empty([len(data)-window])
        for i in range(0,len(data)-window):
            upper = data[i]
            for j in range(1, window):
                upper += data[i+j]
            filtered[i]= upper/window
        return filtered

    def low_pass_filter(self,data,fc=0.1,b=0.08,trim_ends=True):
        N= int(np.ceil((4/b)))
        if trim_ends:
            if N%2 == 0:
                ind = N//2
            else:
                ind = (N-1)//2

            if not N%2: N+=1
            n = np.arange(N)
            sinc_func = np.sinc(2*fc*(n-(N-1)/ 2))
            window = 0.42 - 0.5 * np.cos(2 * np.pi * n / (N - 1)) + 0.08 *
np.cos(4 * np.pi * n / (N - 1))

```

```

    sinc_func = sinc_func * window
    sinc_func = sinc_func / np.sum(sinc_func)

    new_signal = np.convolve(data,sinc_func)
    if trim_ends:
        return new_signal[ind:-ind]
    else:
        return new_signal

##    def find_peaks(self):

#####
#####

def run(data_file,param_file,LM_optimise=False):
    try:
        dataset = pd.read_csv(data_file,header=None)
    except:
        raise Exception("Dataset not found")
        exit()

    em_wav = np.linspace(850,280,num=571,dtype=int)
    ex_wav = np.linspace(230,810,num=59,dtype=int)

    grid = plt.GridSpec(2,3,wspace=0.4,hspace=0.3)
    ax1 = plt.subplot(grid[0,0:2])
    ax2 = plt.subplot(grid[0,2])
    ax3 = plt.subplot(grid[1,0:2])
    ax4 = plt.subplot(grid[1,2])

    _2dfit = _2d_fitting()
    if LM_optimise:
        _2dfit.fit(dataset,param_file,"M0.csv",ex_wav,em_wav)

    _2dfit.evaluate(dataset,param_file,"M0.csv",ex_wav,em_wav)
    emPlot = _1d_slice(ax1,ax2,ax4,em_wav,ex_wav, dataset,_2dfit)
    exPlot = _1d_slice(ax3,ax2,ax4,em_wav,ex_wav,
dataset,_2dfit,emission=False)
    maps = contourMap(ax2,ax4,ex_wav,em_wav,dataset,_2dfit)

    axcolor = "lightgoldenrodyellow"
    updateax = plt.axes([0.8, 0.015, 0.1, 0.04])
    update_button = Button(updateax, "Update", color=axcolor,
    hovercolor="0.975")

```

```

update_button.on_clicked(update)

#optimise button is currently a place holder to call optimise
within the software
optimiseAmpax = plt.axes([0.65, 0.015, 0.1, 0.04])
optimiseAmp_button = Button(optimiseAmpax, "Optimise",
color=axcolor, hovercolor="0.975")

ax1.figure.canvas.mpl_connect("scroll_event",emPlot.onscroll)
ax1.figure.canvas.mpl_connect("axes_enter_event",emPlot.onscroll)
ax3.figure.canvas.mpl_connect("scroll_event",exPlot.onscroll)
ax3.figure.canvas.mpl_connect("axes_enter_event",exPlot.onscroll)
plt.show()

def update(event):
    _2dfit.evaluate(dataset,param_file,"M0.csv",ex_wav,em_wav)
    emPlot.fit_update()
    exPlot.fit_update()
    maps.update()

def optimiseAmp(event):

    emPlot.fit_update()
    exPlot.fit_update()
    maps.update()

##### Example use #####
run("DATASET.csv", "PARAMETER_FILE.csv")

```

A6: Quantification and Engineering of Trap State Emission using Two-Dimensional Fluorescence Spectroscopy for Solid State Zinc Oxide micro/nano structures

Table A6.1 - Purity and molecular weights of binding peptides used in this study.

Peptide Name	Sequence	Purity (%)	$M_r$	
			Expected	Actual
ZA2	GLHVMHKAYSSGAPPMPFF	80	2024.372	2137.579 (M+TFA)
GT-16	GLHVMHKVAPPRGGGC	94	1615.9	1615.8

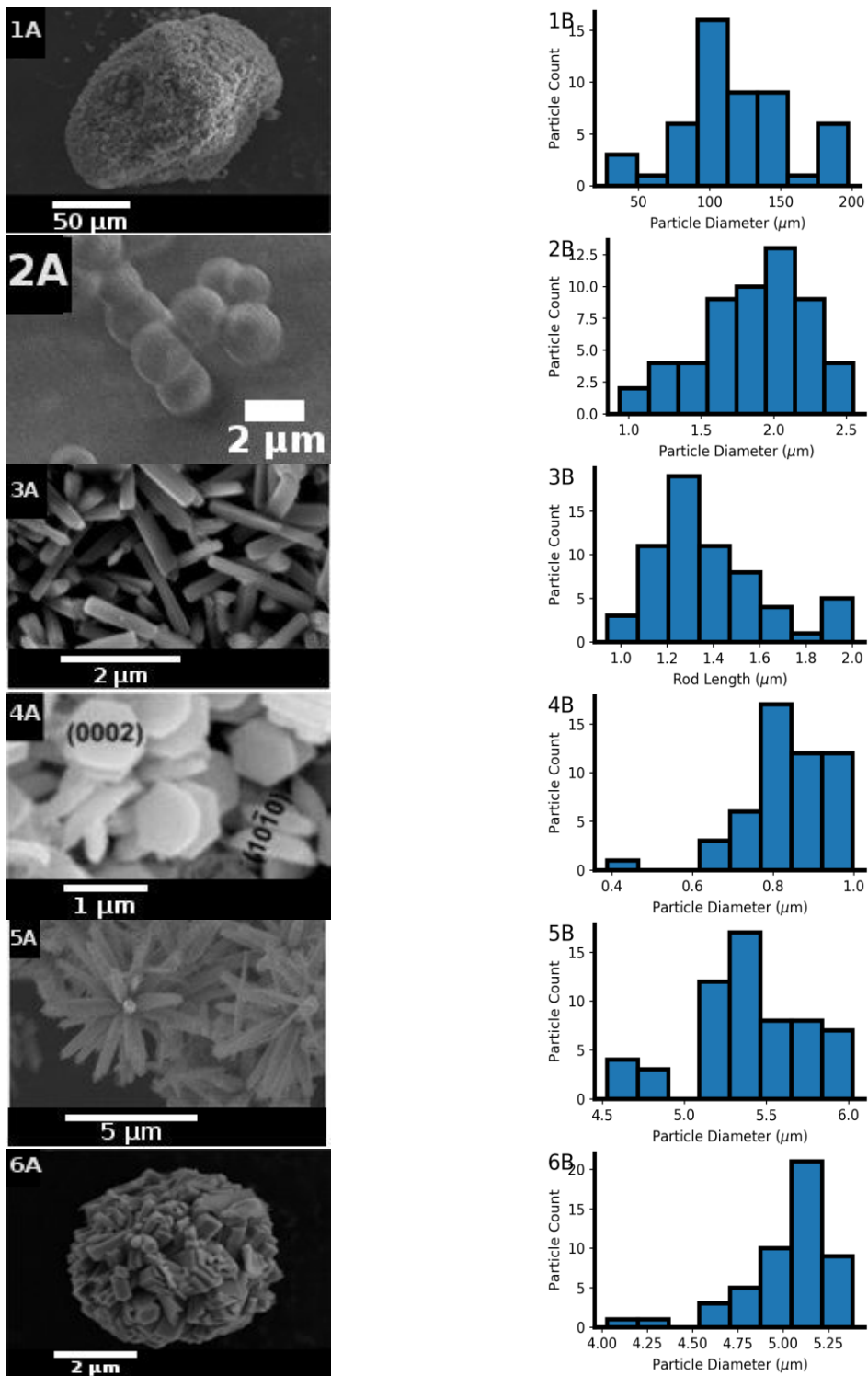


Figure A6.1 - Representative Scanning Electron Microscopy (SEM) micrographs (A) and size distribution data determined from multiple areas (B) for the ZnO library: analytical standard, microspheres, nanorods, nanoplatelets, nanoflowers & ZnOAu samples are denoted by 1-6.

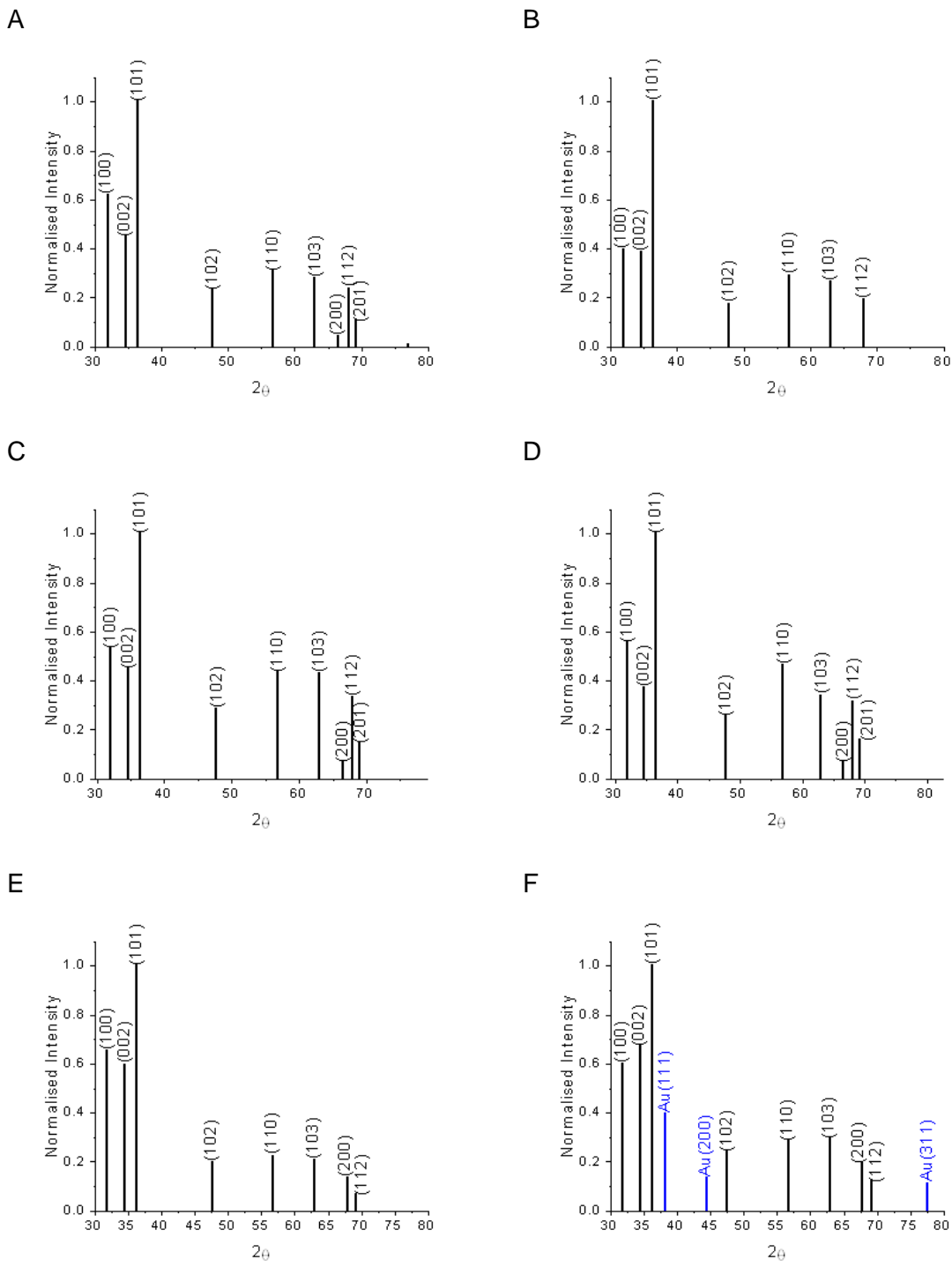


Figure A6.2 - Labelled powder X-ray diffraction line spectra for: A) ZnO analytical standard, B) ZnO microspheres, C) ZnO nanorods, D) ZnO nanoplatelets synthesised in the presence of GT16, E) ZnO nanoflowers synthesised in the presence of ZA2, F) ZnO-ZA2-Au nanocomposite where the blue lines show the Au crystal planes detected.

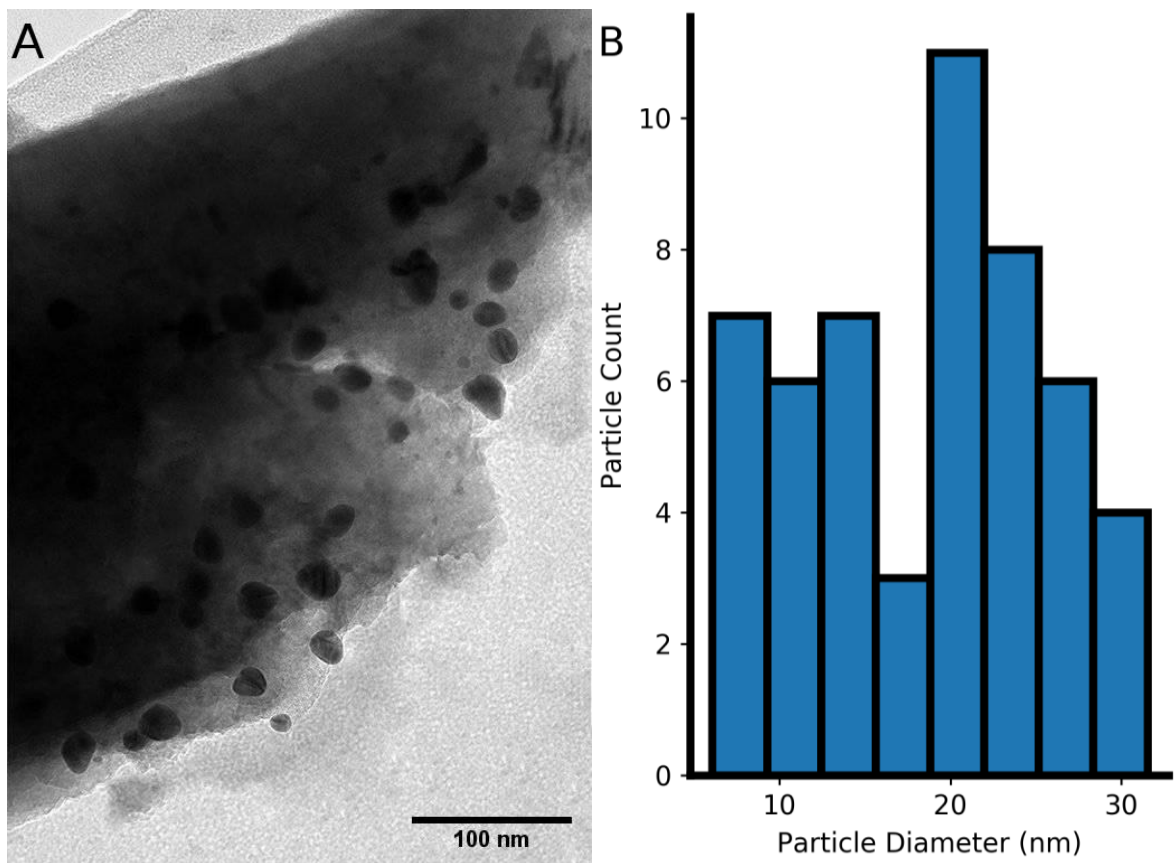


Figure A6.3 - Transmission Electron Microscopy micrograph of ZnO-Au nanocomposite A: Stitched transmission electron micrograph of ZnO-Au from multiple different micrographs to obtain a high resolution image of the microscale sample taking care to avoid artifacting the image. The dark regions in A correspond to embedded gold clusters in the ZnO matrix. B: Size distribution data of pseudo-elliptical inclusions in ZnOAu.

Table A6.2 - Decimalised percentile emission contribution for each transition observed in the untreated ZnO library. The following symbol representation is adopted: CB denotes conduction band, VB denotes valence band,  $V_O$  &  $V_{Zn}$  represent vacancies for oxygen and zinc respectively,  $O_i$  &  $Zn_i$  represent interstitials for oxygen and zinc respectively,  $VO_Zn_i$  represents a complex of an oxygen vacancy and zinc interstitial,  $V_{OO}/Zn_{IO}$  denotes a neutral oxygen vacancy or neutral zinc interstitial and  $O_{Zn}$  is an oxygen antisite. The signs present denote the charge of the defect, no sign or 0 means neutral and + or - denote a positive or negative charge respectively. All charges are single charges unless preceded by a number.

Transitions	Standard	Nanorod	Microsphere	Nanoplatelet	ZnO-ZA2	ZnO-Au
NBE -> VB	0.46	0.02	0.05	0.00	0.00	0.02
NBE -> Oi	0.03	0.00	0.26	0.00	0.00	0.03
$V(O)0$ or $Zni0$ -> $VO_+$	0.04	0.00	0.00	0.01	0.00	0.06
$Zni$ -> $V(Zn)$	0.01	0.00	0.27	0.15	0.12	0.11
$Zni$ -> $OZn$	0.10	0.02	0.00	0.01	0.01	0.01
$Zni$ -> $Oi$	0.10	0.14	0.00	0.04	0.02	0.11
$Zni^+$ -> $Oi$	0.24	0.26	0.00	0.00	0.04	0.00
$VO$ -> $VB$	0.02	0.11	0.02	0.27	0.16	0.09
NBE -> $VO_Zni$	0.00	0.16	0.00	0.01	0.00	0.05
$V(Zn2^-)$ -> $V(Zn^-)$	0.00	0.26	0.00	0.09	0.12	0.09
$V(Zn2^-)$ -> $Oi$	0.00	0.04	0.00	0.24	0.26	0.13
$V(O)0$ or $Zni0$ -> $Oi$	0.00	0.00	0.32	0.00	0.00	0.05
$Zni$ -> $VB$	0.00	0.00	0.00	0.05	0.12	0.12
$Zni$ -> $V(Zn^-)$	0.00	0.00	0.07	0.09	0.12	0.03
$Zni^+$ -> $V(Zn^-)$	0.00	0.00	0.02	0.01	0.02	0.00
NBE -> $OZn$	0.00	0.00	0.00	0.00	0.00	0.01
$V(O)0$ or $Zni0$ -> $OZn$	0.00	0.00	0.00	0.01	0.01	0.00
$V(O)0$ or $Zni0$ -> $VO_Zni$	0.00	0.00	0.00	0.00	0.00	0.00
$Zni^+$ -> $OZn$	0.00	0.00	0.00	0.01	0.01	0.05
$V(O)0$ or $Zni0$ -> $V(Zn)$	0.00	0.00	0.00	0.00	0.00	0.03
$V(Zn2^-)$ -> $V(Zn)$	0.00	0.00	0.00	0.00	0.00	0.01

Table A6.3 - Decimalised percentile emission contribution for each transition observed in the PVA treated ZnO library. The following symbol representation is adopted: CB denotes conduction band, VB denotes valence band,  $V_O$  &  $V_{Zn}$  represent vacancies for oxygen and zinc respectively,  $O_i$  &  $Zn_i$  represent interstitials for oxygen and zinc respectively,  $VO_Zn_i$  represents a complex of an oxygen vacancy and zinc interstitial,  $V_{O0}/Zn_{i0}$  denotes a neutral oxygen vacancy or neutral zinc interstitial and  $O_{Zn}$  is an oxygen antisite. The signs present denote the charge of the defect, no sign or 0 means neutral and + or - denote a positive or negative charge respectively. All charges are single charges unless preceded by a number.

Transitions	Standard	Nanorod	Microsphere	Nanoplatelet	ZnO-ZA2	ZnO-Au
NBE -> VB	0.53	0.07	0.06	0.00	0.01	0.03
NBE -> Oi	0.03	0.00	0.23	0.00	0.00	0.03
$V(O)0$ or $Zni0^-$ -> $VO^+$	0.02	0.00	0.00	0.01	0.00	0.05
$Zni^-$ -> VB	0.10	0.09	0.00	0.07	0.12	0.12
$Zni^-$ -> $OZn$	0.01	0.01	0.00	0.01	0.01	0.01
$Zni^-$ -> $Oi$	0.10	0.05	0.00	0.06	0.07	0.09
$Zni^+ -> Oi$	0.17	0.18	0.00	0.00	0.00	0.00
$VO$ -> VB	0.03	0.05	0.02	0.25	0.12	0.10
NBE -> $VO_Zn_i$	0.00	0.37	0.00	0.01	0.00	0.05
NBE -> $VO^+$	0.00	0.00	0.00	0.00	0.00	0.00
$V(O)0$ or $Zni0^-$ -> $Oi$	0.00	0.03	0.35	0.00	0.00	0.05
$Zni^+ -> V(Zn)$	0.00	0.02	0.00	0.00	0.00	0.00
$V(Zn2^-) -> V(Zn^-)$	0.00	0.08	0.00	0.08	0.08	0.10
$V(Zn2^-) -> Oi$	0.00	0.04	0.00	0.23	0.22	0.15
$Zni^-$ -> $V(Zn)$	0.00	0.00	0.27	0.17	0.24	0.11
$Zni^-$ -> $V(Zn^-)$	0.00	0.00	0.06	0.09	0.10	0.04
$Zni^+ -> V(Zn^-)$	0.00	0.00	0.02	0.01	0.01	0.00
NBE -> $OZn$	0.00	0.00	0.00	0.00	0.00	0.01
$V(O)0$ or $Zni0^-$ -> $OZn$	0.00	0.00	0.00	0.01	0.02	0.00
$V(O)0$ or $Zni0^-$ -> $VO_Zn_i$	0.00	0.00	0.00	0.00	0.00	0.00
$Zni^+ -> OZn$	0.00	0.00	0.00	0.01	0.01	0.05
$V(O)0$ or $Zni0^-$ -> $V(Zn)$	0.00	0.00	0.00	0.00	0.00	0.03
$V(Zn2^-) -> V(Zn)$	0.00	0.00	0.00	0.00	0.00	0.00

Table A6.4 - Decimalised percentile emission contribution for each transition observed in the NaBH<sub>4</sub> treated ZnO library. The following symbol representation is adopted: CB denotes conduction band, VB denotes valence band, Vo & V<sub>Zn</sub> represent vacancies for oxygen and zinc respectively, O<sub>i</sub> & Zn<sub>i</sub> represent interstitials for oxygen and zinc respectively, VoZn<sub>i</sub> represents a complex of an oxygen vacancy and zinc interstitial, Vo<sub>0</sub>/Zn<sub>0</sub> denotes a neutral oxygen vacancy or neutral zinc interstitial and O<sub>Zn</sub> is an oxygen antisite. The signs present denote the charge of the defect, no sign or 0 means neutral and + or - denote a positive or negative charge respectively. All charges are single charges unless preceded by a number.

Transitions	Standard	Nanorod	Microsphere	Nanoplatelet	ZnO-ZA2	ZnO-Au
NBE -> VB	0.79	0.01	0.30	0.00	0.00	0.04
NBE -> Oi	0.06	0.00	0.11	0.01	0.02	0.02
V(O)0 or Zni0 -> VO+	0.01	0.00	0.00	0.01	0.01	0.03
Zni -> VB	0.00	0.04	0.01	0.07	0.19	0.18
Zni -> V(Zn)	0.01	0.03	0.19	0.24	0.31	0.16
Zni -> OZn	0.00	0.02	0.00	0.01	0.01	0.01
Zni -> Oi	0.02	0.13	0.00	0.05	0.05	0.08
Zni+ -> Oi	0.09	0.16	0.00	0.00	0.00	0.00
VO -> VB	0.01	0.07	0.02	0.17	0.05	0.04
NBE -> VoZni	0.00	0.24	0.00	0.01	0.02	0.03
V(O)0 or Zni0 -> V(Zn-)	0.00	0.04	0.00	0.00	0.00	0.00
V(O)0 or Zni0 -> Oi	0.00	0.11	0.28	0.00	0.00	0.09
Zni -> V(Zn-)	0.00	0.01	0.06	0.09	0.07	0.04
V(Zn2-) -> V(Zn-)	0.00	0.10	0.00	0.05	0.04	0.06
V(Zn2-) -> Oi	0.00	0.04	0.00	0.24	0.18	0.10
Zni+ -> V(Zn-)	0.00	0.00	0.02	0.02	0.01	0.00
NBE -> OZn	0.00	0.00	0.00	0.00	0.00	0.01
NBE -> VO+	0.00	0.00	0.00	0.00	0.00	0.00
V(O)0 or Zni0 -> OZn	0.00	0.00	0.00	0.01	0.02	0.02
V(O)0 or Zni0 -> VoZni	0.00	0.00	0.00	0.00	0.01	0.00
Zni+ -> OZn	0.00	0.00	0.00	0.02	0.01	0.03
NBE -> V(Zn)	0.00	0.00	0.00	0.00	0.00	0.02
V(O)0 or Zni0 -> V(Zn)	0.00	0.00	0.00	0.00	0.00	0.05
V(Zn2-) -> V(Zn)	0.00	0.00	0.00	0.00	0.00	0.00

Table A6.5 - Determined quantum yield (QY) values for each transition observed in the untreated ZnO library. The following symbol representation is adopted: CB denotes conduction band, VB denotes valence band, Vo & V<sub>Zn</sub> represent vacancies for oxygen and zinc respectively, O<sub>i</sub> & Zn<sub>i</sub> represent interstitials for oxygen and zinc respectively, VoZni represents a complex of an oxygen vacancy and zinc interstitial, V<sub>Oo</sub>/Zn<sub>io</sub> denotes a neutral oxygen vacancy or neutral zinc interstitial and O<sub>Zn</sub> is an oxygen antisite. The signs present denote the charge of the defect, no sign or 0 means neutral and + or - denote a positive or negative charge respectively. All charges are single charges unless preceded by a number.

Transitions	Standard	Nanorod	Microsphere	Nanoplatelet	ZnO-ZA2	ZnO-Au
NBE -> VB	1.5E-03	1.5E-05	1.8E-03	7.3E-06	1.0E-05	4.8E-06
NBE -> Oi	1.0E-04	0.0E+00	6.5E-03	3.9E-05	1.2E-04	5.7E-06
V(O)0 or Zni0 -> VO+	2.1E-04	0.0E+00	0.0E+00	6.5E-05	1.3E-05	1.3E-05
Zni -> V(Zn)	4.3E-05	0.0E+00	4.9E-03	1.1E-03	3.3E-03	1.9E-05
Zni -> OZn	4.2E-04	6.8E-06	0.0E+00	4.4E-05	2.9E-04	2.1E-06
Zni -> Oi	3.8E-04	8.8E-05	0.0E+00	4.0E-04	6.7E-04	2.2E-05
Zni+ -> Oi	1.2E-03	2.3E-04	0.0E+00	0.0E+00	8.2E-04	0.0E+00
VO -> VB	2.9E-05	6.0E-05	2.2E-04	1.6E-03	3.8E-03	1.3E-05
NBE -> VoZni	0.0E+00	1.8E-04	0.0E+00	5.9E-05	1.1E-04	1.1E-05
V(Zn2-) -> V(Zn-)	0.0E+00	1.5E-04	0.0E+00	6.4E-04	2.9E-03	1.5E-05
V(Zn2-) -> Oi	0.0E+00	2.9E-05	0.0E+00	2.0E-03	6.9E-03	2.4E-05
V(O)0 or Zni0 -> Oi	0.0E+00	0.0E+00	6.5E-03	0.0E+00	0.0E+00	8.1E-06
Zni -> VB	0.0E+00	0.0E+00	3.0E-05	3.8E-04	3.2E-03	2.3E-05
Zni -> V(Zn-)	0.0E+00	0.0E+00	1.5E-03	7.1E-04	3.3E-03	6.3E-06
Zni+ -> V(Zn-)	0.0E+00	0.0E+00	3.5E-04	1.2E-04	3.5E-04	0.0E+00
NBE -> OZn	0.0E+00	0.0E+00	0.0E+00	3.5E-06	3.7E-05	1.7E-06
V(O)0 or Zni0 -> OZn	0.0E+00	0.0E+00	0.0E+00	6.7E-05	1.3E-04	0.0E+00
V(O)0 or Zni0 -> VoZni	0.0E+00	0.0E+00	0.0E+00	4.8E-06	0.0E+00	0.0E+00
Zni+ -> OZn	0.0E+00	0.0E+00	0.0E+00	6.2E-05	1.6E-04	1.0E-05
V(O)0 or Zni0 -> V(Zn)	0.0E+00	0.0E+00	0.0E+00	0.0E+00	0.0E+00	6.7E-06
V(Zn2-) -> V(Zn)	0.0E+00	0.0E+00	0.0E+00	0.0E+00	0.0E+00	1.2E-06

Table A6.6 - Determined quantum yield (QY) values for each transition observed in the PVA treated ZnO library. The following symbol representation is adopted: CB denotes conduction band, VB denotes valence band,  $V_O$  &  $V_{Zn}$  represent vacancies for oxygen and zinc respectively,  $O_i$  &  $Zn_i$  represent interstitials for oxygen and zinc respectively,  $VO_Zn_i$  represents a complex of an oxygen vacancy and zinc interstitial,  $V_{O0}/Zn_{i0}$  denotes a neutral oxygen vacancy or neutral zinc interstitial and  $O_{Zn}$  is an oxygen antisite. The signs present denote the charge of the defect, no sign or 0 means neutral and + or - denote a positive or negative charge respectively. All charges are single charges unless preceded by a number.

Transitions	Standard	Nanorod	Microsphere	Nanoplatelet	ZnO-ZA2	ZnO-Au
NBE -> VB	5.0E-03	1.1E-04	5.8E-03	9.3E-06	5.7E-05	5.2E-06
NBE -> Oi	2.1E-04	0.0E+00	1.2E-02	4.2E-05	4.3E-05	4.4E-06
$V(O)0$ or $Zni0$ -> $VO_+$	2.1E-04	0.0E+00	0.0E+00	5.8E-05	2.8E-05	1.1E-05
$Zni$ -> VB	5.9E-04	1.7E-05	3.0E-05	6.1E-04	1.1E-03	2.1E-05
$Zni$ -> $OZn$	9.3E-05	1.6E-06	0.0E+00	4.4E-05	6.5E-05	2.1E-06
$Zni$ -> $Oi$	6.2E-04	9.3E-06	0.0E+00	6.1E-04	7.3E-04	1.8E-05
$Zni^+$ -> $Oi$	1.6E-03	5.1E-05	0.0E+00	0.0E+00	0.0E+00	0.0E+00
$VO$ -> VB	7.1E-05	7.3E-06	4.7E-04	1.7E-03	8.2E-04	1.3E-05
NBE -> $VO_Zni$	0.0E+00	1.2E-04	0.0E+00	5.3E-05	4.3E-05	9.6E-06
NBE -> $VO_+$	0.0E+00	1.3E-07	0.0E+00	0.0E+00	0.0E+00	0.0E+00
$V(O)0$ or $Zni0$ -> $Oi$	0.0E+00	4.7E-06	1.6E-02	0.0E+00	0.0E+00	6.9E-06
$Zni^+$ -> $V(Zn)$	0.0E+00	4.5E-06	0.0E+00	0.0E+00	0.0E+00	0.0E+00
$V(Zn^{2-})$ -> $V(Zn^-)$	0.0E+00	1.3E-05	0.0E+00	6.5E-04	6.4E-04	1.5E-05
$V(Zn^{2-})$ -> $Oi$	0.0E+00	7.9E-06	0.0E+00	2.1E-03	2.1E-03	2.3E-05
$Zni$ -> $V(Zn)$	0.0E+00	0.0E+00	1.0E-02	1.4E-03	2.1E-03	1.8E-05
$Zni$ -> $V(Zn^-)$	0.0E+00	0.0E+00	2.5E-03	7.7E-04	8.3E-04	6.3E-06
$Zni^+$ -> $V(Zn^-)$	0.0E+00	0.0E+00	6.6E-04	1.2E-04	7.3E-05	0.0E+00
NBE -> $OZn$	0.0E+00	0.0E+00	0.0E+00	3.4E-06	1.6E-05	1.3E-06
$V(O)0$ or $Zni0$ -> $OZn$	0.0E+00	0.0E+00	0.0E+00	6.3E-05	2.0E-04	0.0E+00
$V(O)0$ or $Zni0$ -> $VO_Zni$	0.0E+00	0.0E+00	0.0E+00	4.5E-06	2.5E-06	0.0E+00
$Zni^+$ -> $OZn$	0.0E+00	0.0E+00	0.0E+00	7.2E-05	4.6E-05	8.1E-06
$V(O)0$ or $Zni0$ -> $V(Zn)$	0.0E+00	0.0E+00	0.0E+00	0.0E+00	0.0E+00	4.6E-06
$V(Zn^{2-})$ -> $V(Zn)$	0.0E+00	0.0E+00	0.0E+00	0.0E+00	0.0E+00	3.5E-07

Table A6.7 - Determined quantum yield (QY) values for each transition observed in the NaBH<sub>4</sub> treated ZnO library. The following symbol representation is adopted: CB denotes conduction band, VB denotes valence band, V<sub>O</sub> & V<sub>Zn</sub> represent vacancies for oxygen and zinc respectively, O<sub>i</sub> & Zn<sub>i</sub> represent interstitials for oxygen and zinc respectively, V<sub>OZn</sub> represents a complex of an oxygen vacancy and zinc interstitial, V<sub>O0/Zn<sub>i0</sub></sub> denotes a neutral oxygen vacancy or neutral zinc interstitial and O<sub>Zn</sub> is an oxygen antisite. The signs present denote the charge of the defect, no sign or 0 means neutral and + or - denote a positive or negative charge respectively. All charges are single charges unless preceded by a number.

Transitions	Standard	Nanorod	Microsphere	Nanoplatelet	ZnO-ZA2	ZnO-Au
NBE -> VB	2.0E-02	6.8E-06	4.3E-03	8.9E-06	2.1E-05	1.3E-05
NBE -> Oi	1.2E-03	0.0E+00	9.9E-04	2.9E-05	6.6E-05	5.7E-06
V(O)0 or Zni0 -> VO+	2.8E-04	0.0E+00	0.0E+00	2.9E-05	2.3E-05	8.1E-06
Zni -> VB	3.6E-05	9.9E-06	1.3E-04	2.6E-04	6.7E-04	5.0E-05
Zni -> V(Zn)	1.1E-04	1.9E-05	1.1E-03	8.7E-04	1.0E-03	4.0E-05
Zni -> OZn	1.0E-04	6.8E-06	0.0E+00	3.3E-05	3.4E-05	2.5E-06
Zni -> Oi	4.5E-04	6.7E-05	0.0E+00	2.1E-04	1.7E-04	2.3E-05
Zni+ -> Oi	2.5E-03	1.0E-04	0.0E+00	0.0E+00	0.0E+00	0.0E+00
VO -> VB	6.3E-05	3.0E-05	1.1E-04	4.8E-04	1.2E-04	8.8E-06
NBE -> VoZni	0.0E+00	2.2E-04	0.0E+00	3.2E-05	6.7E-05	7.6E-06
V(O)0 or Zni0 -> V(Zn-)	0.0E+00	2.3E-05	0.0E+00	0.0E+00	0.0E+00	0.0E+00
V(O)0 or Zni0 -> Oi	0.0E+00	7.0E-05	2.1E-03	0.0E+00	0.0E+00	2.1E-05
Zni -> V(Zn-)	0.0E+00	8.0E-06	5.1E-04	3.2E-04	2.0E-04	1.0E-05
V(Zn2-) -> V(Zn-)	0.0E+00	4.5E-05	0.0E+00	2.1E-04	1.3E-04	1.5E-05
V(Zn2-) -> Oi	0.0E+00	2.0E-05	0.0E+00	9.5E-04	5.9E-04	2.4E-05
Zni+ -> V(Zn-)	0.0E+00	0.0E+00	1.4E-04	8.0E-05	2.2E-05	0.0E+00
NBE -> OZn	0.0E+00	0.0E+00	0.0E+00	1.9E-06	5.6E-06	3.5E-06
NBE -> VO+	0.0E+00	0.0E+00	0.0E+00	2.9E-06	2.3E-06	0.0E+00
V(O)0 or Zni0 -> OZn	0.0E+00	0.0E+00	0.0E+00	3.9E-05	4.6E-05	5.5E-06
V(O)0 or Zni0 -> VoZni	0.0E+00	0.0E+00	0.0E+00	1.0E-05	4.1E-05	0.0E+00
Zni+ -> OZn	0.0E+00	0.0E+00	0.0E+00	4.4E-05	1.4E-05	7.2E-06
NBE -> V(Zn)	0.0E+00	0.0E+00	0.0E+00	0.0E+00	0.0E+00	4.0E-06
V(O)0 or Zni0 -> V(Zn)	0.0E+00	0.0E+00	0.0E+00	0.0E+00	0.0E+00	1.7E-05
V(Zn2-) -> V(Zn)	0.0E+00	0.0E+00	0.0E+00	0.0E+00	0.0E+00	1.2E-07

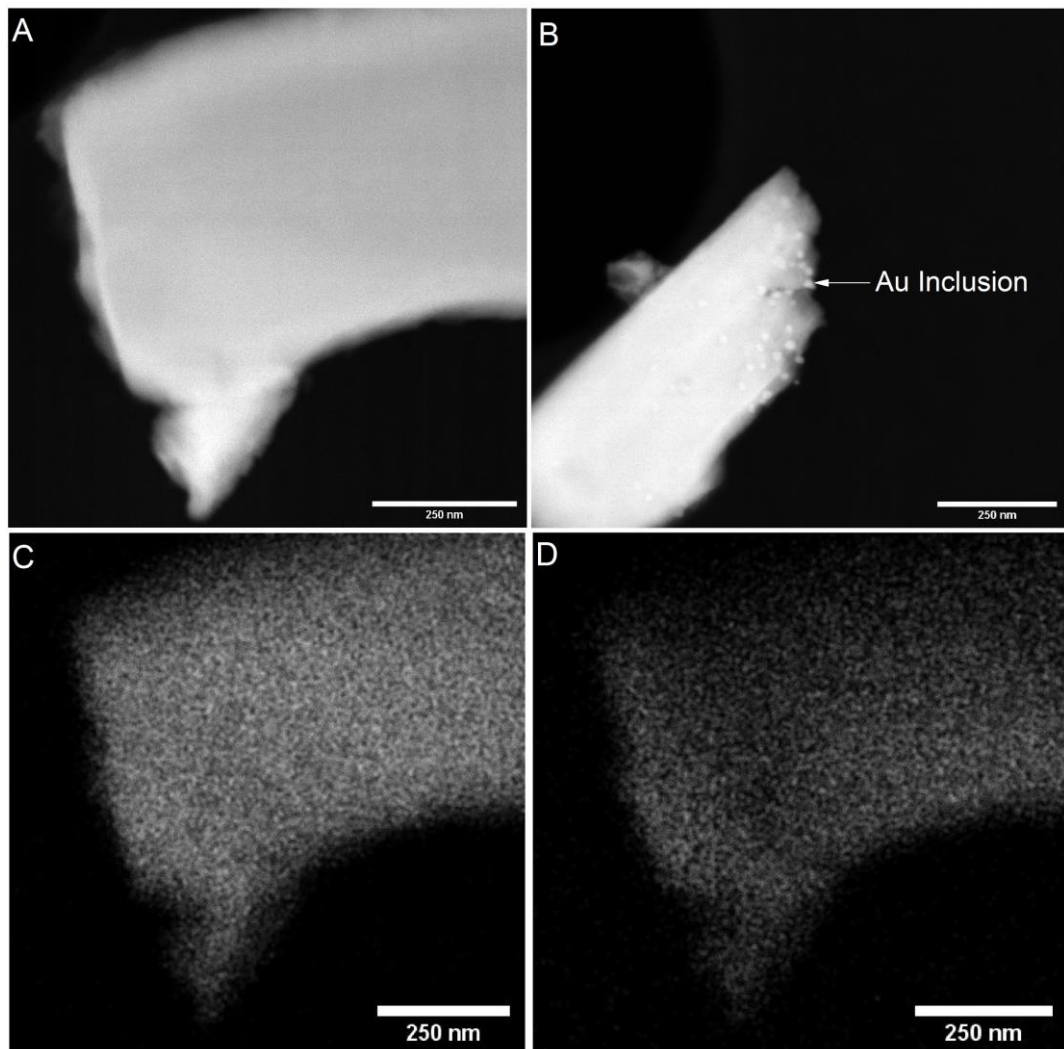


Figure A6.4 - High Annular Dark Field (HADF) STEM and EDX imagine of ZnOZA2 with comparison ZnOZA2Au HADF STEM image. A: HADF image of ZnOZA2 a consistent gray colouration is present over the sample B: HADF image of ZnOZA2Au a brighter gray colouration is present at sites where there are gold inclusions shown by annotation in the image. C&D: EDX maps of ZnOZA2 corresponding to HDAF image A, the co-pesence of Zn and O elements are consistent throughout the sample.

All scale bars in the images are sized at 250nm.

Script A6.1 - Python script developed in house to calculate the Mie scattering spectra for gold nanoparticles between 8-100nm. This script accounts for the effects of different environments such as ZnO or H<sub>2</sub>O through the use of the complex refractive index of the medium (nmed).

```
from scipy.constants import c
from mpmath import besselj, bessely, sqrt, pi, j, im, re, power, mpf,
fabs
import pandas as pd
import matplotlib.pyplot as plt

#Defining Constants
nmed = 1.4+0.1j #media index of ZnO, 1.33+9.2E-10j used for H2O
gammaBulk = 1E14/2.94 #relaxation frequency
vF = 1.4E6 #Fermi Speed
ne = 5.9E28 #Density of conducting electrons
mEFF = 1.1*9.1093897E-31 # Effective mass of conducting electrons
e = 1.60217733E-19 #Electric charge
e0 = 8.854E-12 #Dielectric permittivity of absolute vacuum, F m^-1
wp = sqrt((ne*e**2)/(e0*mEFF)) #plasma frequency

#Defining expansion limit
Lmax=3 #take expansion up to the third order

def nl(l,v):
    return v*sqrt(pi/(2*v))*(besselj(l+0.5,v)+j*bessely(1+0.5,v))

def dnl(l,v):
    upper = sqrt(pi/2)*(0.5*(besselj(-0.5+l,v)-
besselj(1.5+l,v))+0.5*j*(bessely(-0.5+l,v)-bessely(1.5+l,v)))
    lower = sqrt(1/v)
    ad = 0.5*sqrt(pi/2)*(besselj(0.5+l,v)+j*bessely(0.5+l,v))*sqrt(1/v)
    return upper/lower+ad

def wl(l,v):
    return v*sqrt(pi/(2*v))*(besselj(l+0.5,v))

def dwl(l,v):
    upper = sqrt(pi/2)*(besselj(-0.5+l,v)-besselj(1.5+l,v))
    lower = 2*sqrt(1/v)
    ad = 0.5*sqrt(pi/2)*besselj(0.5+l,v)*sqrt(1/v)
    return upper/lower+ad

def aL(enne,nmed,q1,q2,l):
    upper = enne*dwl(l,q1)*wl(l,q2)-nmed*wl(l,q1)*dwL(l,q2)
    lower = enne*dnl(l,q1)*wl(l,q2)-nmed*nl(l,q1)*dwL(l,q2)
    return -upper/lower
```

```

def bL(enne,nmed,q1,q2,l):
    upper = enne*wl(l,q1)*dw1(l,q2)-nmed*dw1(l,q1)*wl(l,q2)
    lower = enne*n1(l,q1)*dw1(l,q2)-nmed*dw1(l,q1)*wl(l,q2)
    return -upper/lower

def cross_section_extinction(enne,nmed,q1,q2,k):
    vals = []
    for l in range(1,4):
        val = (2*l+1)*(aL(enne,nmed,q1,q2,l)+bL(enne,nmed,q1,q2,l))
        vals.append(val)
    tot = sum(vals)
    upper = 2*pi*tot
    lower = (fabs(nmed)*k)**2
    return -upper/lower

coeff = [1.08883,0.3894,-0.03956,0] #CoeffA1, CoeffA2, CoeffA3 &
CoeffA4

for i in range(8,101,1): #Calculating the spectra for particle sizes between 8 and 100nm
    #radius of particles in meters
    diameter = i #nm
    r = diameter/2 *1E-9 # r works between 10-80

    #empiric rescale coefficients to calculate relaxation frequency

    Ax =
    coeff[0]+coeff[1]*(r*1E9)+coeff[2]*(r*1E9)**2+coeff[3]*(r*1E9)**3

    if Ax < 0:
        Ax = 0

    gamma = gammaBulk + (Ax*vF)/r

    mar, mai, ZnOSum = [], [], []

    #importing ZnOZA2 & ZnOZA2Au experimental data and the Literature epsilonBulk values
    epsilonBulk = pd.read_csv("Au_olmon.csv",header=None)

    for i in range(epsilonBulk.shape[0]):
        k = (2*pi)/(epsilonBulk.iloc[i][0]*1E-9)
        w = c*k
        d1 = (w**2)+(gammaBulk**2)
        d2 = (w**2)+(gamma**2)
        enne = sqrt(epsilonBulk.iloc[i][1]+(wp**2)*(1/d1-
        1/d2)+j*(epsilonBulk.iloc[i][2]+((wp**2)*(gamma/d2-gammaBulk/d1))/w)))

```

```

#Book bohren Huffman Chapt4 Eq4.53
#Qiang Fu, Wenbo Sun, AppLOpt 2001, 40(9) 1354

q = (2*pi*1E9/epsilonBulk.iloc[i,0])*r
q1 = q*nmed
q2 = q*enne
cext = cross_section_extinction(enne,nmed,q1,q2,k)
mar.append([epsilonBulk.iloc[i,0],re(cext)])

df_mar = pd.DataFrame(mar)

df_mar.to_csv("MieTheory_{0}nm.csv".format(diameter),header=False,index=False)

```

# Communications

## Publications (<https://orcid.org/0000-0001-7877-0900>)

Publications attained during the PhD are listed below in chronological order followed by submitted papers.

- 1) A. Sola-Rabada, M. Michaelis, **D. J. Oliver**, M. J. Roe, L. Colombi Ciacchi, H. Heinz and C. C. Perry, Interactions at the Silica-Peptide Interface: Influence of the Extent of Functionalization on the Conformational Ensemble, *Langmuir*, 2018, 34, 8255–8263.
- 2) **D. Oliver**, M. Michaelis, H. Heinz, V. V. Volkov and C. C. Perry, From phage display to structure: an interplay of enthalpy and entropy in the binding of the LDHSLHS polypeptide to silica, *Phys. Chem. Chem. Phys.*, 2019, 21, 4663–4672.
- 3) V.V. Volkov, **D. J. Oliver**, C.C. Perry, Polariton condensation and surface enhanced Raman in spherical ZnO microcrystals, *NComms*, **In-Press 04/09/20** DOI(10.1038/s41467-020-18666-4)
- 4) Z. Kuang , K.M. Singh, **D. J. Oliver**, P.B. Dennis, C.C. Perry and R.R. Naik, Gamma Estimator of Jarzynski Equality: Recovering Binding Energies From Noisy Dynamic Data Sets, *NCOMMS*, **under-going editorial revision prior to final acceptance**.

## Oral and Poster Presentations

- 1) Poster presentation – 13th International Conference on Materials Chemistry (MC13), Liverpool, England (10-13th July, 2017). Determination of Peptide-Gold binding behaviour using MP-SPR & QCM-D. **Daniel Oliver**, Victor Volkov, John Wallis and Carole C. Perry.
- 2) Oral and poster presentation – Science and Technology Annual Research Conference (STAR Conference), NTU, Nottingham, England (3-4th May, 2018). Kinetic and thermodynamic investigation of peptide-gold binding interactions. **Daniel Oliver**, Victor Volkov, John Wallis and Carole C. Perry.
- 3) Poster presentation – RSC Materials Chemistry Division Poster Symposium, Burlington House, London, England (23rd November 2018). Effects of crystal facets on gold-peptide binding interactions. **Daniel Oliver**, Victor Volkov, John Wallis and Carole C. Perry.

## Presentation Prizes

- 1) Directed Assembly Network DAGCN Summer School 2020 - (14/07/20 - 01/09/20) Group Presentation prize.